UNIVERSITAT POLITÈCNICA DE VALÈNCIA

Instituto Ingeniería Energética

Modelling and analysis of an air-conditioning system for vehicles based on magnetocaloric refrigeration

PhD Thesis

Bárbara Torregrosa Jaime

Supervisors

Prof. Dr. José Miguel Corberán Salvador

Dr. Jorge Payá Herrero

June 2016

Acknowledgements

I would like to thank all the people who have helped and encouraged me along my PhD studies, who have made me improve my skills and broaden my horizons.

Thanks to my supervisors, José Miguel Corberán and Jorge Payá, for sharing with me their knowledge and experience, and also for their guidance, confidence and support. Learning from you along these years has been a pleasure. Thank you also for giving me the opportunity to develop this project within the international team of the European project ICE.

Thanks to the researchers from DTU Energy, Kurt Engelbrecht, Christian Bahl, Kaspar K. Nielsen for their invaluable collaboration and guidance with the AMR model, and to Tian Lei for his collaboration with the single-blow experiments. Thanks to all of you for making me feel at Denmark like at home. In this sense I owe many thanks to my colleagues and house-mates at DTU Energy, very especially to Stefano Dall'Olio.

Thanks to my colleagues at the Insitute for Energy Engineering (IIE), where I have mostly developed this thesis, for making the work so pleasant with their attitude and friendliness.

And thanks to my family, for their continuous encouragement, confidence, support, help and interest in all the aspects of my life, including my studies. I owe my deepest gratitude to Pedro, not only for the fantastic artwork, but also for being always there for me.

Abstract

This PhD thesis studies the application of the magnetic refrigeration technology in the air-conditioning system of automobiles. Thermal models of each of the components of such a system have been developed with the purpose of determining accurately its global performance.

A dynamic one-dimensional model of a parallel-plate active magnetic regenerator (AMR) has been developed. The model is based in a new numerical scheme that reduces the computation time by 88% compared to the most commonly employed method. The model reproduces very accurately the passive regenerator cases with analytic solution and has been thoroughly validated against experimental results of both passive regenerator and AMR tests. The inclusion in the model of the magnetocaloric properties experimentally measured with a sample of the employed material, the demagnetizing effect, the fluid flow maldistribution and the losses to the ambient in the experimental setup have all been keys to obtain a good agreement with the experiments. The influence of the uncertainties and simplifications assumed when modelling these physical phenomena has been analyzed in detail, which has allowed the validation of different approaches.

Besides, a dynamic model of the air-conditioning (AC) system of an electric vehicle has been developed. Thermal models of each of the system components have been included, namely the cabin, the hydraulic loops with the air-to-coolant heat exchangers and the electric auxiliaries. The modelling methodology employed is based on the combination of the conservation equations with the semi-empirical fitting of the global heat transfer coefficient. Excellent validation results have been obtained with experimental results in a wide range of operating conditions.

The vehicle model has been employed to obtain the cooling and heating demand of a commercial full electric minibus, as well as the working temperatures. A broad optimization study has been carried out with the AMR model with the purpose of determining the design and working parameters of such a refrigerator that fulfil the cooling requirements of the vehicle with a minimum combined total system mass (affecting the weight of the vehicle and the economic cost) and electric consumption. The electric demand of the electrical AC auxiliaries has also been considered. Additionally, the heating performance of the optimal designs has been calculated. The application of AMR refrigerators in mobile air-conditioning systems is analyzed in comparison to the features of current vapor-compression systems.

Resumen

En la presente tesis doctoral se ha estudiado la aplicación de un refrigerador magnético en un sistema de aire acondicionado para automóviles. Con el fin de determinar las prestaciones de dicho sistema de manera global y precisa, se ha desarrollado un modelo térmico de cada uno de sus componentes.

Por un lado, se ha desarrollado un modelo dinámico unidimensional de regenerador magnético activo (AMR) de placas planas paralelas, basado en un nuevo esquema numérico que reduce el tiempo de cálculo hasta en un 88% respecto al esquema más empleado. El modelo reproduce con gran exactitud los casos de regenerador con solución analítica y ha sido validado exhaustivamente con resultados experimentales funcionando como regenerador pasivo y como AMR. Para obtener buenos ajustes ha sido clave la inclusión en el modelo de las propiedades magnetocalóricas medidas experimentalmente con una muestra del material empleado, el efecto desmagnetizante, la mala distribución del fluido y las pérdidas hacia el ambiente del montaje experimental. La influencia de las incertidumbres y las simplificaciones en el modelado de estos fenómenos se ha analizado detalladamente, lo cual ha permitido validar diferentes aproximaciones.

Por otro lado, se ha desarrollado un modelo dinámico del sistema de aire acondicionado de un vehículo eléctrico. Se incluye el modelo térmico de la cabina, los bucles hidráulicos para la distribución de la potencia térmica con los intercambiadores de calor agua-aire y los auxiliares eléctricos. La metodología empleada para el desarrollo de estos modelos, basada en la combinación de ecuaciones de conservación con el ajuste semi-empírico de los coeficientes globales de transmisión de calor, ha producido excelentes resultados de validación con resultados experimentales en un amplio rango de condiciones de funcionamiento.

El modelo del vehículo se ha empleado para obtener la demanda de refrigeración y calefacción de un minibús eléctrico comercial, así como las temperaturas de funcionamiento del sistema. Con el modelo de AMR se ha llevado a cabo un amplio estudio de optimización para determinar los parámetros de diseño y de funcionamiento de dicho refrigerador que cubren las necesidades de refrigeración del vehículo una masa del conjunto del sistema y un consumo eléctrico mínimos, incluyendo el consumo de los auxiliares. Adicionalmente se han calculado las prestaciones de calefacción de las combinaciones óptimas. La aplicabilidad de este sistema en automóviles se analiza en comparación con un sistema equivalente de compresión de vapor.

Resum

En aquesta tesi doctoral s'ha estudiat l'aplicació d'un refrigerador magnètic en un sistema d'aire condicionat per a automòbils. A fi de determinar les prestacions d'aquest sistema de manera global i precisa, s'ha desenvolupat un model tèrmic de cadascun dels components.

D'una banda, s'ha desenvolupat un model dinàmic unidimensional de regenerador magnètic actiu (AMR) de plaques planes paral·leles, basat en un nou esquema numèric que redueix el temps de càlcul fins d'un 88% respecte a l'esquema més emprat. El model reprodueix amb gran exactitud els casos de regenerador amb solució analítica, i ha sigut validat exhaustivament amb resultats experimentals funcionant com a regenerador passiu i com a AMR. Per a obtenir bons ajustos ha sigut clau la inclusió en el model de les propietats magnetocalòriques mesurades experimentalment amb una mostra del material emprat, l'efecte desmagnetitzador, la mala distribució del fluid i les pèrdues cap a l'ambient del muntatge experimental. La influència de les incerteses i les simplificacions en la modelització d'aquests fenòmens s'ha analitzat detalladament, la qual cosa ha permès validar diferents aproximacions.

D'altra banda, s'ha desenvolupat un model dinàmic del sistema d'aire condicionat d'un vehicle elèctric. S'hi inclouen el model tèrmic de la cabina, els bucles hidràulics per a la distribució de la potència tèrmica amb els bescanviadors de calor aigua-aire i els auxiliars elèctrics. La metodologia emprada per al desenvolupament d'aquests models, basada en la combinació d'equacions de conservació amb l'ajust semiempíric dels coeficients globals de transmissió de calor, ha produït excel·lents resultats de validació amb resultats experimentals en un ampli rang de condicions de funcionament.

El model del vehicle s'ha emprat per a obtenir la demanda de refrigeració i calefacció d'un minibús elèctric comercial, així com les temperatures de funcionament del sistema. Amb el model d'AMR s'ha dut a terme un ampli estudi d'optimització per determinar els paràmetres de disseny i de funcionament de la refrigeradora esmentada que cobreixen les necessitats de refrigeració del vehicle, una massa del conjunt del sistema i un consum elèctric mínims, incloent el consum dels auxiliars. Addicionalment s'han calculat les prestacions de calefacció de les combinacions òptimes. L'aplicabilitat d'aquest sistema en automòbils s'analitza comparant-la amb la d'un sistema equivalent de compressió de vapor.

Contents

List of figures

List of tables

Nomenclature

A	Surface (m^2)	h	Convection coefficient (W K^{-1} m^{-2})
A_c	Cross-sectional surface (m^2)	I	Global solar irradiance
a	Acceleration (m s^{-2})		on horizontal surface (W m^{-2})
a_s	Specific surface area (m^2 m^{-3})	I'	Global solar irradiance
B_{rem}	Remanence (T)		on tilted surface (W m^{-2})
Bi	Biot number (-)	i	Specific enthalpy (J kg^{-1})
C	Heat capacity (J K^{-1})	Δi_{vap}	Enthalpy of vaporisation (J kg^{-1})
c	Specific heat capacity (J K^{-1} kg^{-1})	k	Thermal conductivity (W K^{-1} m^{-1})
CFL	Courant-Friedrichs-Lewy	L	Length (m)
	condition (-)	L_t	Thermal entry length (m)
cNu	Nusselt number scaling factor (-)	L_h	Hydrodynamic entry length (m)
COP	Coefficient of performance (-)	M	Magnetization (A m^{-1})
D	Diameter (m)	M^*	Magnet efficiency parameter (-)
D_h	Hydraulic diameter (m)	m	Mass (kg)
d	Displacement (m)	$\dot{m}$	Mass flow rate (kg s^{-1})
DF	Degradation factor (-)	N	Demagnetization factor (-)
E	Energy (J)	N_{avg}	Average demagnetization factor (-)
e	Thickness (m)	n_{ch}	Number of channels (-)
Ec	Eckert number (-)	n_{pass}	Number of passes per tube (-)
EER	Energy Efficiency Ratio (-) (COP for cooling)	n_t	Number of time steps (-)
F	View factor (-)	n_x	Number of nodes in x direction (-)
f	Frequency (Hz)	n_y	Number of nodes in y direction (-)
f_f	Friction factor (-)	n_z	Number of nodes in z direction (-)
H	Magnetic field (A m^{-1})	Nu	Nusselt number [-]
H_f	Channel height (m)	Nu_m	Mean Nusselt number [-]
H_r	Plate height (m)	NTU	Number of transfer units (-)

$\dot{P}$	Electric power (W)		***Greek symbols***	
p	Pressure (Pa)		$\mathcal{A}$	Absorptance (-)
Pe	Péclet number (-)		α	Thermal diffusivity ($\text{m}^2\,\text{s}^{-1}$)
Pr	Prandtl number (-)		β	Air recirculation ratio (-)
$\dot{Q}$	Thermal power (W)		Γ	1D model validity parameter (-)
$\dot{q}$	Specific thermal power (W kg^{-1})		γ	Energy conservation error (-)
R	Heat capacity ratio (-)		δ	Air distribution ratio (-)
R_{cond}	Thermal resistance (K W^{-1})		$\mathcal{E}$	Emissivity (-)
$\boldsymbol{r}$	Position vector (m)		ε	Effectiveness (-)
Re	Reynolds number (-)		ϵ	Porosity (-)
RH	Air relative humidity (-)		η	Efficiency (-)
$RMSE$	Root mean squared error (-)		μ	Viscosity (Pa s^{-1})
S	Entropy (J K^{-1})		ξ	Numerical method parameter (-)
s	Specific entropy (J K^{-1} kg^{-1})		$\mathcal{P}$	Reflectance (-)
ΔS_M	Isothermal entropy change (J K^{-1})		ρ	Density (kg m^{-3})
Δs_M	Isothermal specific entropy change (J K^{-1} kg^{-1})		σ	Temperature distribution in a spatial node (K m^{-1})
T	Temperature (K)		$\mathcal{T}$	Transmissivity (-)
T_{Cu}	Curie temperature (K)		τ	Cycle period (s)
ΔT_{ad}	Adiabatic temperature change (K)		τ_{blow}	Fluid blow time (s)
ΔT_{span}	Temperature span (K)		φ	Thermal utilisation (-)
t	Time (s)			
Δt	Time step length (s)		***Subscripts***	
U	Global heat transfer coefficient (W K^{-1} m^{-2})		a	Air
V	Volume (m^3)		AC	Air conditioning supply
$\dot{V}$	Flow rate (m^3 s^{-1})		amb	Ambient
v	Speed (m s^{-1})		app	Applied
W	Width (m)		aux	Electrical auxiliaries
W_a	Air humidity ratio (kg_{vap} $\text{kg}_{\text{da}}^{-1}$)		avg	Average
$\dot{W}$	Power (W)		B	Bottom side
x	Position (m)		b	Cabin body
Δx	Spatial node length (m)		be	Beam
			C	Cold reservoir (heat source)
			c	Cooling

di	Diffuse		*ret*	Return
dem	Demagnetising		*s*	Sensible heat
dry	Dry condition		*sat*	Saturation
e	External		*sim*	Simulated
eff	Effective		*sky*	Sky
F	Front side		*sol*	Solar
f	Fluid		*sup*	Supply
fd	Fully-developed fluid flow		*surf*	Surface
fin	Fin		*T*	Constant temperature
g	Glazing		*th*	Thermocouple
gap	Magnet gap		*U*	Top side
H	Hot reservoir (heat sink)		*vap*	Water vapour
h	Heating		*ven*	Ventilation
HEX	Heat exchanger		*w*	Water
HP	Heat pump		*wet*	Wet condition
i	Spatial node number		$\mu_0 H$	Constant magnetic field
in	Inlet		0	Initial
ins	Insulation			

L   Left side

l   Latent heat

m   Interior mass

mag Magnet

mot Electric motor

occ Occupancy

out Outlet

p   Constant pressure

pipe Piping

pist Piston

plate Per plate

pump Pump

R   Right side

r   Solid regenerator material

re   Reflected

ref Reference

Upperscripts

n   Time step number

Physical constants

g   Acceleration of gravity, 9.8 m s^{-2}

σ_S Stefan-Boltzmann constant,
       $5.67 \cdot 10^{-8}$ W m^{-2} K^{-4}

μ_0 Permeability of vacuum,
       $4\pi \cdot 10^{-7}$ N A^{-2}

Acronyms and abbreviations

AC	Air conditioning
AHU	Air handling unit
AMR	Active magnetic regenerator
AMRR	Active magnetic regenerator refrigerator
CFC	Chlorofluorocarbon
CHEX	Cold heat exchanger (heat source)
GWP	Global warming potential
HCFCs	hydro-chlorofluorocarbon
HEIS	Hybrid explicit implicit numerical scheme
HEX	Heat exchanger
HHEX	Hot heat exchanger (heat sink)
HP	Heat pump
IMP	Fully implicit numerical scheme
MAC	Mobile air conditioning
MCE	Magnetocaloric effect
MCM	Magnetocaloric material
ODP	Ozone depletion potential
TDMA	Tri-diagonal matrix algorithm

Chapter 1

Introduction

1.1 Motivation

Refrigeration and air-conditioning systems account for nearly 20% of the worldwide energy consumption, which is continuously increasing. However, the widely employed vapor-compression system is already a mature technology that shows a small potential for further improvements in efficiency. Moreover, the traditional refrigerants used in such systems, such as the chlorofluorocarbons (CFCs) and the hydrochlorofluorocarbons (HCFCs), are being progressively restricted due to their ozone depleting potential (ODP) and their global warming potential (GWP). These challenges have led to an increasing interest in the development of alternative refrigeration and air-conditioning technologies over the last decades. One of the most promising alternatives is magnetocaloric energy conversion, i.e., magnetic refrigeration and heat pumping [1].

Magnetocaloric devices present several advantages with respect to vapor-compression systems. Magnetocaloric devices employ solid magnetocaloric materials as refrigerant, which have no ODP and no direct GWP. In such devices, the solid refrigerant is heated and cooled by applying a variable magnetic field. The associated processes are nearly isentropic in several magnetocaloric materials, which can lead to a high energy efficiency. Finally, the working fluid in room-temperature applications is typically an aqueous solution. Compared to the vapor-compression system, which relies on a pressurized gas, the fluid leakages, the maintenance and the operation noise are substantially reduced. These features make magnetic refrigeration and heat pumping a potentially attractive option for mobile air-conditioning systems, as supported by the European Commission through the FP7 Research Project ICE [2].

In the EU, the transport sector represents 32% of the final energy consumption and 22% of the CO_2 emissions [3]. Improving the performance of the air-conditioning (AC) system is a key to reduce the energy consumption of passenger vehicles. In average weather conditions, the use of the AC can reduce the fuel economy of mid-

sized petrol-driven automobiles by 20% [4] and the driving range of electric vehicles by 33% [5]. Peak loads can reduce these quantities by 50% in both cases. On the contrary to conventional cars, in electric vehicles the waste heat from the electric motor is not enough to fulfil the heating needs in winter, so the AC system has to satisfy this demand as well. Given that the current autonomy and comfort levels of electric vehicles represent a barrier for spreading their use, the design of the AC system becomes especially relevant.

At present, magnetic refrigeration is slowly becoming ready for the market. Nevertheless mobile air-conditioning (MAC) is a challenging application for current compact prototypes. Installed cooling and heating capacities in conventional automobiles range from 3 to 5 kW and from 5 to 10 kW respectively. Typical temperature differences between the heat sink and source are 35 to 45 K. These requirements may be revised by re-designing and controlling the MAC system with the focus in energy efficiency [6,7]. In any case, no published compact magnetic refrigerator prototype has approached these features up to date. In order to determine the feasibility of magnetic refrigerators and heat pumps in MAC systems, its performance beyond the state-of-the-art must be analyzed by means of simulation.

1.2 Overview of magnetic refrigeration at room temperature

The implementation of magnetocaloric energy conversion is a highly interdisciplinary task. Thermodynamics, heat transfer, magnetism and fluid dynamics are some of the subjects involved. In this section, the fundamentals of magnetic refrigeration applications at room temperature are described with a special focus on practical aspects.

1.2.1 Working principle

Magnetocaloric technology is based on the magnetocaloric effect (MCE), which is a change in magnetic entropy experimented by a material under a varying magnetic field. Under isothermal conditions, the material releases heat when a magnetic field is applied and absorbs heat when the magnetic field is removed. Under adiabatic conditions, the MCE results in a change in temperature. In this case, the temperature of the material increases when it is magnetized and decreases when demagnetized. These phenomena can be integrated into a thermodynamic cycle with the purpose of satisfying a cooling ($\dot{Q}_c$) or a heating ($\dot{Q}_h$) demand, as pictured in Fig. 1.1.
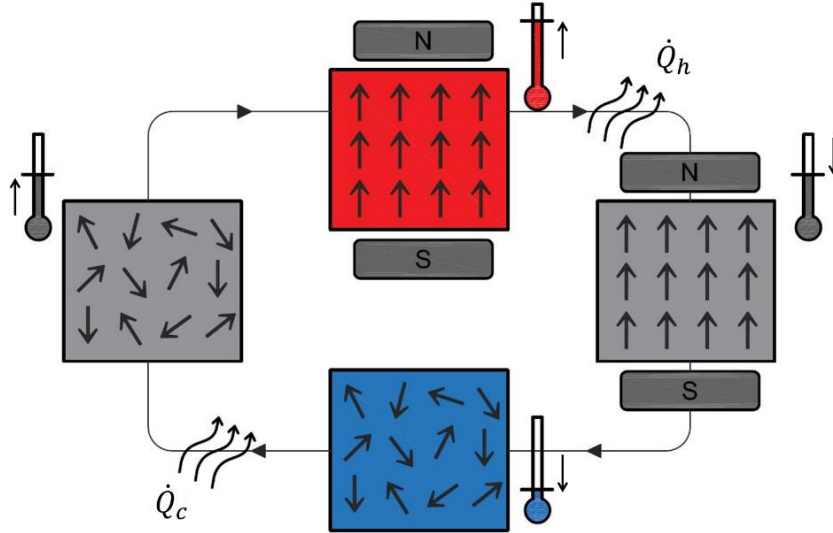
Fig. 1.1. Schematic description of a magnetic refrigeration cycle.

In order to perform practical refrigeration cycles, materials that exhibit an appreciable MCE must be employed. These are known as magnetocaloric materials (MCM). Permanent magnets are usually employed as the magnetic field source. However, under the magnetic fields produced by practical affordable permanent magnets (between 0.8 and 1.5 T), the temperature lift produced by the MCE in current MCMs is rather limited (up to about 5 K). With the purpose of overcoming the larger temperature spans encountered in practical applications at room temperature, most magnetic refrigerator prototypes rely on the active magnetic regenerative principle [1].

The active magnetic regenerative cycle [8] is performed over a porous bed of solid MCM, namely the active magnetic regenerator (AMR), as represented in Fig. 1.2. The AMR is placed between the heat source and the heat sink. A typically aqueous working fluid traverses the AMR bed with the purpose of carrying the heat produced by the MCE from one end to the other. Due to the interaction with this reciprocating flow, a temperature gradient is established along the AMR. Therefore, each infinitesimal part of the MCM undergoes its own thermodynamic cycle at a different temperature. This results in a sort of cascaded refrigeration cycle, which allows for increasing the net temperature span above the magnitude of the MCE.

For practical reasons, the AMR cycle is usually implemented as a Brayton-like thermodynamic cycle [9]. This cycle consists of four stages, which ideally comprise two isofield and two isentropic processes (Fig. 1.2):

1: Magnetization. The magnetocaloric material is magnetized adiabatically. Hence its temperature increases due to the MCE.

2: Cold blow. The working fluid in the cold end (heat source) flows through the voids in the AMR bed, which is still magnetized. The fluid flow cools the magnetocaloric material, and enters the hot side. The heat absorbed by the fluid is rejected in the hot heat exchanger (HHEX) or heat sink.

3: Demagnetization. The magnetic field is removed. The adiabatic demagnetization causes a decrease of the temperature of the magnetocaloric material due to the MCE.

4: Hot blow. The same working fluid flows in the counter-flow direction, from the hot to the cold end of the demagnetized AMR bed. The fluid transfers heat to the magnetocaloric material, which returns to the initial temperature distribution if the periodic steady state has been reached. The cooled fluid entering the cold heat exchanger (CHEX) or heat source can then accept a cooling load.
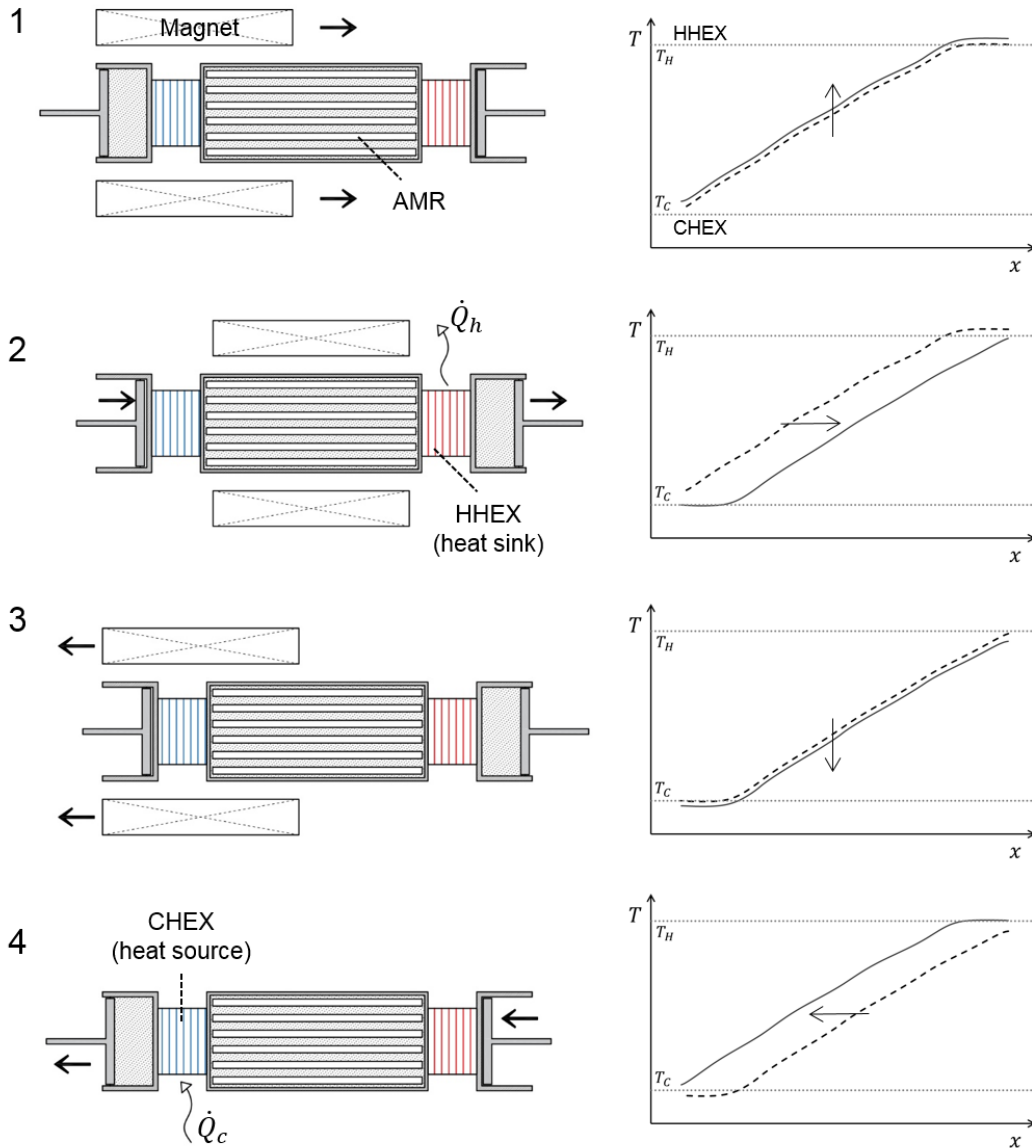
Fig. 1.2. The AMR Brayton cycle and temperature profiles along the AMR.
1: Magnetization. 2: Cold blow. 3: Demagnetization. 4: Hot blow. Adapted from [10].

Fig. 1.3 represents the total AMR Brayton cycle in a T-s diagram. As observed by Kitanovski et al. [1], this scheme reveals that the maximum temperature difference of the working fluid over the heat exchangers at each side cannot exceed the adiabatic temperature change (ΔT_{ad}) of the MCM. This magnitude also defines the maximum

refrigeration and heating capacities of the MCM. Recalling that in current setups the MCE can be up to about 5 K, one can expect that relatively large mass flow rates will be required for the practical application of magnetic refrigeration [11].
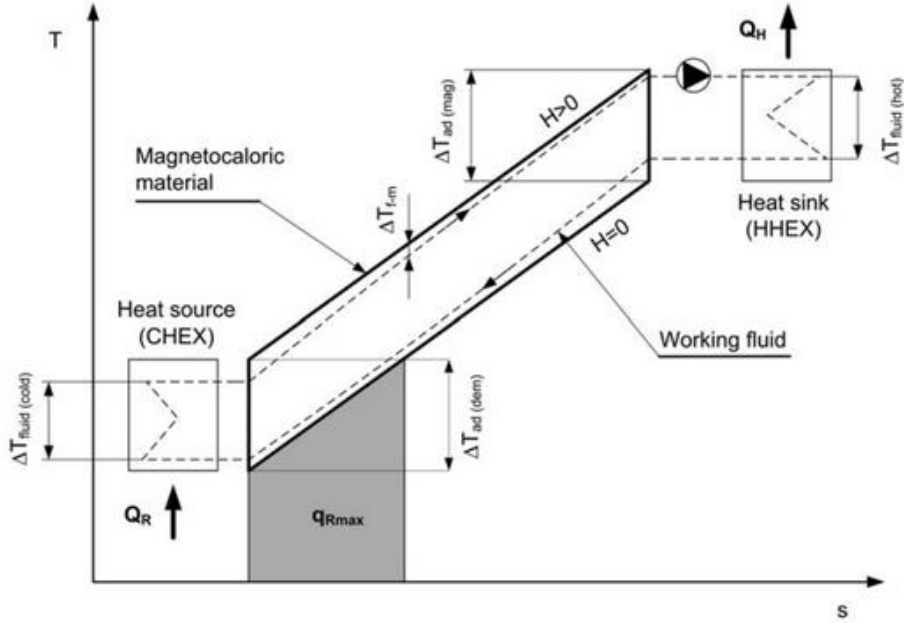
Fig. 1.3. T-s diagram of the total AMR Brayton cycle. Reproduced from [1].

1.2.2 Magnetocaloric materials

The characteristics of MCMs determine in a great extent the performance of AMR devices, where they act as the active substance and also as thermal regenerators. Hence the more decisive features of a MCM are their magnetothermal properties, which determine the intensity of the MCE and its behavior as regenerator.

The intensity of the MCE is characterized as the isothermal entropy change (ΔS_M) or the adiabatic temperature change (ΔT_{ad}) when varying the magnetic field in the MCM. These quantities depend on magnetization of the material (M) and are coupled through its heat capacity at constant magnetic field ($C_{\mu_0 H}$) as follows.

The fundamental Maxwell relation (Eq. 1.1) for isobaric and isochoric conditions relates entropy with magnetization. ΔS_M can be obtained by integrating this expression over an isothermal magnetization process (Eq. 1.2).

$$\left(\frac{\partial S}{\partial H} \right)_T = \mu_0 \left(\frac{\partial M}{\partial T} \right)_{\mu_0 H} \tag{1.1}$$

$$\Delta S_M(T, H) = \mu_0 \int_{H_1}^{H_2} \left(\frac{\partial M(T, H)}{\partial T} \right)_{\mu_0 H} dH \tag{1.2}$$

Besides, the entropy and the temperature are coupled through the definition of the heat capacity at constant magnetic field (Eq. 1.3). If an isentropic process is considered, the ΔT_{ad} can be deduced by combining and integrating Eqs. (1.1) and (1.3) into Eq. (1.4).

$$\left(\frac{\partial S}{\partial T}\right)_{\mu_0 H} = \frac{C_{\mu_0 H}}{T} \tag{1.3}$$

$$\Delta T_{ad}(T,H) = -\mu_0 \int_{H_1}^{H_2} \frac{T}{C_{\mu_0 H}(T,H)} \left(\frac{\partial M(T,H)}{\partial T}\right)_{\mu_0 H} dH \tag{1.4}$$

From these expressions, the MCE is large when a large change in the magnetic field is caused or when the MCM presents a large change in magnetization with temperature. The latter magnitude peaks around the temperature at which the phase transition from ferromagnetic to paramagnetic state occurs, that is the Curie temperature (T_{Cu}). Therefore, the MCE is expected to be significant around that point.

According to their magnetic phase transition order, MCMs are divided into first-order and second-order materials (Fig. 1.4).
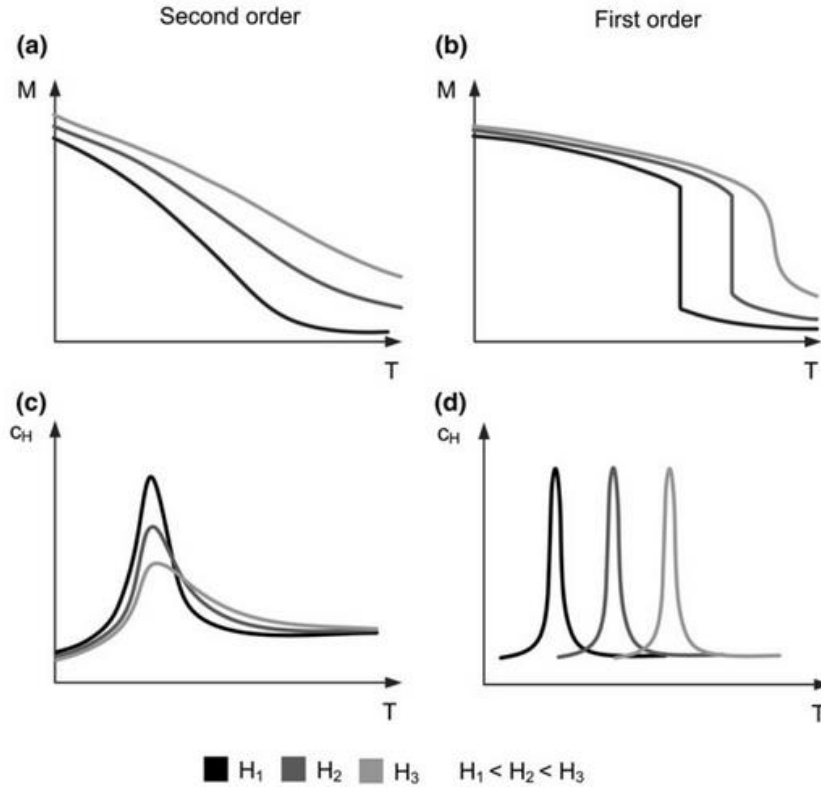
Fig. 1.4. Schematic properties of MCMs according to their magnetic phase transition order. Reproduced from [1].

In a second-order phase transition the magnetization varies continuously with temperature (Fig. 1.4a), while in a first-order phase transition the change is discontinuous due to an additional structural deformation (Fig. 1.4b). Also $C_{\mu_0 H}$ behaves differently. In practical terms, in second-order materials the MCE is virtually reversible, while first-order materials usually present a significantly larger MCE associated to thermal hysteresis. Generally, hysteresis causes a reduction in the performance of AMR devices [12].

As outlined in Fig. 1.4, in most current MCMs the MCE effect is only noticeable over a narrow range of temperatures around T_{Cu}. Two relevant consequences for AMR systems are derived from this fact. Firstly, the MCMs for an application at given temperatures must be selected according to the suitability of their T_{Cu}. Secondly, in applications where a large temperature span must be overcome, a layered AMR bed is required. A layered regenerator is made of successive layers of MCMs with different T_{Cu} along the direction of the temperature gradient. This solution allows for obtaining a larger average MCE along the length of the AMR [13–15].

Succinctly, an ideal MCM for practical AMR applications should have an intense MCE over a wide range of appropriate temperatures, near-zero hysteresis, suitable thermal properties for acting as regenerator, good manufacturing properties that allow for fabricating the regenerator into the suitable shape, high electrical resistivity to prevent eddy currents, resistance to corrosion, be environmentally friendly and have a reduced cost [1,16].

Nevertheless, the ideal MCM properties for AMR applications are not straightforward to deduce since the MCE is coupled with the heat transfer processes in the AMR bed [17]. In general, the value of ΔT_{ad} is more relevant than that of ΔS_M [18]. In certain conditions, the thermal conductivity also affects the AMR performance. In principle a high thermal conductivity is desirable in order to enhance heat transfer between the regenerator and the working fluid. However, a high conductivity can also destroy the thermal gradient established along the AMR and hence reduce its performance [19]. MCMs should hence be compared by considering the particular configuration of the AMR device.

The benchmark MCM for room-temperature applications is gadolinium (Gd), which is the only element that presents a noticeable MCE at near room temperature. Specifically, Gd experiences a second-order magnetic phase transition with negligible thermal hysteresis at around 293 K. The magnetothermal properties of Gd depend on the purity of the sample considered [20]. Commercial-grade Gd samples may exhibit a ΔT_{ad} around 3 K when it is magnetized from 0 to 1 T and a mean $c_{\mu_0 H=0}$ around 300 J kg^{-1} K^{-1} [21].

MCMs with different T_{Cu} are required to build layered AMR beds. With this purpose, Gd can be alloyed with other elements in order to shift up and down its T_{Cu} while keeping similar magnetocaloric properties [11,22]. For instance, Gd-Mn and Gd-Tb alloys can adjust the T_{Cu} from 293 K down to 279 and 270 K respectively [23,24], while GdSi type alloys can rise T_{Cu} up to 336 K [25]. A remarkable group of Gd alloys

are the Gd-Si-Ge compounds, which exhibit a giant MCE associated to a first-order transition [26].

The magnetocaloric and thermal properties of Gd turn it into the best performing MCM currently available for room-temperature applications [1]. Additionally, Gd is compatible with commercial automotive antifreezes and presents fairly good manufacturing characteristics [16]. However, the main drawback of Gd and their alloys is its high price [1,27].

A great effort in developing MCMs for room-temperature applications has been made over the last decades and there are other options besides Gd and its alloys. Detailed reviews on magnetocaloric materials and the magnetocaloric effect can be found in [25,27–29].

1.2.3 Magnetic refrigerator prototypes

Nearly 60 magnetic refrigerator prototypes have been reported since the first one was presented by Brown in 1976 [30]. Although the great majority of devices are based on the AMR cycle, a variety of designs can be found. Recently, a thorough review of the devices built up to the year 2014 and their design aspects has been carried out by Kitanovski et al. [1], while Zimm [10] presented a summary of practical design guidelines for AMRs. This section synthesizes the main design alternatives and highlights the most convenient configurations for the potential application of magnetic refrigeration in small scale commercial air-conditioning systems.

A magnetic refrigerator based in the AMR cycle consists of three main parts: the magnetic field source, the active magnetic regenerator (AMR) and a fluid flow distribution system. In order to perform the AMR cycle, the regenerator must be exposed to a varying external magnetic field synchronized with a reciprocating fluid flow between the heat source and sink (Fig. 1.2).

The magnetic field source in an AMR device can be either an electromagnet or a permanent magnet. The magnetic field produced by an electromagnet can be controlled, but electromagnets usually require a significant amount of cooling. Permanent magnets have proven to be a more efficient field source for small scale applications [14]. Among recent prototypes the most extended permanent magnet design principle is the Halbach array [31], which has been realized in a number of different magnetic assemblies [1].

In order to achieve a variation of the applied field over the AMR bed with a permanent magnet, either the magnet or the AMR bed must be moved relative to the other. This relative movement can be either linear or rotational. Note that the magnetization and demagnetization processes should be realized as fast as possible in order to minimize the heat transfer losses [32,33] and hence approach the adiabatic conditions of the ideal AMR cycle. Reciprocating devices (linear motion) present a high inertia, which in practice limits the operating cycle frequency of the device and

hence the attainable cooling power [1]. For practical applications, the results obtained up to date dismiss the reciprocating configurations in favour of the rotary ones.

Among the different implementations of rotary devices, one of the best and simplest options according to Kitanovski et al. [1] consists of employing multipole rotating magnets and static AMR beds. This configuration avoids the fluid leakages associated to the sealing of a rotary AMR bed. If the fluid flows in the axial direction, that is parallel to the rotation axis, the device can be easily scaled by designing a longer magnet assembly. Note that only one of the four sequential steps of the AMR cycle produces the useful effect (Fig. 1.2). In order to provide continuous cooling, prototypes intended for practical applications must contain several AMRs which are subjected to a different step of the cycle at a time. Fig. 1.5 shows a scheme of a recent prototype with such configuration [34].
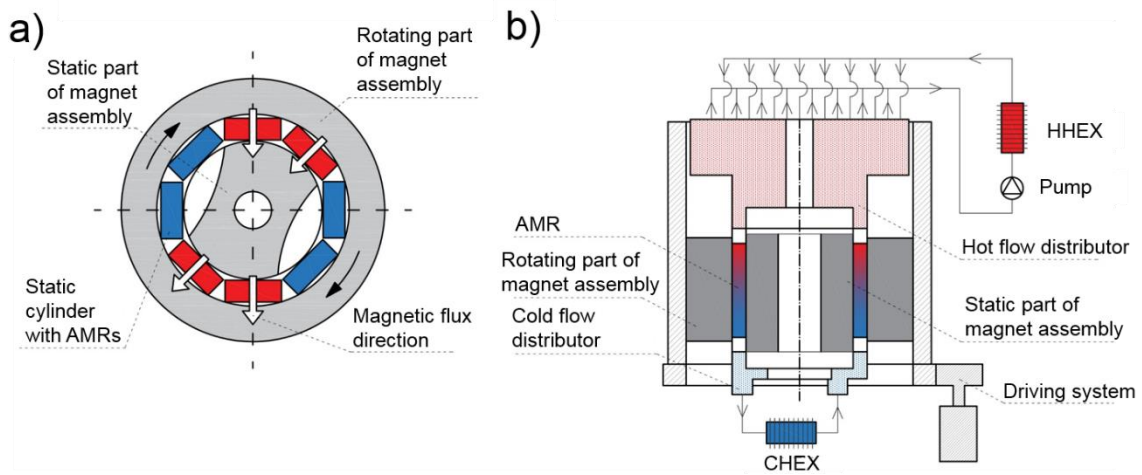
Fig. 1.5. Scheme of an AMR refrigerator with a rotating two-pole magnetic assembly and static AMR beds. a) Top view cross section. b) Longitudinal cross section. Adapted from [1,34].

The fluid flow distribution system pushes the working fluid through the AMR and into the heat exchangers to the cold and hot sources. An ideal working fluid for AMR applications should have low viscosity, high volumetric heat capacity, high thermal conductivity and allow for its oscillatory motion at high frequencies [33,35]. Water with antifreeze and corrosion-inhibition agents is usually employed due to its good heat transfer properties [10]. In order to achieve a reciprocating fluid flow into the AMR, either a bidirectional pump or a valve system can be implemented (Fig. 1.6). The first solution avoids the losses related to the use of valves (Fig. 1.6a), while the second one allows for a more efficient operation of the heat exchangers by providing them with a constant unidirectional flow (Fig. 1.5 and Fig. 1.6b). In any case, the switching of the direction of the fluid must be synchronized with the (de)magnetization processes and be as fast as possible [32,33].
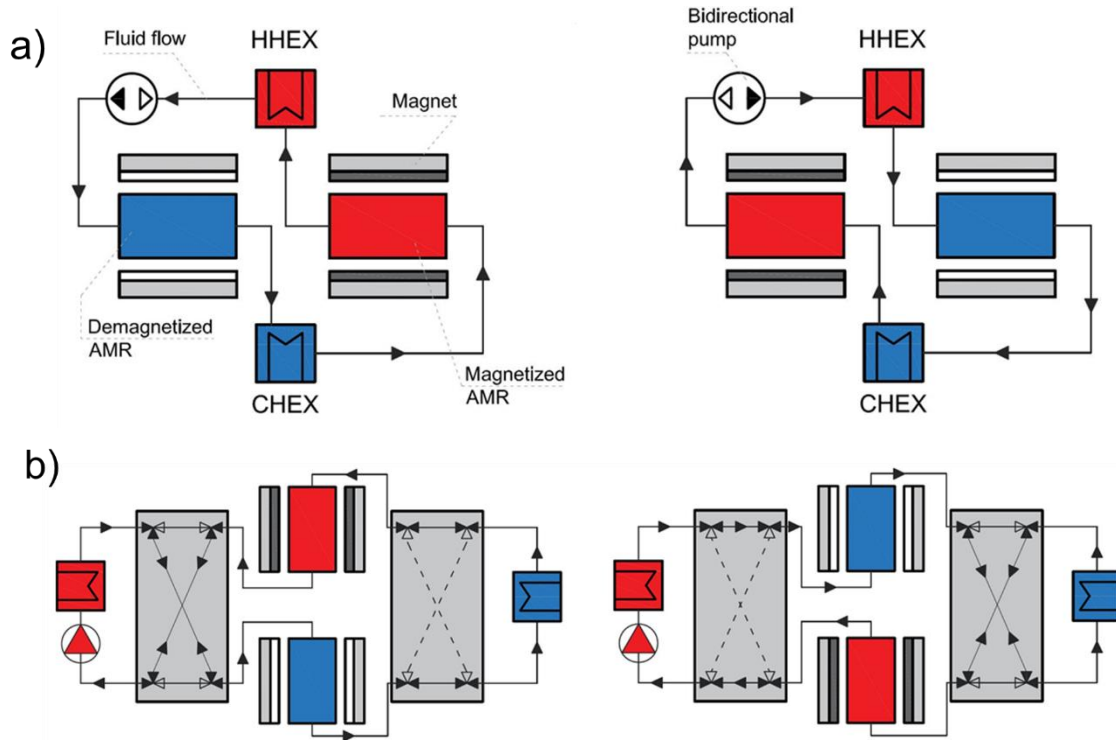
Fig. 1.6. Scheme of the fluid flow distribution system in an AMR with a) bidirectional pump and b) valves. Reproduced from [1].

Besides the composition of the AMR, its geometry is also a main design aspect. The MCM in the AMR is most commonly arranged as packed spheres, followed by packed particles and parallel plates [16]. In general, the structure of the AMR must be as fine as possible in order to enhance heat transfer with the fluid, however this may lead to significant viscous losses. Therefore, the geometry of the AMR should be carefully optimized in order to obtain the best compromise [36–38]. Numerical studies show that parallel plates can reach similar or even higher performance levels that packed spheres, provided that the plates are perfectly aligned [36,37]. The parallel plates present the additional advantage of reduced pressure drop. Nevertheless, the best experimental results up to date have been obtained with packed spheres AMRs. The reason is the flow maldistribution that occurs in the stacks of parallel plates build with relatively high tolerances, which has been shown to affect significantly the AMR performance [39–41].

The demagnetizing effect is another major loss mechanism that must be taken into account when designing AMR devices. Actually, the cause of the MCE in AMRs is the variation in the internal magnetic field induced inside the MCM due to the variation of an applied magnetic field. The magnitude of the internal field is generally lower than the applied field and depends, among other factors, on the geometry and the orientation of the MCM sample with respect to the applied magnetic field [42,43]. In order to minimize the demagnetizing effect, in general the MCM in the AMR must be distributed parallel to the magnetic field [43–45].

Finally, the control parameters of a permanent-magnet AMR device are the cycle frequency (f) and the fluid mass flow rate ($\dot{m}$). The cycle frequency refers to the number of AMR cycles performed by unit time, which is set by the rotational speed of the magnetic assembly (in the case of rotary magnets). An electric motor is commonly employed to drive the system. As for the fluid mass flow rate through the regenerator, it can be varied by means of a variable speed fluid pump. The design of the driving systems must be addressed with care since their associated losses can represent a significant part of the total energy consumption [46–48].

Table 1.1 summarizes the features of some state-of-the-art permanent-magnet AMR rotary prototypes. Magnetic refrigerators are characterized by their performance curves, which relate its cooling capacity ($\dot{Q}_c$) with the temperature span (ΔT_{span}) obtained along the regenerator (for a fixed temperature value of the heat sink). Each pair of control parameters yields a different performance curve. The efficiency of each working point is evaluated by means of the coefficient of performance (COP), which is the relation between the cooling capacity and the electric consumption of the device (electric motor and pump).

Table 1.1. State-of-the-art rotary magnetic refrigerators.

Magnetic refrigerator	AMR type, material, mass	Magnet assembly, magnetic field	f (Hz)	$\dot{m}$ (l min^{-1})	ΔT_{span} (K)	$\dot{Q}_c$ (W) (W kg^{-1})	COP
Astronautics Corporation of America [47]	Layered La-Fe-Si-H particles, 1.52 kg	Rotating Halbach, 1.5 T	4	21.2	0	3042 (2001)	2.5
					12	2090 (1375)	1.6
DTU Energy [34]	Layered Gd-Y spheres, 1.70 kg	Rotating Halbach, 1.13 T	0.75	3	5.5	138 (81.2)	4.6[1]
					16	60 (35.3)	1.35[1]
DTU Energy [46,49–51]	Gd spheres, 2.8 kg	Static Halbach, 0.9 T average	2	6.7	25.4	0	0
			1.8	11.4	0.3	1010 (361)	N.A.
			1.5	5.8	1.5	400 (143)	1.62
				10	13.8	400 (143)	1.04
University of Victoria [48]	Gd spheres, 0.11 kg	Rotating dual Halbach, 1.47 T	1.4	N.A.	29	0	0
				N.A.	2.5	50 (455)	1.6
					10	50 (455)	0.4
University of Salerno [52–54]	Gd spheres, 1.20 kg	Rotating Halbach, 1.1 T average	0.72	7	13.8	0	0
			0.38	5	0	200 (167)	2.5
					6	60 (50)	0.7

[1] Efficiency of electric pump not included.

1.2.4 Practical applications

The design of magnetocaloric devices attending to a specific practical application at around room temperature has been scarcely addressed in published literature, probably due to the state of development of the technology. Some studied applications include residential air-conditioning [11,54,55], refrigerator appliances [56,57], mobile air-conditioning [58,59], electronics cooling [47] and domestic heat pumps [60].

The constraints simultaneously imposed by practical applications are determining for many design choices. Common requirements include cooling or heating demand, source temperatures, acceptable efficiency, volume and weight limitations and, in the case of commercial devices, the economic cost. The complete system must be considered and analyzed in order to optimize its features [55,56,61].

As outlined in this section, there are multiple design and operation parameters that determine the performance of AMR refrigerators (AMRR). Therefore, simulation tools that take into account the coupled thermal, hydraulic and magnetic interactions in the AMR bed are indispensable to assess the design, optimization and operation of AMRRs [1,10].

1.3 Mobile air-conditioning systems

The air-conditioning (AC) system in automobiles guarantees a comfortable and safe inner environment. In summer, from 1 to 5 kW cooling power are required to cool and dehumidify the air. In winter, air heating and window defogging and deicing can take from 5 to 10 kW heating power. As detailed above, these requirements represent by 20% and up to 50% of the average energy consumption in current automobiles [4,5], which makes of the AC the largest auxiliary load on a vehicle.

Mobile air-conditioning (MAC) systems face severe working conditions, including high temperatures and vibrations, which affect their performance and their life. Refrigerant leakage is a major issue in these systems. MAC systems are also restricted in volume and in weight, since any additional load in a vehicle increases fuel consumption. The interaction with the rest of components of the vehicle must also be taken into account.

Fig. 1.7 shows the layout of current AC systems in conventional vehicles with an internal combustion engine and in electric vehicles. A detailed explanation of the main components of a mobile air-conditioning system is given in [62].
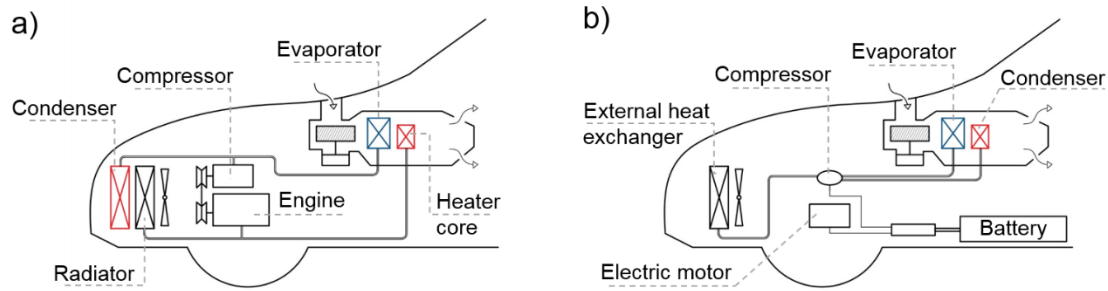
Fig. 1.7. Schematic AC system layout in a) internal combustion engine vehicles and b) electric vehicles. Adapted from [63].

In conventional vehicles (Fig. 1.7a), the core of the AC system is a vapor-compression refrigerator that cools directly the air inside the passengers' compartment by means of the evaporator. The heat rejection to the ambient is realized in the condenser, which is placed in front of the radiator. The mechanical compressor is most commonly driven by the engine. The heating needs of the vehicle are largely covered by the waste heat from the internal combustion engine. The engine cooling system includes a heater core which delivers heating power to the cabin. Both the evaporator and the heater core are placed inside of an air-handling unit (AHU), which regulates the temperature of the air flow to the cabin by mixing the air streams through each of these heat exchangers. This function is realized by means of an electric blower and several doors. The AHU also controls the income of fresh air into the cabin and allows the user to select the air-distribution and working mode (air-conditioning, heating, defogging or ventilation).

The characteristics of electric vehicles (Fig. 1.7b) have called for a redesign of this conventional AC system layout. The main difference is that the waste heat from the electric motor is relatively limited and at a low temperature (around 2 kW at 40 °C). In order to satisfy the heating demand of the vehicle, electric heaters have been traditionally employed. Nowadays commercial vehicles start including reversible heat pumps, which demand by 50% less energy than electric heaters in winter conditions [63,64]. Another substantial difference is that the electric motor stops running when the car is stopped. An electric compressor powered directly by the batteries is typically installed.

A first step to reduce the energy consumption in MAC systems is to reduce the thermal demand, and hence the installed capacity. Some effective actions to reduce the thermal load include controlling the inlet of fresh air to the cabin, installing solar reflective glazing and surfaces or ventilating the car while it is parked. The ventilation load can represent from 7 to 53% of the cooling demand of a vehicle [65], while the two latter solutions may decrease the soak temperature by up to 35% [6].

Secondly, the efficiency of current systems can be improved. The most studied strategy to reduce energy consumption of MAC systems is controlling the capacity of the compressor [62], which can lead to 17% to 27% energy savings [7,66] and can also

be applied to conventional vehicles. Cabin pre-conditioning strategies can lead 25% to 30% savings [7].

As reviewed by Qi [67], the AC systems for electric vehicles are moving towards an integrated layout of the thermal systems, that is the temperature control of the batteries and the cooling system of the inverter and the electric motor. In such systems, the refrigerator is integrated into a hydraulic loop in which a liquid working fluid distributes the cooling and heating power through the different subsystems (Fig. 1.8).
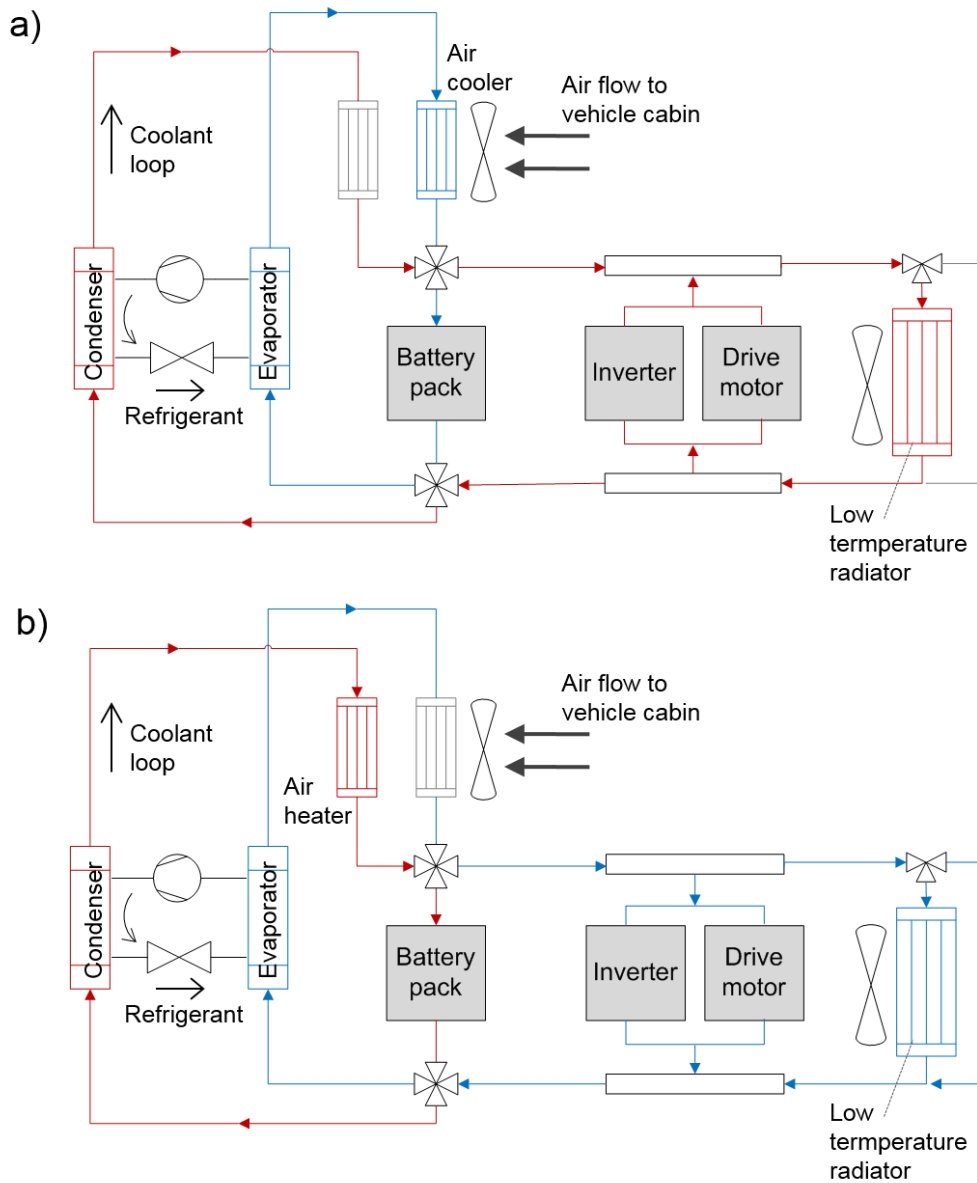
Fig. 1.8. Layout of integrated management of the vehicle thermal systems. a) Cooling mode. b) Heating mode. Adapted from [64].

In general, using an intermediate loop to cool the cabin air results slightly less efficient than cooling the air directly [7,64,68]. The real benefit of this layout is realized when the temperature of the batteries is optimized by means of the refrigerator, consequently enhancing their performance and their life. The recovery of the waste heat also provides energy savings in winter with a minor negative impact in summer conditions. In a preliminary study of such a system, Leighton has found a 22.5% reduction in the energy consumption compared to a conventional AC system [68]. Furthermore, this configuration allows for the use of a compact refrigerator, which facilitates the installation and maintenance while reducing the refrigerant leaks [64].

Employing a magnetic refrigerator would obviously eliminate the problems associated to the use of gaseous refrigerants in MAC systems. The integrated layout is especially convenient for the use of an AMR refrigerator (AMRR). The working fluid typically employed in automotive systems, a mixture of 50% ethylene glycol and water, is compatible with the AMRR. Integrating an AMRR into the hydraulic loop described would avoid the thermal losses associated to intermediate heat exchangers.

The application of magnetic refrigeration in electric vehicles has been studied within the FP7 European Project "ICE: Magnetic Refrigeration for Efficient Electric Air-conditioning" (2010-2014) [2]. In this research project, an AC system based on an AMRR was designed and installed in a commercial electric minibus. The present thesis has been partially developed within this frame.

1.4 Objectives and structure of the work

The **main objective** of this research is **to develop a reliable and efficient simulation tool to assess about the application of AMR refrigerators in the air-conditioning of vehicles.** The models developed with this purpose shall be useful beyond this project, so that they can also be employed for the optimization and design of different AMR applications or MAC technologies and layouts. In order to achieve these goals, the work has been structured as follows:

Firstly, a review of the literature in AMR modelling was carried out, which revealed the possibility of enhancing the simulation speed of current parallel-plate AMR models, as well as of improving the implementation of several physical phenomena that occur in the AMR bed. A new efficient and comprehensive model of a parallel-plate AMR has been developed in collaboration with DTU Energy, as described in Chapter 2.

Chapter 3 and Chapter 4 contain the comparison of the new AMR model with experimental data produced at DTU Energy. The influence in the validation results of the implemented physical phenomena, as well as their associated modelling uncertainties, has been carefully analyzed.

In addition, the requirements of the AC system of a vehicle must be accurately determined in order to obtain a reliable assessment about this specific application.

Simulation tools can assist this task, however they are not widely available in research literature. In Chapter 5 a global model of the AC system of an electric vehicle is developed with this purpose in the frame of the European Project ICE. The global AC system model consists of individual models of its different components, namely the passengers' compartment, the hydraulic loops, the heat exchangers, the electrical auxiliaries and their interaction with a refrigerator. Each of these subsystems has been validated against experimental data from the ICE Project.

Chapter 6 contains an assessment of the application of AMRRs in vehicles. A comprehensive parametric study is conducted with the purpose of finding the design and working parameters of the AMRRs that fulfil the cooling requirements of the vehicle with a minimum electric consumption and weight. The results are presented from a global point of view by including the energy consumption by the electrical auxiliaries of the AC system. In addition, the heating performance of the AMRR designs found is analyzed. The features of AMRRs are compared to those of vapor-compression devices.

Finally, Chapter 7 synthesizes the conclusions obtained from this work, which outline some of the future developments for the application of AMRRs in practical small-scale AC systems.

Chapter 2

The active magnetic regenerator model

2.1 Literature review of AMR models

A number of numerical AMR models have been developed with the purpose of predicting the AMR performance in terms of cooling capacity, temperature span and efficiency. Nielsen et al. [69] provided a detailed review of the AMR models presented up to 2010. More recently, Kitanovski et al. [1] offered a brief overview on this topic.

Two AMR modelling approaches can be found in literature: steady-state and dynamic modelling. On the one hand, steady-state AMR models are useful for estimating the AMR performance in a qualitative manner. Some examples can be found in [70–74]. The main advantage of these approach is its simplicity and computational efficiency. However their predictive capacity is limited, since they are unable to reproduce the interaction among the different processes in the AMR bed. In order to gain a detailed understanding of the AMR cycle, a time-dependent approach is required.

Dynamic AMR models are based in the time-dependent energy equations that describe the heat transfer processes in the solid AMR bed and the fluid. Nielsen at al. [69] discussed the implementation of the main phenomena that occur in the AMR bed. Apart from convective heat transfer and the MCE, the AMR equations usually include the longitudinal thermal conduction in the fluid and in the solid, the thermal dispersion due to hydrodynamic mixing in the fluid and the viscous dissipation. These terms may be negligible under certain circumstances [75]. The heat generation due to the eddy currents is generally neglected.

The MCE can be implemented directly through the adiabatic temperature change or as a source term in the equations (built-in method). In the latter case, the MCE can be calculated either with a theoretical approach or by means of the experimentally

measured MCM properties. If the purpose of the model is to reproduce accurately the behavior of an experimental AMR device, it is crucial to employ the built-in method together with experimental properties of the specific MCM employed [69]. However, this requires detailed and differentiable data sets of material properties, which may not be available. In any case, the thermodynamic properties of MCMs must be included consistently, according to Eqs. (1.1) and (1.3). The specific heat capacity of MCMs varies significantly with temperature and magnetic field so it should not be considered constant.

Other effects that have been included in AMR models are the temperature dependence of the physical properties, the time and spatial dependence of the magnetic field and fluid flow profiles during the AMR cycle, the thermal losses to the ambient, the demagnetizing effect, the fluid flow maldistribution and a layered AMR bed. Very recently, hysteresis has been included in some works that address MCMs with a first-order magnetic transition [12,76].

Regarding the number of dimensions solved in the AMR equations, one-dimensional (1D) models are the most common [11,36,71,77–90], although several 2D models [75,91–94] and a 3D model [95] have been published. Table 2.1 contains a summarized review of the mentioned models, indicating whether they include (cross) or not (void) the effects listed above. Only models that consider an aqueous liquid as the heat transfer fluid have been considered. Most of the reviewed models include a built-in MCE, however only a half of them rely on experimental MCM properties. Some models already include the effect of demagnetization, a few consider the ambient losses and only the model by Engelbrecht et al. [79] has included the effect of flow maldistribution. Nevertheless, these effects can have a significant influence on the simulation results [79]. In order to improve the validation results of AMR models with experimental data, the implementation of these phenomena could be further studied.

A key difference between 1D and 2D or 3D approaches is the implementation of heat transfer between the solid and the fluid, which is a crucial process in the AMR cycle. In 2D and 3D models the solid and the fluid are coupled through an internal boundary condition. On the contrary, in 1D models the conjugate heat transfer is modelled through the heat transfer coefficient (h), which is given by correlations that depend on the operating conditions. Very often the correlations available in literature do not represent exactly the conditions in the AMR bed, which can result in a significant uncertainty [96,97]. Specifically in the case of parallel-plate AMR 1D models, a variety of correlations is employed to calculate the heat transfer coefficient even for similar working conditions. For instance some authors consider the constant wall temperature boundary condition [11,36,84,87], while others assume constant heat flux [80]. The entrance effect is included by several authors [11,36,80]. Finally, Risser et al. [80] took also into account the effect of the rectangular geometry of the channels. However, the impact of these assumptions in the simulation results has not been analyzed in detail.

Parallel-plate AMR 1D models produce similar results to 2D models when the temperature gradients in the direction perpendicular to the fluid flow can be neglected

[98]. This is the case of thin plates and channels, as expected in a practical AMR. Compared to 2D and 3D models, 1D models are computationally less demanding. This feature is especially relevant in AMR applications, for which the performance is determined by a large number of parameters.

The numerical technique employed to solve the regenerator equations is decisive in minimizing numerical errors, instability and computational effort. However, few authors of AMR models specify which numerical approach they employ. The finite differences method with an implicit scheme has been applied in several cases [11,75,86], but also the explicit scheme [87] and the ADI method [92] have been utilized. The finite element method has also been employed [91,99], however compared to the finite differences method, it demands a significantly larger computational time to ensure the energy conservation [92]. Besides this observation by Nielsen et al. [92], who re-wrote the 2D AMR model in [91] and discussed the numerical scheme employed, the suitability of different numerical techniques in AMR applications has not been analyzed yet in depth.

In order to reach the main objective of this research, an accurate and fast AMR model is needed. The 1D approach seems to be the more appropriate for this task. Specifically, a parallel-plate AMR made of Gd is studied given the availability of experimental data for building and validating the model and thus ensuring its reliability.

In conclusion, **the literature review has revealed that the computational cost of current 1D parallel-plate AMR models can be reduced by employing a more suitable numerical scheme.** Besides, there are a number of **phenomena that influence significantly the performance of AMRRs** and hence must be included in a model whose purpose is to reproduce the actual behavior of experimental devices. In this sense, the 1D parallel-plate AMR model by Engelbrecht et al. [79] is a remarkable reference. However, the implementation of several of these effects should be **further studied in order to determine its impact on the simulation results.**

With the purpose of fulfilling the previous tasks, a **new 1D parallel-plate AMR model** is presented in this chapter. The model is **based in an efficient numerical scheme** adapted to the most relevant physical phenomena that occur in the AMR bed, as published in [100]. **In collaboration with DTU Energy, the main phenomena that affect the parallel-plate AMR performance have been discussed and implemented**, in some cases with a greater level of detail than current state-of-the-art 1D models.

Table 2.1. Review of published AMR models with a liquid heat transfer fluid.

Model	Dim.	Geom.	Built-in MCE	Exp. MCE	Solid cond.	F. cond.	Ther. disp.	$\dot{Q}_{vis}$	$\dot{Q}_{amb}$	T-dep. f. prop.	$H(x,t)$	$\dot{m}(t)$	Dem.	Flow maldis.	Graded AMR
[77]	1D	PS	X	X	X	X	X	X		X					
[78]	1D	Porous			X	X	X								
[11,79]	1D	PS, PP	X	X	X	X	X	X	X	X	X	X	X	X	X
[80–82]	1D	PP	X	X	X	X		X			X	X	X		
[83,84]	1D	Wires, PP	X										X		
[85]	1D	PP	X		X	X					X	X			
[36,86]	1D	PS,PP	X		X	X	X	X			X				
[71,88–90]	1D	PS	X		X	X	X				X				X
[87]	1D	PP			X	X	X	X	X						
[45,91,92,101]	2D	PP	X	X	X	X		X	X		X	X	X		X
[93]	2D	PS	X		X	X	X			X					
[75]	2D	PP		X	*	*		*				X			
[94]	2D	PP	X	X	X	X					X	X	X		
[95]	3D	PS	X		X	X							X		

Legend: *Dim.* = Solved dimensions. *Geom.* = AMR geometry: packed spheres (*PS*), parallel-plates (*PP*) or others. *Built-in MCE* = MCE implemented as a source term. *Exp. MCE* = MCE calculated from experimental MCM properties. *Solid cond.* = solid thermal conduction. *F. cond.* = fluid thermal conduction. *Ther. disp.* = thermal dispersion. $\dot{Q}_{vis}$ = viscous dissipation. $\dot{Q}_{amb}$ = heat losses to ambient. *T-dep f. prop.* = temperature dependence of fluid properties. $H(x,t)$ = spatial and time dependent applied magnetic field, opposed to a step-wise change. $\dot{m}(t)$ = continuous fluid flow profile, opposed to a step-wise change. *Dem.* = demagnetizing effect. *Flow maldis.* = effect of fluid flow maldistribution. *Graded AMR* = simulation of a layered AMR bed.

A cross (**X**) indicates that the published model includes the corresponding effect.

* Neglected term after discussing its influence.

2.2 Governing equations

Fig. 2.1 shows a scheme of the system, which is an AMR that consists of a stack of parallel plates made of one or more MCMs. The stack is subjected to a time-dependent fluid flow and limited by a cold and a hot reservoir at T_C and T_H temperatures respectively. The 1D model reproduces an AMR cycle determined by the fluid mass flow rate $(\dot{m}(t))$ at the entrance of the corresponding reservoir and the applied magnetic field $(\mu_0 H_{app}(x,t))$, which are inputs to the model and depend on the specific architecture of the simulated machine. The model calculates the temperature of the fluid $(T_f(x,t))$ and the solid $(T_r(x,t))$ parts of the regenerator at each moment of the AMR cycle.
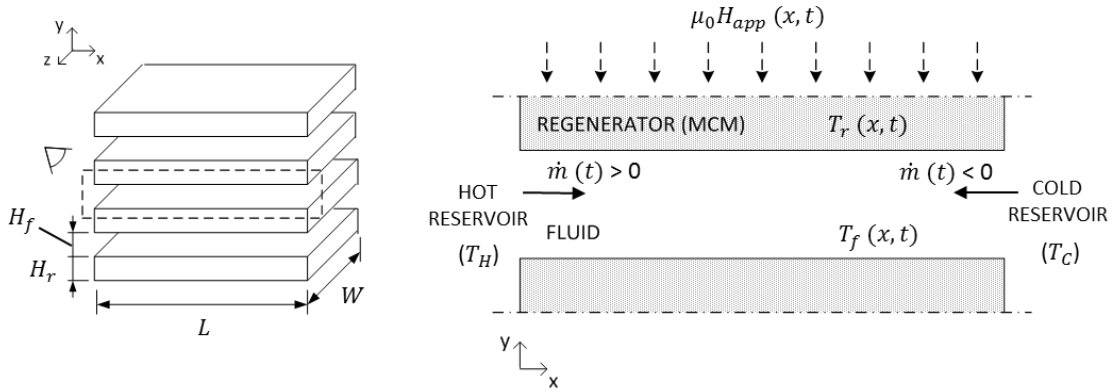
Fig. 2.1. Scheme of the 1D parallel-plate AMR model.

Assuming that the plates are uniformly stacked, the size of one regenerator bed is defined by its length (L), the channel width (W), the channel height (H_f), the plate thickness (H_r) and the number of channels (n_{ch}). The geometry of the regenerator is characterized by its total cross-sectional surface $(A_c$, Eq. 2.1), the specific surface area $(a_s$, Eq. 2.2) and its porosity $(\epsilon$, Eq. 2.3) [11].

$$A_c = n_{ch}W\left(H_f + H_r\right) \tag{2.1}$$

$$a_s = \frac{2W}{W\left(H_f + H_r\right)} \tag{2.2}$$

$$\epsilon = \frac{V_f}{V_f + V_r} = \frac{H_f}{H_f + H_r} \tag{2.3}$$

The governing equations that describe the change in temperature of the system are obtained from energy balances in the fluid (Eq. 2.4) and in the solid (Eq. 2.5).

$$\epsilon A_c \rho_f c_f \frac{\partial T_f}{\partial t} = -\dot{m} c_f \frac{\partial T_f}{\partial x} + \epsilon A_c k_f \frac{\partial^2 T_f}{\partial x^2} + h a_s A_c (T_r - T_f) + \frac{\partial p}{\partial x} \frac{\dot{m}}{\rho_f} \qquad (2.4)$$

$$(1 - \epsilon) A_c \rho_r \frac{\partial c_r T_r}{\partial t} = (1 - \epsilon) A_c k_r \frac{\partial^2 T_r}{\partial x^2} + h a_s A_c (T_f - T_r)$$

$$- (1 - \epsilon) A_c \rho_r T_r \frac{\partial s_r}{\partial \mu_0 H_T} \frac{\partial \mu_0 H}{\partial t} \qquad (2.5)$$

In Eq. (2.4), the term on the left hand side represents the energy storage in the fluid. On the right hand side, the first term is the advection term, the second describes the axial conduction, the third accounts for the convective heat transfer between the fluid and the solid and the fourth, for the heat generation due to viscous dissipation. Given that most AMRs work with liquids similar to water, the fluid is assumed to be incompressible and the variation of its properties with the temperature is neglected [69]. The thermal dispersion due to the eddy mixing of the fluid is ignored for the fluid flow between parallel plates in the laminar regime.

Similarly, in Eq. (2.5) the left-hand-side term describes the energy storage in the regenerator bed. On the right hand side, the first term accounts for the axial conduction, the second represents the convective heat transfer between the fluid and the solid and the third, the magnetocaloric effect (MCE). The heat gain due to the MCE is treated as the internal magnetic field-driven change in the regenerator entropy as in [11,79]. The internal magnetic field is calculated in the model from the applied magnetic field, considering the demagnetizing effect. The specific heat capacity (c_r) and the variation of entropy with the magnetic field at a constant temperature ($\partial s_r / \partial \mu_0 H_T$) are computed as function of the temperature and the magnetic field. Nevertheless the density (ρ_r) and thermal conductivity (k_r) are assumed to be constant, which is a good approximation for Gd [69].

The heat losses to the surroundings have not been included in the AMR governing equations. The relative importance of this term is given by the specific assembly and may be negligible compared to the parasitic losses in other parts of the device [102]. The post-calculation of the thermal losses to the ambient has provided good results with previous 1D models [46,79].

The governing equations of the AMR (Eqs. 2.4 and 2.5) are solved numerically with the finite differences method in a single channel which is assumed to be representative of the entire stack. The numerical solution is calculated at the center of each control volume defined by a spatial grid along the regenerator length (Fig. 2.2). This approach enables the definition of a conservative scheme.
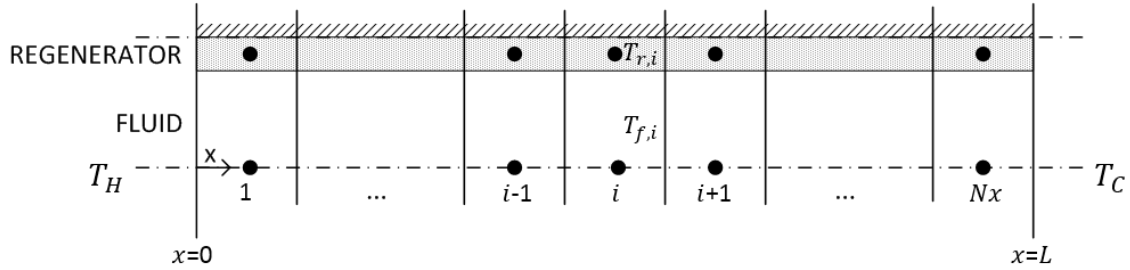
Fig. 2.2. Discretization and nomenclature used in the numerical model.

A new numerical scheme adapted to the most relevant physical phenomena that occur in the regenerator bed has been developed. In particular, the scheme optimally combines an explicit scheme for the fluid part of the regenerator with an implicit scheme for the solid part. The new scheme has been therefore named Hybrid Explicit-Implicit Scheme (HEIS).

2.2.1 Fluid equation

Advection problems are solved best by explicit techniques due to the hyperbolic character of the partial differential equations that describe them. However, diffusion problems have an elliptic character and hence require an implicit treatment. Consequently, **the most suitable numerical scheme to solve Eq. (2.4) depends on the relative importance of each term**, which in a first approach can be estimated with the Péclet number (Pe, Eq. 2.6).

$$Pe = \frac{vL}{\alpha} \tag{2.6}$$

Pe is obtained from the analytical solution of the convection-diffusion equation in steady state. Diffusion is negligible if Pe is greater than 100. Considering the most limiting AMR parameters found in recent literature (v=0.06 cm s^{-1}, L=40 mm, α=1.23 · 10^{-7} m^2 s^{-1} [33]), a value of Pe = 196 is obtained. Most of the published AMR devices work with fluid velocities one and two orders of magnitude larger, so in a typical AMR Pe is expected to be greater than 1000. Therefore, axial thermal conduction in the fluid can be neglected. This hypothesis will be verified in section 2.3.4 considering all the terms in Eq. (2.4).

The importance of the viscous dissipation term in the change of the fluid temperature can be checked with the Eckert number (Eq. 2.7) [103].

$$Ec = \frac{v^2}{c_f \Delta T} \tag{2.7}$$

Considering the highest flow speed found in AMR literature (v=36.7 cm s^{-1} [104]), assuming a boundary layer temperature difference ΔT=2 K and a mixture of water and glycol as the heat transfer fluid, a value of Ec≈2 · 10^{-5} is obtained. Since Ec is

much lower than 1, it can be concluded that the viscous dissipation term is negligible in typical AMR operating conditions. However, viscous dissipation may have a cumulative effect after a large number of cycles and may become important given that the current trend in AMRs is to employ a reduced channel spacing [36]. Therefore, the viscous dissipation term is finally included in the fluid energy equation as a source term.

If conduction in the fluid is neglected, an explicit scheme can be applied to discretize Eq. (2.4). A second order scheme has been developed, since first order schemes produce diffusion when the exact solution cannot be found numerically. **In order to ensure the energy conservation, Eq. (2.4) can be expressed in Eq. (2.8) as a flow-based energy balance for each control volume.**

$$
\frac{d}{dt} \int_{i-\frac{1}{2}}^{i+\frac{1}{2}} \epsilon A_c \rho_f c_f T_f(x,t) dx = v \epsilon A_c \rho_f c_f \left[T_f\left(x_{i-\frac{1}{2}},t\right) - T_f\left(x_{i+\frac{1}{2}},t\right) \right]
$$
$$
+ \int_{i-\frac{1}{2}}^{i+\frac{1}{2}} h a_s A_c \left[T_r(x,t) - T_f(x,t) \right] dx + \int_{i-\frac{1}{2}}^{i+\frac{1}{2}} \frac{\partial p}{\partial x} \frac{|\dot{m}|}{\rho_f} dx
$$

$$(2.8)$$

Eq. (2.8) is the energy balance when the fluid flows from the hot to the cold reservoir as illustrated in Fig. 2.1. In this case the fluid velocity is considered positive ($v > 0$). The expression for $v < 0$, that is when the fluid flows from the cold to the hot end, is analogous.

A constant convection coefficient (h) is assumed during a time step. The temperature at the center of the control volume (T_i) is considered to be equal to the mean temperature in the control volume i ($\bar{T}_i$), which is defined in Eq. (2.9).

$$
T_i = \bar{T}_i = \frac{\int_{i-\frac{1}{2}}^{i+\frac{1}{2}} T(x,t) dx}{\Delta x}
$$

$$(2.9)$$

Therefore, the value of the temperature of the fluid is found by substituting Eq. (2.9) into Eq. (2.8) and integrating over the time step (Eq. 2.10). The viscous dissipation term has been expressed more conveniently by employing the friction factor (f_f) [103].

$$
\bar{T}_{f,i}^{n+1} - \bar{T}_{f,i}^{n} = \int_{t^n}^{t^{n+1}} d\bar{T}_{f,i} = \frac{v}{\Delta x} \int_{t^n}^{t^{n+1}} \left[T_f\left(x_{i-\frac{1}{2}},t\right) - T_f\left(x_{i+\frac{1}{2}},t\right) \right] dt
$$
$$
+ \frac{h a_s}{\epsilon \rho_f c_f} \int_{t^n}^{t^{n+1}} \left(\bar{T}_{r,i} - \bar{T}_{f,i} \right) dt + \frac{f_f |v^3|}{2 D_h c_f} \Delta t
$$

$$(2.10)$$

In the **first term of the right-hand side of Eq. (2.10)**, the values of the temperatures at the boundaries of the control volume, $T_f(x_{i-1/2},t)$ and $T_f(x_{i+1/2},t)$,

are calculated with Eq. (2.4) by considering the change in temperature due to the incoming flow (advection) plus the effect of the heat transfer with the solid (convection) (Fig. 2.3). Viscous dissipation and axial conduction have been neglected in this approach.
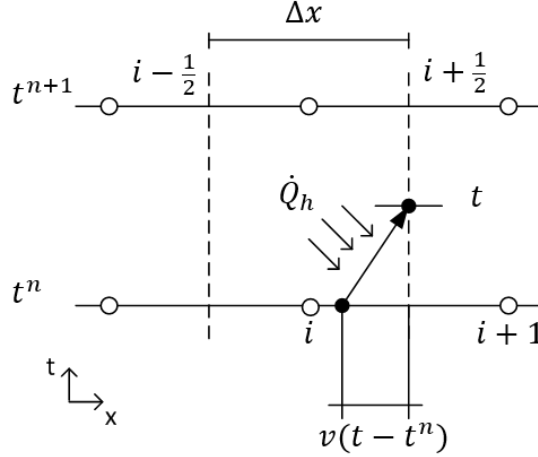
Fig. 2.3. Path followed by a fluid particle during a time step.

The **advection term is solved explicitly**, therefore the Courant-Friedrich-Lewy condition ($CFL{\leq}1$) is a necessary condition for convergence. CFL is defined as the ratio of the distance that the particle travels in one time step to the distance between two adjacent nodes (Eq. 2.11).

$$CFL = \frac{v\Delta t}{\Delta x} \tag{2.11}$$

The exact solution of the transport equation can be found numerically only when $v = \Delta x/\Delta t$, that is $CFL =1$. If $CFL <1$, then $x_i - v\Delta t$ is not defined in the spatial grid, so a linear distribution of the fluid temperature inside each cell i at each time step n is assumed (Eq. 2.12). This definition is consistent with Eq. (2.9).

$$T_f(x, t^n) = \bar{T}_{f,i}^n + (x - x_i)\, \sigma_{f,i}^n \tag{2.12}$$

With the purpose of minimizing the numerical diffusion (section 2.3), the MC Limiter approach [105] was chosen to calculate the slope of the temperature distribution ($\sigma_{f,i}^n$, Eq. 2.13).

$$\sigma_{f,i}^n = minmod\left(\frac{\bar{T}_{f,i+1}^n - \bar{T}_{f,i-1}^n}{2\Delta x}, minmod\left(2\frac{\bar{T}_{f,i}^n - \bar{T}_{f,i-1}^n}{\Delta x}, 2\frac{\bar{T}_{f,i+1}^n - \bar{T}_{f,i}^n}{\Delta x}\right)\right) \tag{2.13}$$

Where the function *minmod* is defined by Eq. (2.14).

$$minmod(a,b) = \begin{cases} a \;\; if \; |a| < |b| \; and \; ab > 0 \\ b \;\; if \; |b| < |a| \; and \; ab > 0 \\ 0 \;\; if \;\; ab \leq 0 \end{cases} \tag{2.14}$$

Regarding the **convection term, four different hypotheses** were tested to calculate heat transfer with the regenerator:

1. HEIS1: constant heat flux. $\Delta T = \bar{T}_{r,i}^n - \bar{T}_{f,i}^n$ is constant.
2. HEIS2: constant heat flux. $\Delta T = T_{r,i,0}^n - T_{f,i,0}^n$ is constant, where subscript 0 indicates that $T_{r,i}$ and $T_{f,i}$ are calculated at the beginning of the time step.
3. HEIS3: the temperature of the solid varies slowly. $T_{r,i}^n = \bar{T}_{r,i}^n$ is constant.
4. HEIS4: the temperature of the solid has a linear distribution in each cell, analogue to Eq. (2.12).

In the **second term of the right-hand side of Eq. (2.10)**, the integral of $\bar{T}_i^n$ can be **approached numerically by different techniques**. Eq. (2.15) was programmed with the purpose of applying the implicit method (ξ=1), the Crank-Nicholson method (ξ=0.5) and the explicit method (ξ=0).

$$\int_{t^n}^{t^{n+1}} \bar{T}_i dt = \left[(1 - \xi)\bar{T}_i^n + \xi \bar{T}_i^{n+1} \right] \Delta t \tag{2.15}$$

Eq. (2.10) is discretized by developing and substituting the previous hypotheses as detailed in Appendix A. The boundary condition is that the fluid enters the regenerator at the temperature of the corresponding reservoir (Eq. 2.16). When the fluid remains stagnant, the ends of the channels are assumed to be adiabatic towards the reservoirs.

$$If \; \dot{m} > 0 \; then \; T_f(x = 0, t) = T_H$$
$$If \; \dot{m} < 0 \; then \; T_f(x = L, t) = T_C \tag{2.16}$$

2.2.2 Regenerator equation

The regenerator equation is formulated in an **analogous way to the fluid equation** so they can be both coupled. Eq. (2.5) is expressed as a flow-based energy balance (Eq. 2.17).

$$\frac{d}{dt} \int_{i-\frac{1}{2}}^{i+\frac{1}{2}} (1-\epsilon)A_c\rho_r c_r T_r(x,t)dx = -k_r(1-\epsilon)A_c \left[\frac{2T_r(x_i,t) - T_r(x_{i-1},t) - T_r(x_{i+1},t)}{\Delta x} \right]$$

$$- \int_{i-\frac{1}{2}}^{i+\frac{1}{2}} ha_s A_c [T_r(x,t) - T_f(x,t)]dx - \int_{i-\frac{1}{2}}^{i+\frac{1}{2}} (1-\epsilon)A_c\rho_r T_r(x,t) \frac{\partial s_r}{\partial \mu_0 H_T} \frac{\partial \mu_0 H}{\partial t} dx \tag{2.17}$$

The time derivative of the magnetic field is approximated by applying the mean value theorem. Eq. (2.18) is obtained by employing the definition in Eq. (2.9) and integrating Eq. (2.17) over the time step. The **magnetocaloric properties** c_r and $\partial s_r / \partial \mu_0 H_T$ show a **significant dependence on the regenerator temperature and on the internal magnetic field**. In order to enable the use of relatively large time steps, these properties are **approximated by their mean values over the time step** (Eq. 2.19).

$$
\bar{T}_{r,i}^{n+1} - \bar{T}_{r,i}^{n} = \int_{t^n}^{t^{n+1}} d\bar{T}_{r,i} = \frac{k_r}{\rho_r \bar{c}_{r_i} \Delta x^2} \int_{t^n}^{t^{n+1}} \left(\bar{T}_{r,i+1} - 2\bar{T}_{r,i} + \bar{T}_{r,i-1} \right) dt
$$

$$
+ \frac{h a_s}{(1-\epsilon)\rho_r \bar{c}_{r_i}} \int_{t^n}^{t^{n+1}} \left(\bar{T}_{r,i} - \bar{T}_{f,i} \right) dt - \frac{1}{\bar{c}_{r_i}} \overline{\frac{\partial s_r}{\partial \mu_0 H}}_{T_i} \left[\frac{\mu_0 H_i^{n+1} - \mu_0 H_i^n}{\Delta t} \right] \int_{t^n}^{t^{n+1}} \bar{T}_{r,i} dt
$$

$$(2.18)$$

$$
\bar{c}_{r_i} = \frac{c_{r_i}^{\,n} + c_{r_i}^{\,n+1}}{2} \tag{2.19}
$$

Eq. (2.18) is discretized by employing Eq. (2.15). The ends of the regenerator are assumed to be adiabatic.

2.2.3 Numerical solution algorithm

Eqs. (2.10) and (2.18) in their discretized forms constitute a system of linear equations. Eq. (2.10) is substituted into Eq. (2.18) so that the latter is solved efficiently with the tri-diagonal matrix algorithm (TDMA). Since the values of $c_{r_i}^{n+1}$ and $\left(\partial s_r / \partial \mu_0 H_T \right)_i^{n+1}$ depend implicitly on $\bar{T}_{r,i}^{n+1}$, the solution is found iteratively. The present model has been implemented in MATLAB [106] as detailed in Appendix B.

2.2.4 Calculation of performance indicators

The AMR produces a cooling effect when the temperature of the fluid flow exiting the regenerator is lower than the one of the cold source. The cooling capacity can be calculated as the difference between the energy leaving and entering the regenerator through the cold side during the AMR cycle (Eq. 2.20). The heating capacity is computed in an analogous manner in the hot side (Eq. 2.21). The estimation of the temperature at the corresponding outlet boundary of the regenerator is included in the numerical scheme (Eq. 2.12).

$$
\bar{Q}_c = \frac{\int_{t=0}^{t=\tau} |v| \epsilon A_c \rho_f c_f \left[T_C - T_f(x = L, t) \right] dt}{\tau} \tag{2.20}
$$

$$
\bar{Q}_h = \frac{\int_{t=0}^{t=\tau} |v| \epsilon A_c \rho_f c_f \left[T_f(x = 0, t) - T_H \right] dt}{\tau} \tag{2.21}
$$

In order to produce the desired effect, the AMR receives a fluid pumping work input and a magnetic work input. The former is given by Eq. (2.22) and the latter can thus be deducted from an energy balance (Eq. 2.23).

$$\bar{W}_{pump} = \frac{\int_{t=0}^{t=\tau} \frac{|\dot{m}|}{\rho_f} \Delta p \, dt}{\tau} = \frac{\int_{t=0}^{t=\tau} \frac{f_f |v^3|}{2D_h} \rho_f \varepsilon A_c L \, dt}{\tau} \tag{2.22}$$

$$\bar{W}_{mag} = \bar{\dot{Q}}_h - \bar{\dot{Q}}_c - \bar{W}_{pump} \tag{2.23}$$

The efficiency of the complete AMRR device as a refrigerator is evaluated with the EER (Eq. 2.24). The COP evaluates the efficiency as a heat pump (Eq. 2.25). These definitions take into account the efficiency of the motor that moves the magnet relative to the AMR (η_{mot}) and the efficiency of the fluid pump (η_{pump}).

$$EER = \frac{\bar{\dot{Q}}_c}{\frac{\bar{W}_{mag}}{\eta_{mot}} + \frac{\bar{W}_{pump}}{\eta_{pump}}} \tag{2.24}$$

$$COP = \frac{\bar{\dot{Q}}_h}{\frac{\bar{W}_{mag}}{\eta_{mot}} + \frac{\bar{W}_{pump}}{\eta_{pump}}} \tag{2.25}$$

2.3 Validation and comparison with the implicit scheme

The purpose of this section is **to verify the newly developed numerical scheme and to quantify the improvement with respect to the implicit scheme** in terms of accuracy, energy conservation and computation time. To do so, **the proposed model has been validated in the limit of several ideal passive regenerator cases with analytic solution** as done by Engelbrecht [11]. Afterwards, it has been employed to simulate both the oscillating passive regenerator and the AMR under typical working conditions. The simulation results are compared to those of the implicit model developed by Engelbrecht [11].

2.3.1 Transport equation

The scheme proposed for the advection term of the fluid equation (Eq. 2.10) is analyzed in this section. With this purpose, the convective, conductive and viscous dissipation effects are not considered. Only the fluid portion of the regenerator is simulated.

The analytic solution of the transport equation considering only advection in the fluid has been compared with the new scheme and with the implicit scheme. A stepwise variation of the temperature of the fluid flow at the inlet of the channel was simulated with the parameters in Table 2.2 and $n_x =100$.

Table 2.2. Parameters employed in the model validation [11].

Parameter	Value	Parameter	Value
T_H	30 K	T_0	0 K
ρ_f	1000 kg m^{-3}	ρ_r	8900 kg m^{-3}
c_f	4200 J kg^{-1} K^{-1}	c_r	500 J kg^{-1} K^{-1}
$\dot{m}$	0.005 kg s^{-1}	A_C	0.001 m^2
L	1 m	ϵ	0.36
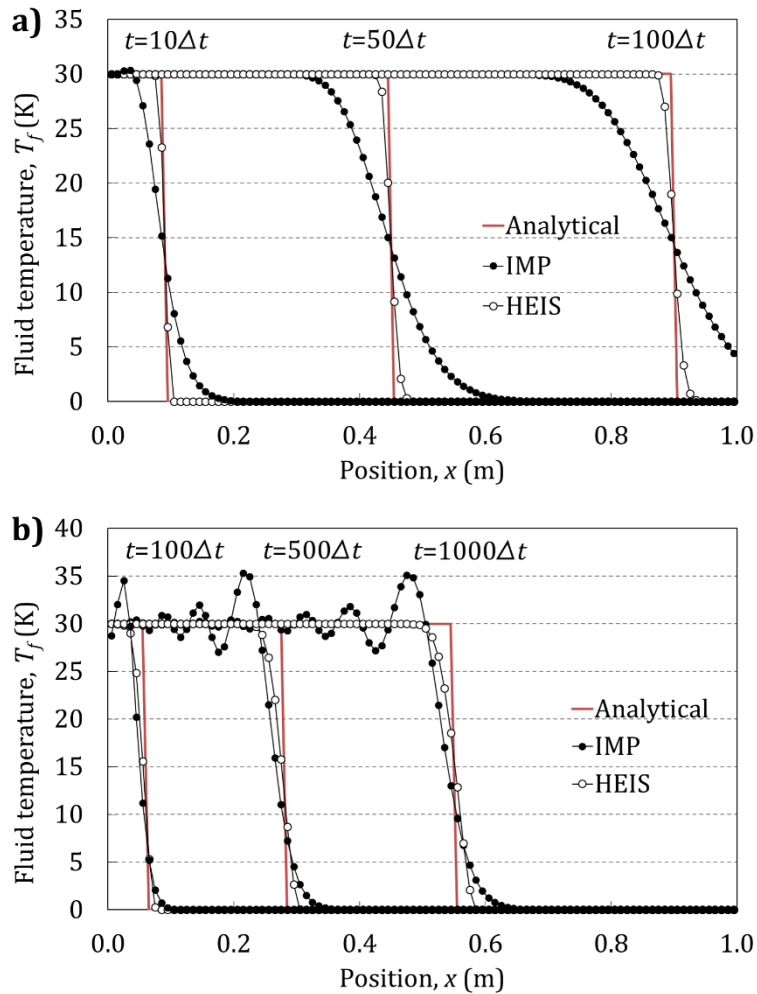
Fig. 2.4. Fluid temperature predicted by the models and analytical solution of the transport equation with a) CFL=0.9 and b) CFL<<1 [100].

Fig. 2.4 shows the calculated fluid temperatures along the channel at several moments of the simulation with different values of *CFL*. **The proposed scheme**

(HEIS) minimizes numerical diffusion with respect to the implicit scheme (IMP) when the model is run with values of *CFL* close to 1 (Fig. 2.4a). Since the advection term is solved explicitly in the presented scheme, the exact solution is achieved when *CFL* =1. If very low values of *CFL* are used, the proposed scheme still resembles the analytical solution while the implicit scheme produces oscillations (Fig. 2.4b).

2.3.2 Single-blow ideal passive regenerator

The model results have been compared with the Schumann solution for a single-blow transient passive regenerator with no axial conduction [107]. As in [11], the simulation has been run with a flow period of 100 s, *NTU*=50 (Eq. 2.26) and the parameters in Table 2.2.

$$NTU = \frac{h a_s A_c L}{\dot{m} c_f} \tag{2.26}$$
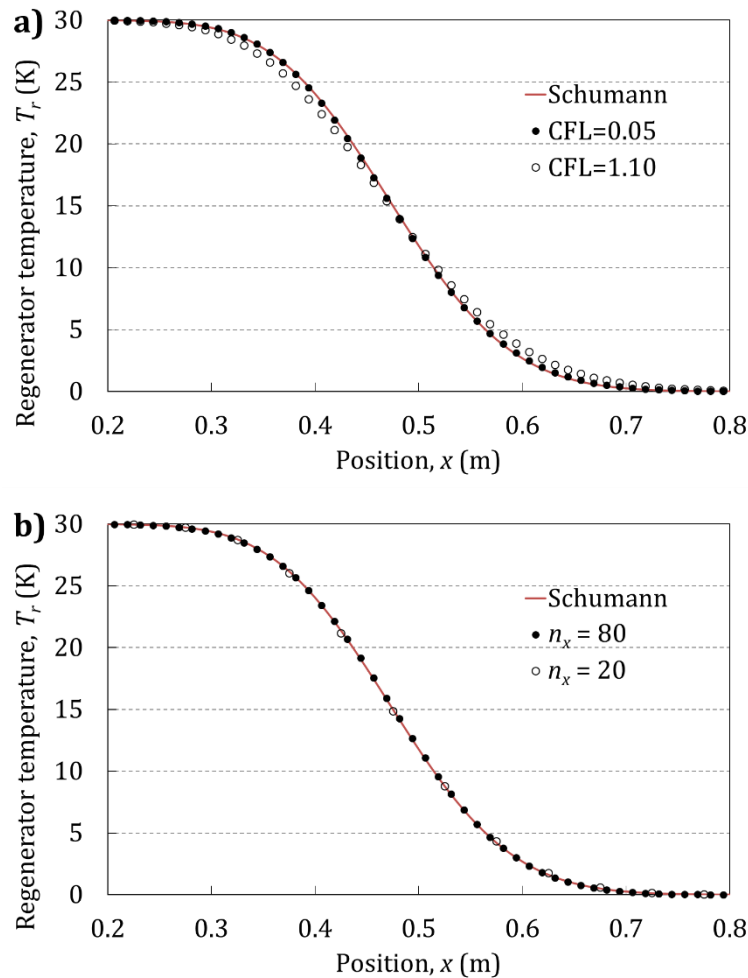
Fig. 2.5. Regenerator temperature predicted by the Schumann solution, a) the implicit model [11] and b) the present model HEIS1 ξ=1. [100]

The implicit scheme reproduces the Schumann solution with n_x=80 provided that the number of time steps (n_t) is high enough [11] (Fig. 2.5a). On the contrary, the proposed model achieves the Schumann solution with *CFL* as large as 0.99, which corresponds to the minimum time step possible for the proposed scheme. Moreover, the number of spatial nodes can also be reduced (Fig. 2.5b). These results are achieved with the approaches HEIS1 and HEIS2 combined with ξ=1 and ξ=0.5. Approaches HEIS3 and HEIS4 behave like the implicit scheme and ξ=0 produces oscillations at the wave front, so they were not further investigated.

Table 2.3 compares the results obtained with the proposed model (HEIS) and the implicit model (IMP) in terms of accuracy, energy conservation error and computation time. The accuracy is determined with the root mean squared error (*RMSE*) taking as a reference the Schumann solution (Eq. 2.27). The energy conservation error (γ) is expressed as the total energy variation along the calculation minus the energy difference between the final and the initial states (Eq. 2.28).

$$RMSE = \frac{\sqrt{\Sigma_i^n \left(T_{ref,i} - T_{sim,i}\right)^2}}{n} \tag{2.27}$$

$$\gamma = \frac{\int_0^t \Delta E - \left(\int_0^L E_t - \int_0^L E_0\right)}{\int_0^L E_t - \int_0^L E_0} \tag{2.28}$$

Table 2.3. Single-blow ideal regenerator simulation results of the proposed model (HEIS) and the implicit model (IMP).

Scheme	CFL	n_x=80			n_x=20		
		RMSE T_r (K)	γ (%)	t (s)	RMSE T_r (K)	γ (%)	t (s)
IMP	1.10	0.0503	$6.5 \cdot 10^{-8}$	0.2172	0.3668	$3.8 \cdot 10^{-5}$	0.0216
IMP	0.05	0.0086	$1.7 \cdot 10^{-10}$	3.9776	0.2299	$2.2 \cdot 10^{-7}$	0.2627
HEIS1 ξ=1	0.99	0.0037	$3.0 \cdot 10^{-11}$	0.0831	0.0183	$4.9 \cdot 10^{-9}$	0.0089
HEIS1 ξ=0.5	0.99	0.0008	$1.4 \cdot 10^{-10}$	0.0827	0.0253	$1.2 \cdot 10^{-10}$	0.0086
HEIS2 ξ=1	0.99	0.0060	$1.6 \cdot 10^{-12}$	0.0124	0.0527	$-5.6 \cdot 10^{-8}$	0.0023
HEIS2 ξ=0.5	0.99	0.0032	$1.7 \cdot 10^{-11}$	0.0130	0.0804	$-1.6 \cdot 10^{-8}$	0.0023

The proposed model approaches more accurately the Schumann solution than the implicit model, particularly if less spatial nodes are employed. The energy conservation error and therefore the numerical dispersion are lower with the presented scheme due to the larger *CFL* which is employed, as discussed in section 2.3.1. With respect to the IMP-*CFL*=0.05 case, **the proposed model reduces significantly the simulation time due to the increase in the time step and to the efficiency of the TDMA.** The simulation times reported were achieved in all cases with an Intel Core i3-2100 3.10 GHz processor.

In general, HEIS1 is more accurate than HEIS2. The results of HEIS2 may be improved by changing the definition of the slope of the temperature distribution in the regenerator. However, HEIS1 already achieves a good compromise so it has been finally chosen among the four proposed approaches.

2.3.3 Oscillating ideal passive regenerator

The model has also been validated against the solution of an oscillating passive regenerator with no entrained fluid heat capacity and no axial conduction. Dragutinovic and Baclic [108] calculated the effectiveness of this regenerator at the cyclical steady state as a function of the NTU (Eq. 2.26) and the thermal utilization (φ, Eq. 2.29) using an oscillating rectangular mass flow rate variation of magnitude $\bar{\bar{m}}$ and period τ. The hypothesis of no entrained fluid capacity can be simulated with the AMR model by setting the porosity (ϵ) very close to 0. The steady state is reached when the change in the regenerator temperatures from cycle to cycle remains below 10^{-5}. Engelbrecht [11] reported these results and found an excellent agreement with the calculations by his implicit model with n_x=100 and n_t=3000. In Fig. 2.6 the results in [11] are compared to the ones of the present model, which predicts practically the same values with n_x=20 and $CFL\approx1$.

$$\varphi = \frac{\bar{\bar{m}}c_f\tau}{2A_cL(1-\epsilon)\rho_r c_r} \tag{2.29}$$
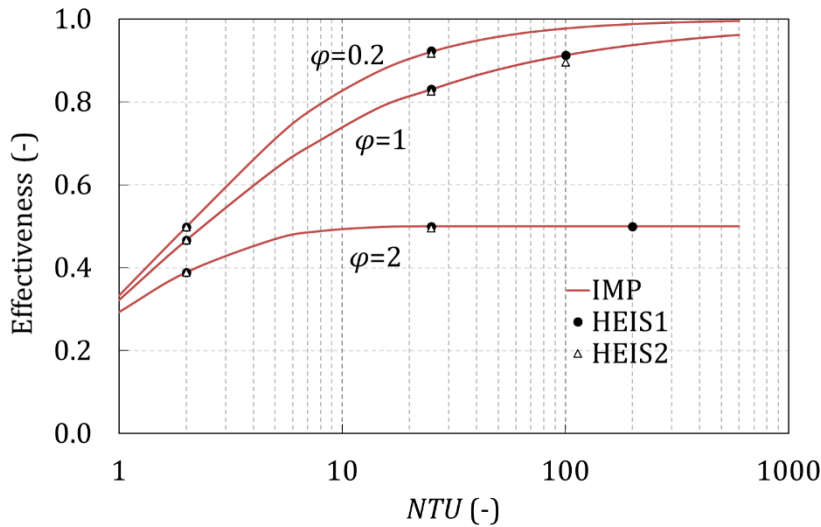
Fig. 2.6. Effectiveness of the oscillating ideal passive regenerator predicted by the implicit (IMP) and the proposed (HEIS) models [100].

In fact, both models predict a similar temperature distribution inside the regenerator (Fig. 2.7). However, in the regions where the convective heat transfer is very low the implicit scheme produces small oscillations due to the low CFL employed. On the contrary, the proposed scheme preserves monotonicity.
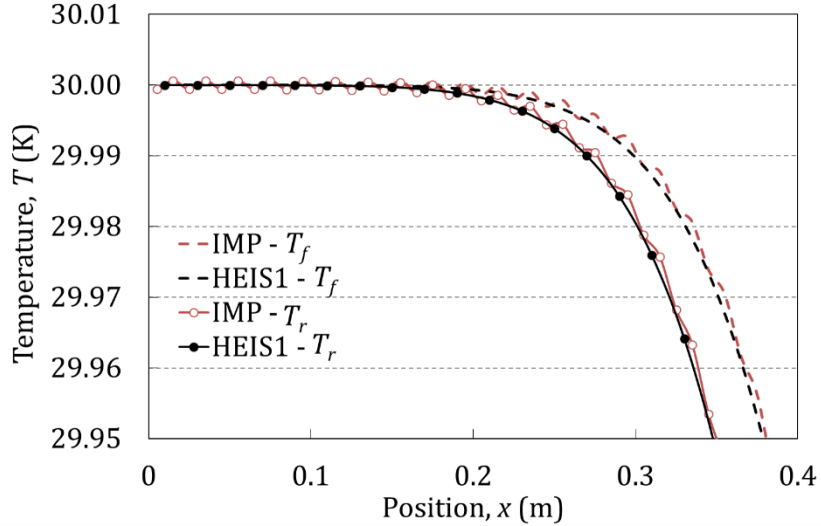
Fig. 2.7. Simulated temperature profiles at the cyclical steady state ($\varphi=1$, NTU=25) [100].

2.3.4 Oscillating passive regenerator

If the term regarding the **magnetocaloric effect is omitted**, Eqs. (2.4) and (2.5) represent the behavior of a **passive regenerator**. While models based in the implicit scheme may consider the complete equations, the proposed model neglects the axial conduction in the fluid. In any case, the passive regenerator equations do not have an analytic solution. The **two models have been compared** in this condition.

Both models have been executed with the parameters given in Table 2.4 until the periodic steady state is reached, which is when the relative change in energy of the regenerator from cycle to cycle is below 10^{-5} [11]. The fluid is a mixture of water and ethylene glycol, while the regenerator plates are made of Gd. In this section the specific heat capacity of Gd is considered constant, c_r=300 J kg^{-1} K^{-1}. Laminar flow between infinitely wide parallel plates is assumed in the calculation of the friction factor (f_f) and the convection coefficient (h) [11]. The former is a function of the Reynolds number (Re, Eq. 2.30) while the latter is obtained by means of the Nusselt number (Nu, Eq. 2.31). Both of these quantities are expressed based in the hydraulic diameter (D_h), whose expression for rectangular ducts is given in Eq. (2.32). In the ideal case of parallel plates, $W \gg H_f$ and $D_h=2H_f$. The inlet mass flow rate function is represented in Fig. 2.8.

$$Re = \frac{D_h \rho_f |v|}{\mu_f} \tag{2.30}$$

$$Nu = \frac{hD_h}{k_f} \tag{2.31}$$

$$D_h = \frac{2WH_f}{W + H_f} \tag{2.32}$$

Table 2.4. Parameters used for regenerator simulations

Parameter	Value	Parameter	Value
T_H	300 K	T_C	289 K
ρ_f	1033 kg m^{-3}	ρ_r	7901 kg m^{-3}
c_f	3799 J kg^{-1} K^{-1}	c_r	Discussed in text
k_f	0.4808 W m^{-2} K^{-1}	k_r	11 W m^{-2} K^{-1}
μ_f	0.002207 Pa s	H_r	0.0025 m
Nu	8.24 [109]	W	0.039 m
f_f	96/Re [109]	L	0.080 m
		ϵ	0.5
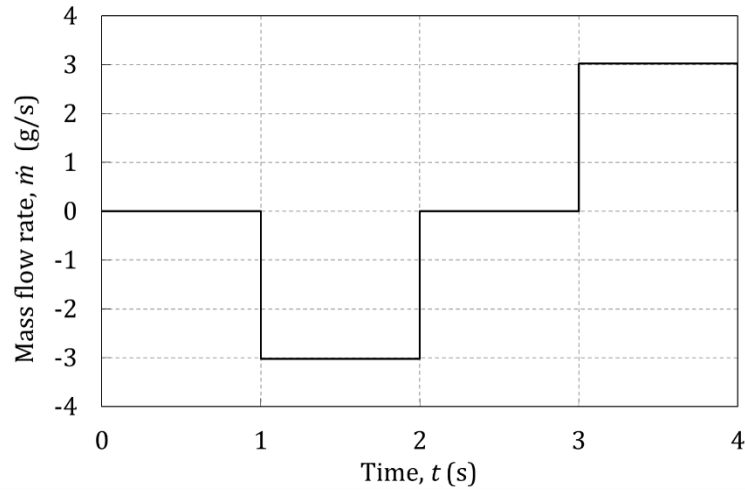
Fig. 2.8. Inlet mass flow rate in passive regenerator simulations

Fig. 2.9 shows the fluid temperature predicted by the models at the periodic steady state. If a fine grid is employed, the maximum fluid temperature difference at the end of the cycle between the two models is 0.025 K. This difference is mainly due to the numerical scheme. In fact, a maximum fluid temperature difference of 0.008 K was obtained between the complete implicit model and neglecting conduction in the fluid.

The proposed scheme HEIS1 ξ=0.5 with n_x=50 and CFL=0.94 employs 0.41 s per cycle and reproduces the solution with n_x=400 with a maximum fluid temperature difference of 0.040 K. The implicit scheme needs n_x=100 and CFL=0.19 to achieve a similar accuracy and employs 3.48 s per cycle. This represents a **reduction in the simulation time by 88%**. As expected from previous results, **the numerical dispersion is also reduced with the new scheme by an order of magnitude** (γ_{NS1}=-3.2 $\cdot$ 10^{-10} while γ_{IMP}=1.9 $\cdot$ 10^{-9}). Omitting conduction in the fluid in the implicit model leads to similar figures. These **results confirm that axial conduction in the fluid is negligible** as supposed in section 2.2.1.
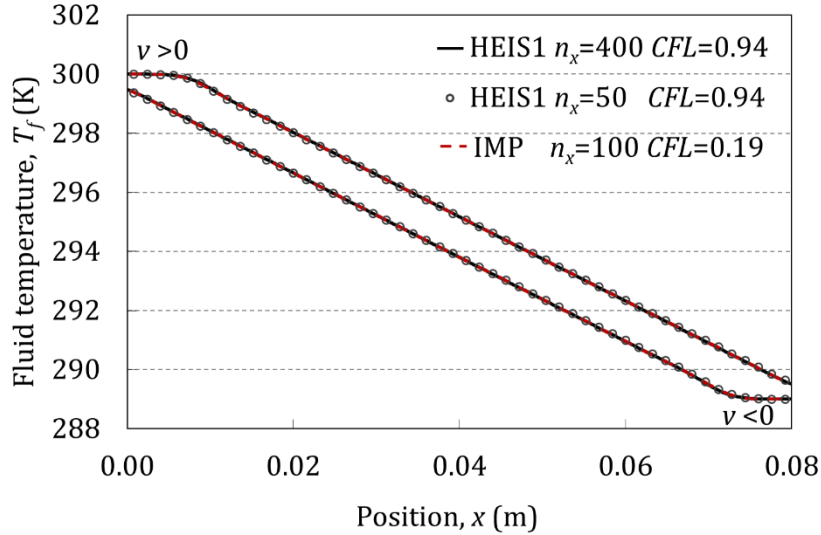
Fig. 2.9. Predicted fluid temperature at the periodic steady state in the oscillating passive regenerator [100].

A similar analysis shows that the viscous dissipation term can also be ignored in the studied application. When executing the implicit model with and without this term, the maximum fluid temperature difference is $1.5 \cdot 10^{-5}$ K after one cycle and 0.001 K when the cyclical steady state is reached after 261 cycles.

2.4 Magnetocaloric material properties

The specific heat capacity (c_r), the derivative of the entropy with respect to magnetic field at a constant temperature ($\partial s_r / \partial \mu_0 H_T$) and the magnetization (M) are the magnetocaloric properties of the MCM which are required by the AMR model. All of them are a non-linear function of the temperature and the magnetic field in the vicinity of the Curie point of the material.

As explained in section 1.2.2, employing the experimentally measured magnetocaloric properties of the MCM chosen is essential to simulate accurately experimental regenerators [69]. $M(T, H)$ and $c_r(T, H)$ can be directly measured and the specific entropy ($s_r(T, H)$) is derived from them. **This section describes the methodology followed to integrate the experimentally measured magnetocaloric properties in the AMR model.**

According to the Maxwell relation in Eq. (1.1), the isothermal variation of the specific entropy with magnetization (Δs_M) can be numerically derived from M (Eqs. (1.2) and (2.33).

$$\Delta s_M(T, H) = \frac{\mu_0}{\rho} \int_{H_1}^{H_2} \left(\frac{\partial M(T, H)}{\partial T} \right)_{\mu_0 H} dH \qquad (2.33)$$

The entropy can also be obtained from $c_r(T, H)$ measurements from its definition in Eq. (1.3) (Eq. 2.34). Hence, Δs_M is the difference between the entropy curves at different magnetic fields (Eq. 2.35).

$$s_r(T, H) = \int_{T_{ref}=0}^{T} \frac{c_r(T, H)}{T} dT \tag{2.34}$$

$$\Delta s_M(T, H) = s_r(T, H) - s_r(T, H = 0) \tag{2.35}$$

Δs_M as calculated with these two methods must be equal [110]. However experimental uncertainties can cause empirical data sets to be thermodynamically inconsistent. **An effective method to ensure that the properties employed in the model are consistent is to implement the $s_r(T, H)$ curves obtained from the experimental data** [11]. In the model, c_r and $\partial s_r / \partial \mu_0 H_T$ are calculated by numerically differentiating the entropy values.

In this work, a fine set of experimental $M(T, H)$ and $c_r(T, H)$ data measured in a commercial-grade Gd sample and corrected for demagnetization was provided by DTU Energy [21]. **A method based on the interpolation of empirical data has been employed to obtain the $s_r(T, H)$ curves.** With this purpose, **two different approaches can be followed.**

As a **first option**, a $s_r(T)$ curve at constant magnetic field $H = H_{ref}$ is calculated with the experimental values of $c_r(T, H_{ref})$ by means of Eq. (2.34), where T_{ref} is the lowest temperature for which data is available and $s_r(T_{ref}, H_{ref}) = 0$ is defined. Besides, $\Delta s_M(T, H)$ values are obtained from $M(T, H)$ with Eq. (2.33). The $s_r(T, H)$ map is obtained by applying Eq. (2.35) to the measured range of magnetic fields. **This approach reproduces perfectly the MCE, but implies rebuilding $c_r(T, H)$.**

As a **second option**, $\Delta s_M(T, H)$ values at a constant temperature $T = T_{ref}$ are obtained from $M(T_{ref}, H)$ with Eq. (2.33). The $s_r(T, H)$ map is obtained from Eq. (2.34) at every value of the magnetic field, taking the corresponding $\Delta s_M(T_{ref}, H)$ value as starting point. **Therefore $c_r(T, H)$ will be predicted exactly, but the MCE will be rebuilt.**

Ideally, T_{ref} should be 0 K. At this point, the entropy at any applied field has the same value [22]. However, the experimental data set available starts far from this temperature. Therefore, the results obtained will depend respectively on the chosen H_{ref} and T_{ref}.

In both cases, **the results must be verified by checking that the original data set can be reproduced with the $s_r(T, H)$ map**. In this sense, the first methodology resulted to provide a better accuracy. This can be explained by the experimental uncertainties associated to the calculation of $\Delta s_M(T, H)$ in each case. The relative error of $\Delta s_M(T, H)$ obtained from magnetization measurements typically ranges between 3-10%, while if $\Delta s_M(T, H)$ is obtained from the specific heat capacity

the error can range between 15-30% [22]. Moreover the first method reproduces better the intensity of the MCE, which is a critical parameter. For these reasons, **the first methodology was finally chosen.**

As noted by Engelbrecht [11], **dealing with experimental data of MCM properties is not trivial** given that numerical integration and differentiation are very sensitive to inconsistencies. In order to minimize the effect of experimental dispersion, the empirical data curves were previously smoothed with the methods available in MATLAB. Then they were interpolated into certain temperature and magnetic field grids.

A displacement between the experimental $c_r(T, H)$ and $M(T, H)$ curves was also found, probably caused by the temperature offsets in the different measurement rigs [111]. The magnitude of the temperature shift can be estimated considering the relationship between $\Delta s_M(T, H)$ and $c_r(T, H)$ as indicated in Eq. (2.36).

$$
\begin{aligned}
c_r(T, H) = T \frac{ds_r(T, H)}{dT} &= T \frac{d[s_r(T, H = 0) + \Delta s_M(T, H)]}{dT} \\
&= c_r(T, H = 0) + T \frac{d\Delta s_M(T, H)}{dT}
\end{aligned}
\tag{2.36}
$$

Therefore, $c_r(T, H) = c_r(T, H = 0)$ at the temperature at which $\Delta s_M(T, H)$ is maximum.

Implications of Eq. (2.36) have not been analyzed thoroughly with experimental data, but in this case the former expression proved to be a useful guide. For $\Delta \mu_0 H = 1$T, Eq. (2.36) predicts a displacement of the studied experimental data of around 1 K. This magnitude supports the hypothesis of the temperature offset.

Several interpolation techniques, resolutions and offsets were analyzed. Finally, the best results were obtained by correcting the empirical curves with the predicted temperature shift of 1K and a spline interpolation technique with a resolution of 2 K and 0.2 T. A finer spacing produced significant noise in the rebuilt MCM properties, while a coarser grid resulted in a loss of information.

Fig. 2.10 and Fig. 2.11 compare some of the experimentally measured values of $c_r(T, H)$ and $\Delta s_M(T, H)$ to the predictions of the $s_r(T, H)$ maps. Since the results obtained with the first methodology depend on H_{ref}, **two different $s_r(T, H)$ maps calculated with $\mu_0 H_{ref} = 0$ and $\mu_0 H_{ref} = 1.1$ T** have been considered.
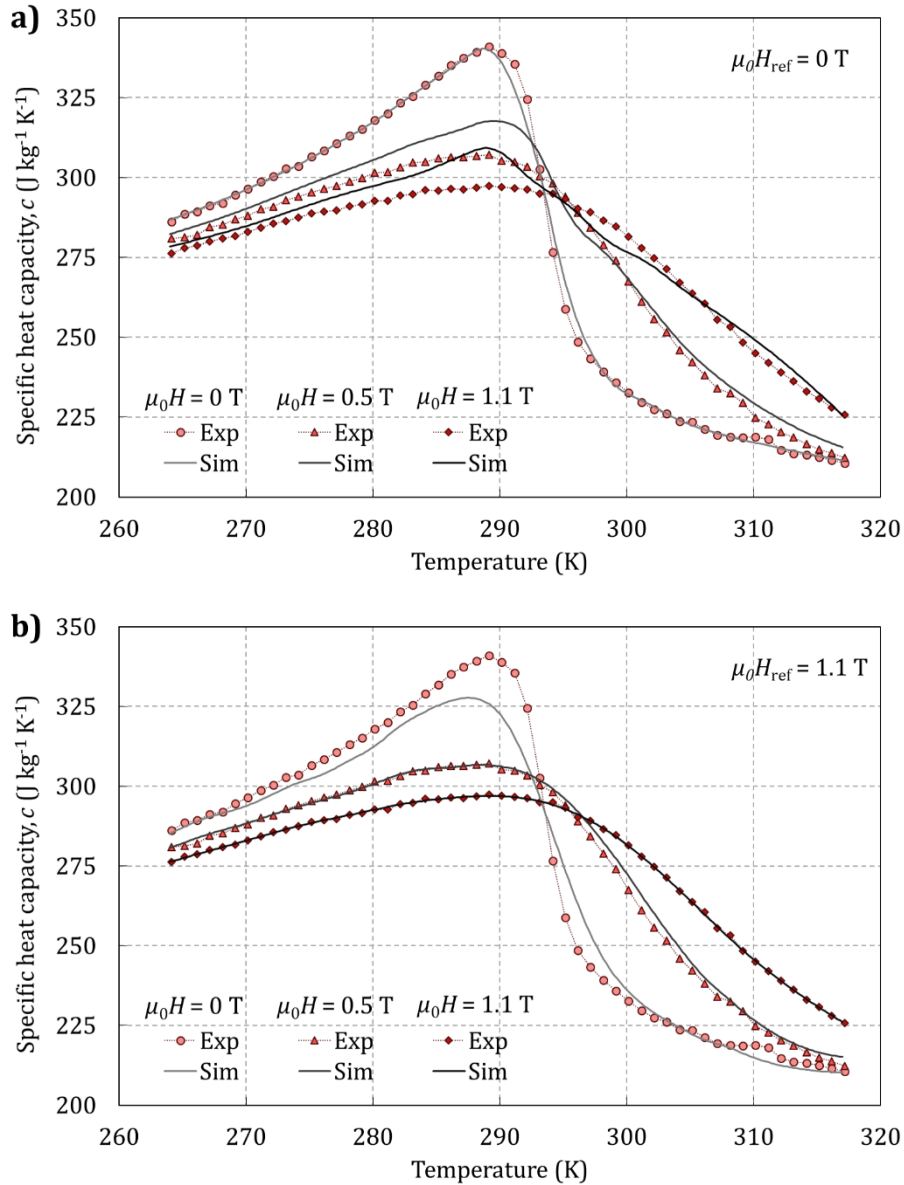
Fig. 2.10. Experimental and rebuilt specific heat capacity of Gd, calculated with a) $\mu_0 H_{ref}=0$ *T and b)* $\mu_0 H_{ref}=1.1$ *T.*

As observed in Fig. 2.10, $c_r(\mu_0 H = 0\,T)$ of Gd experiences a sharp peak near the Curie temperature. As the magnetic field increases, the shape of the $c_r(T)$ curve becomes smoother. Sharp variations of c_r are difficult to measure, hence the data obtained by choosing as H_{ref} the maximum applied magnetic field, 1.1 T in this case (Fig. 2.10b), is expected to be less affected by experimental uncertainty. However in both cases the prediction of $\Delta s_M(T,H)$ is excellent as expected, considering the 1K temperature shift (Fig. 2.11).

With the purpose of analyzing the sensitivity of the AMR simulation results to the curve-building process, both data sets have been tried in the model. The results are discussed in section 4.3.1.
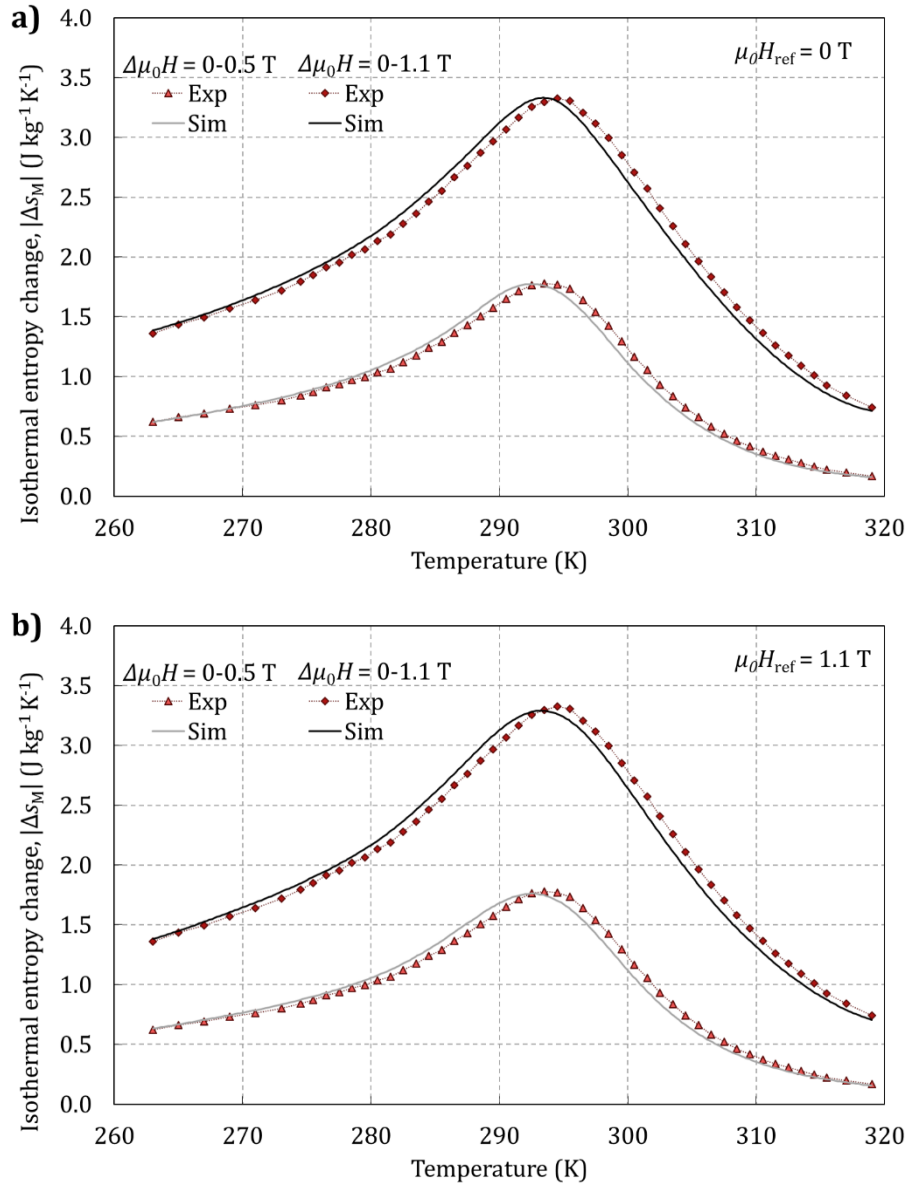
Fig. 2.11. Experimental and rebuilt entropy change with magnetization of Gd, calculated with a) $\mu_0 H_{ref}=0$ T and b) $\mu_0 H_{ref}=1.1$ T.

Finally, it has been observed that the interpolation routines that are employed to compute the properties in the AMR model can increase significantly the simulation time. The computation time depends on the efficiency of the interpolation function, the interpolation method and the resolution of the data set. Among the functions available in MATLAB, *griddedInterpolant* is the fastest. Accurate results were obtained with the minimum computation time by employing a $s_r(T,H)$ map with a resolution of 2 K and 0.2 to 0.3 T and the spline method. $M(T,H)$ has been implemented with a finer grid, especially at a small values of the magnetic field.

2.5 Demagnetizing effect: calculation of the internal magnetic field

The internal magnetic field ($\boldsymbol{H}$) that causes the MCE is given by the applied external field ($\boldsymbol{H_{app}}$) and the demagnetizing field ($\boldsymbol{H_{dem}}$) (Eq. 2.37).

$$\boldsymbol{H} = \boldsymbol{H_{app}} + \boldsymbol{H_{dem}} \tag{2.37}$$

The cause of the demagnetizing field is the magnetization of the material ($\boldsymbol{M}$). In order to ensure the conservation of the magnetic flux, a term of demagnetizing field opposed to the magnetization of the sample appears when it is subjected to an external magnetic field [1]. The demagnetizing field is related to the magnetization by means of the demagnetization factor ($\mathbb{N}$), a tensor that is defined at each position ($\boldsymbol{r}$) of the body and hence depends on its geometry (Eq. 2.38).

$$\boldsymbol{H_{dem}}(\boldsymbol{r}) = -\mathbb{N}(\boldsymbol{r}) \cdot \boldsymbol{M}(T(\boldsymbol{r}), \boldsymbol{H}(\boldsymbol{r})) \tag{2.38}$$

Since the magnetization has a strong dependence on the temperature and the magnetic field around the Curie point of the material, **the calculation of the internal magnetic field has been integrated into the AMR model** as proposed by Nielsen et al. [45].

The internal field of a magnetized body is generally inhomogeneous so numerical methods are required to solve Eqs. (2.37) and (2.38). Christensen et al. [42] presented a 3D numerical magnetostatic model for the case of a stack of identical parallel plates as function of its composition, the stack geometry, the number of plates, the temperature and the orientation and magnitude of the applied field. This model has been provided by DTU Energy and has been employed to calculate the demagnetization factor, which is an input to the AMR model.

In the AMR model, the scalar version of Eqs. (2.37) and (2.38) is employed to calculate the internal magnetic field, where N_{avg} is the average demagnetization factor (Eq. 2.39). This approach is valid since the MCE is not a function of the orientation of the magnetic field, if $\boldsymbol{H}$ and $\boldsymbol{M}$ are assumed to be parallel [45].

$$H(x,t) = H_{app}(x,t) - N_{avg}(x,t) \cdot M(T(x,t), H(x,t)) \tag{2.39}$$

The demagnetization factor obtained with the magnetostatic model is 3D while the present AMR considers only the fluid flow direction (x). Nielsen et al. [45] found that employing average values of N gives a reasonable estimate of the influence of the demagnetizing field in AMRs. The results they obtained by averaging N in the y-z plane (Eq. 2.40) and with total average (Eq. 2.41) were very similar. Nevertheless, implementing $N_{avg}(x)$ may be interesting for the simulation of layered regenerators.

$$N_{avg}(x) = \frac{1}{n_y n_z} \sum_{j=1}^{n_y} \sum_{k=1}^{n_z} \frac{H_{app}(x, y_j, z_k) - H(x, y_j, z_k)}{M(x, y_j, z_k)} \qquad (2.40)$$

$$N_{avg} = \frac{1}{n_x n_y n_z} \sum_{i=1}^{n_x} \sum_{j=1}^{n_y} \sum_{k=1}^{n_z} \frac{H_{app}(x_i, y_j, z_k) - H(x_i, y_j, z_k)}{M(x_i, y_j, z_k)} \qquad (2.41)$$

In Eqs. (2.40) and (2.41), n_x, n_y and n_z are the number of spatial nodes in each direction employed in the demagnetization model.

When the cyclic steady state is reached in the AMR model, the resulting temperature profile may be introduced in the demagnetization model to obtain a new value of $N(r)$. This process shall be repeated until the value of the internal magnetic field remains the same with both models. However, in their validation results Nielsen et al. [45] found that the first run of the demagnetization model with an imposed linear temperature profile provides practically the definitive value of $N(r)$. They concluded that, for a given configuration of the plates stack, one run of the magnetostatic model provides enough information to assess about the demagnetizing effect in an AMR model, for a given configuration of the plates stack.

According to these results, the variation of the average demagnetization factor with the temperature along an AMR cycle may be neglected. Nevertheless, the magnitude of the applied magnetic field varies during the AMR cycle. The influence of the cycle temperature and the applied field on the demagnetization factor and on the AMR simulation results has been analyzed in section 4.3.2.

2.6 Conjugate heat transfer

The determination of the convection coefficient (h) is essential to achieve good predictions with 1D models of conjugate heat transfer. Solutions are presented in literature as a function of the dimensionless Nusselt number (Nu, Eq. 2.31), generally taking the hydraulic diameter (D_h, Eq. 2.32) as the characteristic length. Nu and hence h depend on the conditions of the problem. In general **parallel-plate AMRs present laminar flow forced convection**, but the particular characteristics of the fluid flow in AMRs depend on the architecture of the device and the cycle timing. In the AMR cycle the fluid flow is reciprocating, however in most AMRR prototypes the fluid is stopped before it is reversed in order to perform the magnetization and demagnetization steps of the AMR cycle. Depending on the cycle frequency, these periods may be enough to stop completely the fluid [112] and in practice the bed will experience a unidirectional flow. Besides, the fluid is accelerated and decelerated two times during the AMR cycle. The importance of the unsteady flow periods will depend on its length compared to the constant velocity flow periods.

As in **most reciprocating AMRR prototypes**, the flow in the device employed to validate the present AMR model can be treated as **unidirectional steady flow**

(chapter 4). Therefore, as in previous 1D AMR models [11,36,80,84,87], the conjugate heat transfer has been included under this assumption.

Laminar flow forced convection heat transfer in rectangular channels has been studied in detail in the cases with analytic solution [109]. The standard Nu correlations are valid at least for channels as narrow as 0.2 mm [113], which is in the range of current AMRs. However, the cases presented in literature deal with either constant temperature or constant heat flux boundary conditions, which actually are not representative of the working conditions of an AMR (section 3.4.4). Nevertheless the condition that approaches most to this case is the wall with infinite thermal resistance to the ambient (adiabatic), which equals the constant heat flux boundary condition [109]. If the viscous dissipation and the fluid axial conductivity are neglected, Nu for fully developed laminar flow (Nu_{fd}) in rectangular channels is given by Eq. (2.42).

$$Nu_{fd} = 8.235 \cdot \left[1 - 2.0421\frac{H_f}{W} + 3.0853\left(\frac{H_f}{W}\right)^2 - 2.4765\left(\frac{H_f}{W}\right)^3 + 1.0578\left(\frac{H_f}{W}\right)^4 \right. \\ \left. - 0.1861\left(\frac{H_f}{W}\right)^5\right]$$

(2.42)

Depending on the dimensions of the regenerator and the fluid velocity employed, the hydrodynamic (L_h, Eq. 2.43) and thermal (L_t, Eq. 2.44) entry lengths may not be negligible with respect to the channel length. In such a case, a Nu correlation for **developing flow** should be employed.

$$L_h = 0.05 \, Re \, D_h$$

(2.43)

$$L_t = L_h \, Pr$$

(2.44)

The entry lengths are given by the Reynolds number (Re, Eq. 2.31) and the Prandtl number (Pr, Eq. 2.45). Pr has a significant influence in the Nu values in the entry region. Hence it is convenient to have a correlation which is an explicit function of Pr in order to simulate different heat transfer fluids.

$$Pr = \frac{c_f \mu_f}{k_f}$$

(2.45)

However the literature on Nu correlations for developing flow in rectangular channels or parallel plates is limited. Shah and London [109] reported Nu values for several values of Pr and aspect ratio (H_f/W). Further calculations were performed by Bavière et al. [113], who presented a correlation for Pr=6 that showed agreement with experimental results. Garimella et al. [114] fitted a correlation for the mean Nu in a heat exchanger using glycol as heat transfer fluid (6< Pr<12), but results for the local Nu are not provided. The only suitable local Nu correlation that has been found in

literature which is an explicit function of Pr is the generic model by Muzychka and Yovanovich [115] (Eq. (2.46).

$$Nu_{\sqrt{A_c}} = \left[\left(\frac{0.886}{(1 + (1.909Pr^{1/6})^{4.598})^{\frac{1}{4.598}}} (x^*)^{-\frac{1}{2}} \right)^m \right.$$
$$\left. + \left(\left\{ 0.517 \left(\frac{f_f Re_{\sqrt{A_c}}}{x^*} \right)^{\frac{1}{3}} \right\}^5 + Nu_{fd,\sqrt{A_c}}^5 \right)^{\frac{m}{5}} \right]^{\frac{1}{m}}$$

(2.46)

Where x^* is the dimensionless abcissa introduced to take into account the entrance effect (Eq. 2.47), $f_f Re_{\sqrt{A_c}}$ is the product of the friction factor and the Reynolds number (Eq. 2.48) and m is a curve-fitted blending parameter (Eq. 2.49).

$$x^* = \frac{x}{\sqrt{A_c} Re_{\sqrt{A_c}} Pr}$$

(2.47)

$$f_f Re_{\sqrt{A_c}} = \frac{12}{\sqrt{\frac{H_f}{W}} \left(1 + \frac{H_f}{W} \right) \left[1 - \frac{192r}{\pi^5} \tanh \left(\frac{\pi}{2 H_f/W} \right) \right]}$$

(2.48)

$$m = 2.27 + 1.65 Pr^{1/3}$$

(2.49)

The dimensionless quantities in this correlation are expressed taking the square root of the cross-sectional area of the duct ($\sqrt{A_c}$) as the characteristic length. The quantities calculated taking D_h as the characteristic length must therefore be converted as indicated in Eq. (2.50).

$$Nu_{\sqrt{A_c}} = \frac{Nu \cdot \sqrt{A_c}}{D_h}$$

(2.50)

The present correlation is intended for any duct geometry, however the generic expression for Nu_{fd} proposed by the authors [115] overpredicts by more than 20% the Nu_{fd} for channels with small aspect ratios as the ones typically employed in AMRs. If the expression for Nu_{fd} in Eq. (2.42) is employed instead, the correlation in Eq. (2.46) underpredicts by up to 4% the values measured for $Pr=6$ [113]. This error produces a maximum outlet temperature difference of 0.02 K for $\overline{Re}=24$ and of 0.1 K for $\overline{Re}=342$ in the single-blow simulations detailed in chapter 3.

In order to determine the influence of the variation of Pr with the temperature, additional single blow simulations have been carried out by employing the Nu correlation in Eq. (2.46) computed with temperature-dependent fluid properties and with constant fluid properties, which were calculated at the mean temperature of the

fluid in the experiments in chapter 3. The maximum outlet temperature difference found is $3 \cdot 10^{-4}$ K for $\overline{Re}$=24 and 0.01 K for $\overline{Re}$=342.

In conclusion, the correlation by Muzychka and Yovanovich [115] with the value of Nu_{fd} reported by Shah and London [109] has been employed for calculating the Nu in the AMR model. Consistently with previous assumptions, the fluid properties can be considered to be constant. A validation of this approach is provided in chapter 3.

When the fluid is stopped, there is conductive heat transfer between the fluid and the solid parts of the regenerator. In this periods, h in the governing equations (Eqs. 2.4 and 2.5) should account for this phenomenon as expressed in Eq. (2.51). The Nu when v=0 is thus calculated with its definition in Eq. (2.31).

$$h = \frac{1}{\dfrac{H_f}{2k_f} + \dfrac{H_r}{4k_r}} \; if \; v = 0 \tag{2.51}$$

2.6.1 Effect of fluid flow maldistribution

In parallel-plate AMRs, the fluid flow maldistribution has proved to degrade significantly the heat transfer performance [116]. The fluid flow maldistribution is caused by the difference in the channel heights of a real stack of parallel plates. In order to equalize the pressure drop through the channels, each channel must experience a different fluid velocity. The mean fluid velocity in each channel of the stack (v_i) can be obtained by combining Eqs. (2.52) and (2.53), assuming that the pressure drop through each channel (Δp_i) must be equal [117].

$$\Delta p_i = f_f \frac{\rho_f L v_i^2}{2 D_{h,i}} \tag{2.52}$$

$$\dot{V} = \sum_i^{n_{ch}} \dot{V}_i = \sum_i^{n_{ch}} v_i W H_f \tag{2.53}$$

In Eqs. (2.52) and (2.53), i denotes the ith channel, n_{ch} is the number of channels and $\dot{V}$ is the total volumetric flow rate through the stack.

As noted by Nielsen et al. [116], the thickest channels will receive the largest amount of flow. Thicker channels have poorer heat transfer performance than thinner, hence intuitively the flow maldistribution decreases the overall performance of the stack. Besides, the different temperature distribution reached in each channel causes heat to be transferred between them. This effect is known as thermal cross talk and is perpendicular to the fluid flow, so in principle the flow maldistribution must be

analyzed with models that consider this direction [117]. Nevertheless a modelling approach for 1D models can be obtained. This issue is further discussed in chapter 3.

2.6.2 Effect of transversal conduction in the plates

The 1D model does not take into account the conductive heat transfer across the plates in the direction perpendicular to the flow. The importance of this effect can be evaluated with the Biot number (Bi, Eq. 2.54).

$$Bi = \frac{h}{2k_r/H_r} \tag{2.54}$$

The transversal conduction across the plates is noticeable with respect to convection if Bi>0.1 [103]. According to Engelbrecht [11], this effect can be included in the 1D model by correcting the convection coefficient with a degradation factor (DF), which is given by Eq. (2.55) for the case of parallel plates.

$$DF = \frac{1}{1 + Bi/3} \tag{2.55}$$

2.7 Pressure drop

In section 2.3.3 it was proved that the influence of the pressure losses in the fluid temperature can be neglected in regenerators with channel heights as narrow as 0.25 mm. Nevertheless, the pumping power may be a significant part of the total power input to the device and hence play an important role in the efficiency of the AMR operation.

The pressure drop term is finally included in the model through the friction factor (f_f). Assuming fully developed laminar flow between parallel plates, the friction factor is given by Eq. (2.56) [109].

$$f_f = \frac{96}{Re} \tag{2.56}$$

Chapter 3

Experimental validation of the passive regenerator model

The heat transfer between the working fluid and the regenerator influences significantly the AMRR performance and can be severely affected by the flow maldistribution caused by the manufacturing irregularities in stacks of parallel plates. **The purpose of this chapter is to determine the conjugate heat transfer in an experimental regenerator considering the effect of the fluid flow maldistribution, regardless of the MCE. The behavior of the present 1D model working as a passive regenerator has been verified as a previous step to its validation working as an AMR.**

3.1 Single-blow experimental setup

Experiments have been run in a parallel-plate Gd regenerator in the single-blow test facility at DTU Energy (Fig. 3.1). The single-blow method has been traditionally employed to measure the heat transfer in heat exchangers [118] and has proven to be useful for the present problem [117].
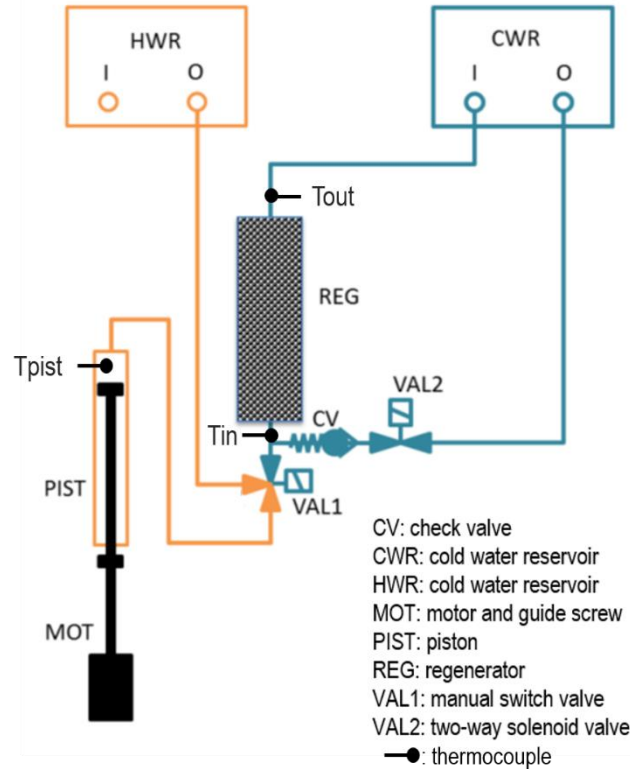
Fig. 3.1. Scheme of the single-blow test facility at DTU Energy.

The single-blow test is performed in two parts. During the first part, the yellow and the blue loops in Fig. 1.3 are separated by the valve VAL1 and the piston is down. In the yellow loop, the electric heater (HWR) heats up the water inside the piston sleeve (PIST). In the blue loop, the chiller (CWR) cools down the water until the value of the temperature at the inlet and the outlet of the regenerator (REG) is the same. Once the system has reached the temperature settings, the second part of the test begins. VAL1 communicates the piston with the regenerator while VAL2 closes the cold water supply. Then the hot water inside the piston sleeve is blown through the regenerator at the programmed piston speed. The temperature of the water is measured with type E thermocouples at the inlet (Tin) and outlet (Tout) sections of the regenerator as pictured in Fig. 3.2, as well as inside the piston sleeve (Tpist). A plastic screen was added to both ends of the regenerator to enhance the mixing of the fluid.

The regenerator tested in this work is described in [102]. Fig. 3.2 is a photograph of the assembly, which consists of 11 flat plates made of commercial grade Gd with dimensions 40 mm in the direction of flow, 25 mm wide and 0.9 mm thick. The plates are placed inside a rectangular opening in a cylindrical plastic housing, whose outer dimensions are 34 mm in diameter by 40 mm long. The plates are separated by ribs uniformly machined in the sides of the opening, creating 10 channels that are 23 mm width. The top and bottom plates are in direct contact with the housing.

Fig. 3.2. Top view of the parallel-plate Gd regenerator inside the housing and thermocouples at the outlet section.

Inspection of Fig. 3.2 reveals that the plates are not uniformly spaced. The channel heights (H_f) were determined by scanning the surfaces at both ends of the stack with a Vantage Laser Scanner following the procedure explained in [40,117]. In this work, the resolution of the scanner was set at 1 µm in the direction perpendicular to the plates and at 500 µm in the direction parallel to the plates. The latter setting yields 47 points along the channel width. The height of each channel at each end is calculated as the average of the distance measured in each of these 47 points. Table 3.1 contains the results. The average channel height in the regenerator is 0.556 mm with a relative standard deviation of 23%.

Table 3.1. Channel heights of the tested parallel-plate Gd regenerator.

Channel	H_f in surface 1 (mm)	H_f in surface 2 (mm)	Average H_f (mm)
1	0.352	0.261	0.306
2	0.667	0.705	0.686
3	0.588	0.654	0.621
4	0.478	0.535	0.506
5	0.784	0.481	0.632
6	0.359	0.549	0.454
7	0.698	0.731	0.714
8	0.595	0.491	0.543
9	0.691	0.592	0.641
10	0.559	0.357	0.458
Average	**0.577**	**0.536**	**0.556**
St. Dev.	**0.144**	**0.148**	**0.127**

3.2 Single-blow experimental results

The single-blow test was performed in the described Gd regenerator at several piston speeds (v_{pist}) by T. Lei from DTU Energy. The heat transfer fluid is deionized water. In all cases, the hot water temperature was 40 ºC and the cold water temperature 15 ºC ($\overline{Pr}$=5.78). The stroke of the piston was set at 194 mm. Each test was repeated twice. Table 3.2 details the experimental runs. $\overline{Re}$ is calculated with the average channel height and Eq. (2.30). The hydrodynamic (L_h) and thermal (L_t) entry lengths are defined in Eq. (2.43) and (2.44) respectively. As can be observed, the entry lengths in these experiments are not negligible with respect to the channel length (L=40 mm).

Table 3.2. Definition and entry lengths in the single blow experiments.

Test	$\overline{Re}$	L_h (mm)	% L	L_t (mm)	% L
v_{pist}= 5 mm/s	24.40	1.3	3.3%	7.7	19.1%
v_{pist}=10 mm/s	48.79	2.6	6.6%	15.3	38.3%
v_{pist}=15 mm/s	73.19	4.0	9.9%	23.0	57.4%
v_{pist}=20 mm/s	97.58	5.3	13.2%	30.6	76.6%
v_{pist}=30 mm/s	146.37	7.9	19.9%	45.9	>100%
v_{pist}=50 mm/s	243.95	13.2	33.1%	76.6	>100%
v_{pist}=70 mm/s	341.53	18.5	46.4%	107.2	>100%

Fig. 3.3 shows the water temperature measured during the test at $\overline{Re}$=97.6 for instance. The temperature is recorded at a frequency of 8 Hz at the end of the piston sleeve (Tpist), at 3 points of the inlet section of the regenerator (Tin) and at 3 points of the outlet section of the regenerator (Tout).
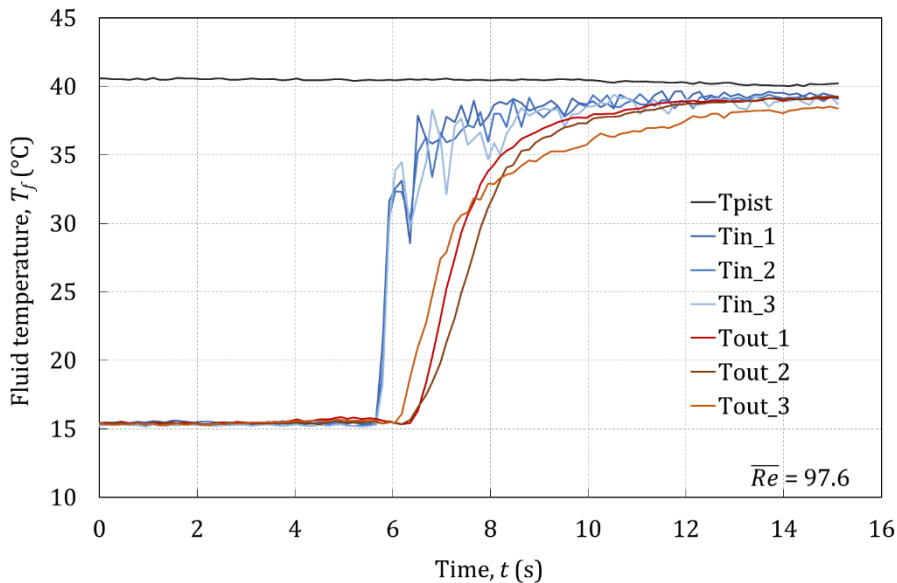
Fig. 3.3. Experimental results of the single-blow test at $\overline{Re}$=97.6.

Before the blow, the temperature at both sides of the regenerator is constant and equal to the cold reservoir temperature, 15 °C. When the blow begins, the temperature at the inlet of the regenerator (Tin) should reach the same value as Tpist in a few seconds. **Heat losses to the ambient can be neglected** since the pipe is insulated and the process is fast. However, temperature fluctuations up to 5 K are observed in the inlet section depending on the position of the thermocouple. Moreover, fluctuations become larger when the piston speed is reduced. Such variations may still be due to the **dead volume of cold water left** in the CV or in the holes of the plastic part where more thermocouples can be placed. The cold stagnant water is swept by the hot water flow but it is **not completely mixed before entering the regenerator**, as suggests the fact that the measure of Tin_3 is generally lower during the first seconds of the test in all cases.

The temperature response recorded at the outlet section of the regenerator (Tout) is also not uniform. Despite the presence of the plastic screen, the flow through the plates is so guided that the differences in the velocity of response of the individual channels due to the flow maldistribution can still be observed across the outlet section.

Besides, the thermocouple Tout_3 records systematically a lower temperature even at the end of the blow. This effect could also be explained by the volume of cold water left at the inlet. If that volume is not completely mixed with the hot stream, the channels close to the valve will receive a colder flow. As in the inlet section, stagnant cold water may also be found at the outlet section due to the geometry of the plastic part that couples the regenerator to the test machine.

3.3 Single-blow modelling

In order to simulate single-blow experiments in a passive regenerator with the 1D AMR model the applied magnetic field was set to 0. The inlet temperature in the simulations is the average of the 3 Tin thermocouples, while the mass flow rate is calculated with the programmed piston speed and the surface of the piston (Ø25 mm). The initial temperature was set at the value measured at the beginning of each experimental run.

Previous studies [39,40,117] proved that flow maldistribution affects noticeably the performance of inhomogeneous parallel-plate heat exchangers similar to the one tested, especially at low values of *Re*. Therefore, adjusting directly a single-channel model to the experiments may mask other effects that affect the heat transfer performance and thus provide an incorrect result. Taking this into account, **the first objective is to reproduce the experimental results with the simulation of the whole stack in order to account for the flow maldistribution effect in the model.** Once the model of the whole stack has been validated, **the second objective is** to find an approximation **to reduce the model to a single representative channel** with the purpose of minimizing the computational cost.

In the limit of low solid thermal conductivity and relatively thick plates, the thermal cross talk between channels can be neglected and the stack can be modelled as individual isolated channels operating in parallel [39]. **Therefore, the regenerator has been simulated as the sum of its 10 isolated channels.** The *Nu* correlation employed in each channel is the one discussed in section 2.6.

3.4 Single-blow simulation results and model validation

3.4.1 Initial simulation results of the complete stack

Fig. 3.4 compares the outlet temperature measured in three experiments at different piston velocities (Tout_EXP and Tout_1,2_EXP) with the simulation results. Tout_ave is the weighted average of the outlet temperature of the 10 channels. Since the thermocouples at the outlet were placed near the center of the stack (Fig. 3.2) and the experimental results suggest that the flow is not completely mixed there, the weighted average of the 3 central channels is also represented (Tout_center). The simulated outlet curve has been delayed to take into account the gap between the thermocouples and the regenerator. The estimated length of each gap is 2 mm. In general **the experimental temperature response is slower than in the simulations**.

Fig. 3.5 shows the simulated outlet temperature of each individual channel compared to the measurements of the Tout thermocouples for one of the cases ($\overline{Re}$=73.2). As explained in section 2.6.1, narrower channels carry less fluid flow than the thicker ones in order to preserve the pressure drop. Therefore their response is slower and have less weight in the average temperature. However, the measured temperatures do not seem to follow a single simulated line. In addition, several combinations of the outlet temperature of the channels were investigated for the different cases but none seems to fit the experimental results.

Several factors that may explain the differences between the measured and simulated temperatures have been studied. Afterwards, the accuracy of the *Nu* correlation chosen is discussed.
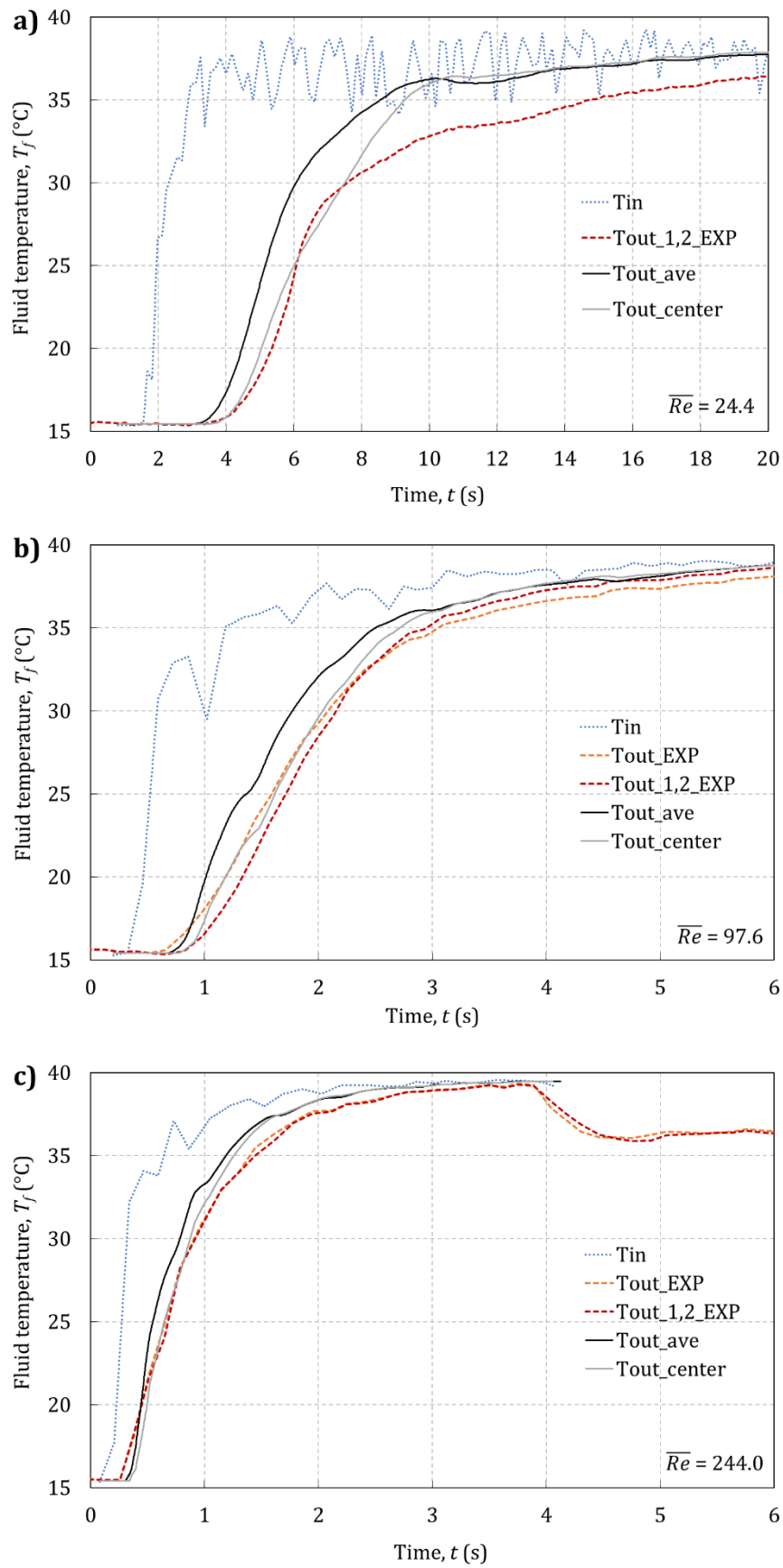
Fig. 3.4. Experimental and simulated average temperatures at different piston speeds.
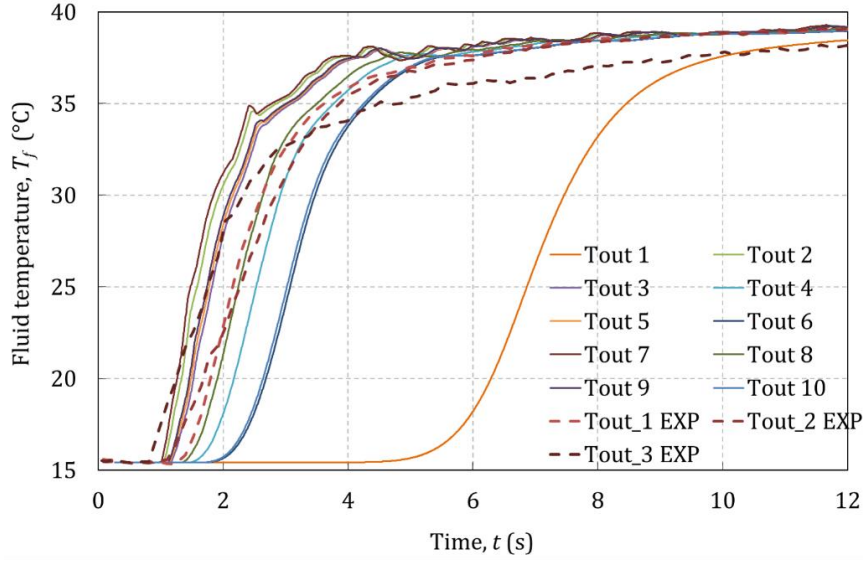
Fig. 3.5. Simulated outlet temperature of each individual channel ($\overline{Re}$=73.2).

3.4.2 Influence of 2D heat conduction in the plates

As explained in section 2.6.2, the importance of conductive heat transfer across the plates in the direction perpendicular to the flow can be evaluated with the Biot number (Bi, Eq. 2.54). Table 3.3 summarizes the calculation of Bi for fully developed flow as function of the channel height (H_f).

Table 3.3. Biot number (Bi) in the regenerator and degradation factor (DF).

H_f (mm)	D_h (mm)	Nu_{fd}	h (W m^{-2} K^{-1})	Bi	DF
0.306	0.604	8.02	7963	**0.33**	0.902
0.556	1.086	7.84	4334	**0.18**	0.944
0.714	1.385	7.74	3352	**0.14**	0.956

Since $Bi \approx 0.1$, the studied case is at the limit in which the 2D effects of conduction in the plates start to be noticeable [103]. From the values of DF (Eq. 2.55) in Table 3.3, **the influence of cross-sectional conduction is expected to be small.**

3.4.3 Influence of thermal inertia

The thermal inertia of the system causes the outlet temperature to raise slowly. The results in Fig. 3.4 suggest that the model has a lack of thermal inertia compared to the experimental system. **Several phenomena related to the thermal inertia have been analyzed.**

Inertia of the thermocouples

The heat storage in the sensitive part of the thermocouples causes a delay in the temperature response measured. Assuming that heat is transferred from the fluid to

the thermocouple wire mainly by convection, the energy balance in the wire (Eq. 3.1) was included into the model.

$$m_{th}c_{p,th}\frac{dT_{th}}{dt} = hA_{th}(T_f - T_{th})$$ (3.1)

The thermocouples are type E ($c_{p,th}$=418 J kg^{-1} K^{-1}, ρ_{th}=8750 kg m^{-3}) and the wire has a diameter of 0.13 mm. The estimated length of the sensitive part is 2 mm. The convection coefficient of a small cylinder in confined cross-flow can be calculated by means of the Nu correlation by Sucker and Brauer [119].

Fig. 3.6 shows the simulation results for $\overline{Re}$=73.2 taking this effect into account. As expected from the dimensions of the wire, it was verified that **the effect of heat storage in the thermocouples is negligible.**
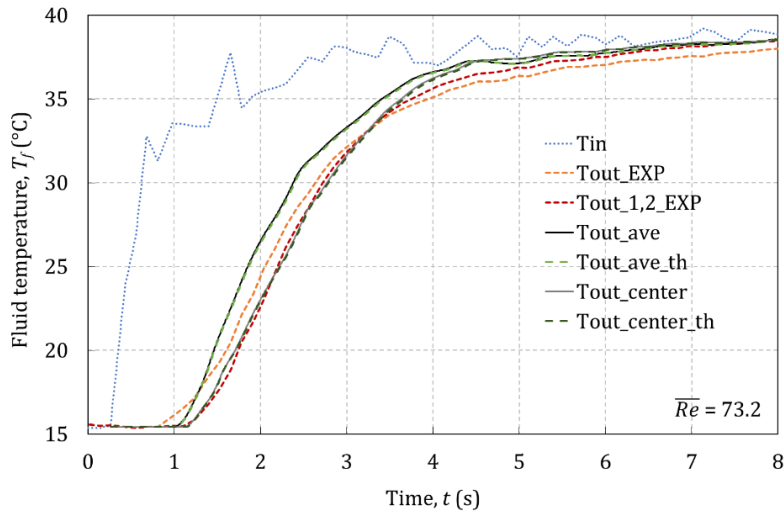
Fig. 3.6. Effect of heat storage in the thermocouples in the outlet temperature.

Uncertainty in the thermophysical properties of Gd

As discussed in section 2.4, there is an uncertainty in the specific capacity at zero magnetic field ($c_{r,H=0}$) of this sample of Gd of up to 4.4 % (Fig. 2.10). $c_{r,H=0}$ is a strong function of the temperature especially around the Curie temperature of the material (T_{Cu}). From other experimental results (chapter 4), the error in the determination of T_{Cu} of the present sample could be up to 2 K. Simulations have been run with the limit values of $c_{r,H=0}$ and T_{Cu} of the present sample of Gd. In the previous simulations, T_{Cu} was 293.4 K and the calculated values of $c_{r,H=0}$ were used. Fig. 3.7 compares those results for $\overline{Re}$=73.2 with three new cases: a) T_{Cu} is changed by 2K, b) the measured $c_{r,H=0}$ is used and c) both T_{Cu} and $c_{r,H=0}$ are changed. The differences observed among the results are negligible, so **the detected uncertainty in the thermophysical properties of Gd is not critical** for the evaluation of heat transfer in the regenerator.
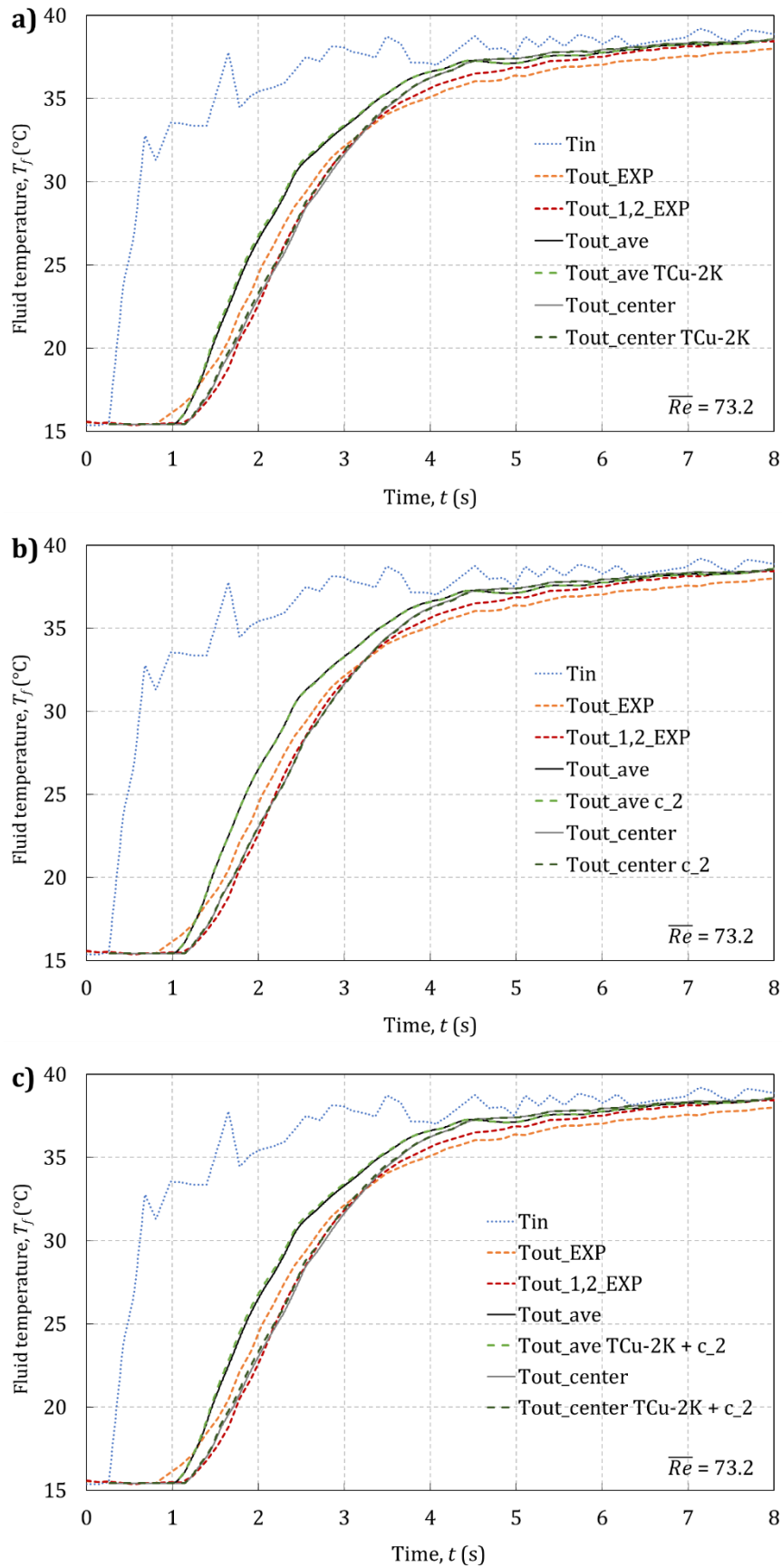
Fig. 3.7. Effect of the uncertainty of the properties of Gd in the outlet temperature.

Volume of cold fluid left in the loop

The measured temperatures (Fig. 3.4) suggest that there is a certain volume of cold fluid left near the thermocouples, maybe due to the geometry of the plastic cylinder that couples the regenerator with the single-blow test machine. In order to evaluate whether this uncertainty influences the experimental results, Fig. 3.8 shows the effect of adding a volume of cold fluid at the outlet of the regenerator. The outlet temperature Tvol_ave is calculated considering a perfect mixture of the Tout_ave temperature with a given volume (V) of cold fluid at the initial temperature of the test. This simple hypothesis can be helpful to obtain qualitative conclusions.
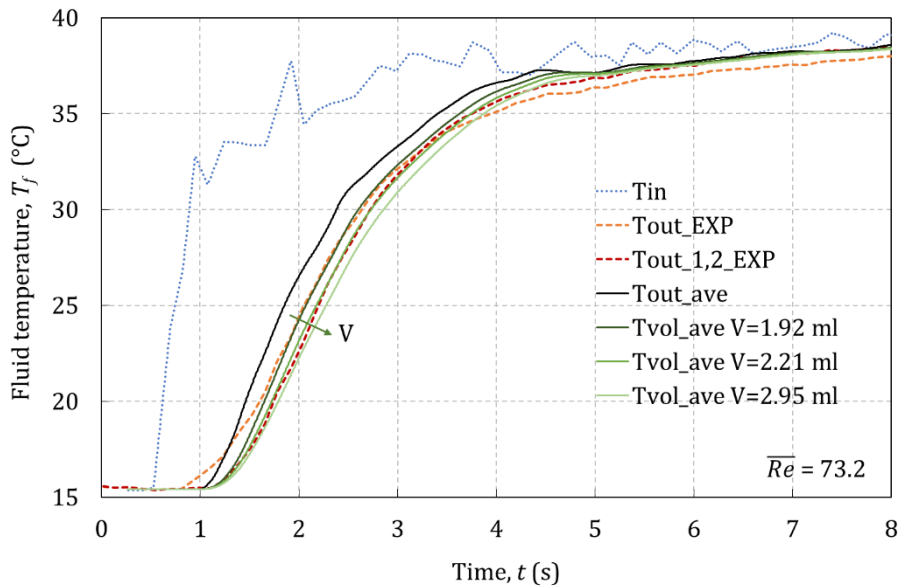
Fig. 3.8. Effect in the measured temperature of adding a volume of cold fluid at the outlet.

The presence of cold fluid at the fluid outlet causes a delay in the beginning of the temperature response. As the mass of cold fluid increases, the slope of the response is decreased. Although a single fitting value of the stagnant fluid mass cannot be found with the present hypothesis, the presence of cold fluid left in the loop can explain the delay of the temperature response.

Energy storage in the regenerator wall

Previous studies [11,120] show that the energy storage in the housing of the regenerator can have a significant influence in the temperature response of the single-blow experiments. The effect is more noticeable in the range of low Re, even for walls of low thermal conductivity. This phenomenon causes a significant delay by the end of the outlet temperature curve very similar in shape to the one observed in the experiment at $\overline{Re}$=24.4 (Fig. 3.4).

Studying the interaction of the housing with the regenerator is beyond the scope of this work. Moreover when working as a regenerator the impact of the housing can be neglected due to its very low diffusivity [120]. In an attempt to include this effect

into the model in a direct way, two approaches were tried: increasing the specific heat capacity of the solid and adding a constant loss term to the fluid equation. However, none of these simplifications produced the desired correction.

Omitting the energy storage in the regenerator wall can lead to unphysical results when fitting the *Nu*. In this context, obtaining a model is convenient for simulating the cases that are difficult to measure.

3.4.4 Validation of the *Nu* correlation

In single-blow experiments, the shape of the outlet temperature curve between the 20% and 80% temperature breakthrough times characterizes the convective heat transfer [118]. When comparing simulation results with experiments, the best fitting can be determined by the minimum root mean squared error (*RMSE*, Eq. 2.27) between these points.

In order to analyze the suitability of the *Nu* correlation chosen (Eq. 2.46), the simulation results have been shifted in time to match the 20% temperature breakthrough point in each case as suggested in [11]. The *RMSE* has been calculated for the different options presented in Fig. 3.4. The comparison of the average temperature curve (Tout_ave) with the measurements from thermocouples 1 and 2 (Tout_1,2_EXP) produces the most consistent results for the experiments with $\overline{Re}$ up to 146. For larger values, $\overline{Re}$=243 and $\overline{Re}$=340, the simulated outlet temperature from the central channels (Tout_center) fits clearly better. Therefore, only the cases with $\overline{Re}$ 146 are considered for comparison, except for the lower piston velocity case ($\overline{Re}$=24) which seems to be severely affected by the thermal inertia effects discussed. Fig. 3.9 shows a **very good agreement between the simulations and the experiments between the 20% and 80% breakthrough times** for the cases with intermediate $\overline{Re}$ values. **These results validate the proposed *Nu* correlation and the approach employed to include the flow maldistribution in the 1D model of the Gd parallel-plate regenerator.**

Recalling the discussion about the boundary condition (sections 2.1 and 2.6), actually neither the constant heat flux (H1) nor constant wall temperature (T) boundary conditions reflect accurately the single-blow experiment (Fig. 3.10). In order to compare both options, additional simulations have been carried out with the present *Nu* correlation adapted to the T boundary condition [109,115]. Despite the values of the convection coefficient predicted by the model are from 9% to 20% lower, the outlet temperature from the regenerator and hence the *RMSE* remain practically the same (Fig. 3.11). Since the H1 boundary condition produced better results when comparing the numerical schemes for solving the conjugate heat transfer equations (section 2.3), the correlation described in section 2.6 has been definitely adopted.
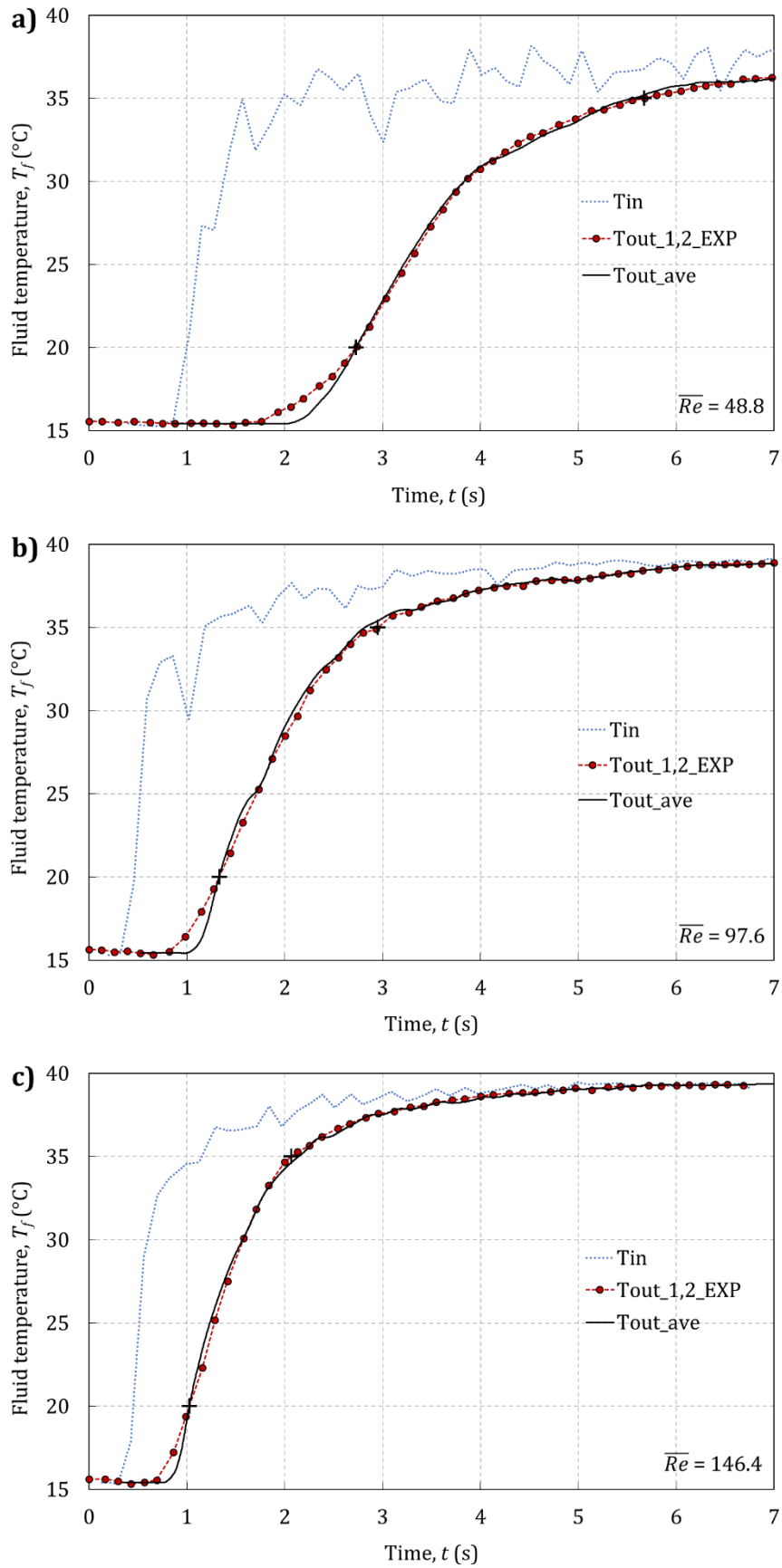
Fig. 3.9. Experimental and simulated average outlet temperatures. The crosses mark the 20% and 80% temperature breakthrough times.
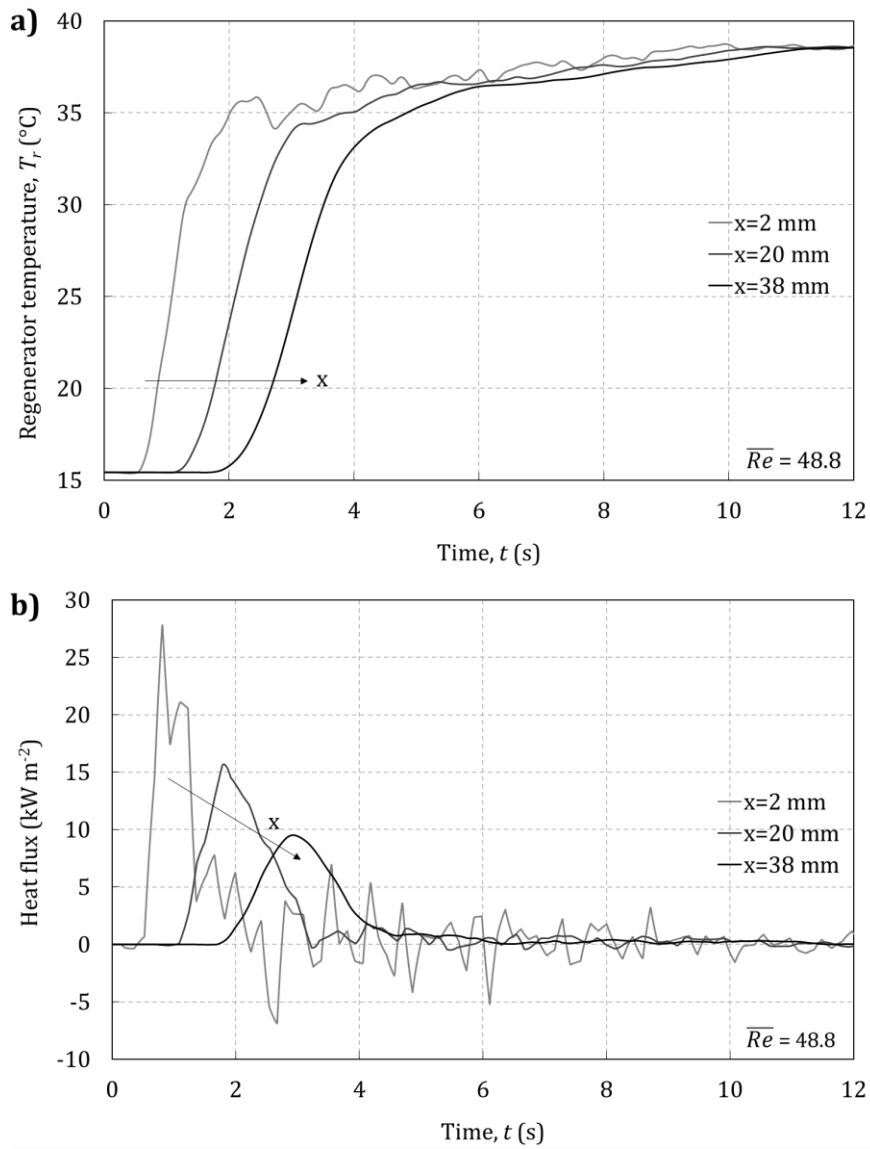
Fig. 3.10. Simulated a) regenerator temperature and b) heat flux at different axial positions.
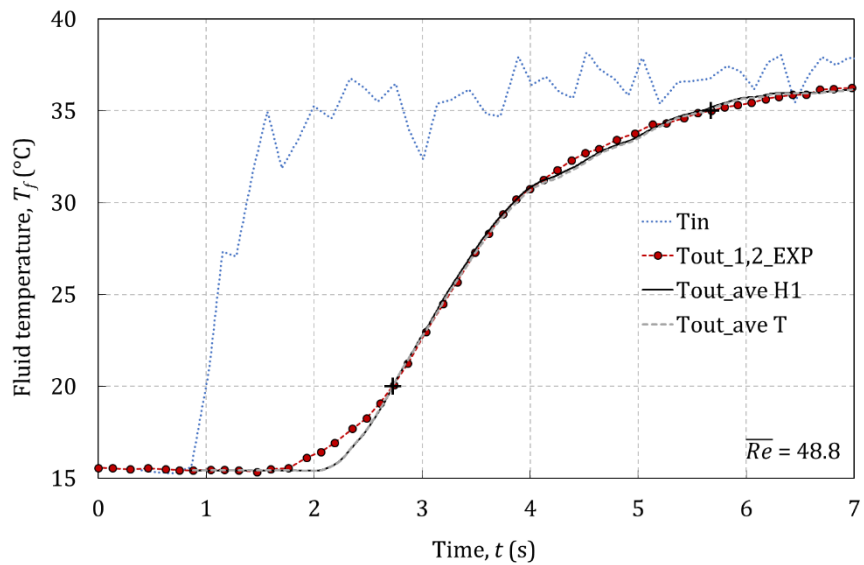
Fig. 3.11. Experimental and simulated temperature with different boundary conditions.

3.5 Single-channel model approach

Simulating all the channels in the stack consumes computation time proportionally. Moreover, if the regenerator studied could not be approached by the sum of its independent channels, a 2D model would be required. According to Engelbrecht et al. [39,79], **the effect of flow maldistribution can be taken into account in 1D single channel models by means of an effective Nusselt number** (Nu_{eff}), which is obtained by adding a scaling factor (*cNu*) to the *Nu*, as expressed in Eq. (3.2). The single channel in the model has the average height of the channels in the stack.

$$Nu_{eff} = cNu \cdot DF \cdot Nu \tag{3.2}$$

The model of the whole stack validated in this chapter has been used as a reference to fit *cNu* in the equivalent single-channel model by employing the previously explained *RMSE* methodology. Using the model rather than the experimental results avoids the experimental uncertainties specially at low *Re*. Fig. 3.12 shows an acceptable agreement between the equivalent single-channel approach, the model of the whole stack and the experimental results of the single-blow test.
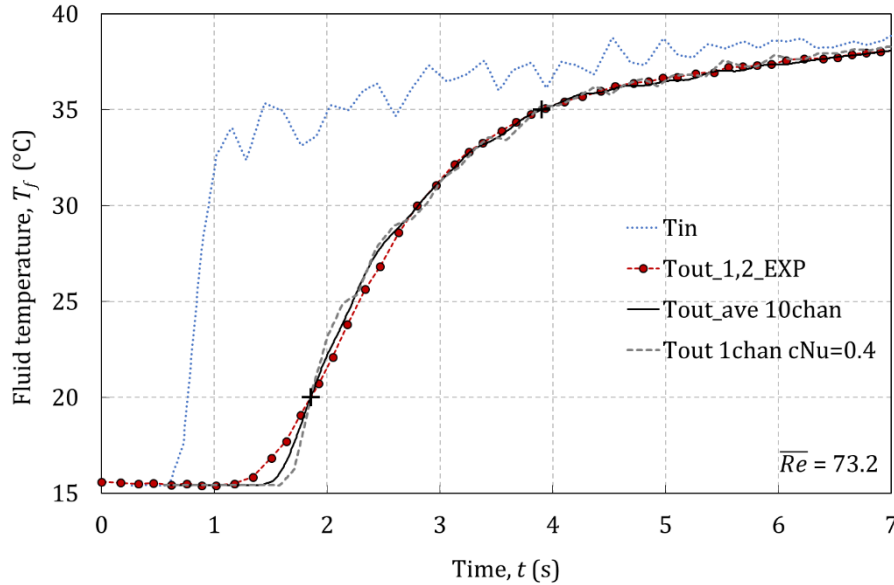
Fig. 3.12. Simulated outlet temperature with the equivalent single-channel model.

The best fit to the experimental results has also been calculated for comparison. Fig. 3.13 shows the values of *cNu* with a tolerance of ±0.05 that provide the best fit of the single-channel model for the cases studied experimentally, for both the model of the whole stack and the experimental curve Tout_1,2_EXP.
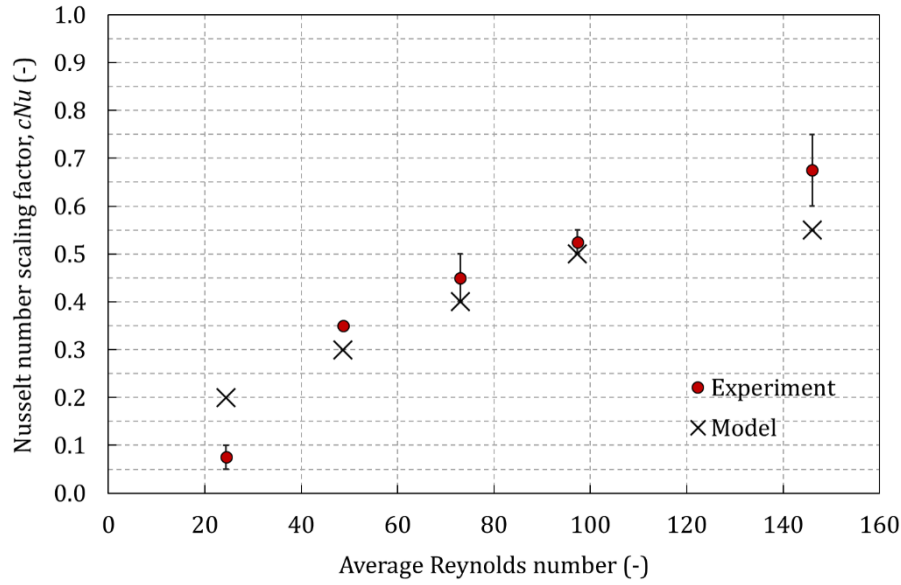
*Fig. 3.13. **Nu** scaling factor (**cNu**) as function of $\overline{Re}$ to account for flow maldistribution in the 1D single-channel model. The bars show the values found in the two experimental runs and the dots represent the average.*

The results confirms that **the flow maldistribution degrades significantly the heat transfer performance of the device tested**, to 55% and down to 20% in the conditions studied. **The degradation becomes larger as $\overline{Re}$ decreases**. This trend agrees with previous results obtained for parallel-plate regenerators with similar solid conductivity [39]. The model results match the best fit to the experiments at intermediate $\overline{Re}$ considering the tolerance, while for the lowest $\overline{Re}$ value the energy storage in the housing causes the underprediction of the Nu_{eff} as observed in previous works [11,120].

Chapter 4

Experimental validation of the AMR model

The developed 1D AMR model has been compared to the experimental results of a reciprocating AMRR prototype built by DTU Energy. A thorough validation of the model has been carried out by considering the variation of three main control parameters that determine the AMRR operation. This chapter describes the experimental setup and details the contribution of each effect included in the model to the prediction of the AMRR performance. **The sensitivity analysis carried out has allowed the validation of different modelling approaches and can be helpful to identify the sources of error when modelling AMRRs.**

4.1 AMRR experimental setup

4.1.1 Description of the experimental apparatus

DTU Energy built a **single-regenerator reciprocating AMRR device** with the purpose of testing different types of regenerators under a wide range of operating parameters. The relatively simple geometry of this apparatus allows for focusing on the regenerator performance rather than in the mechanical aspects. Therefore it is a very convenient device for validating the AMR model. The AMR test machine is described in detail in [33,102]. Fig. 4.1a is a photograph of the device and Fig. 4.1b is a scheme of the experimental setup.
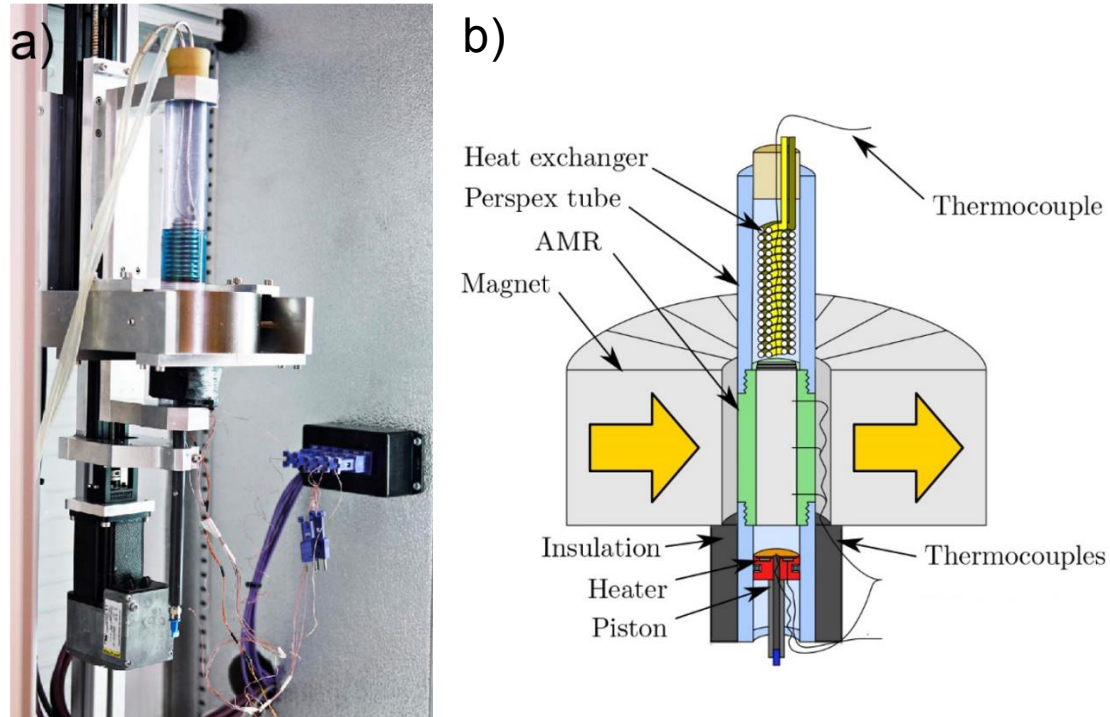
Fig. 4.1. a) AMR test machine at DTU Energy. Reproduced from [121]. b) Scheme of the AMR test machine. Adapted from [40].

The regenerator is placed inside a plastic housing in the central section of the experimental apparatus, where it is screwed onto two Perspex tubes that act as the two reservoirs. At the bottom, the cold reservoir is insulated with foam and contains a plastic piston that pushes the heat transfer fluid up and down through the regenerator. The diameter of the piston is 34 mm. A resistance heater is placed in the cold reservoir to simulate a thermal load. At the top, the fluid in the hot reservoir is maintained at around the ambient temperature by means of a cooling coil connected to an external heat exchanger. The magnetic field is provided by a Halbach cylinder permanent magnet assembly with a bore of 42 mm in diameter and 50 mm long. Fig. 4.2 shows the magnetic flux density profile in the axis of the bore in the fluid flow direction. The average flux density in the bore is 1.03 T [122,123].

A stepper motor moves the regenerator vertically in and out of the magnet synchronized with the movement of the piston in order to perform the AMR cycle. The acceleration, speed and displacement of both the regenerator and the piston can be controlled independently. The entire assembly is placed inside a cabinet where the ambient temperature can be controlled.

The Gd parallel-plate regenerator analyzed in chapter 3 was employed in the present AMR experiments [102]. The specific magnetocaloric properties obtained in section 2.4 correspond to the Gd sample in this regenerator. The dimensions and characteristics of the regenerator were detailed in in section 3.1.
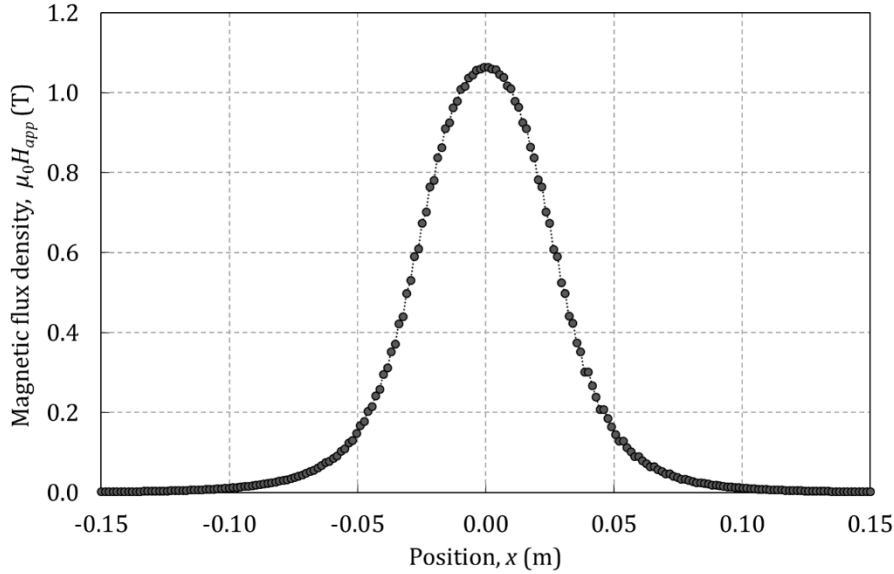
Fig. 4.2. Magnetic flux density in the axis of the magnet bore, where x=0 denotes the center of the bore.

4.1.2 Description of the AMR experiments

Experiments were performed in the described regenerator with the purpose of finding the cycle parameters that maximize the temperature span of the AMRR under no-load conditions. The heat transfer fluid employed was a solution of 75% water and 25% ethylene glycol-based commercial antifreeze. A summary of the experimental results was published in [102] and the complete set of experimental data has been provided by DTU Energy.

The temperature span (ΔT_{span}) is calculated as the difference between the mean temperature of the hot (T_H) and cold (T_C) reservoirs during an AMR cycle once the regenerator has reached the cyclical steady state. The temperatures in the reservoirs, as well as the ambient temperature (T_e), were measured with type T thermocouples calibrated in situ with an estimated uncertainty of 0.2 K [102].

Firstly, experiments varying the stroke and the speed of the piston were performed, keeping constant the ambient temperature at around 24 °C. Fig. 4.3 shows the AMR cycle realized in the test machine, which is determined by the former parameters and is the input to the AMR model. The time and fluid mass flow rate values are normalized to their maximum values in the cycle. The magnetic flux density due to the applied magnetic field is represented in the center of the regenerator.
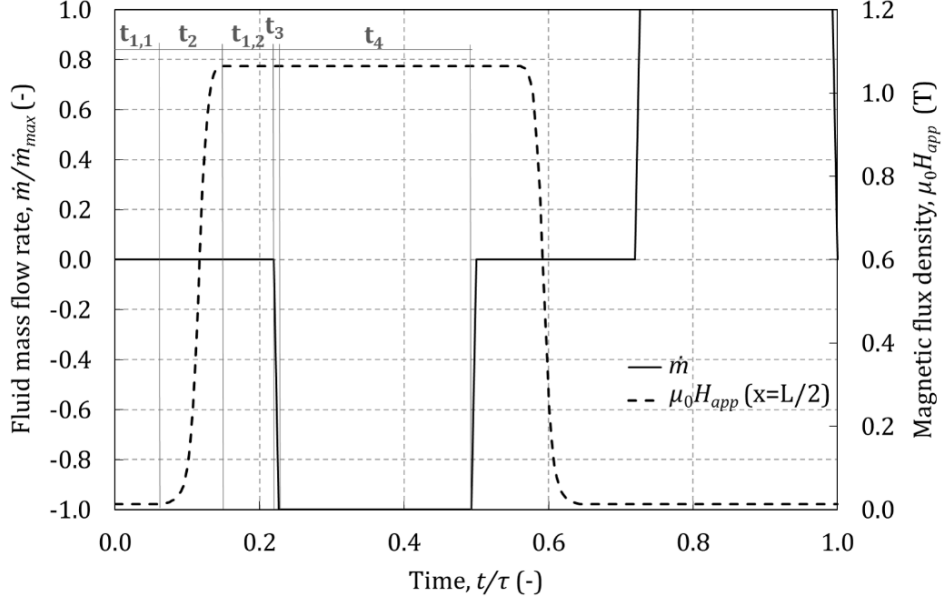
Fig. 4.3. AMR cycle realized in the test machine

The AMR cycle performed is symmetric. There is a lag time (t_1) before the movement of each motor caused by the communication between the control software and the device. The lag time before the regenerator movement is $t_{1,1}$=0.5±0.4 s and the one before the piston movement is $t_{1,2}$=0.6±0.4 s. The (de)magnetization time (t_2) should be minimum in order to maximize the AMRR performance [33,124]. According to the limitations of the present device, in the experiments t_2 was kept constant at 0.89 s. The fluid flow ramp time (t_3, Eq. 4.1) and the constant fluid flow time (t_4, Eq. 4.2) are determined by the piston movement, that is, by the piston speed (v_{pist}) and stroke (d_{pist}). The acceleration of the piston (a_{pist}) was kept constant in the experiments at 0.1 m s^{-2}. The relatively large times between the fluid flow periods and the short ramp time support the hypothesis of unidirectional steady flow.

$$t_3 = \frac{v_{pist}}{a_{pist}} \tag{4.1}$$

$$t_4 = \frac{d_{pist} - a_{pist}t_3^{\ 2}}{v_{pist}} \tag{4.2}$$

In practice, the speed of the piston controls the total mass flow rate through the regenerator ($\dot{m}$, Eq. 4.3) and the stroke determines the thermal utilization (φ, Eq. 4.4).

$$\dot{m} = \rho_f A_{pist} v_{pist} \tag{4.3}$$

$$\varphi = \frac{\bar{\dot{m}}c_f(2t_3 + t_4)}{A_c L(1 - \varepsilon)\rho_r \bar{c}_r} \approx \frac{\rho_f A_p c_f d_{pist}}{A_c L(1 - \varepsilon)\rho_r \bar{c}_r} \tag{4.4}$$

Table 4.1 summarizes the control parameters employed in these experiments and their translation into relevant AMR cycle parameters. The $\overline{Re}$ presented has been calculated with the average channel height (0.556 mm) and Eq. (2.30). The hypothesis of laminar flow regime is confirmed by the low $\overline{Re}$ values.

Table 4.1. AMR experiments varying the piston velocity and stroke.

Test	v_{pist} (mm s^{-1})	d_{pist} (mm)	T_e (°C)	φ	τ (s)	$\dot{m}$ (g/s)	$\overline{Re}$
1	0.5		24.4		16.35	0.469	1.8
2	1		24.4		10.18	0.938	3.6
3	2	3.09	24.4	0.57	7.11	1.876	7.2
4	4		24.3		5.60	3.751	14.4
5		2.09	23.5	0.38	8.18		
6	1	5.09	23.6	0.92	14.18	0.938	3.6

Secondly, experiments at different ambient temperatures were carried out with the piston speed and stroke that maximize the no-load temperature span (v_{pist}=1.25 mm s^{-1} and d_{pist}=3.09 mm). The variation of the ambient temperature results in a variation of the hot end temperature. A total of 9 tests were performed at ambient temperatures between 30 °C and 15 °C.

Additionally, the experiments varying the ambient temperature were repeated with a **regenerator housing with hollow walls** with the purpose of analyzing the thermal losses through the regenerator wall. The results are reported in [102] and show that in the present setup **the heat losses through the regenerator walls are practically negligible**. The authors suggested that there could be a more important heat gain in the cold reservoir from the ambient.

The validity of the 1D approach for the simulation of the proposed AMR experiments has been analyzed. According to Petersen et al. [98], the temperature gradients at the end of the magnetization step can be neglected if $\Gamma \gg 1$ (Eq. 4.5). Similarly, at the end of the fluid blow the temperature gradients will be negligible if $NTU \gg 1$ (Eq. 4.6).

$$\Gamma = \pi^2 \alpha_f \frac{t_2}{H_{f,i}{}^2} \tag{4.5}$$

$$NTU = \frac{h(2W d_{pist})}{\dot{m}_i c_f} \approx \alpha_f \frac{Nu}{H_{f,i}{}^2} \frac{d_{pist}}{v_{pist}} \tag{4.6}$$

In the present setup, Γ ranges between 2.24 and 12.16, for the maximum and minimum channel heights of the stack respectively. *NTU* ranges between 1.62 and 70.50. The lowest *NTU* values occur in the tests at large piston velocities, especially in the thickest channels.

4.2 AMRR simulations setup

The modelling parameters employed to simulate the no-load experiments in the AMR test machine are summarized in Table 4.2. The regenerator has been simulated as the sum of its 10 isolated channels in order to account for the flow maldistribution, as validated in chapter 3.

Table 4.2. Modelling parameters of the AMR experiments

Parameter	Value	Parameter	Value
ρ_f	1033 kg m^{-3}	ρ_r	7901 kg m^{-3}
c_f	3852 J kg^{-1} K^{-1}	k_r	11 W m^{-1} K^{-1}
k_f	0.4808 W m^{-1} K^{-1}	H_r	0.0009 m
μ_f	0.002207 Pa s	W	0.023 m
H_f	Table 3.1	L	0.040 m
MCM properties	Section 2.4	$\overline{N_{avg}(x)}$	0.29

The model inputs are the inlet fluid mass flow rate and temperature and the applied magnetic field profiles of the AMR cycle, which depend on the experimental settings (Fig. 4.3). Following the strategy presented in [11], a function was developed to convert the test machine inputs into model inputs. The applied magnetic field has been implemented as a function of space and time, according to the profile in Fig. 4.2 and to the movement of the regenerator relative to the magnet (Fig. 4.3). The inlet temperature of the fluid flow is calculated with a model of the reservoirs as explained below.

The 1D AMR model coupled with the model of the reservoirs is run until the cyclic steady state is reached, that is when the relative change in the internal energy from cycle to cycle is below a tolerance, in this case 10^{-5} [11]. The initial temperature of the system is set to T_H.

4.2.1 Calculation of the inlet temperatures to the AMR model

The temperature of the fluid flow entering the AMR is given by the temperature of the fluid in the reservoirs of the test machine.

In principle, the mean temperature measured in the hot reservoir experiments (T_H) has been used as an input to the AMR model in order to avoid the uncertainties associated to its calculation from the ambient temperature. However, the variation of T_H during the hot blow may affect the AMR performance.

Regarding the cold reservoir, since its temperature (T_C) is an experimental output, it is convenient to calculate T_C with the model by imposing an applied thermal load (0 in this case). Following the conclusions obtained with the hollow regenerator

experiment, **a significant thermal gain from the ambient may be occurring in the cold reservoir, which will certainly affect the fluid temperature.**

In order to determine the values of T_C and T_H, **a single-node model of each reservoir has been included in the AMR model.** This approach allows for calculating ΔT_{span} as in the experiments. Eq. (4.7) and (4.8) are the mass and energy balances in the cold reservoir respectively, assuming that the fluid in the reservoir is perfectly mixed.

$$\frac{dm_C}{dt} = \dot{m} \tag{4.7}$$

$$\frac{d\left(m_C c_f T_C\right)}{dt} = \dot{m} c_f T_f + UA_C (T_e - T_C) + \dot{Q}_{heater} \tag{4.8}$$

The first term in the right hand side of Eq. (4.8) refers to the fluid flow in or out of the reservoir. When the fluid flows into the cold reservoir ($\dot{m}<0$), T_f is the fluid temperature exiting the regenerator (Eq. 2.12). When the fluid is pushed out of the cold reservoir ($\dot{m}>0$), T_f represents the inlet temperature to the regenerator and is assumed equal to the mean temperature of the cold reservoir (T_C). The second term accounts for the thermal losses to the ambient through a global heat transfer coefficient (UA_C). Finally, the third term refers to the heat load from the resistance heater in the test machine ($\dot{Q}_{heater}$), which equals 0 in the no-load experiments.

The balance equations of the hot reservoir are analogue considering the change in direction of the fluid flow. In this case, UA_H represents the global heat transfer coefficient of the cooling coil. The term that represents the heating load does not apply to the hot reservoir.

The equations of the reservoirs are discretized as explained in section 2.2 (Eq. 2.15 with $\xi=0.5$). The initial value of the fluid temperature into the reservoirs was set at the ambient temperature. The initial volume in the cold reservoir is the dead volume between the piston and the regenerator inlet. The estimated distance between them is 2 mm. Therefore, in the hot reservoir the initial volume must be at least the volume moved by the piston. The magnitude of the dead volume does not affect the temperature results at the cyclic steady state, only the time to reach convergence.

Note that if the variation of the inlet temperatures to the regenerator is neglected, this modelling approach is equivalent to finding the value of T_C that produces a refrigeration capacity in the periodic steady-state equal to 0 for a given value of T_H [80]. However the proposed method fixes the heating capacity, therefore in this case the solution is found with a single run.

4.2.2 Estimation of the thermal losses to the ambient

The global heat transfer coefficient between the cold reservoir and the ambient (UA_C) is given by the sum of the thermal resistances between them (Eq. 4.9). The heat transfer to the environment is assumed to be mainly convective.

$$UA_C = \frac{1}{\frac{1}{A_C h_C} + R_{cond} + \frac{1}{A_e h_e}} \tag{4.9}$$

In Eq. (4.9), R_{cond} represents the conduction resistances through the walls of the reservoir. The lateral walls of the cold reservoir ($R_{cond,r}$) are covered by an insulating foam. The bottom part of the reservoir ($R_{cond,z}$) is limited by the plastic piston. If the resistance of the reservoir walls is assumed to be negligible compared to the resistance of the insulation, R_{cond} is given by Eq. (4.10).

$$R_{cond} = \frac{1}{\frac{1}{R_{cond,r}} + \frac{1}{R_{cond,z}}} = \frac{1}{\frac{2\pi \bar{L}_C k_{ins}}{ln(D_e/D_C)} + \frac{A_{pist} k_{pist}}{e_{pist}}} \tag{4.10}$$

The convection coefficients of the water inside the reservoir (h_C) and the external air (h_e) have been estimated from the results of the experiments performed in the AMR test machine reported in [40]. Despite that this experimental setup is not exactly the same as the one of the AMR experiments analyzed in this work, this information has been useful for obtaining an order of magnitude of the thermal losses. Briefly, the experiments consisted on pouring hot water into the test machine and letting it cool down to the ambient temperature. The temperature of the water during this process was measured at several points, including the cold reservoir. The experiment was repeated with and without the insulation.

Table 4.3 summarizes the values of the parameters employed to calculate the interaction of the cold reservoir with the ambient. $\bar{L}_C$ represents the mean length of the cold reservoir during the AMR cycle. Typical values of the thermal conductivity of the materials have been considered.

Table 4.3. Model parameters related to the cold reservoir.

Parameter	Value	Parameter	Value
D_C	34 mm	$\bar{L}_C$	$d_{pist}/2 + 2$ mm
e_{ins}	13 mm	e_{pist}	10 mm
k_{ins}	0.035 W m^{-1} K^{-1}	k_{pist}	0.35 W m^{-1} K^{-1}
h_C	$100 - 200$ W m^{-2} K^{-1}	h_e	$10 - 20$ W m^{-2} K^{-1}

In the hot reservoir, the global heat transfer of the cooling coil (UA_H) has been adjusted the experimental results so that the average T_H measured matched the simulation.

4.2.3 Time and space grids

Preliminary simulations were carried out to establish the spatial and time grids. The solution remains practically unchanged with 100 spatial steps ($|\Delta T_{span}(n_x{=}100)$ - $\Delta T_{span}(n_x{=}200)| < 0.02$ K). The time step is variable according to the cycle timing (Fig. 4.3). Each of the events in the AMR cycle is simulated with an entire number of time steps in order to ensure the repeatability of the solution if the time grid is varied. A time step of 0.1 s is enough to reproduce consistently the lag times (t_1), while the (de)magnetization periods (t_2) require at least 30 time steps each. The time step in the flow periods t_3 and t_4 is calculated separately to achieve $CFL{\approx}1$.

The simulations were run in a PC with an Intel Core i3-2100 3.10 GHz processor. With the proposed space and time grids, the simulation time of a single channel with the working conditions in Table 4.1 ranges between 0.39 and 0.62 s per AMR cycle. The total simulation time depends on the number of cycles needed to reach the cyclic steady state.

4.3 Validation results and discussion

Figs. 4.4, 4.5 and 4.6 compare the experimental and simulation results of the AMR test machine including in the model all the effects detailed in chapter 2 and the gain from the ambient in the cold reservoir. The dotted lines represent the range in which the simulation results could be found, depending on the different modelling hypotheses. As can be observed **the modelling uncertainties have a limited influence in the simulation results, by up to 5%**.
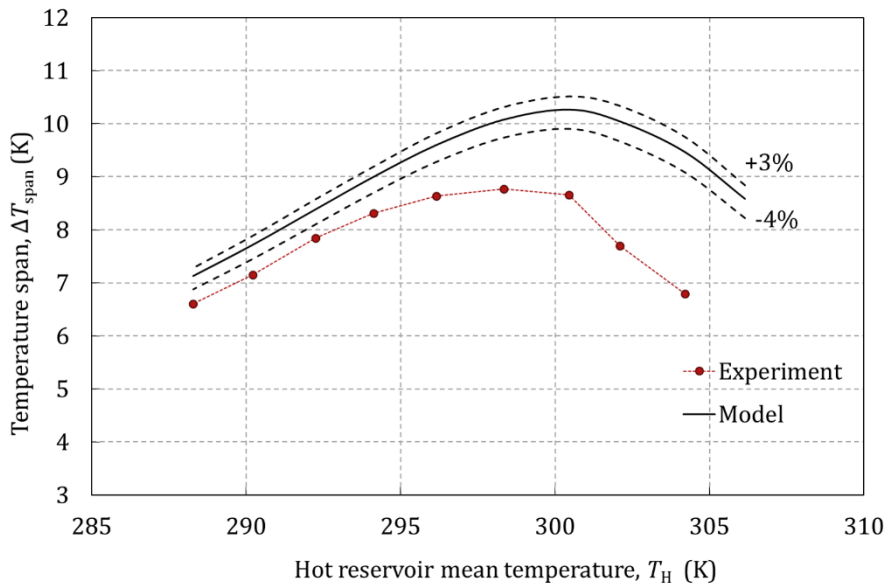
Fig. 4.4. Experimental and simulation results of the AMR tests varying the ambient temperature.

Fig. 4.4 shows the results of the tests at different ambient temperatures, that is, different hot inlet temperatures (T_H) to the AMR. The variation of the AMR performance as function of T_H is mainly related to the magnetocaloric properties of the material. In this case the model overpredicts by 0.5 to 2.5 K (8% to 39%) the no-load temperature span.

Although the predicted and measured trends are similar, the simulation results are shifted by around 1 to 2 K. The most probable cause of this shifting is the offset of the thermocouples employed in the different apparatus. Another source of error is the position of the thermocouples in the reservoirs and the stratification. If the temperature measured differs from that of the fluid actually entering the regenerator, the same displacement effect is produced. Also the differences between the Curie temperature of the sample measured and the average of the regenerator can explain this effect.
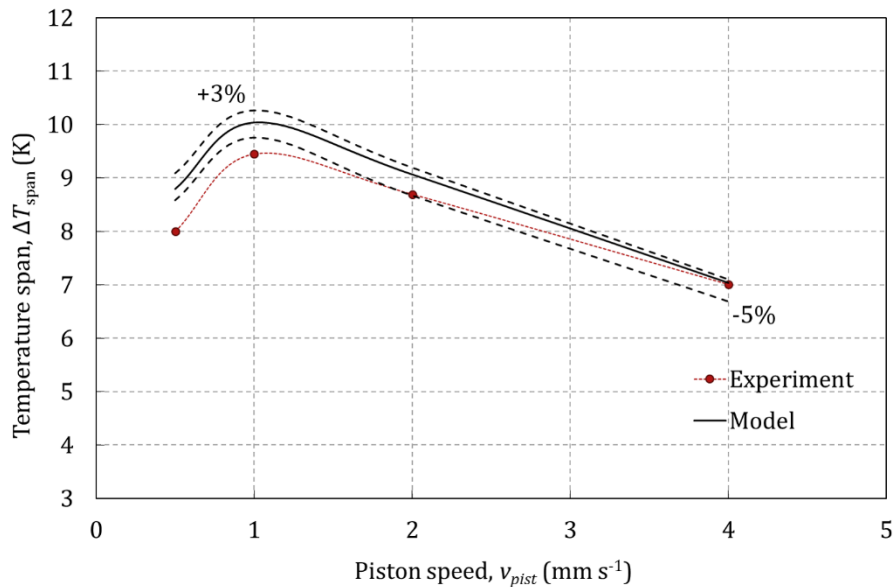
Fig. 4.5. Experimental and simulation results of the AMR tests varying the piston speed.

Fig. 4.5 shows the results of the tests at different piston speeds, at a constant ambient temperature that results in $T_H \approx 297$ K. The piston speed determines the fluid mass flow rate but also affects the duration of the blow period. Hence the performance of the AMR is mainly affected by the conjugate heat transfer process and, at low cycle frequencies, also by the thermal losses. In this case the simulation results differ from the experiments by a maximum of 10%. The slight overprediction of up to 1 K is in agreement with the results in Fig. 4.4 and is within the range of the experimental uncertainty.

As expected, the largest discrepancy occurs at low piston speeds (low frequency and low *Re*), at which the thermal losses have a greater impact and the heat storage in the regenerator housing may have an effect.
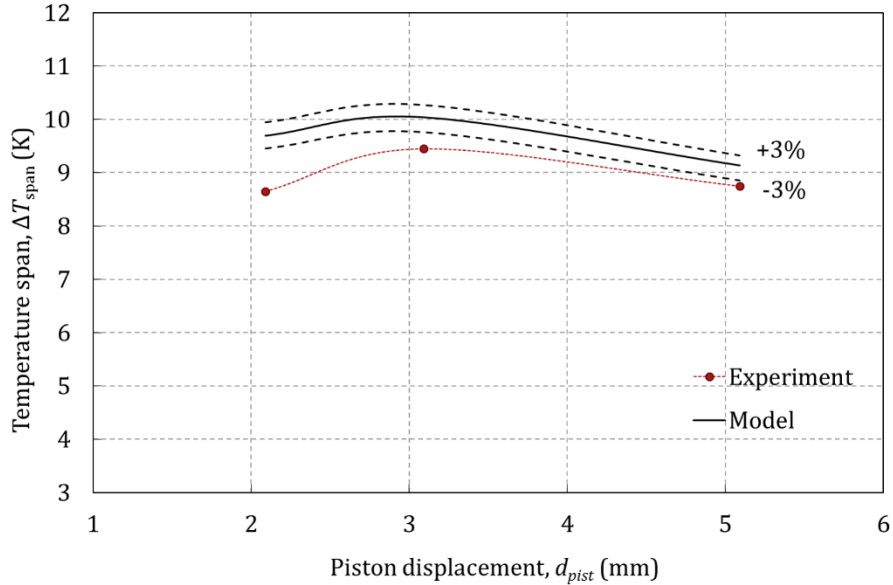
Fig. 4.6. Experimental and simulation results of the AMR tests varying the piston displacement.

Fig. 4.6 contains the results of the experiments at different piston strokes at a constant ambient temperature. In this case, the resulting average T_H varied around 1 K between the experiments ($T_H \approx 297 \pm 0.4$ K). The reason is that the variation in the hot reservoir temperature along the AMR cycle increases as the piston displacement becomes larger.

The fluid displacement controls the utilization while keeping the flow rate, so it also affects the frequency. The cases with larger piston strokes are therefore more affected by the thermal losses, however the decrease in the hot inlet temperature may be distorting the curve. Again the results are slightly over predicted by up to 1K (from 12% to 6%).

The limitations of the 1D model must be taken into account when analyzing the accuracy of the simulation results. In the studied experiments the thermal gradients perpendicular to the fluid flow may be relevant due to the relatively thick channels and plates and the low thermal conductivity of Gd (*Bi* is around 0.1). However, from the value of the degradation factor (*DF*=0.95, Eq. 2.55) this effect is expected to have a small influence. Besides, the boundaries of the regenerator are not included in the model. Actually the experimental device contains 11 plates and the top and bottom plates of the stack are in contact with the housing. In the model, ten pairs plate-channel have been considered. Finally, the 3D effect of the demagnetizing factor is omitted and may interact with the flow maldistribution.

In general, **the 1D AMR model reproduces very well the influence of the main control parameters that determine the operation of an AMRR. In most cases the magnitude of the error, less than 1 K, is within the range of the experimental uncertainty. In the following sections, the modelling uncertainties and the influence of the major losses mechanisms in the studied AMRR are thoroughly analyzed.**

4.3.1 Uncertainties in the magnetocaloric properties

In section 2.4 two magnetocaloric properties data sets were obtained for the Gd sample in the studied regenerator, according to different assumptions made in the curve-building process. Fig. 4.7 compares the simulation results with the two sets to the experimental results of the tests varying the ambient temperature.
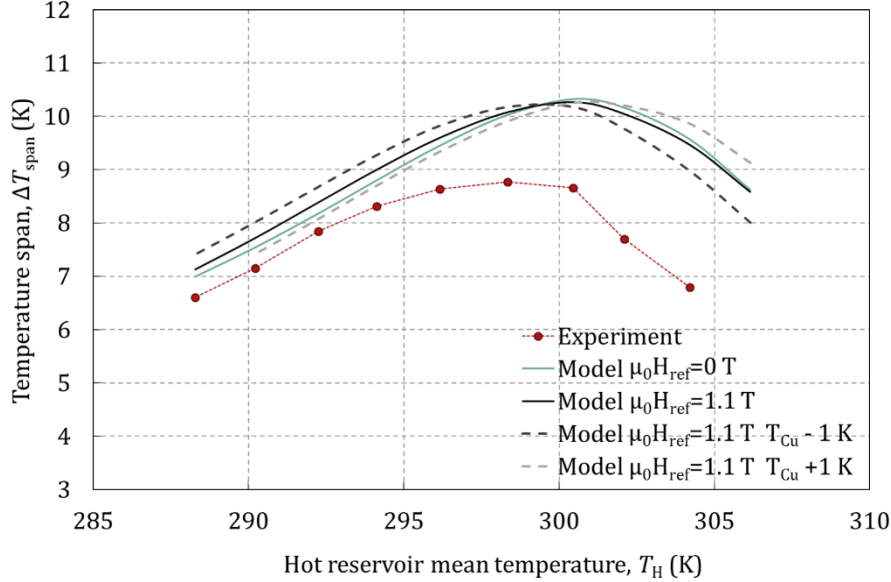
Fig. 4.7. Effect in the validation results of the uncertainties in the determination of the MCM properties.

The differences in the magnetocaloric properties caused by the curve-building process have little influence in the simulation results. In general the temperature span predicted by the $\mu_0 H_{ref}$=1.1 data set built is slightly higher, according to the lower specific heat capacity values predicted by this set [18].

There is also an uncertainty in the determination of the Curie temperature of the sample. The dotted lines in Fig. 4.7 show the effect of shifting the Curie temperature by ±1 K.

4.3.2 Computation of the demagnetization

As explained in section 2.5, the internal magnetic field is calculated with the average demagnetization factor (N_{avg}) and the magnetization of the material (M). Both of these quantities depend on the temperature of the regenerator and on the applied magnetic field.

Fig. 4.8 shows the value of N_{avg} as function of the position along the fluid direction, for several values of the applied field and the regenerator temperature. For the studied application, $N_{avg}(x)$ is a weak function of the magnitude of applied field and the temperature. The average value of $N_{avg}(x)$ ranges between 0.286 and 0.298.

Fig. 4.8a shows the impact in $N_{avg}(x)$ of the variation of the applied magnetic field during the cycle, assuming a linear temperature gradient between 304 and 297 K. On the one hand, the applied field varies during the (de)magnetization processes. Besides, the applied magnetic field is not constant along the magnet bore (Fig. 4.2). In this case, there is a negligible difference in the N_{avg} values for constant applied fields between 0.35 and 0.98 T. $N_{avg}(x)$ calculated with the flux profile in the centre of the magnet bore (dotted line) can be approached by $N_{avg}(x)$ calculated with the average flux value, 0.98 T (black line).

Fig. 4.8b represents $N_{avg}(x)$ for different values of the temperature gradient (full lines) and for a constant temperature along the regenerator (dotted line). As expected from [125], N_{avg} decreases with the temperature.
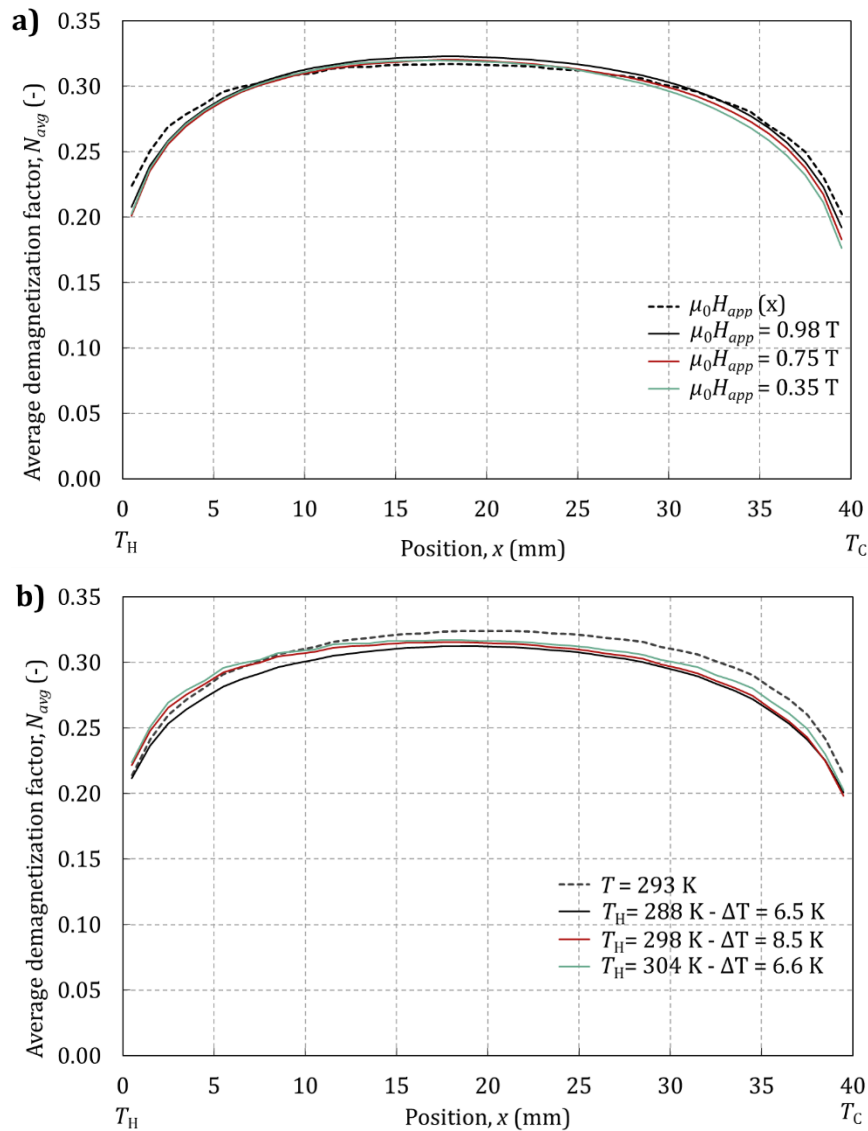
Fig. 4.8. Average demagnetization factor along the AMR as function of a) the applied field and b) the temperature gradient.

The influence of the position-dependence of N_{avg} in the calculation of the internal magnetic in the 1D AMR model is shown in Fig. 4.9. The evolution of the internal magnetic field during the AMR cycle is represented in the hot end (x=0), the center (x=$L/2$) and the cold end (x=L) of the studied regenerator. The demagnetization effect is ill defined for low field values and causes convergence problems in the model, so it is not computed for applied field values lower than 0.20 T. The full-line profiles have been obtained with $N_{avg}(x)$ (Eq. 2.40) while the dotted-line profiles have been obtained with N_{avg}=0.29 (Eq. 2.41). According to the shape of the $N_{avg}(x)$ curve, the largest differences are observed at both ends of the regenerator, especially at the cold end (up to -20%). At the center of the regenerator the differences are up to +4.5%.
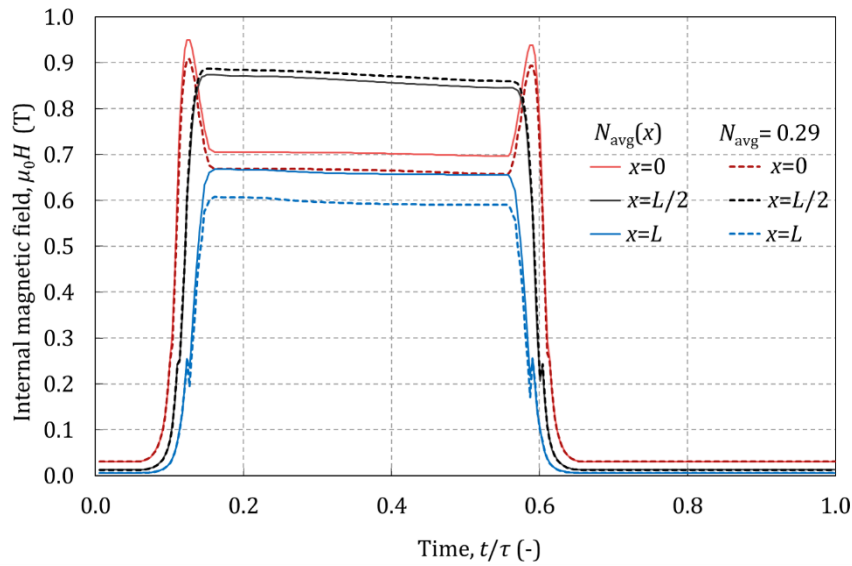
Fig. 4.9. Internal magnetic field calculated with N_{avg} (x) and N_{avg}=0.29.
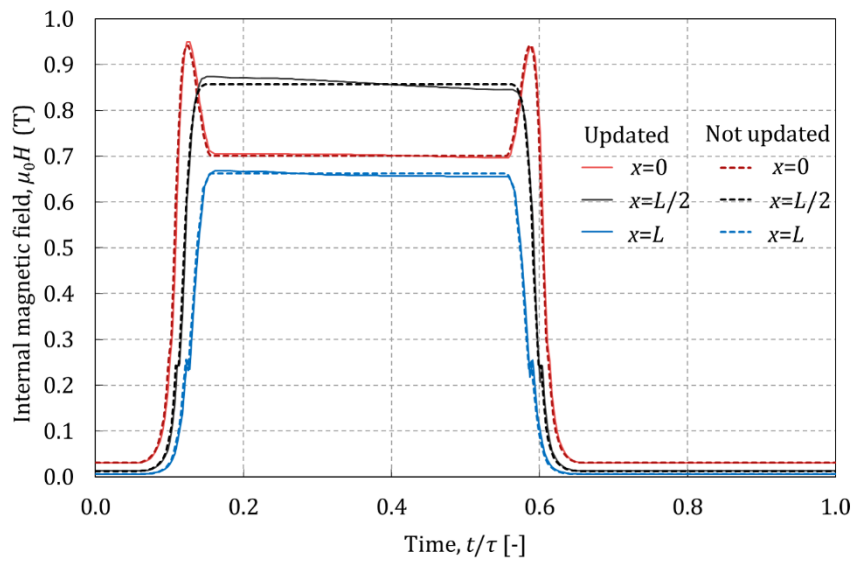
Fig. 4.10. Internal magnetic field updated after every time step and calculated with a linear temperature profile (not updated).

The internal magnetic field is calculated iteratively in the model at every time step because M depends on the temperature of the regenerator and on the internal field. However this is a time-consuming process. A simplification employed in literature [79] consists of calculating the internal magnetic field only once at the beginning of the simulation based on a linear temperature gradient. Fig. 4.10 compares the results obtained with both approaches and $N_{avg}(x)$. The profiles obtained are very similar. The largest differences are observed in the center of the regenerator (up to 2.3%), where the temperature profile resembles less the linear assumption.

The AMRR tests varying the ambient temperature have been simulated with the former assumptions in order to analyze their influence in the validation results, as shown in Fig. 4.11. The results of the model omitting the demagnetizing effect (blue dotted line) have been included to prove that this is a relevant loss mechanism. However the computation of the internal magnetic field does not have a significant effect in the simulation results. Despite the differences observed in Fig. 4.9, the effect of the variation of N_{avg} along the fluid direction is negligible in agreement with [45] (grey dotted line). Also the change in temperature during the AMR cycle can be obviated in this case, which makes unnecessary to update the internal magnetic field at every time step (green dotted line). This simplification yielded 25% savings in computation time.

In conclusion, the internal magnetic field may be calculated only once at the beginning of the simulation with a mean N_{avg} value without losing accuracy, provided that the initial internal magnetic field is calculated based at least on a linear temperature profile. Employing the constant initial temperature instead (T_H in this case) overpredicts slightly the AMR performance (green full line).
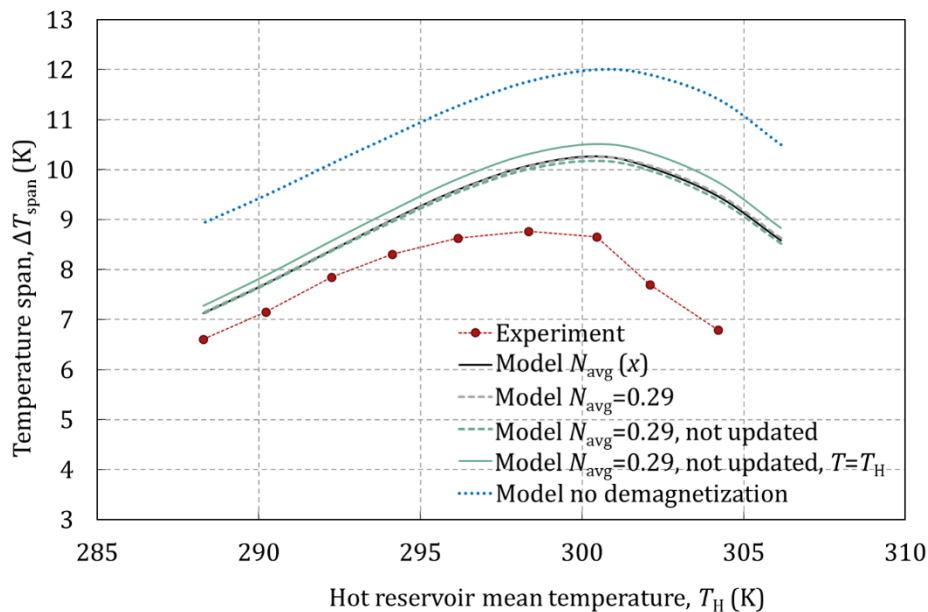
Fig. 4.11. Influence of the demagnetizing effect in the validation results of the AMR tests varying the ambient temperature.

4.3.3 Conjugate heat transfer correlations and fluid flow maldistribution

The effect of the conjugate heat transfer and the flow maldistribution is related to the characteristics of the fluid flow through the channels. Hence the AMRR tests varying the piston speed and stroke have been chosen to analyze these phenomena. The AMR model of the complete stack has been run with different Nu correlations. Another set of simulations was performed with a single channel in order to omit the effect of the fluid flow maldistribution. The results are shown in Fig. 4.12.
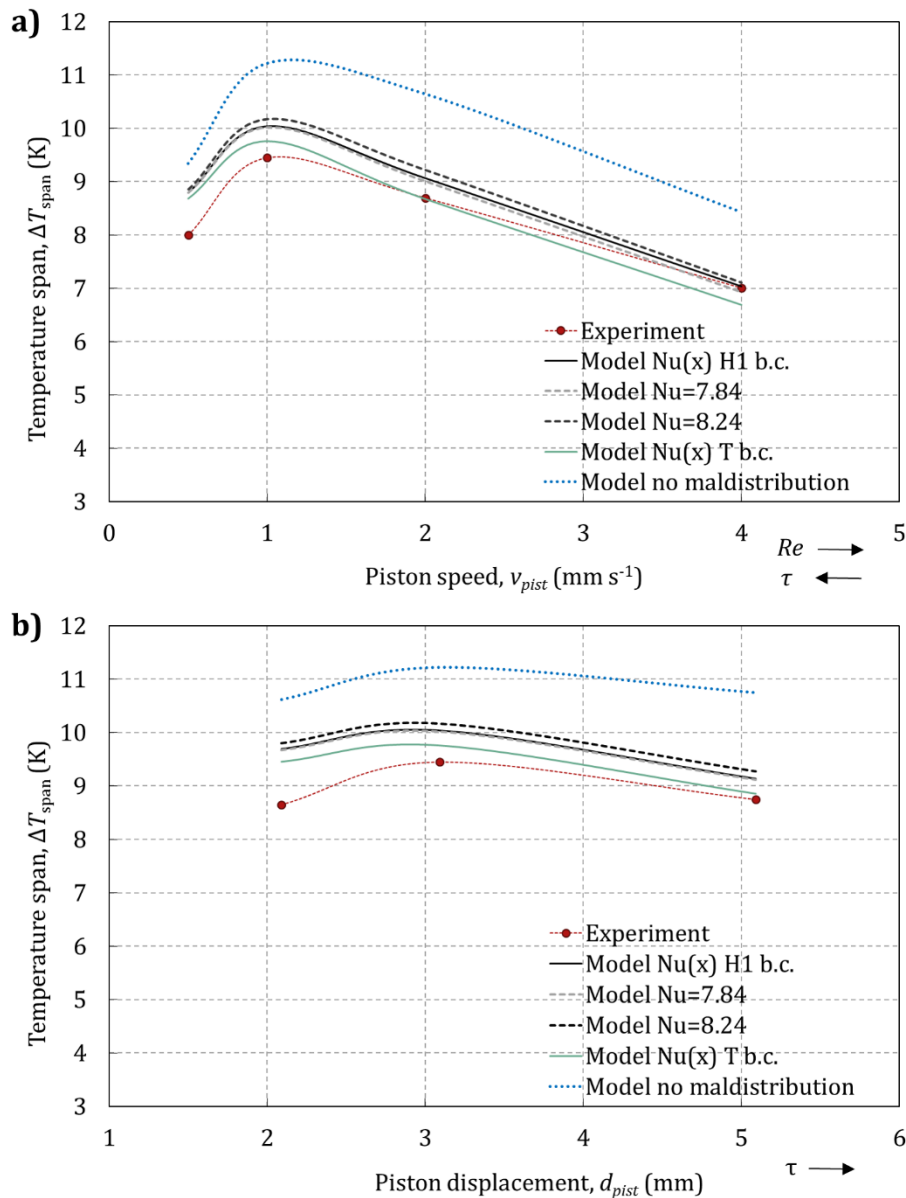
Fig. 4.12. Influence of the Nu correlation and the flow maldistribution in the validation results of the AMR tests varying a) the piston speed and b) the piston stroke.

As discussed in section 2.1, there is not an agreement in literature about the most suitable *Nu* correlation for parallel-plate AMRR devices. Several options have been compared in Fig. 4.12. The full black line has been obtained with the *Nu* correlation detailed in section 2.6, which considers the entrance effect, the actual rectangular geometry of the channel and the constant heat flux boundary condition (H1 b.c.). The dotted grey line omits the entrance effect, which results in a constant *Nu*=7.84. The results show that in these experiments the entrance effect is negligible, especially at the lowest *Re* values. The dotted black line considers additionally the simplification of the channel geometry to parallel-plates, which results in *Nu*=8.24. This 5% variation in the *Nu* has a very small impact in the simulation results. Finally, the full green line includes the entrance effect and the actual geometry, but assumes the constant temperature boundary condition (T b.c.). The difference in the boundary condition represents a 10% variation of the fully-developed *Nu* value. Although this difference was negligible in the single-blow experiments, it affects to a certain extent the AMR simulation results. **In conclusion, in the range of narrow channels, low fluid velocities and small displacements, the conjugate heat transfer correlation employed does not imply a significant source of error.**

As expected, **the flow maldistribution produces a significant decrease in the regenerator performance** in both cases (blue dotted line compared to black line). From the results in Fig. 4.12a, the losses in the conjugate heat transfer process have a greater impact in the performance of the points with a high piston speed and hence a short blow period, even though the degradation due to flow maldistribution is reduced as the fluid velocity increases as discussed below. However the opposite trend is observed in Fig. 4.12b. In this case, the detrimental effect of flow maldistribution increases in a larger extent as the distance covered by the fluid increases.

Assuming that the thermal cross talk between channels is negligible in the present case (section 3.4.4), the effect of the fluid flow maldistribution can be analyzed as follows. As explained in section 3.5, the flow maldistribution can be accounted for with a single-channel model by adding a scaling the factor to the *Nu* correlation that fits the results of the whole stack model. Therefore, the scaling factor (*cNu*) reveals the relative degradation of the heat transfer performance. Table 4.4 the values of *cNu* that reproduce the simulation results of the whole stack with a maximum difference of 0.04 K.

Table 4.4. Scaling factor for the Nusselt number (cNu) as function of Re and d.

Re	cNu (d = 7.7%)	d	cNu (Re=3.6)
1.8	0.61	5.2%	0.66
3.6	0.65	7.7%	0.65
7.2	0.67	12.7%	0.54
14.4	0.68	Single-blow (100%)	0.29

In agreement with [39], *cNu* increases as the *Re* increases, that is, **the effect of flow maldistribution is reduced as the fluid velocity increases**. A dependence of *cNu* with the relative distance covered by the fluid flow (*d*) has also been observed. Specifically, *cNu* decreases and hence **the effect of flow maldistribution increases as the distance swept increases**. This result is supported by the fact that the *cNu* values obtained with the single-blow test are significantly lower. Finally, the simulation results of the experiments at a constant piston speed (*Re*=4.5) and displacement (7.7%) can be consistently reproduced with *cNu*=0.66.

4.3.4 Variation of the inlet temperatures due to the losses to the ambient

Fig. 4.13 represents the effect of the thermal gain from the ambient in the cold reservoir. **The addition of the thermal losses to the model has a significant impact in the simulation results. However the uncertainty in the estimation of the thermal resistances is not critical in this case.**

As expected, the gain from the ambient is larger as the temperature span increases, given that the temperature of the cold reservoir is further from the ambient temperature (Fig. 4.13a). The cases with a larger cycle time are also more affected by the ambient losses (Fig. 4.13b). The apparently opposite trend in Fig. 4.13c can be explained by considering that the cold reservoir has more inertia in the cases with a larger fluid displacement. Since the model of the reservoir calculates a uniform temperature, the larger inertia results in a lower increase of T_C, and hence the regenerator performance is less reduced.

Regarding the variation of the hot inlet temperature, the proposed single-node model of the hot reservoir does not reproduce the magnitude of temperature variation measured. As a result, the simulation results employing the hot reservoir model or assuming a constant hot inlet temperature are practically the same. The cause of the variable hot inlet temperature registered could be due to the stratification in the reservoir instead.
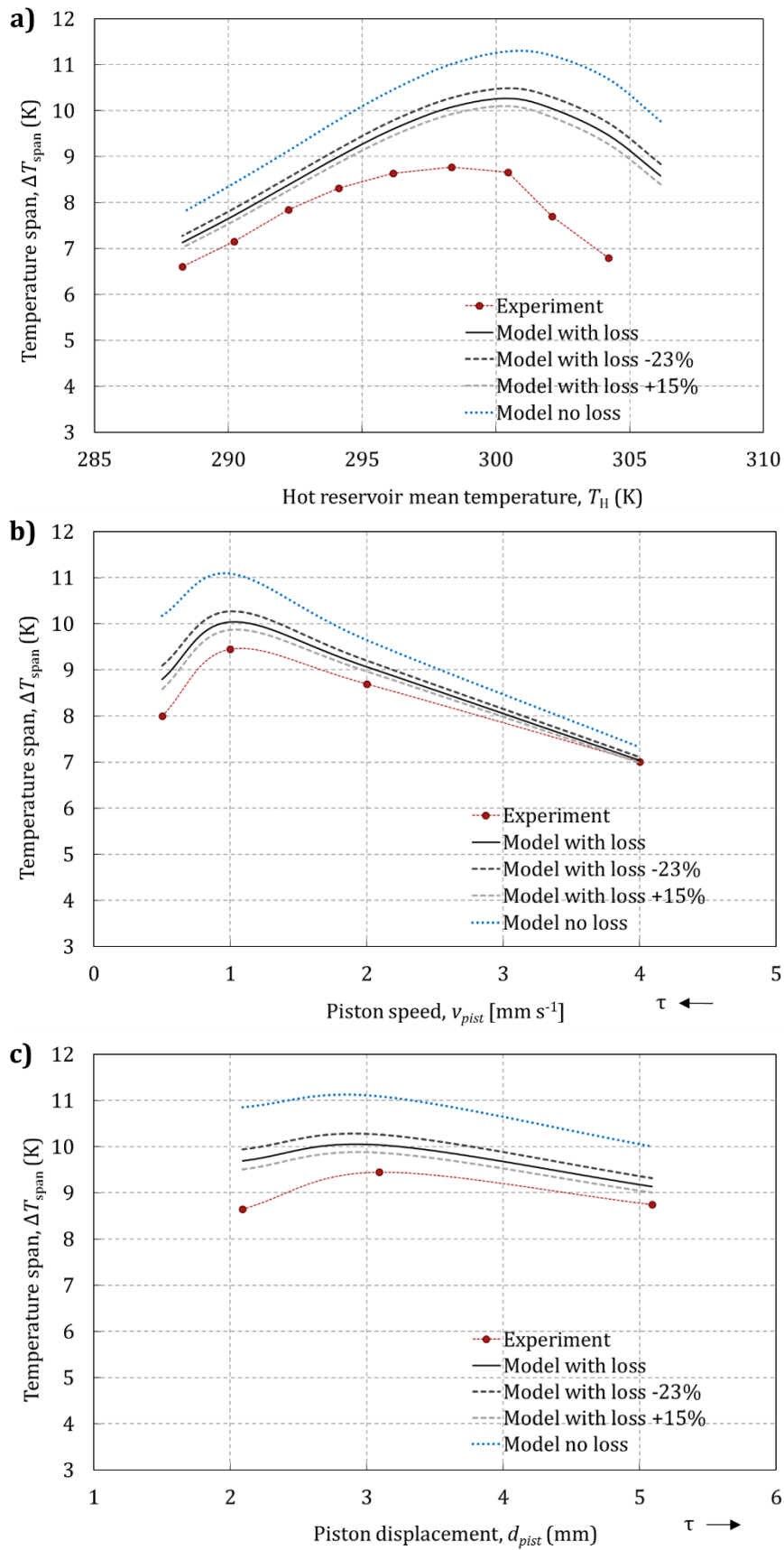
Fig. 4.13. Influence of the ambient losses in the cold reservoir in the results of the AMR tests varying a) the ambient temperature, b) the piston speed and c) the piston stroke.

4.3.5 Uncertainty in the lag time

The AMR simulations were repeated with the extreme measured values of the lag times in order to analyze the effect of this experimental uncertainty in the model predictions. As can be observed in Fig. 4.14, **including the lag times improves the validation results but their variation in the experiments is not critical**. While decreasing the lag time by 30% does not affect the simulation results, including or increasing the lag time affects in a larger degree the cases that are more sensible to the thermal losses, as explained above.
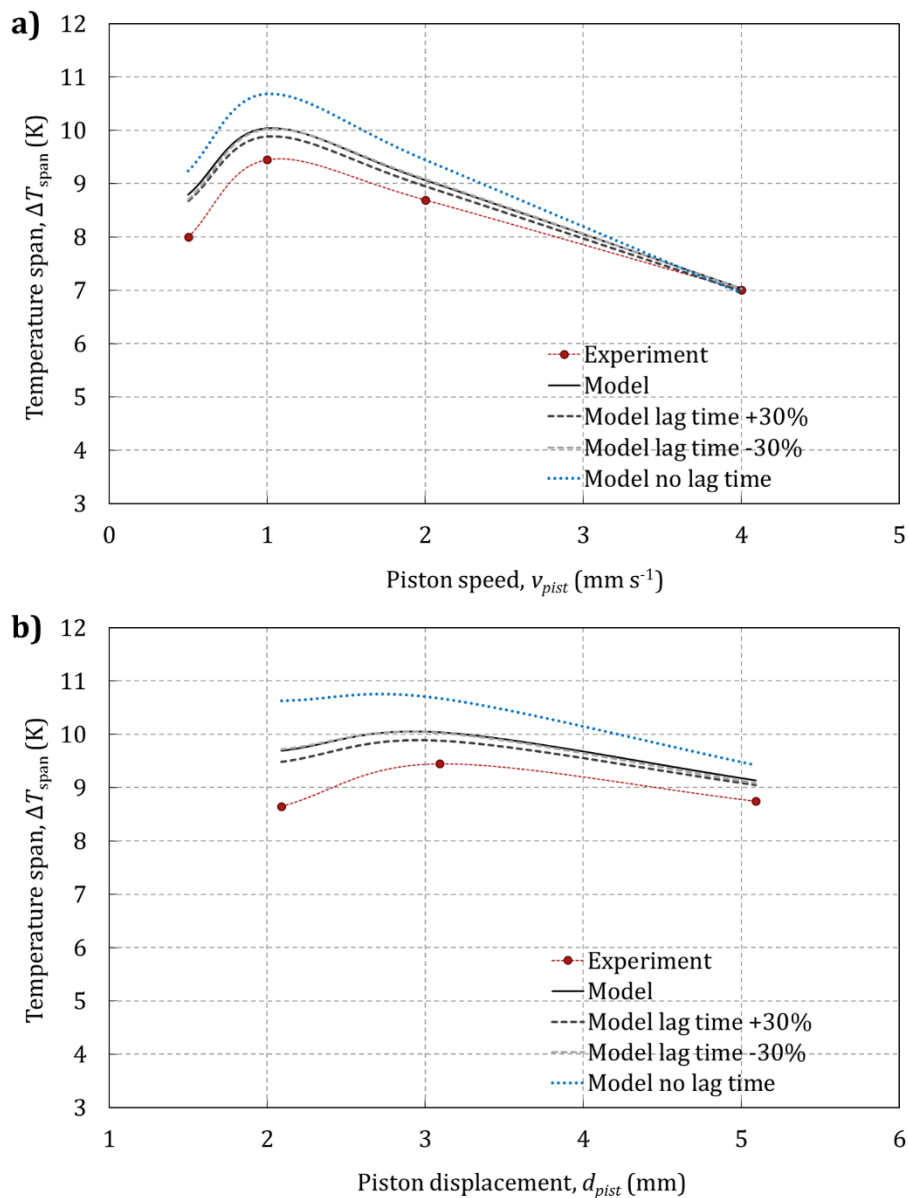
Fig. 4.14. Influence of the uncertainty in the lag time in the results of the AMR tests varying a) the piston speed and b) the piston stroke.

Chapter 5

The mobile air-conditioning system model

This chapter presents a global model of a mobile air-conditioning (MAC) system for an electric vehicle which can predict the thermal requirements of this application. This model is one of the outcomes of the European Project ICE so the specific modelled layout and components correspond to the MAC system developed within. Nevertheless the aim of this work is to develop a **generic simulation tool** for MAC systems which can be employed to predict its performance and assist its design from the energy consumption point of view.

5.1 Description of the modelled system

A MAC system has been developed during the ICE Project for the Iveco Daily Electric commercial minibus. Fig. 5.1 is an outline of the system into the minibus cabin and Fig. 5.2 shows the layout of the thermal power distribution loops.
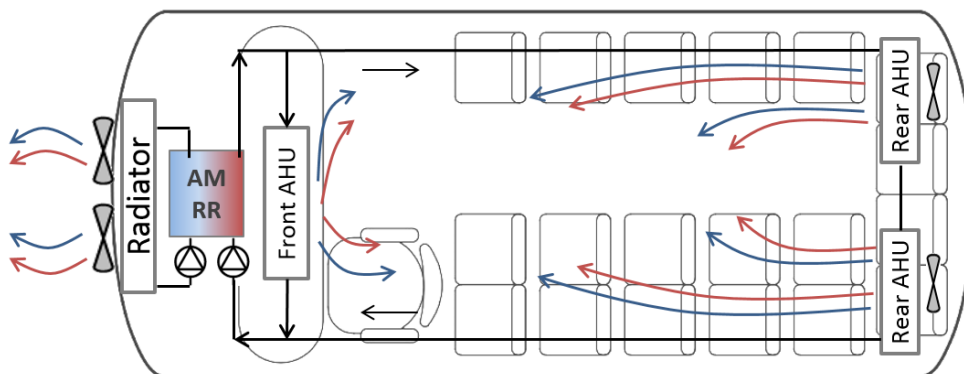
Fig. 5.1. Outline of the MAC system in the Iveco Daily minibus.
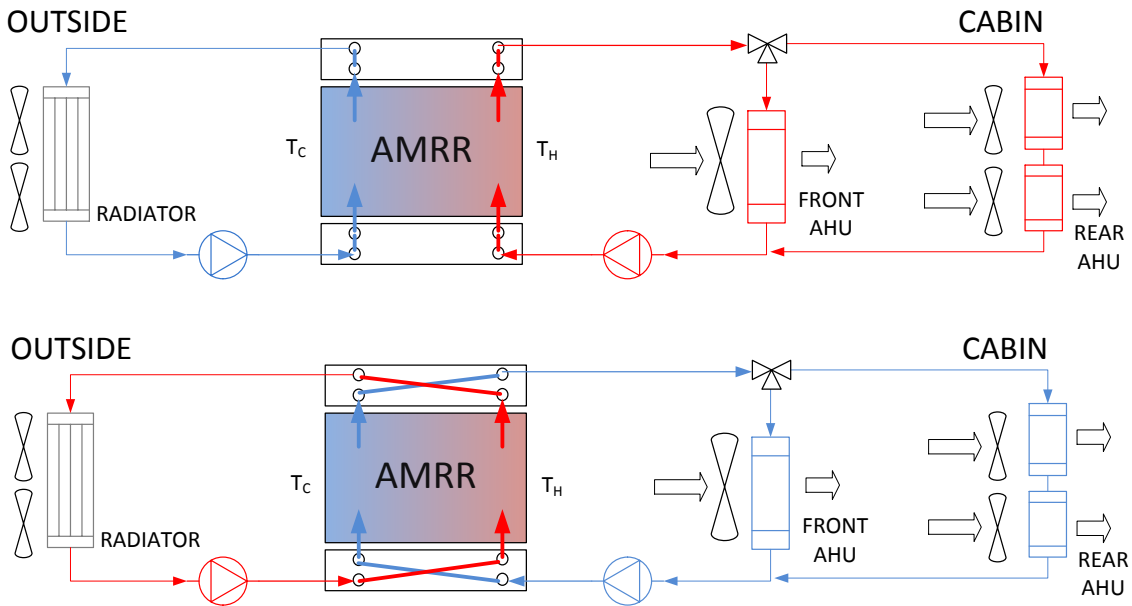
Fig. 5.2. Proposed layout of a MAC system based on an AMRR.

The proposed MAC system is similar to the state-of-the-art layouts for electric vehicles (section 1.3), substituting the conventional compact refrigerator for an AMRR. The AMRR is connected to two hydraulic loops that carry the aqueous working fluid to each side of the system. A valve system is employed to change between cooling and heating modes. The internal loop delivers the cooling or heating power to the cabin of the minibus. The working fluid is divided between an air-handling unit (AHU) in the dashboard (driver's zone) and another two AHUs in series in the rear part of the vehicle (passengers' zone). Each AHU contains an air-to-water heat exchanger that transfers the thermal power to the cabin air assisted by a blower. Depending on the selected recirculation ratio, the air inside the cabin can be mixed with air from the outside. The external loop is in charge of absorbing or rejecting heat to the outside ambient. In order to do so the AMRR is connected to the radiator of the vehicle, which communicates the working fluid with the ambient air. The air is pushed through the radiator by means of two independent fans. Note that the radiator is also in charge of the thermal management of the powertrain of the vehicle and batteries. The proposed layout would enable the integration of the AC system with the thermal system of the vehicle.

The specific characteristics and dimensions of the selected components are detailed along the next sections.

5.2 The global MAC system model

The **global model** has been conceived as a **system-level model made from the integration of component-level models**. The **models are dynamic** as the working conditions in automotive applications. In order to achieve a compromise

among generalization capabilities, accuracy and simulation time, the grey-box modelling approach has been mainly employed [126].

Fig. 5.3 is a diagram of the global model which is composed by the models of the different parts in a MAC system, namely the water-to-water reversible refrigerator (RR), the cabin of the vehicle and the internal and external thermal power distribution loops including the electrical auxiliaries. The inputs to the global model are the external ambient conditions of temperature (T_e), relative humidity (RH_e) and solar irradiance (I); the speed of the vehicle (v) and the control settings that manage the electrical devices (AMRR, fans, pumps). The main outputs are the air conditions inside each zone of the cabin (T_i and RH_i), the air conditions at the air-conditioning outlets (T_{AC} and RH_{AC}) and the power consumption ($\dot{P}$) of all the electrical components.
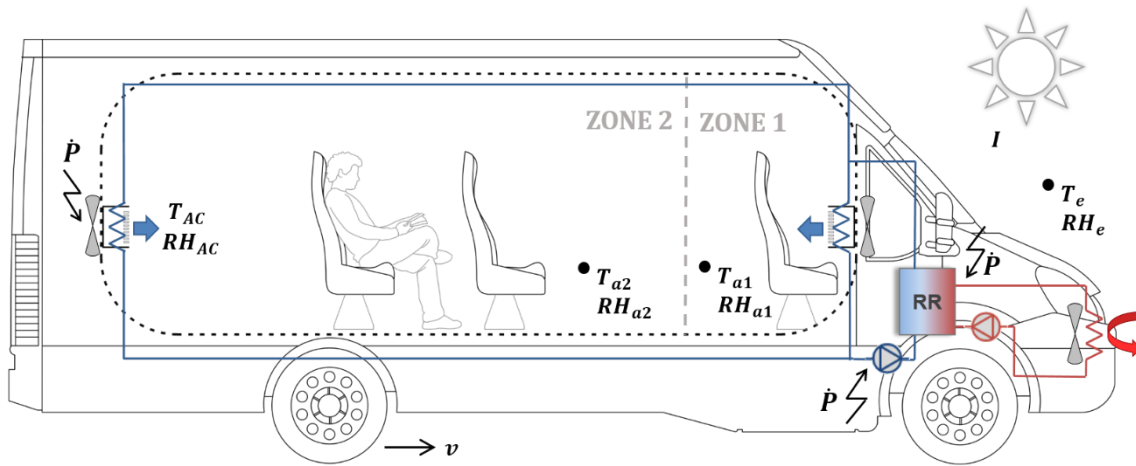
Fig. 5.3. Diagram of the global MAC system model.

Fig. 5.4 depicts the interaction among the component-level models in the global model. The working fluids flowing through the system link the different components, which receive the inlet temperature (and humidity in the case of the air) and mass flow rate of these fluid flows and calculate the outlet values depending on the external conditions and the control settings.

The global MAC system model has been implemented in MATLAB-Simulink. Particularly, the *S-Function* tool has been employed to implement the component models that contain differential equations. In order to enhance convergence and computation time, the algebraic loops in the model were broken by setting the convenient model inputs as the outputs from the previous time step. This approach computed with the solver *ode113* provided the same numerical results as the algebraic loop solver in Simulink. The described global model simulates 1 hour of MAC system operation in 6.3 min.

The following sections describe the component-level models of the studied MAC system.
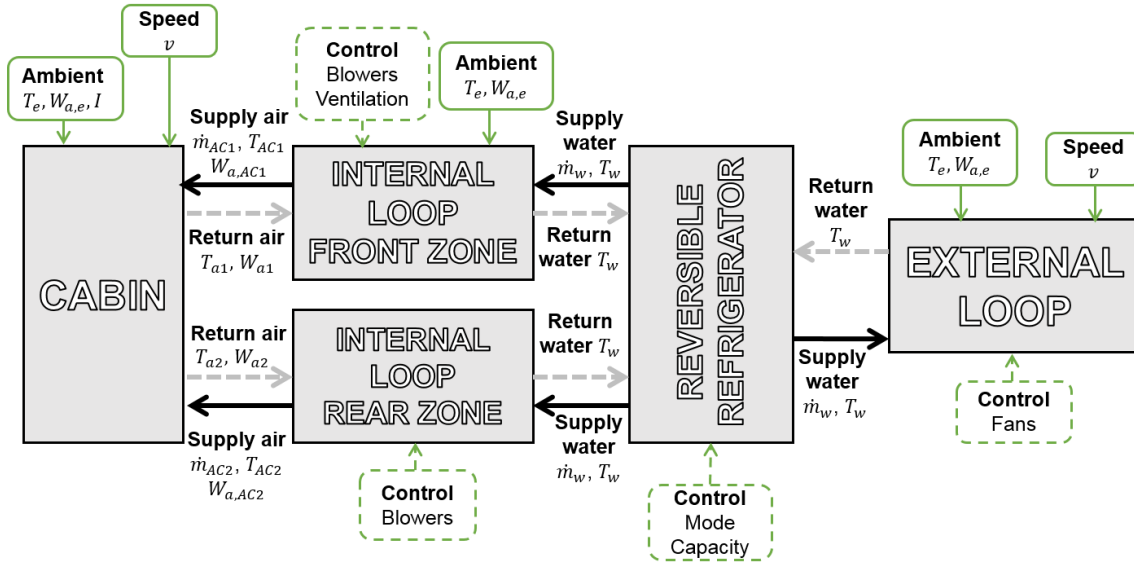
Fig. 5.4. Interaction among subsystems in the global MAC system model.

5.3 The cabin model

5.3.1 Literature review

The thermal model of the cabin simulates the transient thermal behavior of the passengers' compartment of a vehicle. In the context of the global MAC system model, **the function of the cabin model is to calculate the mean temperature and relative humidity of the air inside the vehicle.** These are essential parameters for determining the thermal comfort of the passengers and therefore for the design and control of MAC systems.

Among published literature on cabin thermal models, 3D CFD models or lumped-parameter models have been developed [127]. 3D models are employed to analyze in detail thermal comfort aspects, while lumped-parameter models are more appropriate for the integration of the cabin model with the AC system or a control system. In fact, since lumped-parameter models assume that the air properties are uniformly distributed, they offer a better compromise between accuracy and computational cost.

Several lumped-parameter thermal models of cabins have been reported up to now [128–137]. Their main purpose is to predict the air temperature inside the cabin. In addition, some of them predict the relative humidity [128–131,137], which also affects comfort and window fogging.

For design purposes, it is often convenient to evaluate the internal temperatures when exposed to severe conditions, such as for high ambient temperatures, intensive radiation or with a significant passenger load. Some of the reviewed studies [130–134,137] include the calculation of the solar radiation in detail in order to reproduce dynamic conditions. However, only Mezrhab and Bouzidi [134] include radiation heat

transfer between surfaces. Few models consider other potentially significant loads such as heat from engine and exhaust [132] or from auxiliaries [131].

Heat storage in the external and internal structures also has a significant influence on the air temperature within the time which is necessary for a cool-down or a warm-up of a vehicle [138]. In order to take this effect into account, several authors [133,134,137] consider the composition of the cabin walls in detail. This approach requires full information about the cabin characteristics, which is generally not given in manufacturer data of the vehicle. Using a global heat transfer coefficient can avoid this issue, but the models which employ them usually neglect heat storage in the cabin walls [128–131,135] or/and in the objects installed inside the cabin, which are referred to as the interior mass [128,131,132,135,136].

Furthermore, there is generally not a thorough validation with experimental data. An exception can be found at Conceição et al. [133], who provide dynamic tests under real outdoor conditions for a railway car parked during several hours and running at a fixed speed during an hour. Nevertheless, to the author knowledge simulation results have not been validated yet with measurements under different ambient conditions or along several days.

None of the models reviewed can reproduce accurately the temperature change in a new specific vehicle if the composition of its walls is unknown. In order to cover the needs of the ICE Project, a **new lumped-parameter thermal model of a cabin was developed** by the author [62]. **Unlike previous models, it includes the thermal inertia of the cabin walls and the interior mass using the global heat transfer coefficient approach.** Although the thermal behavior of the cabin depends on specific characteristics of the simulated vehicle, a **general methodology to obtain the parameters is explained and validated.** The former cabin model was further upgraded by Bjurling [139], who included the directional effect of solar irradiation and verified the model with experimental tests under different ambient conditions. A description of the present cabin thermal model is detailed in this section as published in [65].

5.3.2 Governing equations

Fig. 5.5 is a scheme of the proposed cabin model. The air inside the cabin is confined by the cabin body and the interior mass. The cabin is divided into two thermal zones: the driver's region (zone 1) and the passengers' region (zone 2). This approach is interesting in mobile air conditioning since the occupation of the passengers' region can be very variable.
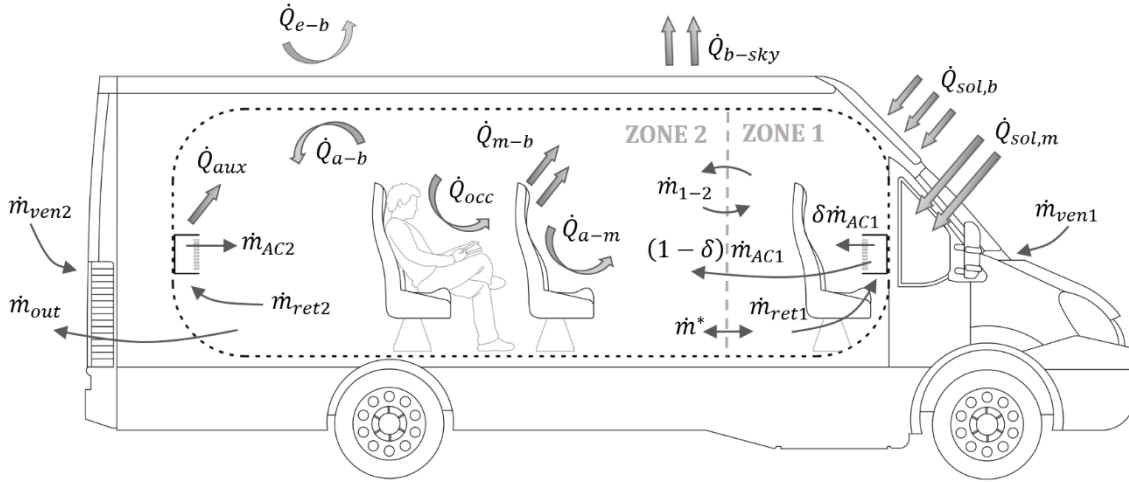
Fig. 5.5. Scheme of the cabin model. The thin arrows represent mass flows and the thick ones energy flows [65].

In each thermal zone, the air conditions are affected by several energy and mass flows: convection with surrounding surfaces ($\dot{Q}_{a-b}$ and $\dot{Q}_{a-m}$), air supply from the AC system ($\dot{m}_{AC}$), air circulation between zones ($\dot{m}_{1-2}$), load due to the occupants ($\dot{Q}_{occ}$) and load due to electrical auxiliaries ($\dot{Q}_{aux}$) such as the blowers. The ventilation air flow ($\dot{m}_{ven}$) does not enter the cabin directly but affects the air mass balance. The excess air ($\dot{m}_{out}$), if any, leaves the cabin through the vents located at the rear of the vehicle. In addition, a distribution ratio (δ) has been introduced to account for the supply air from the AHU in the dashboard (zone 1) which goes directly to the passengers' region (zone 2).

At the same time, the temperature of the cabin body is influenced by heat transfer with the ambient ($\dot{Q}_{e-b}$) and with the air inside the cabin ($\dot{Q}_{a-b}$); by incident solar radiation ($\dot{Q}_{sol,b}$) and also by heat transfer by long wave radiation between the vehicle body and the sky ($\dot{Q}_{b-sky}$) and with the internal mass of the vehicle ($\dot{Q}_{m-b}$).

The temperature of the interior mass also changes dynamically due to the convective heat transfer with the cabin air ($\dot{Q}_{a-m}$), to the solar radiation passing through the glazing ($\dot{Q}_{sol,m}$) and to radiation heat transfer with the cabin body ($\dot{Q}_{m-b}$).

In electric vehicles the motor and the batteries operate at relatively low temperatures [136] so heat transfer with their compartments can be ignored.

The cabin model receives as time-dependent inputs the external temperature (T_e), the solar irradiance measured on a horizontal surface (I), the mean sky temperature (T_{sky}), the mass flow rate ($\dot{m}_{AC}$), temperature (T_{AC}) and humidity content ($W_{a,AC}$) of the air supply from the AC system, a control setting which defines the amount of air recirculated (β) and the number of occupants. The outputs from the model are the temperature (T_a) and moisture of the cabin air (W_a), as well as the temperature of the cabin body (T_b) and of the interior mass (T_m). The model is based in the lumped capacitance method and assumes that the temperature of each element and the relative humidity of the air are spatially uniform.

Eqs. (5.1), (5.2) and (5.3) represent the energy balances of the cabin air, the cabin body and the interior mass, respectively, for zone 1. The equations for zone 2 are analogue. Conduction between zones is neglected due to the narrow contact surface. The air density (ρ_a) and specific heat capacity at constant pressure ($c_{p,a}$) are considered to be constant.

$$C_{a1}\frac{dT_{a1}}{dt} = \dot{Q}_{sup1} + \dot{Q}_{aux1} + \dot{Q}_{occ1,s} - \dot{Q}_{a1-b1} - \dot{Q}_{i1-m1} - \dot{V}_{1-2}\rho_a c_{p,a}(T_1 - T_2) \quad (5.1)$$

$$C_{b1}\frac{dT_{b1}}{dt} = \dot{Q}_{a1-b1} + \dot{Q}_{e-b1} + \dot{Q}_{sol,b1} + \dot{Q}_{m1-b1} - \dot{Q}_{b1-sky} \quad (5.2)$$

$$C_{m1}\frac{dT_{m1}}{dt} = \dot{Q}_{a1-m1} + \dot{Q}_{sol,m1} - \dot{Q}_{m1-b1} \quad (5.3)$$

Eqs. (5.4) and (5.5) are the moisture mass balances in the cabin air for zone 1 and zone 2 respectively.

$$V_{a1}\rho_a\frac{dW_{a1}}{dt} = \dot{V}_{AC1}\rho_a(\delta W_{a,AC1} - \beta_1 W_{a1} - (\delta - \beta_1)W_a^*) + \frac{Q_{occ1,l}}{\Delta i_{vap}}$$
$$-\dot{V}_{1-2}\rho_a \cdot (W_{a1} - W_{a2}) \quad (5.4)$$

$$V_{i2}\rho_a\frac{dW_{a2}}{dt} = \dot{V}_{AC1}\rho_a((1 - \delta)W_{a,AC1} + (\delta - \beta_1)W_a^* - (1 - \beta_1)W_{a2})$$
$$+\dot{V}_{AC2}\rho_a(W_{a,AC2} - W_{a2}) + \frac{Q_{occ2,l}}{\Delta i_{vap}} + \dot{V}_{1-2}\rho_a(W_{a1} - W_{a2}) \quad (5.5)$$

Where W_a^* is equal to W_{a1} if $\delta > \beta_1$ or W_{a2} if $\delta < \beta_1$ and β is the recirculation ratio (Eq. 5.6), which expresses the amount of air supplied by the AHU in each zone that is recirculated from the cabin. This parameter has been introduced to represent conveniently the air mass balance illustrated in Fig. 5.5 and is used as the control parameter for the air recirculation in the MAC system.

$$\beta = \frac{\dot{m}_{ret}}{\dot{m}_{AC}} \quad (5.6)$$

In Eq. (5.4), the first term of the right hand side represents the moisture mass which enters and leaves the control volume of zone 1 due to the air supply from air-conditioning and air renewal. The second term accounts for the moisture mass due to the latent heat emitted by the occupants in zone 1. Finally, the third term is the moisture mass that enters and leaves the zone 1 due to air circulation between zones.

Similarly, in Eq. (5.5) the first term of the right hand side accounts for the moisture mass from the air supply in zone 1 that enters the zone 2, as well as for the air renewal from zone 1 as illustrated in Fig. 5.5. The second term is the moisture mass associated to the air supply from air-conditioning in zone 2. The third and fourth terms are

analogue to Eq. (5.4) and represent the moisture mass due to the latent heat from the occupants and to the air circulation between zones respectively.

Load due to the air supply

The sensible thermal load due to the air supply from air-conditioning and air renewal ($\dot{Q}_{sup}$) is included in the equations by considering the air mass balance in each thermal zone illustrated in Fig. 5.5 and the definition of the recirculation ratio (β) (Eqs. 5.7 and 5.8).

$$\dot{Q}_{sup1} = \dot{V}_{AC1}\rho_a c_{p,a}(\delta T_{AC1} - \beta_1 T_{a1} - (\delta - \beta_1)T^*) \tag{5.7}$$

$$\begin{aligned}\dot{Q}_{sup2} = \dot{V}_{AC1}\rho_a c_{p,a}((1-\delta)T_{AC1} + (\delta - \beta_1)T^* - (1 - \beta_1)T_{a2} \\ + \dot{V}_{AC2}\rho_a c_{p,a}(T_{AC2} - T_{a2})\end{aligned} \tag{5.8}$$

Where T^* is equal to T_{a1} if $\delta > \beta_1$ or T_{a2} if $\delta < \beta_1$.

Load from the electrical auxiliaries

The main electrical auxiliaries that bring heat inside the cabin are the blowers of the AC system. Their associated heat load ($\dot{Q}_{aux}$) is introduced directly in the model from manufacturer data.

Load from the occupants

The load from occupants is divided into sensible ($\dot{Q}_{occ,s}$) and latent heat ($\dot{Q}_{occ,l}$). In each thermal zone, the latter gains are calculated by multiplying the number of occupants by the heat load generated per person. According to ASHRAE [140], a seated person emits 70 W of sensible heat and 35 W of latent heat.

Heat transfer between air and surfaces

In order to account for the convective heat transfer between air and surfaces combined with the conductive processes inside the solid bodies, a lumped capacitance has been fitted for each air-solid interaction. Eq. (5.9) corresponds to the heat transfer between the cabin air and the cabin body ($\dot{Q}_{a-b}$). A similar expression applies for the heat transfer between the ambient air and the cabin body ($\dot{Q}_{e-b}$) or between the cabin air and the interior mass ($\dot{Q}_{a-m}$).

$$\dot{Q}_{a-b} = U_{a-b}A_b(T_a - T_b) \tag{5.9}$$

Air circulation between zones

Since there is no physical barrier between the two defined thermal zones, the air can circulate freely between them. The air flow due to the stack effect between zones

communicated by a single aperture of height L_{1-2} and surface A_{1-2} can be expressed as in Eq. (5.10) [140], where zone 1 is warmer than zone 2.

$$\dot{V}_{1-2} = A_{1-2}\,(0.40 + 0.0045|T_1 - T_2|)\sqrt{gL_{1-2}(T_1 - T_2)/T_1} \qquad (5.10)$$

Solar radiation load

Solar radiation acts as an energy gain on the cabin body and it depends on the incident irradiance on each side of the vehicle (I'_{side}) as well as on the mean absorptivity of the cabin body ($\mathcal{A}_b$), which includes both metallic and glazed surfaces (Eq. 5.11).

$$\dot{Q}_{sol,b} = \mathcal{A}_b \sum I'_{side} A_{side,b} \quad (side = R, L, F, B \text{ and } U) \qquad (5.11)$$

In addition, the incident radiation penetrates through the glazing and consequently, the energy gain in the internal masses includes the incident solar irradiance multiplied by the transmissivity of the glasses ($\mathcal{T}_g$) and by the absorptivity of the interior mass ($\mathcal{A}_m$) (Eq. 5.12). For simplicity, and given that the seats and the dashboard are black, the interior mass is considered a black body.

$$\dot{Q}_{sol,m} = \mathcal{A}_m\,\mathcal{T}_g \sum I'_{side} A_{side,g} \quad (side = R, L, F \text{ and } B) \qquad (5.12)$$

The transmissivity of the glazing decreases if the angle of incidence of the sun rays increases. Nevertheless, this effect was analyzed initially with the model and it is hardly noticeable given that it only affects in the sunrise and sunset, when the incident radiation is small. In order to keep the computational cost lower, a constant transmissivity has been used.

A key point to obtain good validation results with the model was to include the effect of the variable sun position [139]. The incident radiation on each side of the vehicle was introduced by means of the calculation scheme followed by many simulation programs such as TRNSYS [141]. Firstly, the components of radiation on a horizontal surface are calculated from experimental data of I and T_e. Then, the radiation components on a tilted surface are computed: beam irradiance (I'_{be}), reflected irradiance (I'_{re}) assuming ground is an isotropic reflector and diffuse irradiance (I'_{di}). Finally, the global irradiance on a tilted surface (I') is given by the contribution of these components (Eq. 5.13).

$$I' = I'_{be} + I'_{re} + I'_{di} \qquad (5.13)$$

Radiation heat transfer

Eq. (5.14) expresses the radiation heat transfer between the cabin body and the interior mass ($\dot{Q}_{m-b}$). A two surface enclosure approach has been applied in each thermal zone [103] and the internal surfaces inside the vehicle are assumed to behave as blackbodies. The glazing is considered to be opaque to long wave radiation [134].

$$\dot{Q}_{m-b} = \sigma_S A_m F_{m-b} \left(T_m^4 - T_b^4 \right) \tag{5.14}$$

The radiation heat transfer between the cabin body and the sky ($\dot{Q}_{b-sky}$) is expressed in Eq. (5.15) assuming that the cabin body behaves as a small convex object in a large cavity [103].

$$\dot{Q}_{b-sky} = \sigma_S \mathcal{E}_b A_{U,b} \left(T_b^4 - T_{sky}^4 \right) \tag{5.15}$$

5.3.3 Validation

The cabin model has been validated for the Iveco Daily Electric minibus by means of **two experimental tests under different ambient conditions** which were carried out in the frame of the ICE Project by the partner CRF. The first one is a warm-up and cool-down inside a garage, while the second one is under ambient conditions for several days, including solar radiation.

The minibus dimensions were taken from manufacturer data and they are listed in Table 5.1. The radiation heat transfer parameters, which are summarized in Table 5.2, were obtained from literature and are also coherent with existing models [132,136].

Table 5.1. Dimensions of the Iveco Daily minibus [65].

Dimension	Zone 1	Zone 2
Height	2.000 m	2.000 m
Length	1.776 m	4.379 m
Width	1.996 m	1.996 m
A_b	18.4 m^2	39.2 m^2
A_m	3 m^2	30 m^2
$A_{U,b}$	2.170 m^2	8.450 m^2
$A_{R,b}$	2.391 m^2	8.706 m^2
$A_{R,g}$	0.824 m^2	2.450 m^2
$A_{L,b}$	2.391 m^2	8.706 m^2
$A_{L,g}$	0.540 m^2	2.450 m^2
$A_{B,b}$	-	3.647 m^2
$A_{B,g}$	-	0.747 m^2
$A_{F,b}$	2.011 m^2	-
$A_{F,g}$	1.215 m^2	-

Table 5.2. Radiation heat transfer parameters for the Iveco Daily minibus [65].

Parameter	Description	Value
$\mathcal{A}_b$	Absorptivity of cabin body [142]	0.19
$\mathcal{A}_m$	Absorptivity of interior mass	1
$\mathcal{T}_{g1}$	Transmissivity of regular glass [142]	0.8
$\mathcal{T}_{g2}$	Transmissivity of tinted glass [142]	0.6
$\mathcal{P}$	Reflectance of asphalt [143]	0.14
$\mathcal{E}_b$	Emissivity of white paint [103]	0.95
F_{m-b}	View factor between interior mass and cabin body	1

On the other hand, some of the parameters of the model cannot be deduced from manufacturer data or literature due to the complex geometry of the vehicle. These are the global heat transfer coefficients (U) and the thermal capacities of the cabin body (C_b) and the interior mass (C_m).

The global heat transfer coefficients are mainly convective. Upper and lower limits have been established based on literature [103] and the exact values for this application have been obtained by calculating the heat transfer coefficients which minimize the *RMSE* between the experimental tests and the simulations. The results are shown in Table 5.3.

Table 5.3. Global heat transfer coefficients [65].

Global heat transfer coefficient	Garage test (W m^{-2} K^{-1})		Solar radiation test (W m^{-2} K^{-1})
	Warm-up	Cool-down	
U_{e-b}	1.7	1.7	4.5
U_{a-b}	4.4	3.0	4.0
U_{a-m}	4.4	3.0	12

The heat transfer coefficients of the internal surfaces (U_{a-b} and U_{a-m}) in the garage test are larger during the warm-up since there is forced convection induced by the fans, which are off during the cool-down. Since the internal surfaces of the vehicle reach similar temperatures, U_{a-b} and U_{a-m} were given the same value in each case. However, in the tests with radiation the temperature gradients inside the vehicle are higher, which explains why the convective heat transfer is higher than during the cool-down inside the garage. Moreover, in the test with solar radiation the interior mass heats up considerably and acts as a heated plane facing upwards [103]. Therefore it is logical to obtain higher convective coefficients than in the cabin body. Additionally, the heat transfer coefficient with the ambient air (U_{e-b}) is logically higher in the tests with radiation given that these were carried out in open-air conditions whereas the other tests were carried out inside a garage, consequently with less movement of air. In any case, the values obtained are coherent with those found in literature on cabin models [137,144]. However, the correlations presented in heat transfer bibliography [103] lead to lower values of the heat transfer coefficient, ranging

from 2 to 4 W m^{-2} K^{-1}. This fact was also observed by Conceiçao et al. [133] and can be explained by the vehicle geometry. While the empirical correlations in [103] refer to simple isolated surfaces, the vehicle geometry is rather complex.

Regarding the heat capacity, C_b and C_m were estimated considering the mass of the vehicle (3700 kg) and the average specific heat capacity of its main components, such as steel, glass and plastic ($C = mc_p$). The values obtained were tuned in order to minimize the mean square deviation between the measurements and the simulations. On the other hand, C_a was calculated directly from the cabin volume and the air properties. The results are shown in Table 5.4.

Table 5.4. Mass and specific heat of the minibus elements [65].

	Zone 1		Zone 2	
	c_p	m	c_p	m
	(J kg^{-1} K^{-1})	(kg)	(J kg^{-1} K^{-1})	(kg)
Internal air	1005	8.64	1005	21.12
Body	600	650	600	1250
Interior mass	900	15	900	190

The initial conditions for the simulations correspond to the temperature measurements at the beginning of each test.

Experimental test 1: warm-up and cool-down in a garage

The first validation test was carried out by F. Di Sciullo at CRF with the minibus parked inside a garage with the purpose of **validating the model regardless of solar radiation**. Two fan-heaters of 2000 W each were placed along the corridor of the vehicle. They were turned on at the beginning of the test in order to heat up the cabin. After 160 minutes, the fan-heaters were turned off and the cabin cooled down due to natural convection. The temperature of the air inside the cabin was measured with T-Type thermocouples with an uncertainty of ± 0.5 K. The thermocouples were placed at four locations at head level, as shown in Fig. 5.6. Temperature measurements were registered every 30 s.

In order to simulate this test, the thermal load due to the fan heaters was considered as a sensible heat gain. Additionally, during the warm-up part the stack effect was enhanced to take into account the air circulation imposed by the activation of the fan heaters. A value of 4000 W K^{-1} equilibrates the temperatures obtained in both zones.
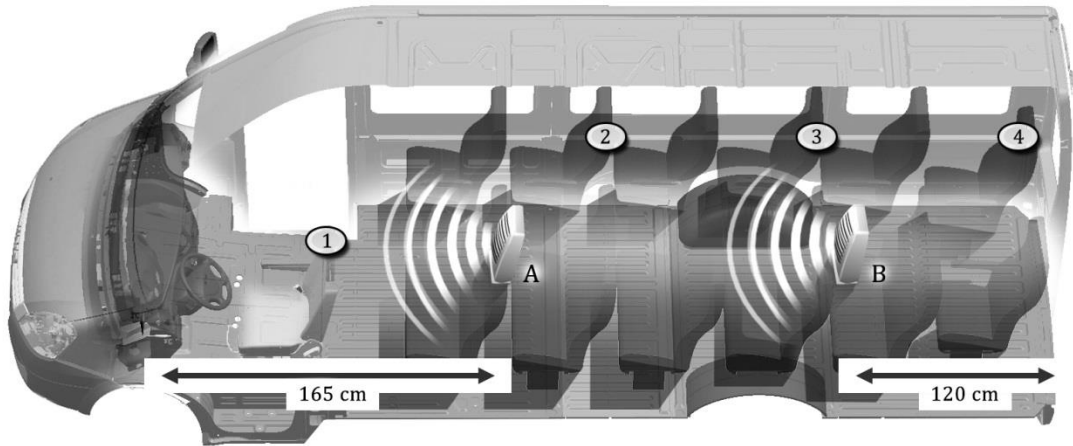
Fig. 5.6. Thermocouples (1-4) and fan-heaters (A,B) position in cabin test 1 [65].

Fig. 5.7 shows the experimental and simulation results of test 1 on the cabin air temperature. The ambient temperature measured is the input to the model (T_e). The results are only shown for zone 1 because they are almost identical for zone 2. In fact, the maximum temperature difference between the two zones is 0.7 K. This is due to the lack of a physical barrier between both zones, as well as to the air mixing produced by forced convection. Despite the initial part of the warm-up, which can be influenced by the inertia of the thermocouples, **the model reproduces very well the experimental results**.
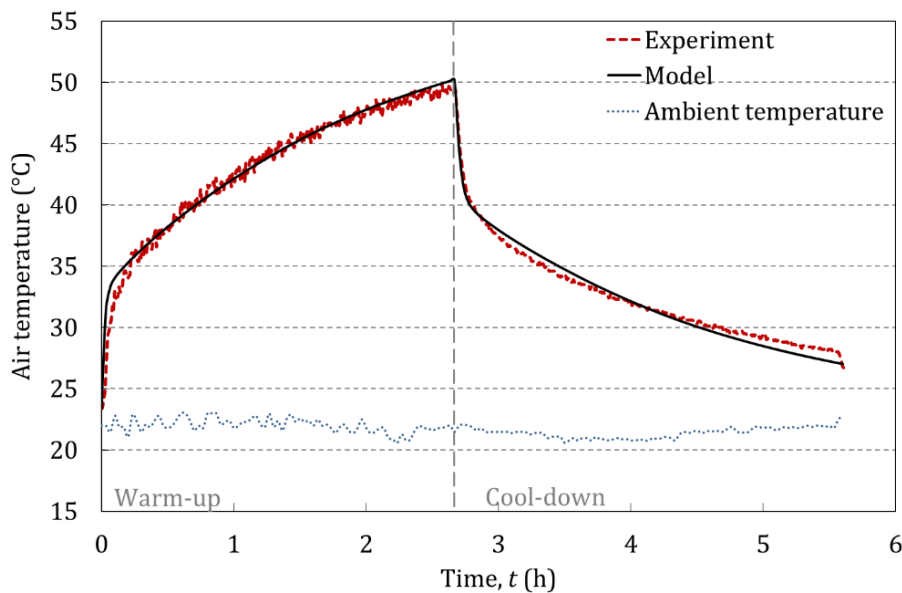

Fig. 5.7. Measured and simulated cabin air temperature in zone 1 (test 1) [65].

Experimental test 2: minibus parked under the sun

A second experimental test was carried out by F. Di Sciullo and J. Payá in Torino (Italy) during **several days of July when the minibus was parked under the sun** facing west. The temperatures inside the vehicle were measured by means of T-Type thermocouples with an uncertainty of ± 0.5 K. In total, twelve thermocouples were placed: two for the air temperature plus two for the interior mass in zone 1 and four for the air temperature at head level plus four in the seats in zone 2 (Fig. 5.8).
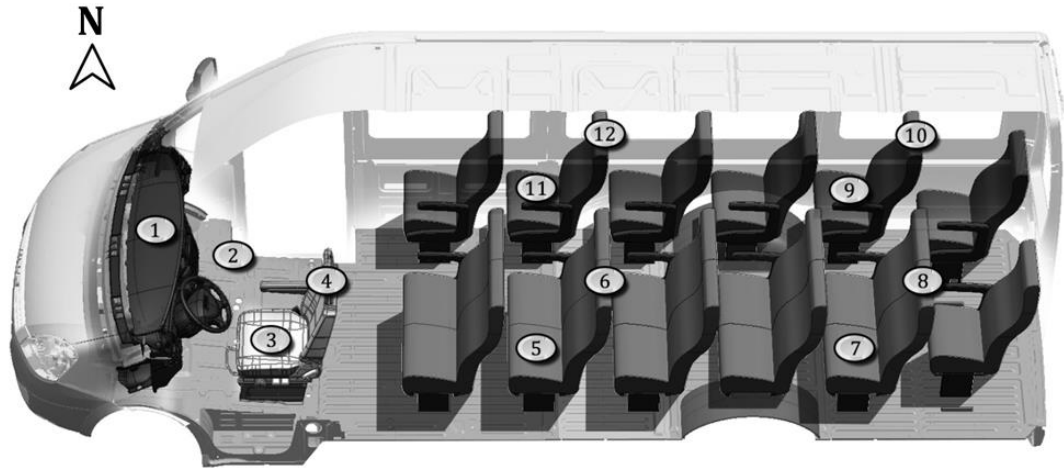

Fig. 5.8. Thermocouples position in cabin test 2 [65].

Additionally, a pyranometer Lp pyra 02 delta ohm (uncertainty 1.5% at T=23 °C and RH=50%) was placed on the roof of the minibus to measure the global solar irradiance on horizontal surface. The ambient temperature was also measured by means of a T-Type thermocouple (uncertainty of ± 0.5 K) protected against the solar radiation.

Fig. 5.9 shows the ambient temperature and the global solar irradiance on horizontal surface measured during the experimental campaign, which started at 0:00 h. These data, as well as the mean sky temperature in Torino [145], were introduced as inputs in the cabin model. Fig. 5.10 and Fig. 5.11 show the comparison between measured and simulated results.

In Fig. 5.9, the global solar irradiance on horizontal surface (I) changes abruptly when it is cloudy and takes then a value around 0.2 kW m^{-2} ($I \approx I_d$). If Fig. 5.9 is compared to Fig. 5.10 and Fig. 5.11, it is observed that solar irradiance affects directly to the temperatures inside the vehicle, causing peaks. In contrast, the variation of the external temperature makes the internal temperatures change smoothly.
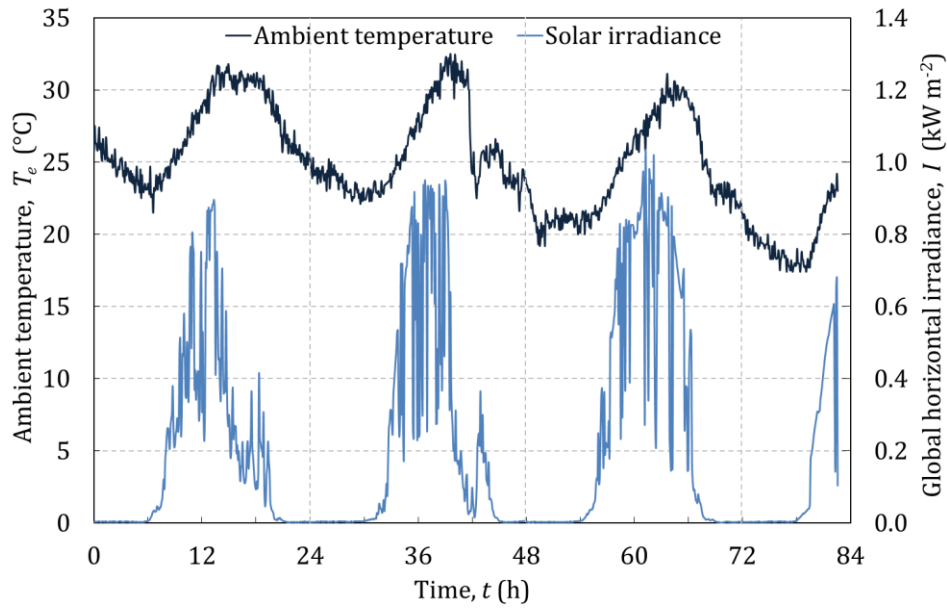
Fig. 5.9. Ambient temperature and global horizontal irradiance measured during test 2 [65].

Fig. 5.10 shows the results for the mean air temperature in zone 1. As in test 1, the values obtained in zone 2 are very similar due to the lack of a physical barrier between zones. The maximum difference between zones is 1.5 K. As can be observed, **the model predicts very accurately the experimental results, even the peaks caused by solar irradiance**. On the contrary, the heat transfer coefficients predicted by literature [103] provide less accurate results. These coefficients have a lower value, therefore heat transfer between the cabin air and the cabin walls decreases. The heat from solar irradiation is then blocked inside the cabin causing the air temperature to increase.
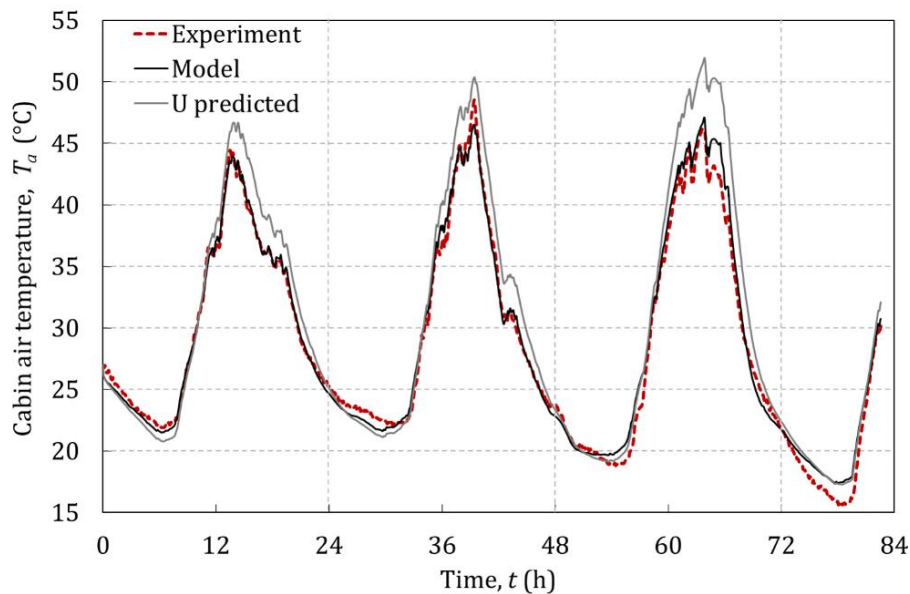

Fig. 5.10. Measured and simulated cabin air temperatures in zone 1 (test 2) [65].

Fig. 5.11 shows the mean temperature of the interior mass in both zones. The temperatures reached in zone 2 are lower due to the tinted glazing in the passengers' region (lower transmissivity). The minibus was facing west, which explains why in the evening the solar radiation affects mainly the zone 1. The model reproduces accurately the experimental results, although it slightly overpredicts the temperature in zone 2 for high solar irradiance. This can be due to the fact that a single global heat transfer coefficient was fitted for both zones. In fact, the temperatures predicted in zone 2 are very close to the cabin air temperature shown in Fig. 5.10. In addition, the temperature was measured only in the seats, while the model considers a lumped heat capacity for all the objects installed inside the cabin.
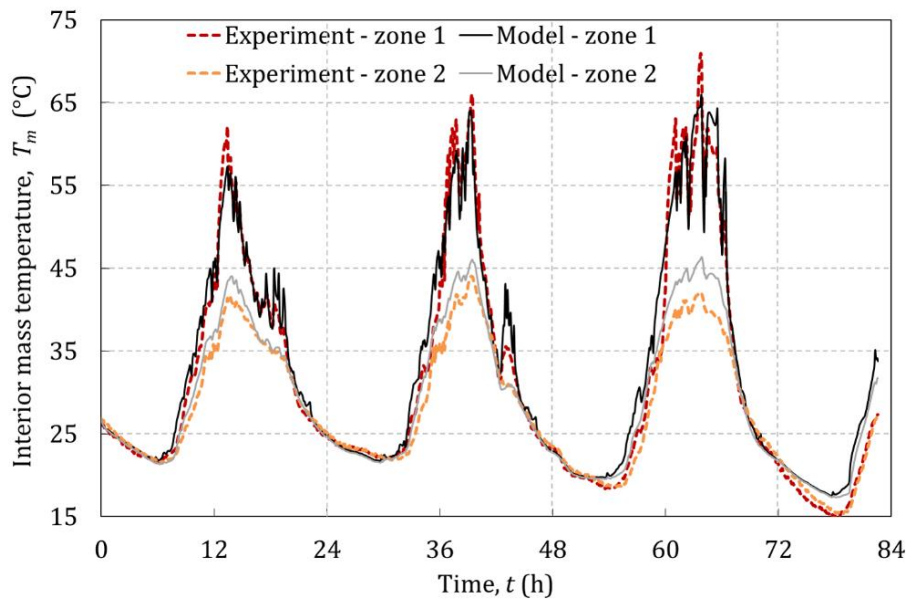

Fig. 5.11. Measured and simulated interior mass temperatures (test 2) [65].

5.4 The thermal power distribution loop model

The thermal power distribution loops communicate the reversible refrigerator with the external ambient and with the cabin air by means of a heat transfer fluid, which in automotive applications is typically a 50% ethylene glycol solution. In the global MAC system model, **the function of the hydraulic loops model is to calculate the mass flow rates and return temperatures to each side of the reversible refrigerator, the conditioned air flow conditions (T_{AC}, $W_{a,AC}$ and $\dot{m}_{AC}$) and the power consumption of the electrical auxiliaries.** Furthermore, the power consumption of the blowers that push the air to the cabin turns entirely into a thermal load which must be introduced in the cabin model ($\dot{Q}_{aux}$).

The specific layout of the hydraulic loops was depicted in Fig. 5.2 and Fig. 5.12 is a scheme of a generic model of a thermal power distribution loop. The intermediate fluid at the supply temperature from the refrigerator (T_{sup}) is pushed by the pump, which sets the mass flow rate in the loop ($\dot{m}_w$) as a function of the pressure drop in

the loop and the fluid properties. The fluid traverses the corresponding pipes to the heat exchanger (HEX), increasing its temperature up to $T_{in,HEX}$ mainly due to the losses to the ambient. In the HEX, the fluid transfers heat to the air ($\dot{Q}_{HEX}$) and reaches the temperature $T_{out,HEX}$. On the other side of the HEX, the air flow temperature and humidity also change between the inlet ($T_{a,in}$, $W_{a,in}$) and the outlet ($T_{a,out}$, $W_{a,out}$) sections. The air flow rate ($\dot{m}_a$) is established by the characteristics of the fan and the HEX. After traversing the piping, the fluid finally reaches the refrigerator at the return temperature (T_{ret}).
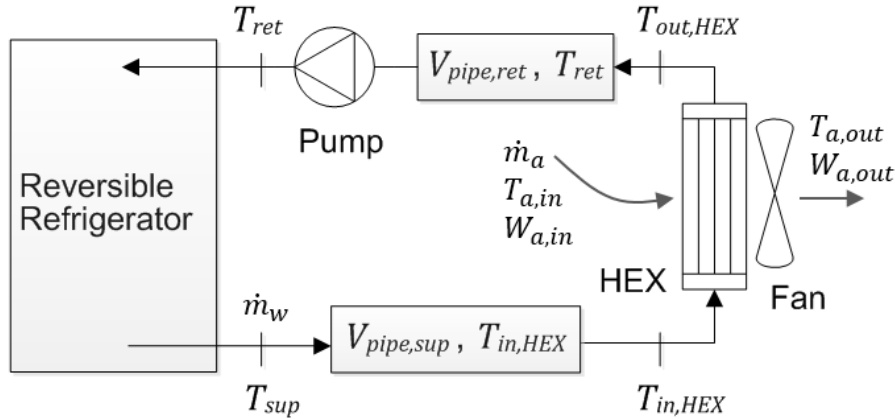

Fig. 5.12. Scheme of the thermal power distribution loop model.

The described loop is comprised by three different elements: the pipes, the heat exchanger and the fluid transport equipment (pump and fan). The proposed model is an ensemble of blocks that represent each of these components and can be repeated as many times as necessary to simulate a specific layout.

5.4.1 The piping model

The piping model calculates the outlet temperature of the fluid after traversing the piping (e.g. $T_{in,HEX}$) and the corresponding pressure drop. The time-dependent inputs to this block are the inlet temperature to the pipe (e.g. T_{sup}) from the corresponding element of the loop, the external ambient temperature (T_e) and the fluid mass flow rate ($\dot{m}_w$).

The temperature of the fluid inside the pipe is considered spatially uniform and equal to the outlet temperature. In the frame of the global MAC system model, this approach is sufficient to have an estimate of the thermal losses in the pipes. For instance, Eq. (5.16) represents the energy balance in the volume of the supply pipe ($V_{pipe,sup}$). The right hand side term accounts for the thermal inertia of the fluid inside the pipe. In the left hand side, the first term represents the fluid flow entering and exiting the volume and the second term, the heat transfer to the ambient. The effect of the viscous dissipation in the temperature rise of the fluid has been neglected.

$$V_{pipe,sup}\rho_w c_{p,w}\frac{dT_{in,HEX}}{dt} = \dot{m}_w c_{p,w}\left(T_{sup} - T_{in,HEX}\right) + UA_e\left(T_e - T_{in,HEX}\right) \qquad (5.16)$$

The losses to the ambient are estimated with a typical value of the global heat transfer coefficient (U), taking into account the conduction through the pipe walls and the free convection with the air in a closed space ($U\approx2$ W/m^{2}K). A_e is the external surface area of the pipe.

The pressure drop in the piping has been calculated with the open software SF Pressure Drop [146] as function of the characteristics and dimensions of the ICE Project layout. A polynomic expression as function of the fluid flow rate has been introduced in the model.

5.4.2 The electrical auxiliaries model

The model of each electrical auxiliary computes its power consumption as function of the selected fluid flow rate and the pressure drop through the corresponding part of the system. These quantities depend on the specific characteristics of the standard components employed in the hydraulic installation, and therefore have been introduced in the model from their manufacturer data.

Circulation pumps for the studied automotive application typically provide between 10 and 20 m^3 h^{-1} and consume by 50 W. The specific pump employed in the present layout is the model CWA 50 by Pierburg Pump Technology [147] and the curves are confidential.

The performance of the fans of the radiator was experimentally measured by the ICE Project partner CRF (Table 5.5). The number of activated fans can be controlled.

Table 5.5. Characteristics of the fans of the radiator.

Number of fans	Air flow (m^3 h^{-1})	Power input (W)
1	1254	109.7
2	2188	234.63

The AHU in the front of the Daily minibus can handle fresh air or recirculated air. The blower inside has several distribution modes and four fixed speeds (positions) among which the user can choose. Each working mode determines the air flow and the energy consumption (Table 5.6).

The AHUs installed at the rear part of the minibus for the ICE project will only recirculate air. Each of them includes a blower with three fixed speeds (Table 5.7) which can be selected.

Table 5.6. Characteristics of the blower in the front AHU.

Position	Air flow (m^3 h^{-1}) 100% Floor distribution	Air flow (m^3 h^{-1}) 100% Head distribution	Power input (W)
1	60	88	48.0
2	96	137	102.0
3	146	195	171.6
4	264	311	290.4

Table 5.7. Characteristics of the blower in the rear AHUs.

Position	Air flow (m^3 h^{-1})	Power input (W)
1	90	143
2	170	159
3	250	175

5.5 The heat exchanger model

5.5.1 Literature review

In the global MAC model, **the task of the heat exchanger (HEX) model is to calculate the outlet conditions of the fluids that traverse it, given their inlet conditions and flow rates.** The performance of a HEX is determined by its geometric characteristics and the working conditions. In ICE Project, **compact louver-fin flat tube HEXs** have been selected. They must **work under dynamic dry and wet conditions in both cooling and heating modes.**

Compact louver-fin flat tube HEXs are widely employed in automotive applications. There are numerous studies about their performance especially under dry conditions, as reviewed by Park and Jacobi [148,149]. Finding general laws for compact HEXs is difficult given their complex fin geometries. Park and Jacobi [149] provided a comprehensive characterization of the thermo-hydraulic performance of the air-side of compact HEXs under dry and fully wet conditions. However the accuracy of the correlations they report is limited by the complexity of the phenomena and the large number of parameters to be considered. Partially wet conditions are avoided in that study, nevertheless they are usual in air cooling applications. More recent studies [150–152] generally focus on operating conditions that differ from those of the air conditioning. An exception is found in the work by Jokar et al. [153], who presented a test facility consisting of an automotive reversible refrigerator with secondary coolant loops in which five different air-to-coolant compact HEXs were tested. The discussion of the results focuses on the coolant side and the effect of

condensation on the air side is not analyzed. **In order to simulate accurately the HEXs of the ICE Project, new experimental data is needed.**

In the context of a global MAC system model, lumped-parameter models of the HEXs are more convenient than multi-node models due to its simplicity and speed. However, the traditional effectiveness approach is not accurate when the HEX works under dynamic dry and wet conditions, since the boundary between the dry and wet surfaces moves. Several authors have developed simple dynamic HEX models for cooling coils with dehumidification [154–156]. Among them, the approach by Braun et al. [154] has demonstrated a good accuracy with minimal modelling effort and computation time. This method was formulated for counter-flow coils and has been adapted in this work to develop a compact HEX model.

The approach by Braun et al. [154] is based in the effectiveness-NTU method, which relies on the global heat transfer coefficient multiplied by the heat transfer surface area (UA). If the purpose of the model is to assist the system design, a model of a HEX based on the UA is more convenient than one based on the effectiveness, since the former allows for scaling up and down the HEX and therefore finding its optimum size for the studied application.

The UA depends on the HEX geometry and working conditions. With the aim of improving the interpolation and extrapolation of the values during the simulations, it is desirable to employ a correlation for the UA. **A comprehensive experimental campaign was carried out as a part of the ICE Project on the specific HEXs employed inside the cabin. As a novelty, partially wet working conditions that are usual in air-conditioning applications were intentionally included. From this results, a general methodology to fit a single everywhere correlation of the UA of the compact HEX for both cooling and heating modes has been developed** and published in [157].

5.5.2 Governing equations

Following Braun et al. [154], **the operation of the HEX is divided into three cases, namely the outer surface of the HEX is completely dry, it is completely wet or it is partially wet.**

In the **completely dry case**, the humidity content of the air remains constant, that is, $W_{in}=W_{out}$. The outlet temperature of the coolant ($T_{w,out}$) and the air ($T_{a,out}$) can be obtained from an energy balance in the HEX neglecting the thermal losses (Eq. 5.17).

$$\dot{Q}_{HEX} = \dot{m}_w c_{p,w}\left(T_{w,out} - T_{w,in}\right) = \dot{m}_a c_{p,a}\left(T_{a,in} - T_{a,out}\right) \qquad (5.17)$$

The heat transfer rate ($\dot{Q}_{HEX}$) can be calculated from the effectiveness (ε) of the HEX, which is defined as the ratio of the actual to the maximum possible heat transfer (Eq. 5.18).

$$\varepsilon_{dry} = \frac{\dot{Q}_{HEX}}{\dot{m}_a c_{p,a}\left(T_{a,in} - T_{w,in}\right)} \tag{5.18}$$

In order to verify that the HEX is completely dry, the surface temperature at the air outlet ($T_{surf,out}$) is calculated (Eq. 5.19). If $T_{surf,out}$ is greater than the inlet air dew point, then the HEX is completely dry as supposed. Otherwise, at least a portion of the HEX is wet.

$$T_{surf,out} = T_{w,in} + \frac{c_{p,a} \cdot \dot{m}_a}{c_{p,w} \cdot \dot{m}_w} \cdot \frac{NTU}{NTU_w}(T_{a,out} - T_{w,in}) \tag{5.19}$$

If the **HEX is completely wet**, the outlet conditions of the fluids are calculated by means of an energy balance formulated in terms of the air enthalpy (i_a) (Eq. 5.20).

$$\dot{Q}_{HEX} = \dot{m}_w c_{p,w}\left(T_{w,out} - T_{w,in}\right) = \dot{m}_a\left(i_{a,in} - i_{a,out}\right) \tag{5.20}$$

Analogously, the effectiveness of the HEX in this case is defined by Eq. (5.21), where $i_{sat,w,in}$ refers to the saturated air enthalpy at the inlet temperature of the coolant.

$$\varepsilon_{wet} = \frac{\dot{Q}_{HEX}}{\dot{m}_a\left(i_{a,in} - i_{sat,w,in}\right)} \tag{5.21}$$

The air enthalpy is given by the air temperature and humidity content (Eq. 5.22). The vaporization enthalpy of water is Δi_{vap}=2501 kJ kg^{-1} K^{-1} and the specific heat capacity of the water vapor is $c_{p,vap} = 1.85$ kJ kg^{-1} K^{-1}.

$$i_a = c_{p,a}T_a + W_a(\Delta i_{vap} + c_{p,vap}T_a) \tag{5.22}$$

If dehumidification has occurred in the HEX, an additional equation is needed to determine the air outlet conditions. From Braun et al. [154] the air outlet temperature can be determined from an effective surface temperature ($T_{surf,eff}$) with Eq. (5.23), which is obtained by integrating the balance equations along the coil. $T_{surf,eff}$ can be determined from the corresponding air saturation enthalpy ($i_{sat,surf,eff}$, Eq. 5.24) by means of the T - i_{sat} relationship proposed for instance by ASHRAE [140] (Eq. 5.25).

$$T_{a,out} = T_{surf,eff} + (T_{a,in} - T_{surf,eff})e^{-NTU_a} \tag{5.23}$$

$$i_{sat,surf,eff} = i_{a,in} + \frac{i_{a,out} - i_{a,in}}{1 - e^{-NTU_a}} \tag{5.24}$$

$$T = 0.00001i_{sat}^3 - 0.00401i_{sat}^2 + 0.63205i_{sat} - 5.43233 \tag{5.25}$$

In order to verify that the HEX is completely dry, the surface temperature at the air inlet ($T_{surf,in}$) is calculated (Eq. 5.26). If $T_{surf,in}$ is less than the inlet air dew point, then the HEX is completely wet as supposed. Otherwise, at least a portion of the HEX is dry.

$$T_{surf,in} = T_{w,out} + \frac{\dot{m}_a}{c_{p,w} \cdot \dot{m}_w} \cdot \frac{NTU}{NTU_w} (T_{a,out} - T_{w,in})$$ (5.26)

Following the previous results, if the inlet air dew point is greater than the surface temperature at the air inlet but less than the surface temperature at the air outlet, then the **HEX is only partially wet**. In this case, Braun et al. [154] propose to assume that the HEX is either completely dry or completely wet. Either condition will tend to underpredict the actual heat transfer, so the model must chose the one that yields the larger heat transfer rate. This approach avoids iterating to determine the fractions of the HEX that are dry and wet, thus reducing computation time.

Effectiveness-NTU correlation

A specific ε-*NTU* correlation for an unmixed cross-flow unit with n_{pass} passes per tube (n_{pass} =2 in this case) has been applied (Eqs. 5.27 to 5.30) [158]. Compared to the commonly employed ε-*NTU* relationship for an infinite number of tube rows [159], the present expression does not have any limitation on the heat capacity of the fluid flows and fitted better the experimental results shown below.

$$\varepsilon = \frac{1}{R} \left(1 - \left(\frac{K}{2} + \left(1 - \frac{K}{2} \right) e^{2KR} \right)^{-1} \right)$$ (5.27)

$$K = 1 - exp\left(-\frac{NTU}{n_{pass}} \right)$$ (5.28)

$$NTU = \frac{UA}{c_a^* \cdot \dot{m}_a}$$ (5.29)

$$R = \frac{C_a}{C_w} = \frac{c_a^* \cdot \dot{m}_a}{c_{p,w} \cdot \dot{m}_w}$$ (5.30)

In Eqs. (5.29) and (5.30), c_a^* equals the specific heat capacity of air ($c_{p,a}$) if the HEX is dry and c_{sat} (Eq. 5.31) if it is wet [154].

$$c_{sat} = \frac{i_{sat,w,in} - i_{sat,w,out}}{T_{w,in} - T_{w,out}}$$ (5.31)

Analogous to Eq. (5.29), the coolant-side NTU (NTU_w) and the air-side NTU (NTU_a) are defined by Eqs. (5.32) and (5.33) respectively. The UA in the coolant side $(UA)_w$ and in the air side $(UA)_a$ compose the total UA of the HEX (Eq. 5.34).

$$NTU_w = \frac{(UA)_w}{c_{p,w} \cdot \dot{m}_w} \tag{5.32}$$

$$NTU_a = \frac{(UA)_a}{c_a{}^* \cdot \dot{m}_a} \tag{5.33}$$

$$UA = \frac{1}{\dfrac{1}{(UA)_w} + \dfrac{1}{(UA)_a}} \tag{5.34}$$

Global heat transfer coefficient

Convection is the dominant heat transfer mode in a heat exchanger [160], hence the UA can be expressed by Eq. (5.35).

$$UA = \frac{1}{\dfrac{1}{h_w \cdot A_w} + \dfrac{1}{h_a \cdot \left(A_a + \eta_{fin} A_{fin}\right)}} \tag{5.35}$$

The HEX surfaces and the fin efficiency (η_{fin}) are characteristic and constant for a given HEX. The convection coefficient (h) can be expressed as function of the Nu and other constant parameters for a given setup (k_f and D_h) (Eq. 2.31). The Nu can be generally expressed as a function of Pr and Re as in Eq. (5.36), where K, n and m depend on the flow conditions.

$$Nu = K \, Re^n \, Pr^m \tag{5.36}$$

Pr (Eq. 2.45) and Re (Eq. 2.30) depend on the thermophysical properties of the fluids, which in turn depend on the temperature. In air-conditioning applications, the variation of the properties due to the temperature difference along the HEX is assumed to be negligible. Consequently, Pr remains constant and Re depends only on the fluid mass flow rate. Therefore, Eq. (5.35) can be rewritten as Eq. (5.37), where K_1, K_2, n_1 and n_2 are unknown constants to be fitted.

$$UA = \frac{1}{\dfrac{1}{K_1 \cdot \dot{m}_w^{n1}} + \dfrac{1}{K_2 \cdot \dot{m}_a^{n2}}} \tag{5.37}$$

5.5.3 Validation

Three units of the commercial compact HEX A51-KS423 by the partner MAHLE Behr (Fig. 5.13) were chosen for the coolant loop to the minibus cabin. This model is **louvered-fin flat-tube aluminum heat exchanger with two passes per tube** and is **usually employed as heater core**.
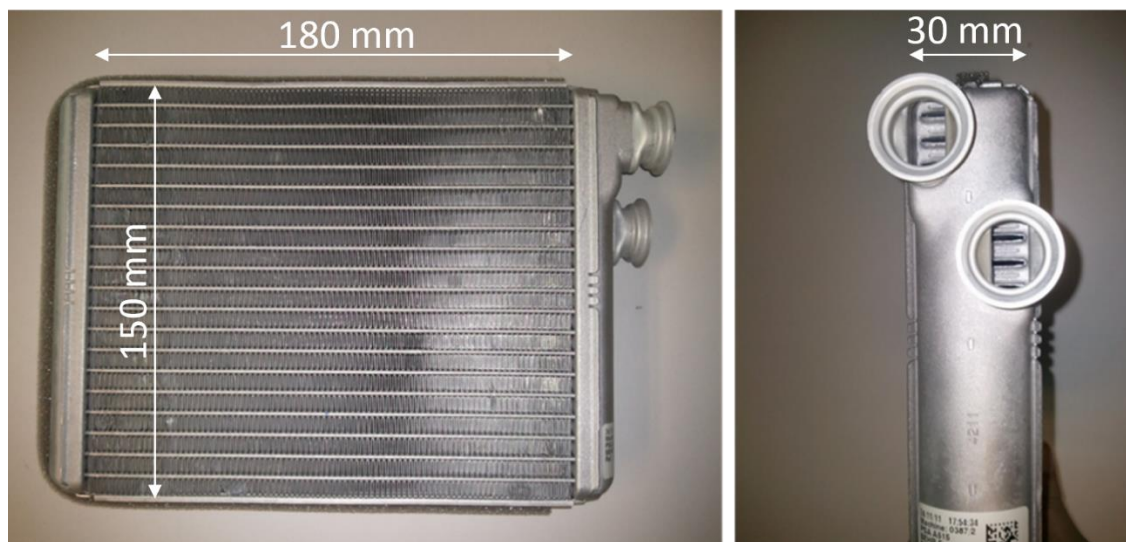

Fig. 5.13. A51-KS423 compact heat exchanger by MAHLE Behr and approximate dimensions [157].

A **comprehensive experimental campaign** was carried out by MAHLE Behr with the purpose of **characterizing the thermal performance of this HEX for its novel use in the air conditioning of an electric vehicle**. In order to obtain on-board performance data, the HEX was mounted inside one of the rear AHUs of the minibus, which basically consists of a short wind tunnel and a variable speed centrifugal fan. The experimental setup was placed inside a climatic chamber in order to control the inlet air temperature and humidity (Fig. 5.14). The outlet air temperature was measured with a grid of 16 temperature sensors placed on the HEX. The mass flow rate of condensate was also registered. In the coolant side, a solution of 50% in volume of ethylene glycol in water typical for automotive applications was employed. The experimental facility allowed for controlling the flow rate and inlet temperature of the coolant, as well as for recording the outlet temperature of the coolant.

Fig. 5.14. Experimental setup: HEX inside HVAC unit (left) and HVAC unit in the test bench (right) [157].

The HEX was tested under a wide range of temperatures and flow rates which are representative of the working conditions of an AC system (Table 5.8). In total, 279 operation points were measured, 180 in heating mode and 99 in cooling mode.

Table 5.8. AC operation points tested by MAHLE Behr.

Mode	Air inlet T (°C) / RH (%)	Coolant inlet T (°C)	Air flow rate (m³ h⁻¹)	Coolant flow rate (m³ h⁻¹)
Heating	0/70, 10/60, 20/50	30, 35, 40, 50	100, 200, 250, 300, 400	0.3, 0.6, 0.9
Cooling	20/40[1], 25/50, 30/60	5, 10, 15	150, 200, 250, 300	0.3, 0.6, 0.9

[1] 20°C/40% conditions were tested under air flow rates of 100, 200 and 300 m³ h⁻¹

The results of the experimental campaign have been employed to find a correlation for the UA of the studied HEX with the form of Eq. (5.37). The exponents n_1 and n_2 have been found in literature considering the characteristics of the coolant and air flows respectively through the measured HEX.

In the coolant side, Re in the tests ranges between 115 and 688 so the flow regime is laminar. It is assumed that the mean Nusselt number (Nu_m) for hydrodynamically developed laminar flow in flat tubes can be approached by the expression for parallel plates (Eqs. 5.38 to 5.40) [161].

$$Nu_m = (Nu_1^3 + Nu_2^3)^{1/3} \tag{5.38}$$

$$Nu_{m,T,1} = 7.541 \tag{5.39}$$

$$Nu_{m,T,2} = 1.841\sqrt[3]{RePrD_h/L} \tag{5.40}$$

Under the conditions measured and due to the geometry of the HEX the value of Nu_m approaches Nu_2, so the rest of the terms in Eq. (5.38) can be neglected. Since n_1 refers to the exponent of the Re in the coolant side, then $n_1=0.33$.

Similarly, n_2 is the exponent of the Re in the air side. Several correlations for plate-fin surfaces with louvered fins have been tried to find the value of n_2 for the tested air flow range. The best results were obtained with the correlation by Webb and Kim [162], which gave $n_2=0.58$.

The constants K_1 and K_2 in Eq. (5.37) have been calculated in order to minimize the sum of the $RMSE$ (Eq. 2.27) of the heat transfer rate ($\dot{Q}_{HEX}$, Eqs. 5.17 and 5.20). If the purpose is to predict the HEX performance, fitting the heat transfer rate provides greater accuracy than fitting the UA values. The value of the heat transfer rate computed in the coolant side has been employed as in [153], since measuring the flow rate and the temperature in the air side is more difficult than in the coolant side. A significant dispersion was observed in the experimental results at low air flow rates. On the contrary, the measurements in the coolant side are much more accurate.

K_1 refers to the heat transfer conditions in the coolant side, so its value should remain the same regardless the type of process in the air side (sensible or latent). However, in the air side the energy transfer rate during a latent process increases significantly compared to the one in a sensible process. Therefore, K_2 is expected to be larger if the HEX is wet. Two values of K_2 have been fitted: one to the cases in which the HEX surface in the air side is mainly dry ($K_{2,dry}$) and the other to the points in which it is mainly wet ($K_{2,wet}$). Table 2 summarizes the values obtained for the parameters in Eq. (5.37).

Table 5.9. Parameters for UA correlation

Constant	Value
K_1	545.28
n_1	0.33
$K_{2,dry}$	1810.11
$K_{2,wet}$	3318.72
n_2	0.58

Fig. 5.15 and Fig. 5.16 compare the experimental values of the heat transfer rate in the coolant side with the values obtained by means of the correlation. **The correlation proposed achieves a good accuracy for all the conditions tested in both cooling and heating modes: the average relative error is 2.4% and the maximum, 14.0%.**
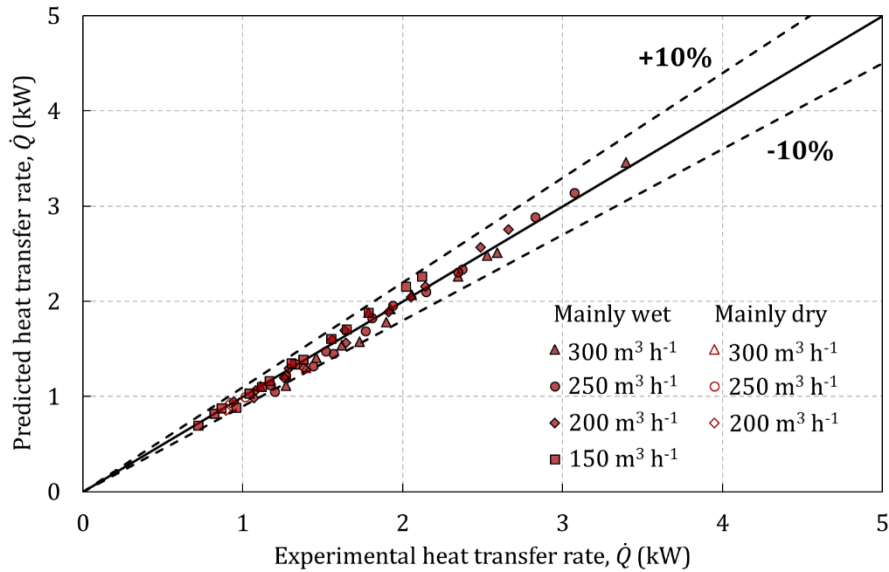
Fig. 5.15. Experimental and predicted heat transfer rate as function of the air flow rate for partially wet working conditions [157].

Fig. 5.15 shows the cases in which the coil was partially wet. Although different values of the condensate mass flow rate were measured, treating each working point as if the HEX surface was either all wet or all dry provides a good accuracy. Compared to fitting a single value for K_2, differentiating between mainly wet ($K_{2,wet}$) and mainly dry ($K_{2,dry}$) conditions reduced the average relative error by 1.2 percentage points and the maximum by 5.1. The largest errors, up to -12.4%, are produced by the cases in which the latent heat load is low but the working conditions are still closer to all wet. As noted by Braun et al. [154], in these conditions the heat transfer rate is underpredicted.

Fig. 5.16 shows the cases in which the HEX was completely dry. As expected, a single value of the constants in Eq. (5.37) fits both air cooling and heating modes. The largest errors, up to 14.0%, correspond mainly to cases with low air flow rates, which are difficult to measure. Some of these cases produced experimental effectiveness values larger than one, nevertheless the correlation achieved good predictions.

The outlet temperature of the fluids is the output of the HEX model. Fig. 5.17 is deducted from the results of the heat transfer rate and compares the experimental temperature differences in the HEX with the predictions of the model in air cooling mode, including partially wet and completely dry working conditions. Since the inlet temperatures are inputs to the model, **the maximum deviation in the coolant outlet temperature is 0.41 K and in the air outlet temperature, 1.74 K. These results definitely validate the employed approach.**
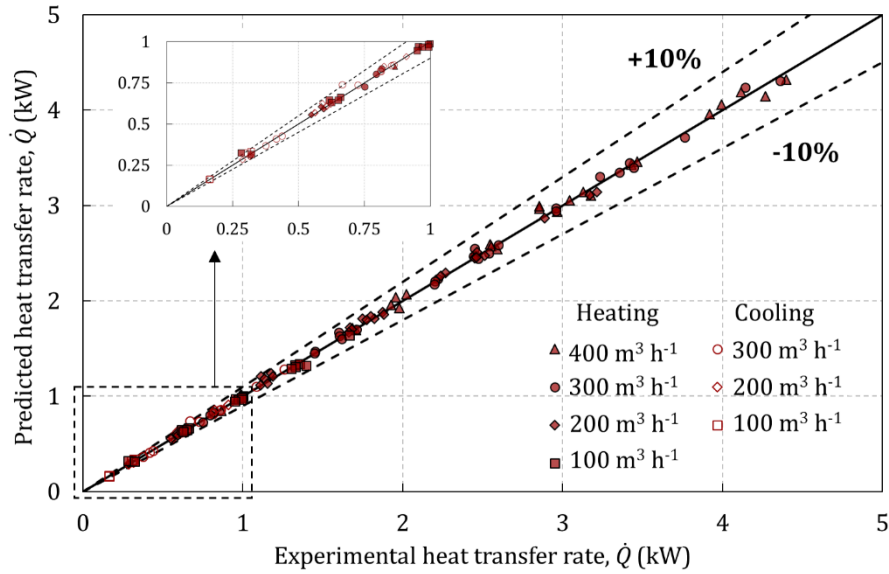
Fig. 5.16. Experimental and predicted heat transfer as function of the air flow rate for completely dry working conditions [157].
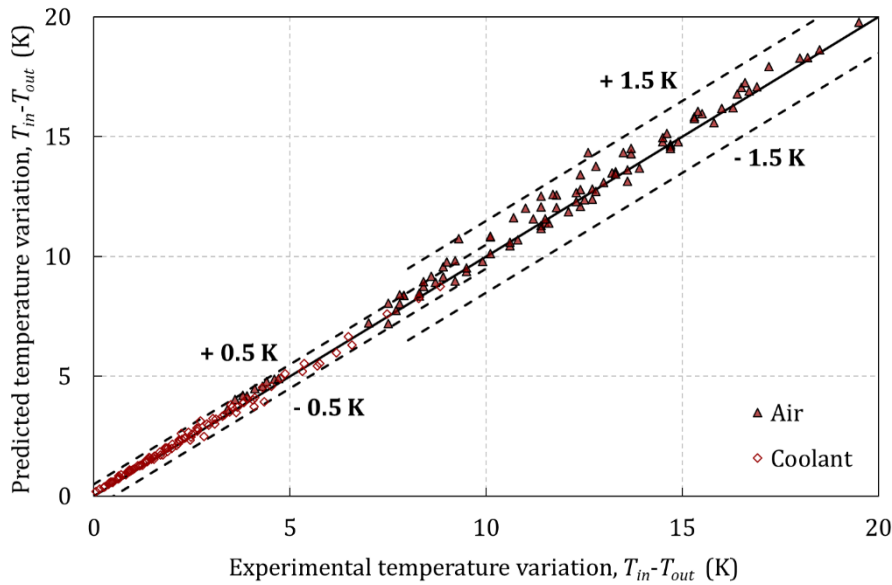

Fig. 5.17. Experimental and predicted fluid temperature variation in both sides of the HEX for cooling model [157].

In the external loop, the radiator of the vehicle is used in the MAC system. The radiator is also a compact louvered-fin heat exchanger with two passes per row. Since an experimental characterization of this device in air conditioning working conditions was not available, the radiator has been included in the global model by scaling the correlation found for the air-coolers.

5.6 The reversible refrigerator model interface

The main purpose of the reversible refrigerator model into the global model is to calculate its power consumption for satisfying the thermal demand in the cabin under dynamic working conditions. Refrigerators are complex devices so in global system models they are usually implemented as black or grey box models for compatibility reasons [126]. The validity of such approaches depends on the system dynamics and should be carefully analyzed for the AMRR. In any case, this section describes the requirements to communicate a generic refrigerator model with the proposed MAC system model. Fig. 5.18 is a scheme of this interface.
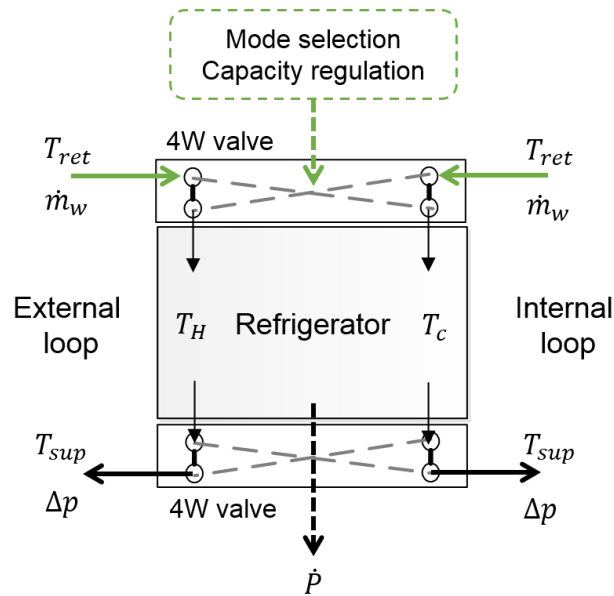
Fig. 5.18. Scheme of the reversible refrigerator model interface.

The time-dependent inputs to the refrigerator model from the other components of the MAC system are the return temperatures (T_{ret}) and fluid flow rates ($\dot{m}_w$) from the hydraulic loops at each side. A four way valve guides the flow from each loop to the corresponding side of the refrigerator depending on the working mode selected, cooling or heating. The refrigerator model should also receive the necessary control signals to regulate the cooling or heating capacity delivered.

The time-dependent outputs that are needed to integrate the refrigerator model are the supply temperatures (T_{sup}) to each loop and the pressure drop in the path traversed by the heat transfer fluid that comes back to the loops (Δp). Besides, for the purpose of the global model at least the resulting electric power consumption ($\dot{P}$) is required as an output.

Chapter 6

Design of an AMRR for a mobile air-conditioning system

In this chapter, **the feasibility of the magnetic refrigeration technology in MAC systems is analyzed by means of the models developed.**

First, the vehicle model is employed to determine the requirements of the targeted application for both cooling and heating modes. These comprise the thermal demand, the working temperatures and other issues such as mass and efficiency. The features of vapor-compression devices currently employed in MAC systems are provided as a reference.

Once the design specifications are established, an optimization study is conducted with the developed AMR model with the purpose of determining the design and working parameters that fulfil those requirements with a minimum combined electric consumption and device mass. Several design points obtained with different settings of the electrical auxiliaries have been considered. **The results are compared in terms of global consumption and to the features of current vapor-compression systems.**

6.1 Literature review on AMRR parametric studies

Comprehensive parametric studies have already been performed with the purpose of finding the design and operating parameters that optimize the parallel-plate active magnetic regenerator (AMR) performance. Nielsen et al. [124] analyzed the effect of the channel and plate thicknesses between 0.2 and 1 mm combined with cycle

frequencies (f) from 0.14 to 4 Hz and thermal utilizations (φ) between 0.14 and 6.4, for a range of temperature spans. Among other trends, they found that φ should range between 0.2 and 1. Tušek et al. [36] studied in detail the optimal geometry of the AMR from the thermohydraulic point of view. They considered a fixed temperature span of 15K, two values of the frequency (0.5 and 3 Hz) and the corresponding optimal fluid flow rate. The analysis included plates from 0.1 to 1 mm thick, channels from 0.01 to 0.1 mm high and regenerators from 40 to 200 mm long. Under these conditions, they found that a channel height of 0.035 mm maximized the specific cooling capacity and 0.075 mm maximized the *EER* regardless of the other parameters. However, both of these studies were based in material properties modelled with the mean field theory and did not consider the demagnetizing effect, which leads to an overestimation of the AMR performance [69].

The optimization of the AMRR mass and performance, including both the magnet and the AMR, has also been addressed by a number of researchers. These studies focus in the overall cost of the device as the target variable. The parameters varied include the applied magnetic field, some of the regenerator dimensions, the operating parameters (f and φ) and in some cases the thermal requirements. Bjørk et al. [163] determined the minimum building cost of an AMRR based on its total mass. Tura and Rowe [61] minimized the total cost of a packed-spheres AMRR, that is the sum of its building and operating costs, with the purpose of identifying target refrigerant properties. To do so, they employed an analytical AMR model and considered an ideally graded regenerator bed. Recently, Bjørk et al. [56] performed a similar lifetime analysis focused on a realistic practical application for current small AMRRs, specifically a domestic refrigerator. Unlike the former studies, they employed experimental Gd properties and swept all the parameters related to the dimensions of a packed-sphere AMRR. They considered cycle frequencies up to 10 Hz, achievable by current prototypes. In agreement with Tura and Rowe [61], they found an optimal magnetic field around 1.4 T.

As the latter study, **the present work considers the possibilities of current AMRR prototypes and MCM materials, including the demagnetizing effect**. However **a much more demanding application is targeted**. Another main **novelty is the analyzed parameter space**, which includes 5 different design parameters of parallel-plate AMRRs (instead of packed-spheres) and the 2 operating parameters. Moreover, **the range of AMR dimensions explored goes beyond the published studies** to the knowledge of the authors. A significant difference with respect to the previous analyses is that the electric consumption and the mass of the device are not merged into only one target variable. Therefore, **the solution shown is a line of optimal pairs efficiency-mass and moreover, its interaction with the complete systems is analyzed.** Finally, **the performance of the AMRR working as a heat pump is calculated, which is not frequent** in the literature.

6.2 Mobile air-conditioning requirements

The thermal requirements of the Daily minibus have been calculated under the design conditions fixed by the ICE Project consortium (Table 6.1). They refer to the steady operation of the AC system with an average occupancy and the vehicle stopped. Demisting and defrosting the windows is not included in the specifications of this AC system.

Table 6.1. MAC system design conditions.

	Summer	**Winter**
Comfort target	25 °C at 50% RH	20 °C
External conditions	35°C at 60% RH, $I=0$	0 °C at 80% RH, $I=0$
Air mode - Driver	Full recirculation with 100% head distribution	Fresh air with 100% floor distribution
Air mode - Passengers	Full recirculation	Full recirculation
Occupants	8 (driver + 7 passengers)	8 (driver + 7 passengers)

The fluid in the hydraulic loops is a solution of 50% ethylene glycol for automotive applications. The fluid properties which are relevant for the simulations are detailed in Table 6.2.

Table 6.2. Fluid properties.

Property	Value	Property	Value
ρ_f	1030.7 kg m^{-3}	μ_f	3.2 mPa s
c_f	3551 J kg^{-1} K^{-1}	k_f	0.394 W m^{-1} K^{-1}

6.2.1 Thermal load

The thermal load in the minibus cabin has been calculated with the cabin model (section 5.3). Fig. 6.1 details the different heat gains in the two thermal zones of the minibus under the conditions in Table 6.1. The negative gains contribute to the thermal comfort, while the positive must be overcome by the AC system.

In general, the largest contribution to the thermal demand is caused by the temperature difference with the external ambient. In the steady state the temperatures of the cabin body and the interior masses reach a value which is different from the cabin air temperature, so the large surface of these elements results in a relatively large gain or loss ($\dot{Q}_{i-b}$ and $\dot{Q}_{i-m}$). The occupancy load ($\dot{Q}_{occ}$) is also significant in the passengers' zone and in winter can reduce the heating demand by 25%. The load due to the auxiliaries ($\dot{Q}_{aux}$) may be relevant depending on the blower settings, so both the maximum and minimum values have been represented in Fig.

6.1. Moreover, the blower settings have a great impact in the ventilation load ($\dot{Q}_{ven}$), which appears when the AHU works in fresh air mode (winter, zone 1). In that case, the difference in the air mass flow rate given by the lower and higher blower speed settings (Table 5.6) can double the thermal demand.
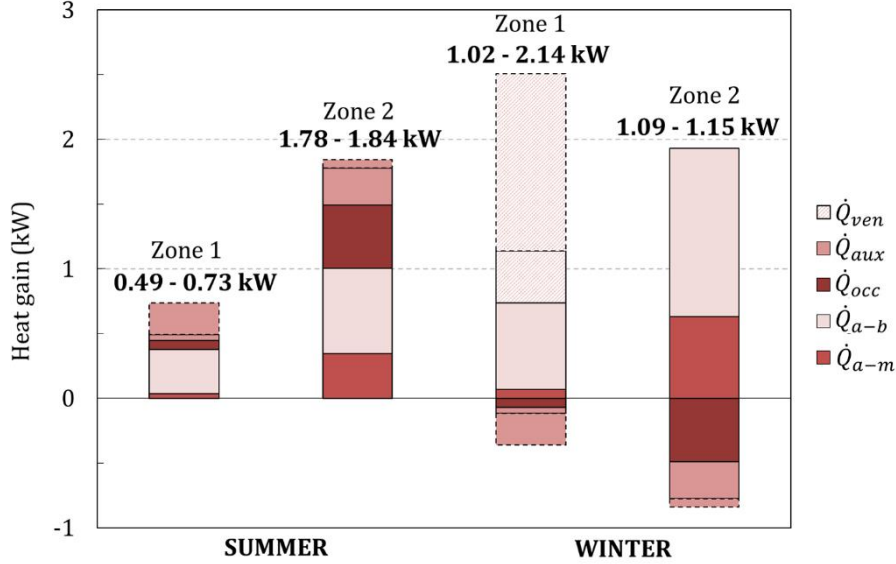

Fig. 6.1. Thermal loads in the cabin minibus.

The total cooling ($\dot{Q}_c$) or heating ($\dot{Q}_h$) capacity required to reach and maintain comfort conditions equals the thermal demand in the cabin plus the thermal losses from the AC system to the ambient. In order to estimate the total capacity, the heat balance equations (Eqs. (6.1) and (6.2) for heating mode and Eqs. (6.1) and (6.3) for cooling mode) are placed into the refrigerator model interface.

$$\dot{Q}_h = \dot{Q}_c + \dot{W} \qquad (6.1)$$

$$COP = \frac{\dot{Q}_h}{\dot{W}} \qquad (6.2)$$

$$EER = \frac{\dot{Q}_c}{\dot{W}} \qquad (6.3)$$

In the internal loop, the working fluid is distributed among the heat exchangers considering the thermal demand in each zone (Fig. 6.1). The fluid mass flow rate in each loop was selected in order to establish a typical temperature difference around 5 K in the HEXs. The air flow rate delivered by the blowers was varied between their minimum and maximum values, while the fans in the radiator were kept at their maximum speed in order to enhance the heat transfer to the ambient.

The vehicle model was run with different constant cooling ($\dot{Q}_c$) and heating ($\dot{Q}_h$) capacities to find the values that can keep the target comfort conditions at the steady

state. A typical *EER* and *COP* value of 2.5 was employed in the simulations, as discussed in next section. Table 6.3 summarizes the results, which are presented as a range comprising all the blower settings.

Table 6.3. Minimum and maximum required cooling and heating capacities.

	Summer	Winter
Sensible load (W)	$2271 - 2577$	2007 - 3233
Latent load (W)	280	-
Ambient losses (W)	170 - 270	180 - 300
Total capacity (W)	**2803 - 3027**	**2307 - 3413**

The losses to the ambient in the AC system may represent by 5% to 10% of the total load, depending on the air mass flow rate pushed through the heat exchangers. This range is due to the fluid temperature established in the loops as explained below.

6.2.2 Working temperatures

The working temperatures are key in the design of an AMRR, given that the MCMs must be selected to operate near their Curie temperature. The simulations with the vehicle model run in the former section can provide a preliminary estimation of the temperatures reached within the system.

Given a thermal capacity and a target temperature, the temperature level in the ambient side is affected by the *COP* or *EER* set. In heating mode, increasing the *COP* increases the heat absorbed from the ambient ($\dot{Q}_c$), therefore the temperature span also rises. On the contrary, in cooling mode increasing the *EER* decreases the heat rejected ($\dot{Q}_h$), causing a decrease in the temperature span. Nevertheless, the influence of the reference *COP* or *EER* is not critical. Doubling the reference value set causes a change in the predicted temperature span by less than 1 K.

However **the air flow rate delivered by the blowers has a significant influence in the system performance**. The effect of the air flow rate is twofold. On the one hand, increasing the air flow rate reduces the temperature span with the ambient and hence the thermal losses. On the other hand, it increases the thermal loads due to the auxiliaries and especially to the ventilation. Therefore, **there is a compromise between the temperature span and the cooling or heating capacity**. Moreover, **if the consumption of the MAC system is evaluated globally, the consumption of the blowers can make a difference**.

Since the requirements of temperature span and capacity follow opposite trends, **two design options achieved with different blower settings are considered for each mode**. Both of them maintain the target temperature while the *RH* is inside the comfort range 30%-70% [140]. Table 6.4 contains the results of the supply temperatures to the heat pump, the corresponding required capacity and the electric consumption of the blowers.

Table 6.4. Design specifications of the AMRR MAC system.

	Summer 1	Summer 2	Winter 1	Winter 2
Total capacity (W)	3027	2803	2706	2307
Cabin side T (°C)	12.78	6.79	28.58	31.54
Ambient side T (°C)	42.13	41.60	-2.43	-2.21
Temperature span (K)	29.4	34.8	31.0	33.8
Blowers' consumption (W)	640	366	522	398

6.2.3 Mass

In automotive applications **the mass of the auxiliary systems must be minimal given that any additional load implies increasing fuel or electric consumption by the powertrain**. Moreover the cost of AMRRs is directly related to its mass [163], so it is definitely a parameter to me minimized. Automotive vapor-compression devices weight from 12 to 15 kg approximately.

6.2.4 Efficiency

In order to set a reference value for the desired AMRR efficiency, the consumption of the described MAC system with a vapor-compression device has been calculated. Specifically, the state-of-the-art water-to-water refrigerator defined in the ICE Project has been considered, which includes a variable-speed compressor and uses R134a as refrigerant [66,164].

The electric consumption associated to the refrigerator is the sum of the power demanded by the device itself and the one due to the coolant pumping through it. The power demand has been calculated under the conditions in Table 6.4 by means of simulation [164]. The pumping power depends on the working fluid flow rate, which in conventional systems is usually selected to achieve a compromise between heat transfer efficiency and pressure drop. A typical design parameter is the difference between the supply and return temperatures to the refrigerator, which usually ranges between 3 and 5 K in water-to-water devices. In the case of 2.3 to 3 kW thermal power, this yields from 7.5 to 17 l min^{-1} flow rate of the 50% ethylene glycol solution employed. The corresponding pressure drop through the mentioned vapor-compression device is 5 to 15 kPa in each side. Considering that circulation pumps present a typical 60% efficiency, pumping the fluid through the conventional refrigerator requires between 2.8 and 14.2 W electric power. Table 6.5 summarizes the total electric consumption by the reference vapor-compression device and its corresponding performance.

Table 6.5. Vapor-compression device performance.

	Summer 1	Summer 2	Winter 1	Winter 2
Total capacity (W)	3027	2803	2706	2307
Cabin side T (°C)	12.78	6.79	28.58	31.54
Ambient side T (°C)	42.13	41.60	-2.43	-2.21
Power consumption (W)	1245	1530	824	740
EER / COP (-)	2.43	1.83	3.28	3.12

6.3 AMRR definition

A **permanent-magnet AMRR with rotary architecture and axial fluid flow** is studied in this work, since this configuration seems to be the most suitable for practical applications [1]. In order to approach realistically its behavior an experimental magnetic field profile has been considered, which corresponds specifically to the machine published by Eriksen et al. [34]. The working fluid is the 50% ethylene glycol solution employed in the AC loops (Table 6.3). The synchronization of the fluid and magnetic profiles has an impact in the AMR performance [32], but the no-flow times have a detrimental effect [124]. Therefore, the length of the blow period (τ_{blow}) is a variable parameter in this work. For simplicity in the analysis, a nearly step-wise profile has been considered. Fig. 6.2 shows the applied magnetic field ($\mu_0 H_{app}$) and fluid flow ($\dot{m}$) profiles along the AMR cycle, normalized to an arbitrary maximum value. A negative value of $\dot{m}$ indicates that the fluid flows from the cold end ($x=L$) to the hot end ($x=0$) of the regenerator bed.
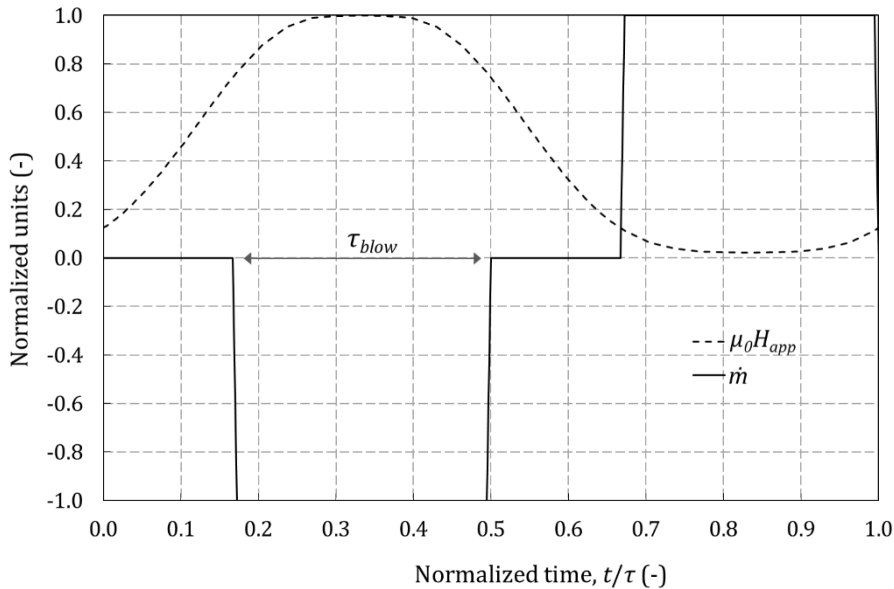
Fig. 6.2. Normalized applied magnetic field and fluid flow profiles [38].

The **AMR is arranged as parallel plates of MCM accurately aligned**, that is, the fluid flow maldistribution effect is negligible. Regarding the AMR composition, a **multimaterial bed with suitable Curie temperatures** is needed to reach the large thermal requirements of the vehicle with a reasonable amount of MCM. Given the availability of detailed experimental data set of commercial-grade Gd properties, **the behavior of the Gd alloys has been approximated by shifting the former properties** as described by Monfared and Palm [165]. The specific AMR composition considered is presented in section 6.5.1.

6.3.1 Calculation of the AMRR performance

Similarly to the conventional refrigerator, **the electric power consumption ($\dot{P}$) of the AMRR is given by the sum of the electric power required to move the magnet and to pump the working fluid** through it (Eq. 6.4).

$$\dot{P} = \frac{\dot{W}_{pump}}{\eta_{pump}} + \frac{\dot{W}_{mag}}{\eta_{mot}} \tag{6.4}$$

The pumping power ($\dot{W}_{pump}$) and the magnetic power ($\dot{W}_{mag}$) of the AMRR can be calculated from Eqs. (2.22) and (2.23) respectively. The thermal losses to the ambient and the pressure drop through the valves of the device have not been considered. The *EER* and the *COP* were defined in Eqs. (2.24) and (2.25).

The AMRR performance is calculated by means of the AMR model presented in chapter 2. A single pair plate-channel representative of an entire plates stack is simulated. The modelling assumptions explained along this work have been employed, which in the present study present the following limitations.

The *Nu* correlation proposed does not consider the effect of the frequency, however to the best knowledge of the author this effect is not included in any suitable correlation for the present case. Some studies conclude that the heat transfer coefficient may be enhanced in reciprocating flow at high frequency with respect to unidirectional flow [166], so the study carried out in this work is conservative in this aspect.

In stacks of parallel plates, the average demagnetization factor (N_{avg}) depends not only on the geometry of the plate but also on the number of plates stacked and the distance between them [42]. Therefore, the effect of demagnetization will be affected by the particular arrangement of the MCM in beds, which is a further step of the design process. For the plate dimensions considered in this study, N_{avg} can range between 0.2 and 0.3. For the purpose of this analysis, N_{avg} has been set to 0.25 for all the studied cases and a sensitivity analysis has been performed for some of them.

6.3.2 Calculation of the AMRR mass

The mass of the AMRR is assumed to be the sum of the mass of the magnet assembly and the mass of MCM. These magnitudes are directly related to the cost of the machine [56]. The rest of the components (electric motor, valves, etc.) are expected to represent a small percentage of the total mass and cost and are not taken into account.

The **total mass of MCM** (m_r) needed to meet the thermal demand ($\dot{Q}$) of the vehicle with a given AMR configuration is inversely proportional to its specific cooling or heating capacity ($\dot{q}$) (Eq. 6.5).

$$m_r = \frac{\dot{Q}}{\dot{q}} = \dot{Q}\frac{\rho_r WLH_r}{\dot{Q}_{plate}} \tag{6.5}$$

Where $\dot{Q}$ refers to the total cooling or heating capacity of the AMRR and $\dot{Q}_{plate}$ to the capacity per pair plate-channel which is the output of the AMR model (Eqs. 2.20 and 2.21).

The **mass of the magnet assembly** (m_{mag}) required to generate a given magnetic field amplitude ($\mu_0 H_{app}$) over the volume occupied by the AMR is estimated with the approach proposed by Bjørk et al. [163]. If an assembly that generates a constant magnetic field in the gap is considered, the volume of the gap is related to the volume of magnet material with remanence B_{rem} through the figure of merit M^* (Eq. 6.6).

$$M^* = \left(\frac{\mu_0 H_{app}}{B_{rem}}\right)^2 \frac{V_{gap}}{V_{mag}} \tag{6.6}$$

The value of M^* depends on the specific magnet design considered. In order to obtain a plausible estimation of the magnet assembly mass, the expression for the ideal Halbach cylinder of infinite length has been considered as by Bjørk et al. [163] (Eq. 6.7). As reviewed in section 1.2, the Halbach-like arrays are widely employed in AMRR prototypes [1].

$$M^* = \frac{\left(\frac{\mu_0 H_{app}}{B_{rem}}\right)^2}{e^{2\frac{\mu_0 H_{app}}{B_{rem}}} - 1} \tag{6.7}$$

In rotary prototypes the AMR is usually placed inside the magnet gap, and consequently this is the volume which is available for the AMR [1]. However in actual finite cylinders the field drops towards the ends of the magnet. The useful magnet length depends on the dimensions of the bore. In their study, Tura and Rowe [61] considered a 85% useful length and their results agree with the detailed analysis by Bjørk et al. [56]. Taking this into account, the magnet mass required can be expressed

by arranging Eqs. (6.6) and (6.7) following the deduction by Bjørk et al. [163] (Eq. 6.8).

$$m_{mag} = m_r \frac{\rho_{mag}\left(e^{2\mu_0 H_{app}/B_{rem}} - 1\right)}{0.85\rho_r(1 - \epsilon)} \tag{6.8}$$

6.4 AMRR simulation setup

6.4.1 Methodology

The AMRR performance and hence its resulting mass depend on multiple design and working parameters. With the purpose of determining the most appropriate values for vehicle applications, an optimization study has been carried out. Performing a complete parametric study instead of employing an optimization routine will allow for detecting trends that can be useful for future design purposes. **The objective is to determine the combinations of these parameters that define an AMRR that fulfils the requirements of the vehicle (Table 6.4) with lower combined device mass and electric consumption.**

A key issue in the design of an AMRR is the selection of the MCMs, whose Curie temperature must be adapted to the working temperatures. To the knowledge of the author, there is not an established methodology to optimize the composition of the AMR bed for two working modes (cooling and heating). As a first step in the design process, **the Curie temperature of the MCMs has been selected to work optimally in cooling mode** for the two summer design points set in Table 6.4. The reason is that in the application studied the cooling mode is more demanding than the heating mode.

Firstly, the cooling performance of the AMRR is analyzed for the design point Summer 1 (S1). The results are presented in terms of the AMRR mass and electric consumption which are required to overcome the corresponding thermal demand. A parametric study (section 6.4.2) is carried out in **two stages**. In the **first run, a coarse grid of the varied parameters** has been defined (third column of Table 6.7). The aim of this initial parametric study is to find which values should be studied in more detail, as well as to outline performance trends that can help reducing the number of simulations. **Based on the results obtained in the first run, a new finer grid of the same parameters has been defined** (fourth column of Table 6.7). A **second run of simulations is then carried out** with this finer grid in order to determine the optimal values of the studied parameters. The results of this study have been partially published in [38].

Secondly, the second run of simulations is repeated with the conditions of the design point Summer 2 (S2) and the corresponding AMR bed

composition. The optimal combinations of the AMRR parameters are determined also for this case. **The performance results obtained for both summer design points is compared in terms of global energy consumption**, that is, including the corresponding consumption of the blowers.

Afterwards, **the heating performance of the optimal AMRR designs found in the former simulations is calculated under the winter design conditions** in Table 6.4. Note that, although the working temperatures change, the AMR bed composition is kept as the one found for the summer design points. The purpose of this simulations is to determine whether the AMRRs designed for cooling mode would also cope with the heating requirements of the studied vehicle.

6.4.2 Parameter space

In the simulations, the hot (T_H) and cold (T_C) end temperatures were fixed to the corresponding values reported in Table 6.4 for each design point. Table 6.6 details the parameters employed in the model that remain constant for all the studied cases. These also include the fluid properties specified in Table 6.2. Table 6.7 shows the parameters which have been varied and their range of values.

Table 6.6. Constant model parameters.

Parameter	Value
ρ_r	7900 kg m^{-3}
k_r	11 W m^{-1} K^{-1}
ρ_{mag}	7400 kg m^{-3}
B_{rem}	1.4 T
W	25 mm
η_{pump}	0.60
η_{mot}	0.85

Table 6.7. Variable model parameters.

Parameter	Range	Values for first run	Values for second run
H_f	$0.1 - 0.01$ mm	0.1, 0.05, 0.01 mm	0.05, 0.04, 0.03, 0.02 mm
ϵ	$0.25 - 0.48$	0.25, 0.33, 0.40	0.33, 0.36, 0.40, 0.44, 0.48, 0.52, 0.55
L	$50 - 12.5$ mm	50, 25, 12.5 mm	30, 25, 20, 15, 10, 7.5 mm
$\mu_0 H_{app}$	$1 - 1.4$ T	1, 1.2, 1.4 T	1.4 T
τ_{blow}/τ	0.25, 0.33, 0.4	0.33	0.33
N_{avg}	$0.20 - 0.30$	0.25	0.25
f	$1 - 10$ Hz	1, 2, 4, 6, 8 Hz	2, 3, 4, 5, 6, 8, 10 Hz
φ	$0.2 - 1$	0.2, 0.4, 0.6, 0.8, 1	0.2, 0.3, 0.4, 0.5, 0.6, 0.7, 0.8

The **variable design parameters** include the regenerator dimensions (except for the regenerator width W), the amplitude of the applied magnetic field ($\mu_0 H_{app}$) and the duration of the blow time (τ_{blow}) with respect to the total cycle time (τ).

The range of channel heights (H_f) and porosities (ϵ) starts at the state-of-the-art dimensions of experimental Gd regenerators [44]. The corresponding plate thicknesses can be deducted from Eq. (2.3). The dimensions of current parallel-plate AMRs (for instance, H_f=0.1 mm and H_r=0.3 mm) should be further decreased in order to increase the AMR specific cooling capacity [36] and hence reach the requirements of the vehicle. Therefore, the proposed parameter space considers channel and plate thicknesses up to an order of magnitude less. The regenerator length (L) is varied accordingly starting from a typical value in literature, 50 mm. With respect to $\mu_0 H_{app}$, proposed values can be currently reached with permanent magnets and in this work are limited by the magnetocaloric properties data set employed. Finally, sensitivity analyses have been performed on the influence in the AMRR performance of the relation τ_{blow}/τ and of the demagnetization factor (N_{avg}).

The **working parameters** of the AMRR are the cycle frequency (f) and the fluid mass flow rate ($\dot{m}$). The latter can be obtained from the thermal utilization (φ, Eq. 4.4), which has been defined based on an average c_r value of the MCMs considered, $\bar{c}_r$=300 J kg^{-1} K^{-1}. The proposed range of frequencies correspond to the reported possibilities of experimental rotary devices [34], while the utilization has been varied in the optimal range found by Nielsen et al. [124].

The combinations of these parameters results in minimum NTU=3.5 and Γ=2.25 for the cases with H_f=0.1 mm and f=10 Hz. Since these parameters are greater than 1, the proposed space can be studied with the 1D model [98].

6.5   Cooling performance

6.5.1   Selection of MCMs

A graded AMR bed made of a series of Gd-like MCMs with suitable Curie temperatures has been considered. A detailed discussion of the optimal AMR bed composition is out of the scope of this work, nevertheless the selection of MCMs is key to maximize the device performance. Therefore, a sensitivity analysis with near-optimal approaches has been carried out.

According to Monfared and Palm [165], the maximum cooling capacity can be obtained by choosing a Curie temperature for each MCM layer equal to its average temperature during the AMR cycle. Assuming a linear temperature distribution along the material yielded near-optimal results. **The AMR bed was thus divided in equal length layers made of Gd-like materials whose Curie temperature equals the mean temperature of the range covered by the layer.**

Fig. 6.3 and Fig. 6.4 show the AMRR performance as function of the composition of the bed and the working parameters (f and φ), considering the working temperatures of the design points S1 (T_H=42.13 °C and T_C=12.78 °C) and S2 (T_H=41.60 °C and T_C=6.79 °C) respectively. The results shown were obtained with $\mu_0 H_{app}$=1 T, H_f=0.035 mm, ϵ=0.33, L=25 mm and $\tau_{blow}/\tau = 0.33$. Similar qualitative results were obtained with other values of the parameters of Table 6.7.
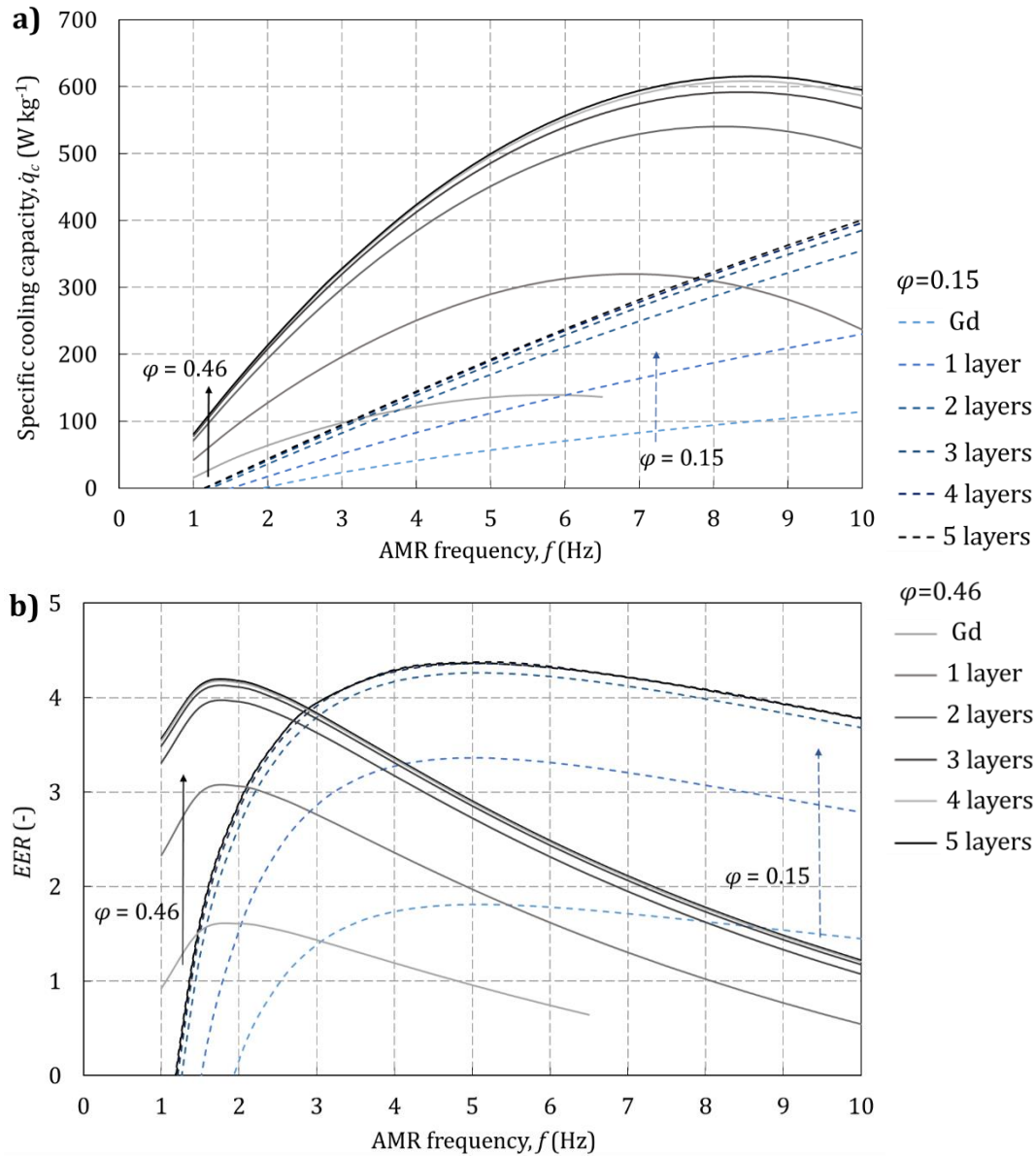
Fig. 6.3. AMRR a) specific cooling capacity and b) EER for the design point S1, as function of the composition of the bed, f and φ. The arrows indicate the evolution of the curves as the number of MCM layers is increased.
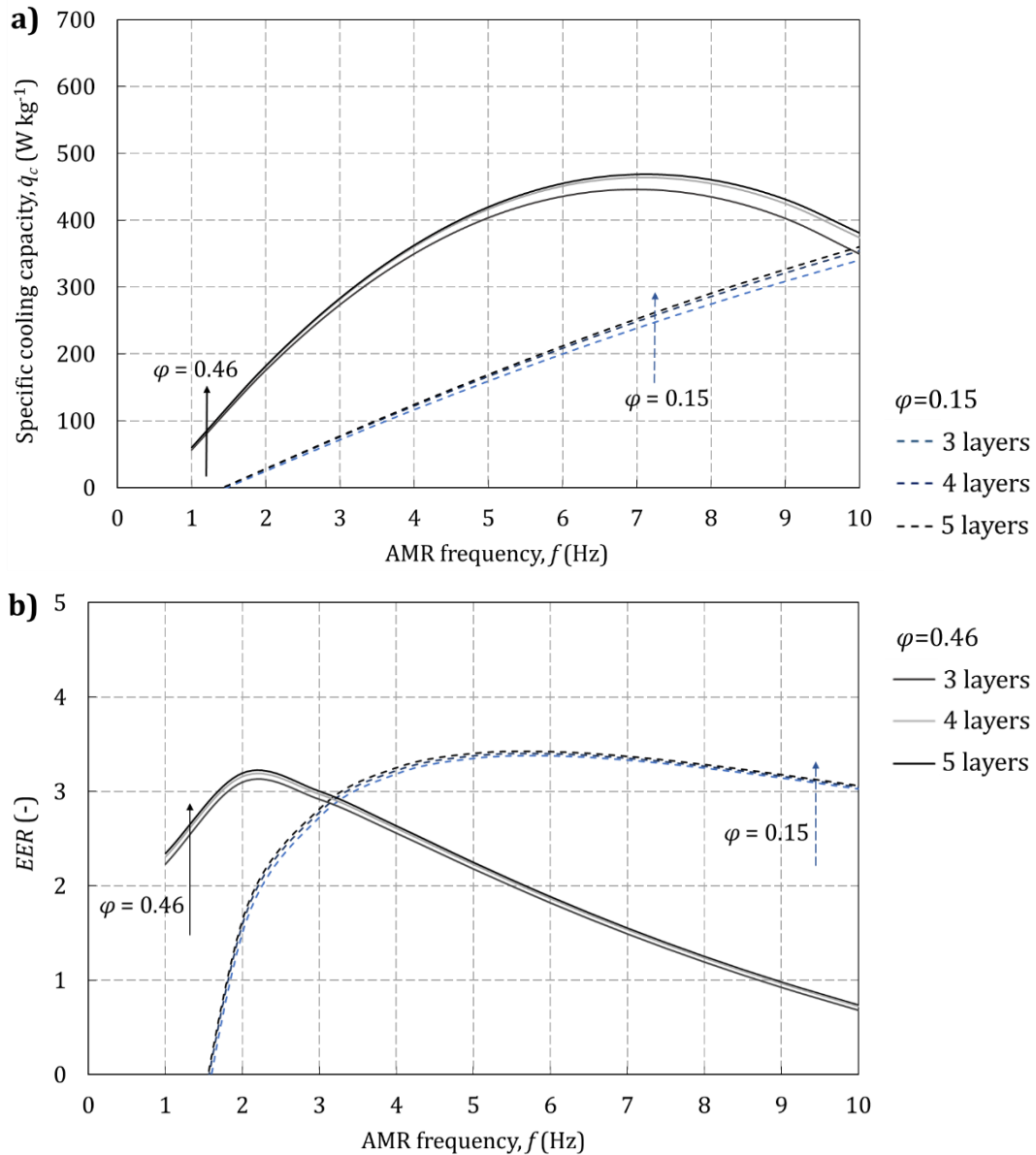
Fig. 6.4. AMRR a) specific cooling capacity and b) EER for the design point S2, as function of the composition of the bed, f and φ. The arrows indicate the evolution of the curves as the number of MCM layers is increased.

The AMRR cooling capacity and EER increase with the number of layers of MCM up to a certain point, which is 4 layers in both studied cases regardless the 5.5 K difference in ΔT_{span} between them. Therefore, for all the simulations performed in the following sections, the AMR bed is composed of 4 MCM layers uniformly distributed. Adding more layers does not provide a significant improvement even though the Curie temperatures are adapted to each case, so in principle the summer design point with the largest ΔT_{span} is expected to be less performing in the parameter range studied.

6.5.2 Case S1: 3027 W at 29.4 K span

Initial parametric study

A **first sweep** was performed **over the entire parameter space** with the values contained in the third column of Table 6.7 (2,025 simulations). The simulation of several combinations of the parameters resulted in a negative cooling capacity, mainly those with a too short regenerator length or a too high utilization and frequency. Fig. 6.5 shows the results of the valid cases sorted according to their channel height (H_f) and length (L).
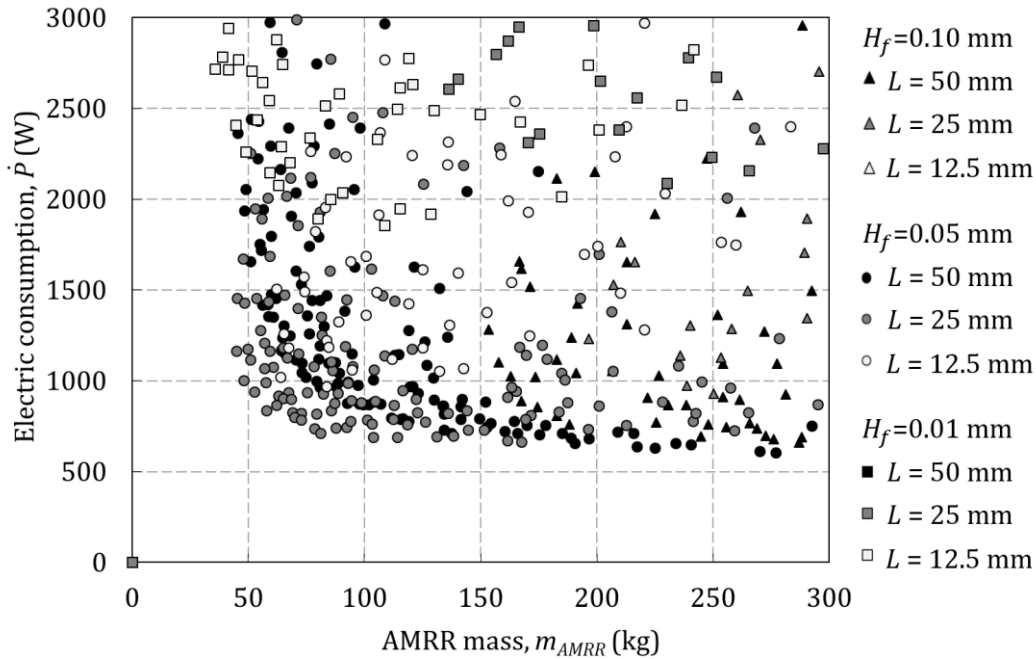
Fig. 6.5. AMRR consumption and mass as function of H_f and L [38].

The simulation results in Fig. 6.5 show that **there is an optimal channel height around 0.05 mm that provides a compromise between heat transfer efficiency and pressure losses**, that is, between specific cooling capacity and pumping work. The specific cooling capacity is related to the AMRR mass through Eqs. (6.5) and (6.8), while the pumping power is a part of the electric consumption (Eq. 6.4). Larger channel heights present reduced pressure losses but low specific cooling capacity, so they are placed in the bottom right-hand side of the map. Narrower channel heights are found in the opposite side. As the channel height decreases, the optimal regenerator length becomes shorter due to the increased pressure losses.

Fig. 6.6 shows the trends produced by the applied magnetic field ($\mu_0 H_{app}$), the utilization (φ) and the frequency (f). **In all the studied cases, the lowest combined mass and power consumption was found with the maximum value of the applied magnetic field considered, 1.4 T.** This value was also observed

by Tura and Rowe [61] and Bjørk et al. [56]. The optimum values of the utilization are in between 0.2 and 0.6, while the optimum frequency depends on the utilization.
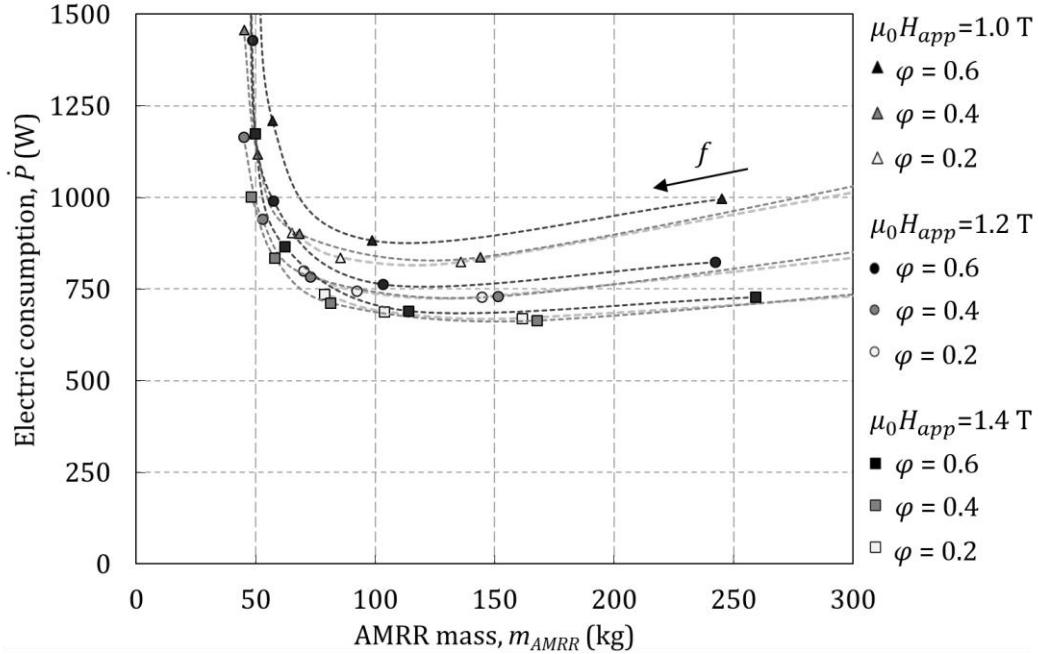
Fig. 6.6. AMRR consumption and mass as function of $\mu_0 H_{app}$, φ and f, for the case H_f=0.05 mm, ε=0.40, L=25 mm. The lines are guides to eye and indicate the trend due to the variation of f [38].

Regarding the effect of the porosity (ϵ), the best results were obtained with ε=0.40, the highest value simulated in this first run. Therefore, in order to draw conclusions about its effect in the AMRR performance, the range simulated has been enlarged and refined as described in the following section.

Finally, **sensitivity analyses** have been carried out **on the value of the blow time** with respect to the cycle time (τ_{blow}/τ) **and on the value of the average demagnetization factor** (N_{avg}). Simulations were performed with a channel height H_f=0.05 mm and the three values of τ_{blow}/τ and N_{avg} contained in the second column of Table 6.7. The rest of the parameters took the values detailed in the third column of that table (2,700 additional simulations).

Fig. 6.7 shows the results of the simulations varying τ_{blow}/τ. **For the magnetic field profile considered both $\tau_{blow}/\tau = 0.33$ and 0.40 produce similar results, while shorter blow times such as $\tau_{blow}/\tau = 0.25$ degrade significantly the AMRR performance.**
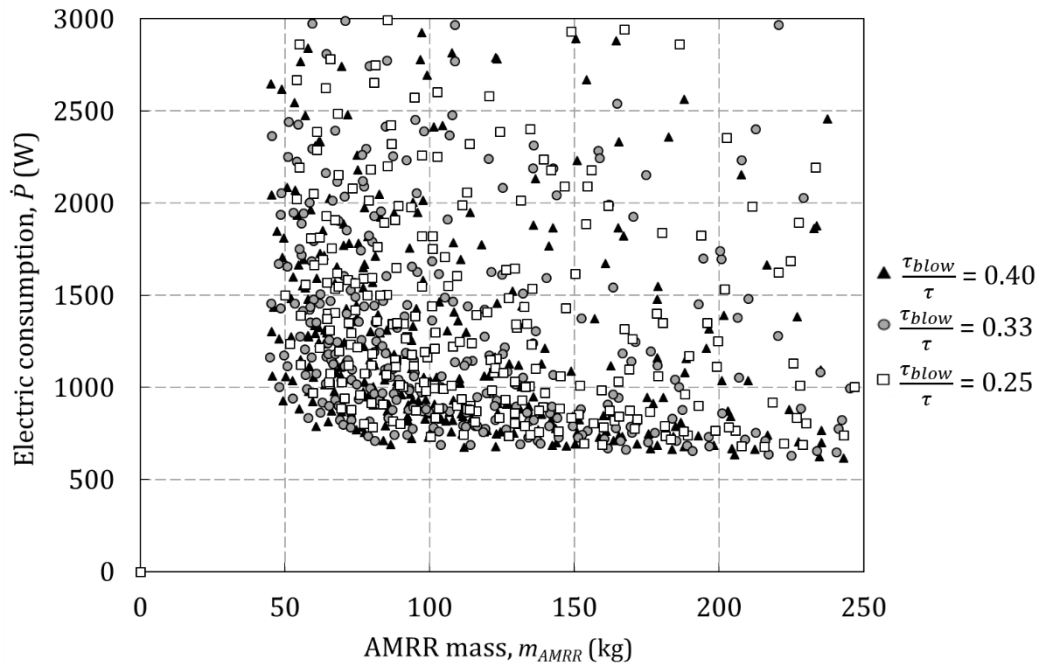
Fig. 6.7. AMRR consumption and mass for the cases with H_f=0.05 mm as function of the blow time [38].

Fig. 6.8 shows the results of the sensitivity analysis on N_{avg}. **If the working points in the optimal front are compared, a difference of ±0.05 with respect to N_{avg}=0.25 causes an average ± 5.1% difference in the AMRR mass and ±2.7% in the electric consumption.** These differences decrease as the points move to lower electric consumptions but higher AMRR masses, and increase for the opposite cases.
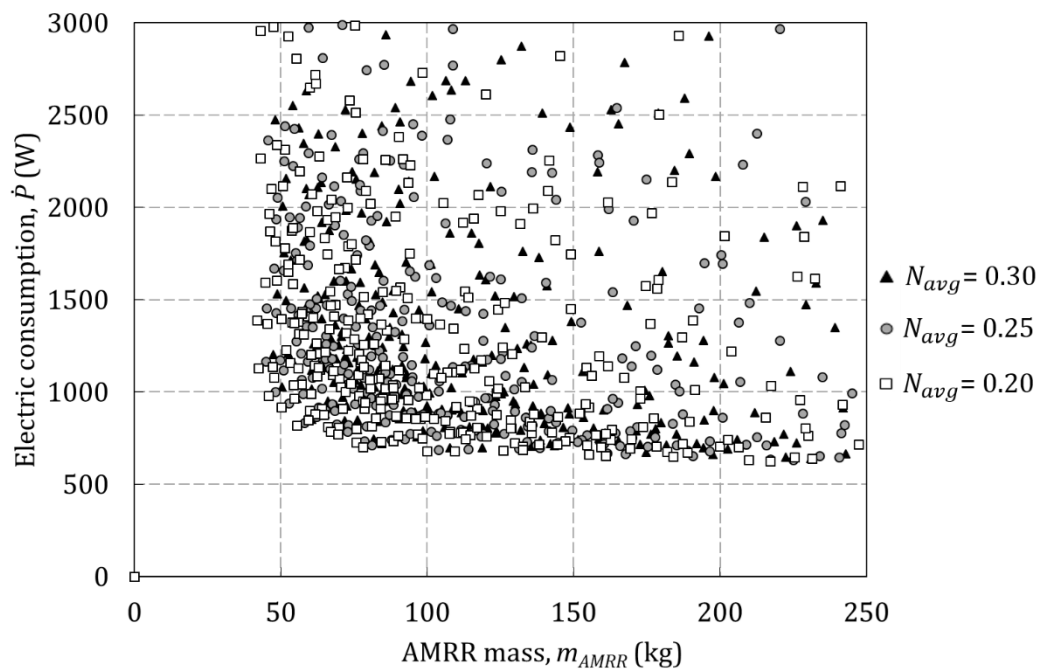
Fig. 6.8. AMRR consumption and mass for the cases with H_f =0.05 mm as function of N_{avg}.

Detailed parametric study

The results obtained in the initial parametric study allowed the definition of a **second parameter sweep around the optimal design values found**, which are detailed in the fourth column of Table 6.7 (1,756 simulations). Fig. 6.9 shows the relevant results of this second run. As can be observed, **the optimal AMRRs would fulfil the cooling requirements of the vehicle with an efficiency similar to the vapor-compression system, but would be heavier**.
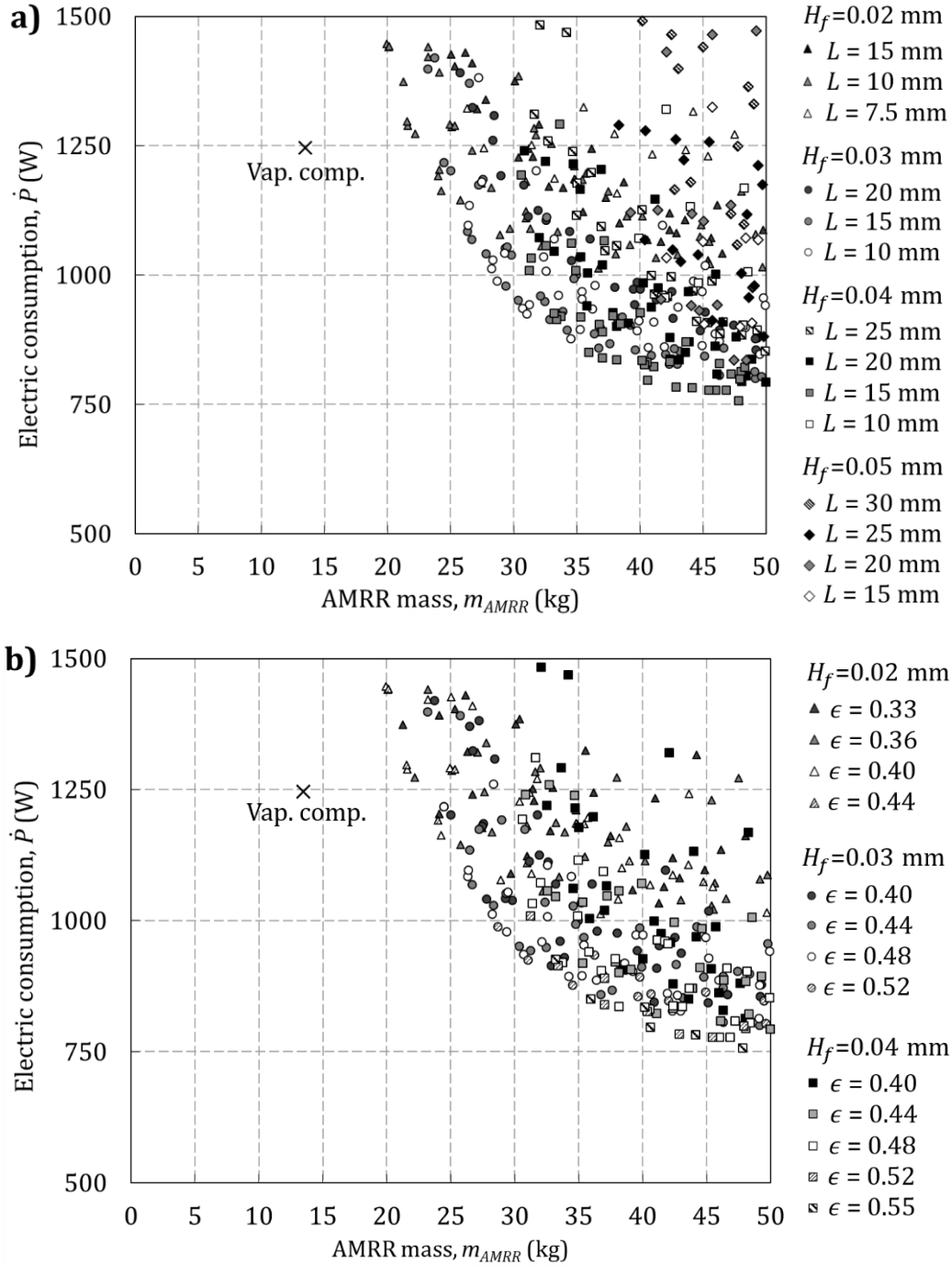
Fig. 6.9. AMRR consumption and mass compared to vapor-compression systems for case S1 as function of a) H_f and L and b) H_f and ϵ.

The trends derived from the results in Fig. 6.5 are confirmed by this detailed parametric study (Fig. 6.9). For the conditions set in this work, **the optimal channel height is found between 0.04 and 0.02 mm, depending on mass or efficiency priority.** The order of magnitude matches the one predicted by Tušek et al. [36] for less demanding conditions, 0.035 to 0.075 mm. **A new result is that the regenerator length has a significant influence in the studied conditions. Thinner channels require shorter regenerator lengths in order to cope with the increase of the pressure drop** (Fig. 6.9a).

The optimal porosity is reduced as the channel height decreases (Fig. 6.9b). For a channel height of 0.02 mm the optimal porosity range was found between 0.33 and 0.44, while channel heights of 0.03 mm work better with a porosity between 0.40 and 0.52. **Therefore, there is an optimum plate thickness between 0.03 and 0.04 mm for all cases.** These results agree with the AMR application range predicted by Kitanovski et al. [1].

In general the cases that minimize both electric consumption and mass were obtained with an AMR frequency of 10 Hz, the maximum considered. The optimal utilization is generally found between 0.5 and 0.8. This settings demand similar magnetic work inputs, however the energy needed to pump the fluid increases as the channel height decreases (Fig. 6.10). Considering the dimensions of the channels, the mentioned values of the working parameters result in **optimal flow rates from 51.5 to 82.16 l min^{-1}** and pressure drops of 0.44 to 2.36 bar. In the upper limit of the pressure drop range, which is produced with the 0.02 mm high channels, the energy consumption of the pump and the electric motor are practically the same. **Compared to the typical values of flow rates in vapor-compression based MAC systems, the ones obtained for AMRRs are significantly higher** in agreement with previous findings [11].
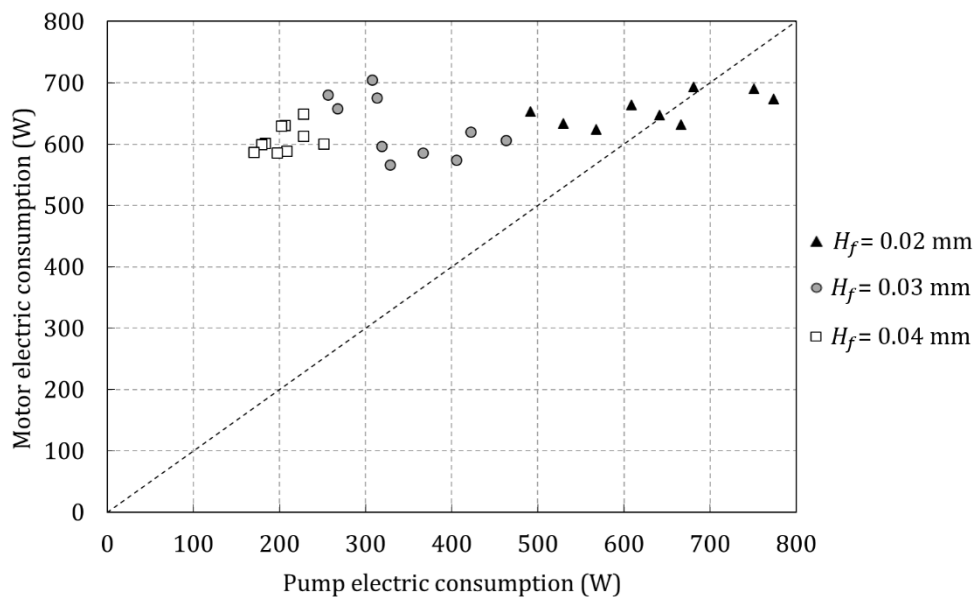
Fig. 6.10. Pump and motor electric consumption of the points in the optimal front as function of H_f.

The compacity of the proposed AMRRs would depend on the physical arrangement of the different parts. If an estimation is made with the obtained mass values, the regenerator would be from 0.33 to 0.81 liters and the magnet assembly, from 2.69 to 6.46 liters.

In summary, Table 6.8 contains the values of the studied parameters that define the points in the optimal front outlined in Fig. 6.9.

Table 6.8. Optimal parallel-plate AMRR features for case S1: 3027 W at 29.4 K span.

Device	m_{AMRR} (kg)	m_r (kg)	$\dot{P}$ (W)	EER (-)	H_f (mm)	ϵ (-)	L (mm)	$\mu_0 H_{app}$ (T)	f (Hz)	φ (-)	$\dot{m}$ (l min^{-1})
S1-1	19.93	1.57	1447	2.09	0.02	0.40	10	1.4	10	0.8	62.50
S1-2	20.10	1.68	1441	2.10	0.02	0.36	10	1.4	10	0.7	58.51
S1-3	21.24	1.84	1374	2.20	0.02	0.33	10	1.4	10	0.6	55.02
S1-4	21.56	1.59	1298	2.33	0.02	0.44	10	1.4	10	0.8	63.44
S1-5	21.59	1.70	1289	2.35	0.02	0.40	10	1.4	10	0.7	59.22
S1-6	22.18	1.85	1272	2.38	0.02	0.36	10	1.4	10	0.6	55.34
S1-7	24.00	1.77	1192	2.54	0.02	0.44	10	1.4	10	0.7	61.78
S1-8	24.25	1.90	1163	2.60	0.02	0.40	10	1.4	10	0.6	57.02
S1-9	25.77	2.15	1144	2.65	0.02	0.36	10	1.4	10	0.5	53.57
S1-10	26.64	1.96	1070	2.83	0.03	0.44	15	1.4	10	0.6	58.77
S1-11	27.80	2.18	1042	2.91	0.03	0.40	15	1.4	10	0.5	54.48
S1-12	28.20	1.94	1013	2.99	0.03	0.48	10	1.4	10	0.8	77.42
S1-13	28.66	1.83	989	3.06	0.03	0.52	10	1.4	10	0.9	82.16
S1-14	29.36	2.02	980	3.09	0.03	0.48	15	1.4	10	0.6	60.46
S1-15	30.33	2.24	952	3.18	0.03	0.44	15	1.4	10	0.5	55.76
S1-16	30.66	2.11	937	3.23	0.03	0.48	10	1.4	10	0.7	73.67
S1-17	31.00	1.98	926	3.27	0.03	0.52	10	1.4	10	0.8	78.99
S1-18	32.84	2.58	915	3.31	0.03	0.40	15	1.4	10	0.4	51.48
S1-19	34.21	2.35	895	3.38	0.03	0.48	15	1.4	10	0.5	58.71
S1-20	34.48	2.20	877	3.45	0.03	0.52	10	1.4	10	0.7	76.88
S1-21	35.94	2.16	851	3.56	0.04	0.55	15	1.4	10	0.7	75.42
S1-22	36.99	2.36	841	3.60	0.04	0.52	15	1.4	10	0.6	70.70
S1-23	38.13	2.62	837	3.62	0.04	0.48	15	1.4	10	0.5	65.45
S1-24	40.53	2.79	832	3.64	0.04	0.48	15	1.4	8	0.6	66.77
S1-25	40.56	2.44	797	3.80	0.04	0.55	15	1.4	10	0.6	72.96
S1-26	42.84	2.73	784	3.86	0.04	0.52	15	1.4	10	0.5	68.23
S1-27	44.09	2.65	783	3.87	0.04	0.55	15	1.4	8	0.7	74.03
S1-28	45.43	2.90	778	3.89	0.04	0.52	15	1.4	8	0.6	69.46
S1-29	47.78	2.87	757	4.00	0.04	0.55	15	1.4	10	0.5	71.62

6.5.3   Case S2: 2803 W at 34.8 K span

The detailed parametric study (fourth column of Table 6.7) was partially repeated with the working conditions and the AMR bed composition determined for the case S2 (Table 6.4) (486 simulations). The relevant results are shown in Fig. 6.11.
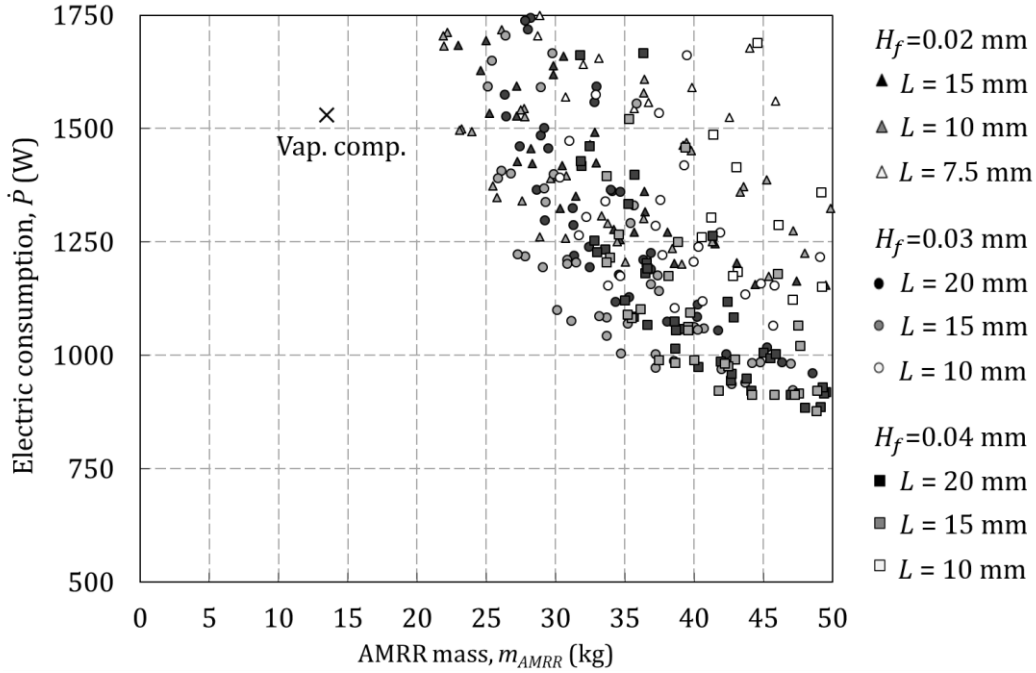
Fig. 6.11. AMRR consumption and mass compared to vapor-compression systems for case S2 as function of H_f and L.

The trends observed are very similar to the ones found in the previous case (Fig. 6.9). The optimal dimensions of the channels are the same, as well the working frequency. The optimal utilization ranges between 0.4 and 0.7. Table 6.9 contains the combinations of parameters that define the optimal front in Fig. 6.11.

Table 6.9. Optimal parallel-plate AMRR features for case S2: 2803 W at 34.8 K span.

Device	m_{AMRR} (kg)	m_r (kg)	$\dot{P}$ (W)	EER (-)	H_f (mm)	ϵ (-)	L (mm)	$\mu_0 H_{app}$ (T)	f (Hz)	φ (-)	$\dot{m}$ (l min⁻¹)
S2-1	23.23	1.83	1500	1.87	0.02	0.40	10	1.4	10	0.7	65.84
S2-2	25.49	1.88	1373	2.04	0.02	0.44	10	1.4	10	0.7	67.77
S2-3	25.79	2.03	1347	2.08	0.02	0.40	10	1.4	10	0.6	62.64
S2-4	27.26	1.88	1224	2.29	0.03	0.48	15	1.4	10	0.7	67.66
S2-5	27.77	2.05	1219	2.30	0.03	0.44	15	1.4	10	0.6	63.28
S2-6	29.03	2.28	1196	2.34	0.03	0.40	15	1.4	10	0.5	58.77
S2-7	30.07	2.07	1100	2.55	0.03	0.48	15	1.4	10	0.6	63.98
S2-8	31.11	2.29	1077	2.60	0.03	0.44	15	1.4	10	0.5	59.08
S2-9	33.66	2.64	1043	2.69	0.03	0.40	15	1.4	10	0.4	54.50
S2-10	34.70	2.39	1005	2.79	0.03	0.48	15	1.4	10	0.5	61.51
S2-11	37.19	2.74	973	2.88	0.03	0.44	15	1.4	10	0.4	56.51
S2-12	41.78	2.51	923	3.04	0.04	0.55	15	1.4	10	0.6	77.64
S2-13	44.16	2.82	914	3.07	0.04	0.52	15	1.4	10	0.5	72.66
S2-14	45.77	2.75	913	3.07	0.04	0.55	15	1.4	8	0.7	79.38
S2-15	47.99	3.06	886	3.16	0.04	0.52	20	1.4	10	0.4	63.16
S2-16	48.85	2.94	878	3.19	0.04	0.55	15	1.4	10	0.5	75.64

6.5.4 Comparison of summer design points

Fig. 6.12a shows the optimal AMRR mass-consumption fronts for both studied summer design points, S1 ($\dot{Q}_c$=3.03 kW at ΔT_{span}=29.4 K, Table 6.8) and S2 ($\dot{Q}_c$=2.80 kW at ΔT_{span}=34.8 K, Table 6.9). In terms of AMRR performance, the decrease of the cooling demand by 7.4% achieved with the reduction of the auxiliaries' load in case S2 does not compensate for the increase of ΔT_{span} by 5.5 K caused by the corresponding reduction of the air flow rate.

However, achieving the working conditions of case S1 requires a larger power demand by the blowers (Table 6.4). The rest of the auxiliaries' settings remained the same. When the consumption of the blowers is added to the one of the AMRR, case S2 results globally more efficient (Fig. 6.12b). As the specific cooling power of the AMRR increases, the AMRR becomes relatively more inefficient and from a certain point on the total energy consumption of case S2 is larger than the one of case S1.
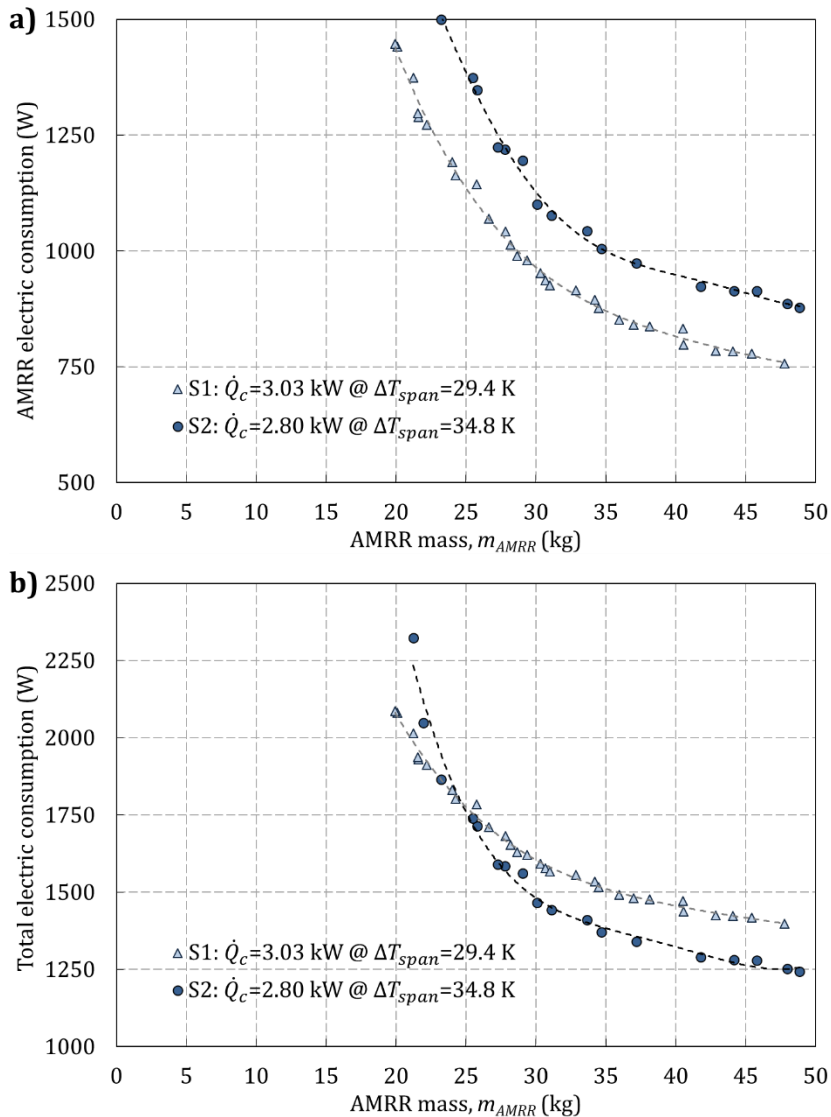
Fig. 6.12. Electric consumption and AMRR mass for the summer design points. a) Consumption of the AMRR. b) Consumption of the AMRR and the blowers.

6.6 Heating performance

The parametric studies conducted in the former section defined a series of AMRRs that can optimally fulfill the cooling requirements of the vehicle. The MCMs in these AMRRs were selected to work in temperature ranges that correspond to summer climatic conditions. Each of these devices is defined by the applied magnetic field, the dimensions of the regenerator and the total mass of MCM, which determines the number of plates.

In this section, the heating performance of these devices is calculated. Note that, although the temperature range in this new case corresponds to winter conditions, the AMR bed composition remains unchanged. The mass of MCMs is also fixed and will determine the total heating power provided by the device (Eq. 6.5).

In order to simulate the heating mode, the hot (T_H) and cold (T_C) end temperatures were set to the winter values specified in Table 6.4. Simulations were carried out with the design parameters defined in Table 6.8 and Table 6.9. In these tables each row defines a different AMRR. For each AMRR, the working parameters were varied in the ranges f=[2,10] and φ=[0.2,1] in order to find the working point that provides the target heating capacity of both W1 and W2 design conditions with minimum electric consumption (839 simulations).

Fig. 6.13 shows the optimal results obtained in terms of AMRR mass and electric consumption. The cooling performance of the analyzed devices has been included for reference. As explained above, each of these points represents a different AMRR which is defined by an AMRR mass value. Therefore, the points with the same AMRR mass correspond to different operation points of a same device.

Fig. 6.13a contains the heating performance of the devices defined for S1 design conditions (Table 6.8). Most of these devices could not achieve the target heating capacity considering the maximum operating frequency of this study (f=10). The 6 devices that can reach the target capacity demand a minimum electric consumption when operating at a frequency of 10 Hz and a utilization between 0.7 and 0.9. Oppositely to the vapor-compression device, the AMRRs optimized for case S1 consume more in winter working conditions than in summer ones. The reason is that, despite that the heating demand is significantly lower than the cooling one, the regenerator is operating far from the Curie temperatures of the MCMs selected. In these regions the MCE is significantly lower and hence both the specific capacity and the efficiency of the AMRR decrease.

Similarly, Fig. 6.13b shows the results obtained with the **AMRRs defined for S2 design conditions** (Table 6.9). This set **included MCMs with a wider range of Curie temperatures**, and hence significantly **better winter performances** have been obtained. In fact most devices could reach both target heating demands with an **electric consumption comparable to that of the vapor-compression device**. To do so, both the frequency and the utilization must be regulated.
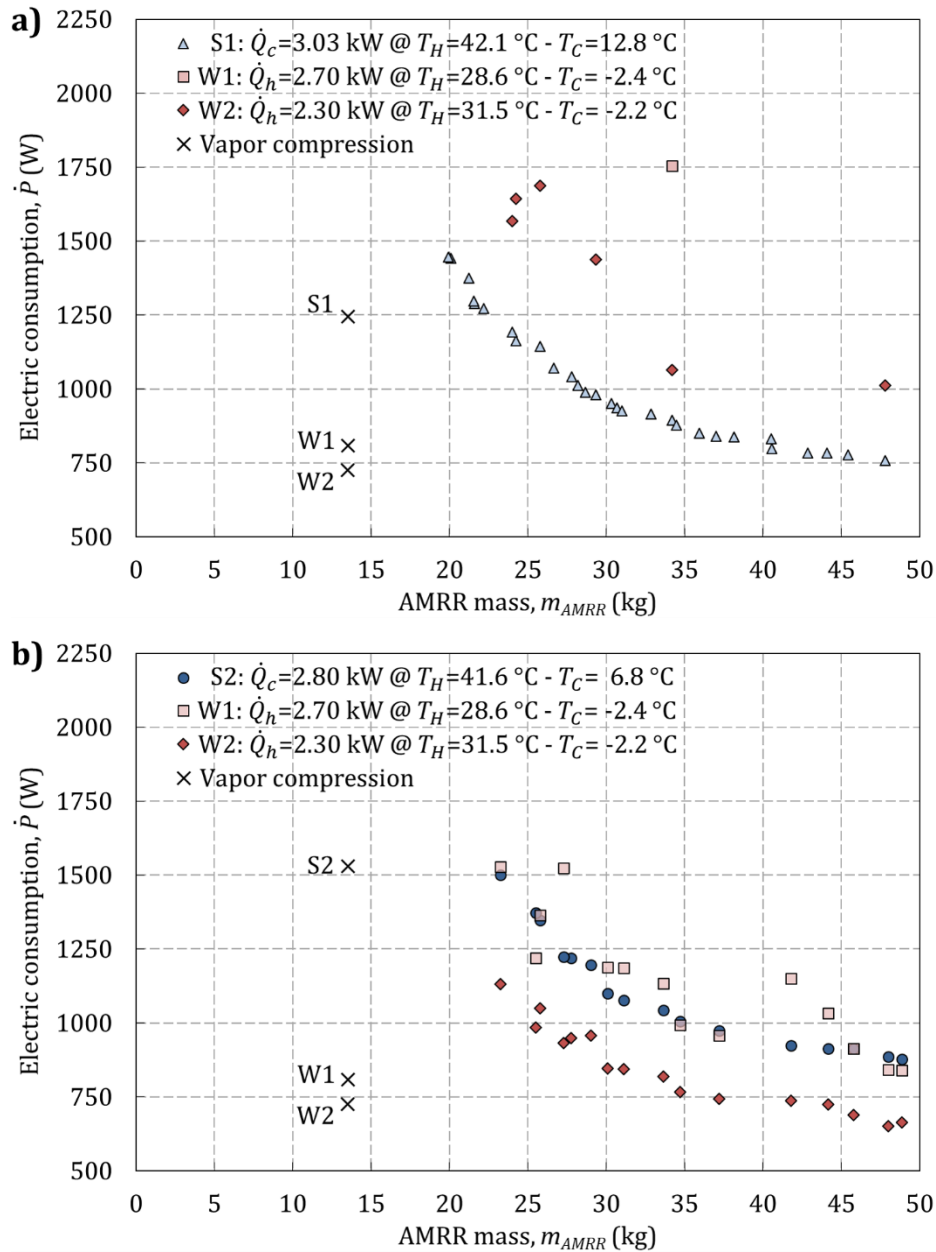
Fig. 6.13. Electric consumption in cooling and heating mode of the AMRR devices that optimally fulfil a) S1 design conditions and b) S2 design conditions.

For instance Fig. 6.14 shows the performance map of the device S2-5 (Table 6.9), under W2 conditions. A target part load heating capacity can be obtained with several combinations of the operating parameters f and φ. However each of these combinations yields a different COP. **In the plotted region, f should be maximized while φ is regulated in order to achieve a maximum COP and hence a minimum electric consumption.** This trend was generally observed in all the studied cases.
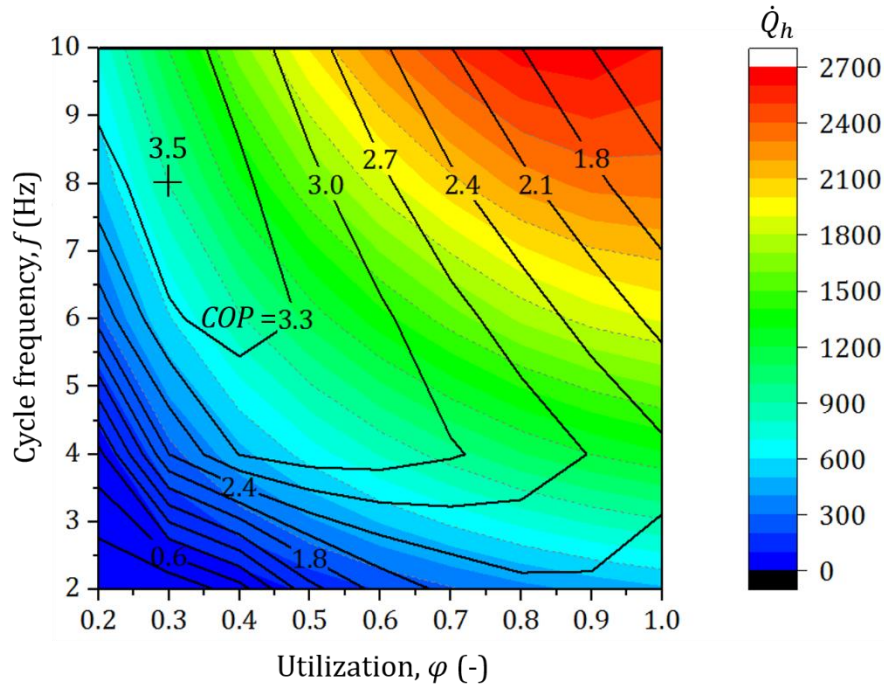
Fig. 6.14. Heating performance map of case S2-5, as function of f and φ.

Finally, Fig. 6.15 compares all the winter cases in terms of global energy consumption, that is, considering the consumption of the blowers. On the contrary to the summer cases, in case W2 the 14.7% savings in the heating demand achieved with the reduction in the ventilation load did compensate for the 2.8 K increase in the temperature span in all cases (Fig. 6.13), despite the MCMs were not adapted to the winter working temperatures. Since these working conditions were realized with less power demand by the blowers, case W2 results even more efficient in global terms than case W1 if the devices with the same composition are compared.
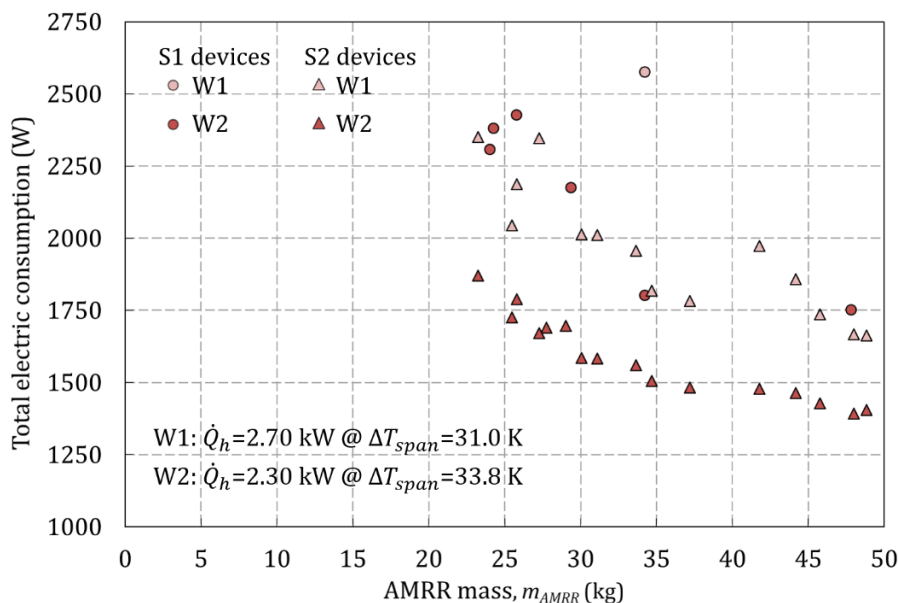
Fig. 6.15. Electric consumption in heating mode of the AMRR devices and the blowers.

Chapter 7

Conclusions

7.1 On the AMR model

A dynamic 1D model of a parallel-plate active magnetic regenerator (AMR) has been developed in collaboration with DTU Energy. **The model relies on a new computationally efficient numerical scheme and includes a detailed description of the main physical phenomena that affect the AMR performance.** As a novelty in 1D AMR models literature, the present model includes the spatial and time dependence of the demagnetizing field, the fluid flow maldistribution, the time dependence of the inlet temperatures to the AMR due to the ambient losses and a methodological approach for implementing the experimental properties of the magnetocaloric material (MCMs).

The new numerical scheme has been adapted to the main physical phenomena that occur in the parallel-plate AMR bed. The effect of the thermal conduction of the fluid along the fluid path was demonstrated negligible in typical AMR applications, which has enabled the explicit discretization of the fluid equation and hence the use of a time step as large as CFL=1. In order to guarantee the consistency of the model with relatively large time steps, the MCM properties are calculated as function of the mean temperature of the regenerator during the time step.

The present 1D AMR model has been thoroughly validated along several stages and procedures. The detailed characterization of the experimental device, especially with regard to the magnetocaloric properties, has been a key to obtain a good agreement with the experimental cases.

Firstly, the model was verified against several **passive regenerator cases with an analytic solution. Extremely accurate results** have been obtained. Compared to the widely employed fully implicit scheme, the new hybrid explicit-implicit scheme (HEIS) prevents numerical diffusion and oscillations, achieving conservation and

monotonicity with less computational effort. The **simulation time is reduced by 88%** while preserving or even improving the accuracy of the numerical solution.

In a second stage, the model was validated against experimental results of a **single-blow passive regenerator test** with the purpose of analyzing the conjugate heat transfer performance regardless of the other phenomena in the AMR bed. The fluid flow maldistribution due to the different channel heights in the analyzed regenerator has a significant detrimental effect in the heat transfer performance. In the limit of relatively thick plates and low thermal conductivity, the thermal cross connection between the channels may be neglected. Therefore, **the fluid flow maldistribution effect was included in the 1D model** by computing the mean outlet temperature of the isolated channels. With this approach, the standard Nusselt correlations for rectangular channels provided a **very good agreement with the experiments**, validating thus the former simplification in the studied working conditions.

Finally, the model was compared to a series of **AMR experiments** with the aim of studying the influence of the implemented physical phenomena under a wide range of operating conditions. **The model reproduces very well the variation of the three main control parameters of the system** (hot inlet temperature, fluid flow rate and utilization). Although the model tends to overpredict the no-load temperature span between both ends of the regenerator, the error is in most cases of the order of magnitude of the experimental uncertainty, around 1 K.

The simulation time with the present model is short compared to existing models. In a personal computer, the full model simulates AMR cycles of 5.60 and 16.32 s in 0.39 to 0.62 s per channel.

A **detailed analysis** has been performed on the effect in the AMR simulation results of the **newly included physical phenomena. Certain simplifications have been verified.**

The value of the internal magnetic field is influenced by the spatial dependence of the average demagnetization factor (N_{avg}). On the contrary, the variation of the regenerator temperature along the AMR cycle has a limited effect. In any case, the impact of these phenomena in the AMR performance results is negligible in the analyzed setup. Therefore, **the AMR model can be simplified by calculating the internal magnetic field at the beginning of the simulation based on a linear temperature profile and a mean value of N_{avg},** as proposed in [79]. This simplification yields 25% savings in computation time.

The entrance effect is not significant in the global performance of the AMR so it could be neglected in the studied conditions. **Fully developed flow between parallel plates can be assumed with a maximum deviation in the simulation results of 5%.**

The **degradation of the heat transfer performance due to the flow maldistribution is significant and depends on the fluid velocity** as expected

from the previous results. **A new finding is that this detrimental effect increases with the fluid displacement.**

Finally, **the variation of the temperature in the cold reservoir due to the ambient losses can have a significant effect, so it should be included in the model.**

7.2 On the MAC system model

A simulation tool to assess the performance of mobile air-conditioning (MAC) systems under dynamic conditions has been developed in the frame of the European Project ICE. The model calculates the spatial mean temperature in the cabin of the vehicle and the electric consumption of the MAC system, given the external conditions and the control settings as function of time.

The global vehicle model is dynamic, flexible, comprehensive, fast and accurate. It is a modular model which includes the thermal models of the main components of the MAC system, namely the cabin, the hydraulic loops with the coolant-to-air heat exchangers, the electrical auxiliaries and an interface for including a refrigerator. **The methodology followed to model these components, based in conservation equations and global heat transfer coefficients fitted to relatively simple experiments, has provided excellent validation results under a wide range of working conditions** as detailed below.

The cabin model presents several new features with respect to published lumped-parameter models, which are the division of the cabin in two thermal zones, the consideration of all the main heat gains including the electric auxiliaries and the computation of both the thermal inertia of the cabin body and the internal masses. The model has been successfully validated against experiments under variable ambient conditions, with and without solar radiation.

The coolant-to-air heat exchangers model simulates both the cooling and heating modes, including partially wet working conditions. A semi-empirical methodology for fitting a single everywhere correlation for the global heat transfer coefficient (UA) has been developed, based on the experimental characterization of the device. The obtained correlation predicts the experimental heat transfer rate in both cooling and heating modes within 10% error. The temperature difference across the heat exchanger is reproduced with an error up to 1.5 K in the air side and 0.5 K in the coolant side.

7.3 On the application of AMRRs in MAC systems

The application of AMR refrigerators (AMRR) in MAC systems has been analyzed and compared to the features of the current vapor-compression technology. A broad **optimization study** comprising 6,581 simulations has been performed with the purpose of determining the parallel-plate **AMRR design and working parameters that fulfil the cooling requirements of a full electric minibus with minimum combined mass and electric consumption**. The combination of parameters and the range of values covered is new in the literature. Another significant novelty is the **analysis of the heating performance** of the resulting optimal devices with 839 additional simulations.

Firstly, the MAC system model was employed to determine the cooling and heating requirements of an electric minibus. The air flow rate through the heat exchangers inside the cabin has a significant influence in the definition of the design point. Increasing the air mass flow rate reduces the temperature span between the two sides of the refrigerator (ΔT_{span}), but increases the auxiliaries and ventilation loads, as well as the electric consumption of the blowers. In order to evaluate globally the energy consumption of the MAC system, two design points have been defined for each working mode depending on the settings of the blowers. The cooling requirements are 3 kW at ΔT_{span} =30 K or 2.8 kW at ΔT_{span} =35 K. The heating requirements are 2.7 kW at ΔT_{span} =31 K or 2.3 kW at ΔT_{span} =34 K.

In a second stage, the composition of the AMR bed was adapted to the working temperatures determined for cooling mode following a nearly-optimal approach. A graded bed made of 4 layers of Gd-like magnetocaloric materials (MCM) with tuned Curie temperatures has been considered. An interesting finding is that adding more MCM layers does not enhance further the AMR performance in the studied conditions.

Once the thermal requirements and the composition of the AMR were determined, the optimization study was carried out with the AMR model. The optimal AMRR has a channel height between 0.02 and 0.04 mm, depending on mass or efficiency priority respectively, and a plate height between 0.03 and 0.04 mm. The optimal regenerator length decreases with the channel height due to the effect of the pressure drop and is found between 10 and 20 mm. The optimal applied field is 1.4 T, the maximum considered according to the characteristics of current permanent magnets. With respect to the operating parameters, the optimal operating cycle frequency is 10 Hz, the maximum studied according to the features of current rotary AMRRs, while the optimal utilization is in between 0.5 and 0.8. The corresponding optimal flow rate range from 50 to 80 l min^{-1}.

The two proposed cooling design points have been compared considering the global electric consumption, that is, the sum of the AMRR and the blowers. **As the efficiency of the refrigerator increases, the electric consumption of the**

blowers becomes more relevant. In order to determine the design that minimizes the total energy consumption of MAC systems, all the components must be taken into account.

Finally, the heating performance of the optimal AMRR designs was analyzed. Consequently with the MCMs selected, the AMRRs sized to meet the T_H=42 °C - T_C=13 °C case in cooling mode could generally not reach the heating requirements at T_H≈30 °C - T_C≈-2 °C. However the AMRRs sized for the T_H=42 °C - T_C=7 °C cooling mode case could work successfully also in heating mode.

With the obtained designs, the AMRR would weigh between 20 and 50 kg and would work with an EER from 2 to 4 and a COP from 2 to 3.5. Hence the AMRR would work with a similar efficiency as current vapor-compression systems. However the mass of the AMRR would probably be from 1.3 to 3 times larger, with a consequent overconsumption of the vehicle. The optimal coolant flow rates in the AMRR system would be considerably high, from 3 and up to 10 times larger than in the vapor-compression system.

7.4 Future work

The latest AMRR prototypes can achieve high cycle frequencies, which affects the conjugate heat transfer in the AMR. In order to study the AMR behavior with the 1D model in these conditions, a Nusselt number correlation for unsteady reciprocating flow should be developed. Other interesting studies about the AMR performance can be systematic analyses of the influence of the fluid displacement in detrimental effect of the fluid flow maldistribution and of the effect of variable inlet temperatures to the AMR.

A relevant new feature in the MAC system model would be the inclusion of a dynamic model of the thermal management system of the powertrain and the batteries. The calculation of the thermal load due to the demisting and defrosting of windows would be an interesting new output. Additionally, the study of the performance of the heat exchangers in frosting conditions would improve the simulation results in winter conditions.

Regarding the application of magnetic refrigerators in MAC systems, the optimization study could be repeated considering better actual MCMs, for both summer and winter working modes. In order to do so, an accurate characterization of the MCMs is required. Other future works can address the specific design of the hydraulic loops for AMRR-based MAC systems and the determination of the global impact of these systems in the energy consumption of the vehicle.

References

[1]   A. Kitanovski, J. Tušek, U. Tomc, U. Plaznik, M. Ozbolt, A. Poredoš, *Magnetocaloric Energy Conversion From Theory to Applications*, 1st ed., Springer, 2015.

[2]   ICE Project FP7, GC-SST.2010.7-2, Grant Agreement no 265434, www.ice-mac-ev.eu, 2014.

[3]   *EU energy in figures. Statistical pocketbook 2014*, 2014.

[4]   R.B. Farrington, J.P. Rugh, *Impact of Vehicle Air-Conditioning on Fuel Economy, Tailpipe Emissions and Electric Vehicle Range*, NREL Report, 2000.

[5]   J.T. Lee, S.K. Kwon, Y.S. Lim, M.S. Chon, D.S. Kim, Effect of Air-Conditioning on Driving Range of Electric Vehicle for Various Driving Modes, *SAE Tech. Pap.* 2013-01-00 (2013).

[6]   D. Bharathan, L. Chaney, R.B. Farrington, J. Lustbader, M. Keyser, J. Rugh, An Overview of Vehicle Test and Analysis from NREL ' s A / C Fuel Use Reduction Research, in: *Veh. Therm. Manag. Syst. Conf. Exhib.*, Nottingham, England, 2007.

[7]   M. Eisele, *Transient performance evaluation of automotive secondary loop systems*, University of Maryland, 2012.

[8]   J.A. Barclay, W.A. Steyert, *Active magnetic regenerator*, 1982.

[9]   A. Kitanovski, U. Plaznik, J. Tušek, A. Poredoš, New thermodynamic cycles for magnetic refrigeration, *Int. J. Refrig.* 37 (2014) 28–35.

[10]   C.B. Zimm, Magnetic Refrigerator: Design and Performance, in: *Encycl. Mater. Sci. Technol.*, 2nd ed., Elsevier, 2008: pp. 1–5.

[11]   K. Engelbrecht, *A Numerical Model of an Active Magnetic Regenerator Refrigerator with Experimental Validation*, University of Wisconsin-Madison, 2008.

[12]   L. von Moss, *Hysteresis in Magnetocaloric Materials. An experimental and modelling approach*, Technical University of Denmark, 2014.

[13]   A. Rowe, A. Tura, Experimental investigation of a three-material layered active magnetic regenerator, *Int. J. Refrig.* 29 (2006) 1286–1293.

[14]   C. Zimm, A. Boeder, J. Chell, A. Sternberg, A. Fujita, S. Fujieda, K. Fukamichi, Design and performance of a permanent-magnet rotary refrigerator, *Magn. Refrig. Room Temp.* 29 (2006) 1302–1306.

[15]   J. Tušek, A. Kitanovski, U. Tomc, C. Favero, A. Poredoš, Experimental comparison of multi-layered La–Fe–Co–Si and single-layered Gd active magnetic regenerators for use in a room-temperature magnetic refrigerator, *New Dev. Magn. Refrig.* 37 (2014) 117–126.

[16]   J. Lozano, *Designing a Rotary Magnetic Refrigerator*, Federal University of Santa Catarina, 2015.

[17]   V.K. Pecharsky, K.A. Gschneidner, Advanced magnetocaloric materials: What does the future hold?, *Int. J. Refrig.* 29 (2006) 1239–1249.

[18]   K. Engelbrecht, C.R.H. Bahl, Evaluating the effect of magnetocaloric properties on magnetic refrigeration performance, *J. Appl. Phys.* 108 (2010) 123918.

[19]   K.K. Nielsen, K. Engelbrecht, The influence of the solid thermal conductivity on active magnetic regenerators, *J. Phys. D. Appl. Phys.* 45 (2012) 145001.

[20]   S.Y. Dan'kov, A.M. Tishin, V.K. Pecharsky, K.A. Gschneidner Jr., Magnetic phase transitions and the magnetothermal properties of gadolinium, *Phys. Rev. B.* 57 (1998) 3478–3490.

[21]   R. Bjørk, C.R.H. Bahl, M. Katter, Magnetocaloric properties of LaFe13−x−yCoxSiy and commercial grade Gd, *J. Magn. Magn. Mater.* 322 (2010) 3882–3888.

[22]   V.K. Pecharsky, K.A. Gschneidner Jr, Magnetocaloric effect and magnetic refrigeration, *J. Magn. Magn. Mater.* 200 (1999) 44–56.

[23]   T. V. Jayaraman, L. Boone, J.E. Shield, Near room temperature magnetic entropy changes in as-cast Gd100−xMnx (x=0, 5, 10, 15, and 20at.%) alloys, *J. Alloys Compd.* 509 (2011) 1411–1417.

[24]   J. Kaštil, P. Javorský, J. Kamarád, E. Šantavá, Magnetocaloric effect of Gd–Tb alloys: influence of the sample shape anisotropy, *Appl. Phys. A.* 104 (2010) 205–209.

[25]   K.A. Gschneidner Jr, V.K. Pecharsky, A. Tsokol, Recent developments in magnetocaloric materials, *Reports Prog. Phys.* 68 (2005) 1479–1539.

[26]   V.K. Pecharsky, K.A. Gschneidner, Jr., Giant Magnetocaloric Effect in Gd 5 (Si 2 Ge 2), *Phys. Rev. Lett.* 78 (1997) 4494–4497.

[27]   A. Smith, C.R.H. Bahl, R. Bjørk, K. Engelbrecht, K.K. Nielsen, N. Pryds, Materials Challenges for High Performance Magnetocaloric Refrigeration Devices, *Adv. Energy Mater.* 2 (2012) 1288–1318.

[28]   J. Liu, Optimizing and fabricating magnetocaloric materials, *Chinese Phys. B.* 23 (2014) 047503.

[29]   A.M. Tishin, Y.I. Spichkin, *The Magnetocaloric Effect and its Applications,*

CRC Press, 2003.

[30]   G. V. Brown, Magnetic heat pumping near room temperature, *J. Appl. Phys.* 47 (1976) 3673.

[31]   K. Halbach, Design of permanent multipole magnets with oriented rare earth cobalt material, *Nucl. Instruments Methods.* 169 (1980) 1–10.

[32]   R. Bjørk, K. Engelbrecht, The influence of the magnetic field on the performance of an active magnetic regenerator (AMR), *Int. J. Refrig.* 34 (2011) 192–203.

[33]   C.R.H. Bahl, T.F. Petersen, N. Pryds, A. Smith, A versatile magnetic refrigeration test device, *Rev. Sci. Instrum.* 79 (2008) 93906.

[34]   D. Eriksen, K. Engelbrecht, C.R.H. Bahl, R. Bjørk, K.K. Nielsen, A.R. Insinga, N. Pryds, Design and experimental tests of a rotary active magnetic regenerator prototype, *Int. J. Refrig.* 58 (2015) 14–21.

[35]   J. Wu, C. Liu, P. Hou, Y. Huang, G. Ouyang, Y. Chen, Fluid choice and test standardization for magnetic regenerators operating at near room temperature, *Int. J. Refrig.* 37 (2014) 135–146.

[36]   J. Tušek, A. Kitanovski, A. Poredoš, Geometrical optimization of packed-bed and parallel-plate active magnetic regenerators, *Int. J. Refrig.* 36 (2013) 1456–1464.

[37]   T. Lei, K. Engelbrecht, K.K. Nielsen, C.T. Veje, Study of geometries of active magnetic regenerators for room temperature magnetocaloric refrigeration, *Appl. Therm. Eng.* (2015).

[38]   B. Torregrosa-Jaime, J. Payá, J.M. Corberán, Application of magnetic cooling in electric vehicles, *Sci. Technol. Built Environ.* (2016).

[39]   K.K. Nielsen, K. Engelbrecht, C.R.H. Bahl, The influence of flow maldistribution on the performance of inhomogeneous parallel plate heat exchangers, *Int. J. Heat Mass Transf.* 60 (2013) 432–439.

[40]   J.B. Jensen, *Non-Uniform Heat Transfer in Thermal Regenerators*, Technical University of Denmark, 2011.

[41]   A. Tura, K.K. Nielsen, A. Rowe, Experimental and modeling results of a parallel plate-based active magnetic regenerator, *Int. J. Refrig.* 35 (2012) 1518–1527.

[42]   D. V Christensen, K.K. Nielsen, C.R.H. Bahl, A. Smith, Demagnetizing effects in stacked rectangular prisms, *J. Phys. D. Appl. Phys.* 44 (2011) 215004.

[43]   R. Bjørk, C.R.H. Bahl, Demagnetization factor for a powder of randomly packed spherical particles, *Appl. Phys. Lett.* 103 (2013) 102403.

[44]   J. Tušek, A. Kitanovski, S. Zupan, I. Prebil, A. Poredoš, A comprehensive experimental analysis of gadolinium active magnetic regenerators, *Appl. Therm. Eng.* 53 (2013) 57–66.

[45] K.K. Nielsen, A. Smith, C.R.H. Bahl, U.L. Olsen, The influence of demagnetizing effects on the performance of active magnetic regenerators, *J. Appl. Phys.* 112 (2012) 94905.

[46] J.A. Lozano, K. Engelbrecht, C.R.H. Bahl, K.K. Nielsen, D. Eriksen, U.L. Olsen, J.R. Barbosa Jr., A. Smith, A.T. Prata, N. Pryds, Performance analysis of a rotary active magnetic refrigerator, *Appl. Energy.* 111 (2013) 669–680.

[47] S. Jacobs, J. Auringer, A. Boeder, J. Chell, L. Komorowski, J. Leonard, S. Russek, C. Zimm, The performance of a large-scale rotary magnetic refrigerator, *Int. J. Refrig.* 37 (2014) 84–91.

[48] A. Tura, A. Rowe, Permanent magnet magnetic refrigerator design and experimental characterization, *Int. J. Refrig.* 34 (2011) 628–639.

[49] K. Engelbrecht, D. Eriksen, C.R.H. Bahl, R. Bjørk, J. Geyti, J.A. Lozano, K.K. Nielsen, F. Saxild, A. Smith, N. Pryds, Experimental results for a novel rotary active magnetic regenerator, *Int. J. Refrig.* 35 (2012) 1498–1505.

[50] J.A. Lozano, K. Engelbrecht, C.R.H. Bahl, K.K. Nielsen, J.R. Barbosa Jr., A.T. Prata, N. Pryds, J.R. Barbosa, A.T. Prata, N. Pryds, Experimental and numerical results of a high frequency rotating active magnetic refrigerator, *Int. J. Refrig.* 37 (2014) 92–98.

[51] C.R.H. Bahl, K. Engelbrecht, D. Eriksen, J.A. Lozano, R. Bjørk, J. Geyti, K.K. Nielsen, A. Smith, N. Pryds, Development and experimental results from a 1 kW prototype AMR, *Int. J. Refrig.* 37 (2014) 78–83.

[52] C. Aprea, A. Greco, A. Maiorino, R. Mastrullo, A. Tura, Initial experimental results from a rotary permanent magnet magnetic refrigerator, *Int. J. Refrig.* 43 (2014) 111–122.

[53] C. Aprea, A. Greco, A. Maiorino, C. Masselli, The energy performances of a rotary permanent magnet magnetic refrigerator, *Int. J. Refrig.* 61 (2016) 1–11.

[54] C. Aprea, A. Greco, A. Maiorino, GeoThermag: a geothermal magnetic refrigerator, *Int. J. Refrig.* 59 (2015) 75–83.

[55] K.L. Engelbrecht, G.F. Nellis, S.A. Klein, Predicting the performance of an active magnetic regenerator refrigerator used for space cooling and refrigeration, *HVAC R Res.* 12 (2006) 1077–1095.

[56] R. Bjørk, C.R.H. Bahl, K.K. Nielsen, The lifetime cost of a magnetic refrigerator, *Int. J. Refrig.* (2015).

[57] B. Monfared, R. Furberg, B. Palm, Magnetic vs. vapor-compression household refrigerators: A preliminary comparative life cycle assessment, *Int. J. Refrig.* 42 (2014) 69–76.

[58] B. Torregrosa-Jaime, C. Vasile, M. Risser, C. Muller, J. Corberan, J. Payá, Application of Magnetocaloric Heat Pumps in Mobile Air-Conditioning, *SAE Int. J. Passeng. Cars - Mech. Syst.* 6 (2013) 520–528.

[59]   U.L. Olsen, C.R.H. Bahl, K. Engelbrecht, K.K. Nielsen, Y. Tasaki, H. Takahashi, Modeling of in-vehicle magnetic refrigeration, *Int. J. Refrig.* 37 (2014) 194–200.

[60]   C.R.H. Bahl, Developing a magnetocaloric domestic heat pump, in: *6th Int. Conf. Magn. Refrig. Room Temp. (Thermag VI). Proc. Victoria, Canada, Sept. 7-10, 2014.*, International Institute of Refrigeration, 2014: p. LP1571.

[61]   A. Tura, A. Rowe, Concentric Halbach cylinder magnetic refrigerator cost optimization, *Int. J. Refrig.* 37 (2014) 106–116.

[62]   B. Torregrosa-Jaime, *Modelado y análisis de un sistema de aire acondicionado para vehículos basado en la refrigeración magnética*, Universitat Politècnica de València, 2011.

[63]   T. Suzuki, K. Ishii, Air Conditioning System for Electric Vehicle, *SAE Tech. Pap.* (1996) 960688.

[64]   C. Kowsky, E. Wolfe, L. Leitzel, F. Oddi, Unitary HPAC system, *SAE Int. J. Passeng. Cars - Mech. Syst.* 5 (2012) 1016–1025.

[65]   B. Torregrosa-Jaime, F. Bjurling, J.M. Corberán, F. Di Sciullo, J. Payá, Transient thermal model of a vehicle's cabin validated under variable ambient conditions, *Appl. Therm. Eng.* 75 (2015) 45–53.

[66]   F. Bjurling, J.M. Corberán, J. Payá, B. Torregrosa-Jaime, Control strategies for the air-conditioning in electric vehicles, in: A. Coronas, J.C. Bruno (Eds.), *Av. En Ciencias Y Técnicas Del Frío VII Libr. Actas*, Tarragona, Spain, 2014: pp. 769–777.

[67]   Z. Qi, Advances on air conditioning and heat pump system in electric vehicles – A review, *Renew. Sustain. Energy Rev.* 38 (2014) 754–764.

[68]   D. Leighton, Combined Fluid Loop Thermal Management for Electric Drive Vehicle Range Improvement, *SAE Int. J. Passeng. Cars - Mech. Syst.* 8 (2015) 711–720.

[69]   K.K. Nielsen, J. Tusek, K. Engelbrecht, S. Schopfer, A. Kitanovski, C.R.H. Bahl, A. Smith, N. Pryds, A. Poredos, Review on numerical modeling of active magnetic regenerators for room temperature applications, *Int. J. Refrig.* 34 (2011) 603–616.

[70]   T. Burdyny, A. Rowe, Simplified modeling of active magnetic regenerators, *Int. J. Refrig.* 36 (2013) 932–940.

[71]   C. Aprea, A. Greco, A. Maiorino, A numerical analysis of an active magnetic regenerative refrigerant system with a multi-layer regenerator, *Energy Convers. Manag.* 52 (2011) 97–107.

[72]   L. Zhang, S.A. Sherif, T.N. Veziroglu, J.W. Sheffield, Second law analysis of active magnetic regenerative hydrogen liquefiers, *Cryogenics (Guildf).* 33 (1993) 667–674.

[73]   A.M. Rowe, J.A. Barclay, Ideal magnetocaloric effect for active magnetic regenerators, *J. Appl. Phys.* 93 (2003) 1672.

[74]   A. Kitanovski, P.W. Egolf, Application of magnetic refrigeration and its assessment, *J. Magn. Magn. Mater.* 321 (2009) 777–781.

[75]   P.A. Oliveira, P. V Trevizoli, J.R. Barbosa Jr., A.T. Prata, A 2D hybrid model of the fluid flow and heat transfer in a reciprocating active magnetic regenerator, *Int. J. Refrig.* 35 (2012) 98–114.

[76]   C. Aprea, A. Greco, A. Maiorino, C. Masselli, A Comparison Between Rare Earth And Transition Metals Working As Magnetic Materials In An Amr Refrigerator In The Room Temperature Range, *Appl. Therm. Eng.* 91 (2015) 767–777.

[77]   B.M. Siddikov, B.A. Wade, D.H. Schultz, Numerical simulation of the active magnetic regenerator, *Comput. Math. with Appl.* 49 (2005) 1525–1538.

[78]   G. Tagliafico, F. Scarpa, F. Canepa, A dynamic 1-D model for a reciprocating active magnetic regenerator; influence of the main working parameters, *Int. J. Refrig.* 33 (2010) 286–293.

[79]   K. Engelbrecht, J. Tušek, K.K. Nielsen, A. Kitanovski, C.R.H. Bahl, A. Poredoš, Improved modelling of a parallel plate active magnetic regenerator, *J. Phys. D. Appl. Phys.* 46 (2013) 255002.

[80]   M. Risser, C. Vasile, T. Engel, B. Keith, C. Muller, Numerical simulation of magnetocaloric system behaviour for an industrial application, *Int. J. Refrig.* 33 (2010) 973–981.

[81]   M. Risser, C. Vasile, B. Keith, T. Engel, C. Muller, Construction of consistent magnetocaloric materials data for modelling magnetic refrigerators, *Int. J. Refrig.* 35 (2012) 459–467.

[82]   M. Risser, C. Vasile, C. Muller, A. Noume, Improvement and application of a numerical model for optimizing the design of magnetic refrigerators, *Int. J. Refrig.* (n.d.).

[83]   D. Vuarnoz, T. Kawanami, Numerical analysis of a reciprocating active magnetic regenerator made of gadolinium wires, *Appl. Therm. Eng.* 37 (2012) 388–395.

[84]   D. Vuarnoz, T. Kawanami, Experimental validation of a coupled magneto-thermal model for a flat-parallel-plate active magnetic regenerator, *Appl. Therm. Eng.* 54 (2013) 433–439.

[85]   J. Roudaut, A. Kedous-Lebouc, J.-P. Yonnet, C. Muller, Numerical analysis of an active magnetic regenerator, *Int. J. Refrig.* 34 (2011) 1797–1804.

[86]   J. Tušek, A. Kitanovski, I. Prebil, A. Poredoš, Dynamic operation of an active magnetic regenerator (AMR): Numerical optimization of a packed-bed AMR, *Int. J. Refrig.* 34 (2011) 1507–1517.

[87]   P. Nikkola, C. Mahmed, M. Balli, O. Sari, 1D model of an active magnetic regenerator, *Int. J. Refrig.* 37 (2014) 43–50.

[88]   C. Aprea, A. Maiorino, A flexible numerical model to study an active magnetic refrigerator for near room temperature applications, *Appl. Energy.* 87 (2010) 2690–2698.

[89]   C. Aprea, A. Greco, A. Maiorino, Modelling an active magnetic refrigeration system: A comparison with different models of incompressible flow through a packed bed, *Appl. Therm. Eng.* 36 (2012) 296–306.

[90]   C. Aprea, A. Greco, A. Maiorino, The use of the first and of the second order phase magnetic transition alloys for an AMR refrigerator at room temperature: A numerical analysis of the energy performances, *Energy Convers. Manag.* 70 (2013) 40–55.

[91]   T.F. Petersen, N. Pryds, A. Smith, J. Hattel, H. Schmidt, H.-J.H. Knudsen, Two-dimensional mathematical model of a reciprocating room-temperature Active Magnetic Regenerator, *Int. J. Refrig.* 31 (2008) 432–443.

[92]   K.K. Nielsen, C.R.H. Bahl, A. Smith, R. Bjørk, N. Pryds, J. Hattel, Detailed numerical modeling of a linear parallel-plate Active Magnetic Regenerator, *Int. J. Refrig.* 32 (2009) 1478–1486.

[93]   M. Liu, B. Yu, Numerical investigations on internal temperature distribution and refrigeration performance of reciprocating active magnetic regenerator of room temperature magnetic refrigeration, *Int. J. Refrig.* 34 (2011) 617–627.

[94]   S. Lionte, C. Vasile, M. Siroux, Numerical analysis of a reciprocating active magnetic regenerator, *Appl. Therm. Eng.* 75 (2015) 871–879.

[95]   J. Bouchard, H. Nesreddine, N. Galanis, Model of a porous regenerator used for magnetic refrigeration at room temperature, *Int. J. Heat Mass Transf.* 52 (2009) 1223–1229.

[96]   B. Torregrosa-Jaime, K. Engelbrecht, J. Payá, J.M. Corberán, A new numerical scheme for the simulation of active magnetic regenerators, in: *6th Int. Conf. Magn. Refrig. Room Temp. (Thermag VI). Proc. Victoria, Canada, Sept. 7-10, 2014.*, International Institute of Refrigeration, Victoria, BC, Canada, 2014: pp. MON–S1–1508.

[97]   A. Sarlah, A. Poredos, Dimensionless numerical model for simulation of active magnetic regenerator refrigerator, *Int. J. Refrig.* 33 (2010) 1061–1067.

[98]   T.F. Petersen, K. Engelbrecht, C.R.H. Bahl, B. Elmegaard, N. Pryds, A. Smith, Comparison between a 1D and a 2D numerical model of an active magnetic regenerative refrigerator, *J. Phys. D. Appl. Phys.* 41 (2008) 105002.

[99]   J. Dikeos, A. Rowe, Validation of an active magnetic regenerator test apparatus model, *Int. J. Refrig.* 36 (2013) 921–931.

[100] B. Torregrosa-Jaime, J.M. Corberán, J. Payá, K. Engelbrecht, An efficient

numerical scheme for the simulation of parallel-plate active magnetic regenerators, *Int. J. Refrig.* 58 (2015) 121–130.

[101]   C.R.H. Bahl, D. Velazquez, K.K. Nielsen, K. Engelbrecht, K.B. Andersen, R. Bulatova, N. Pryds, High performance magnetocaloric perovskites for magnetic refrigeration, *Appl. Phys. Lett.* 100 (2012) 121905.

[102]   K. Engelbrecht, C.R.H. Bahl, K.K. Nielsen, Experimental results for a magnetic refrigerator using three different types of magnetocaloric material regenerators, *Int. J. Refrig.* 34 (2011) 1132–1140.

[103]   F.P. Incropera, D.P. Dewitt, T.L. Bergman, A.S. Lavine, *Fundamentals of Heat and Mass Transfer*, John Wiley & Sons, Hoboken, 2007.

[104]   P. V Trevizoli, J.R. Barbosa Jr., R.T.S. Ferreira, Experimental evaluation of a Gd-based linear reciprocating active magnetic regenerator test apparatus, *Int. J. Refrig.* 34 (2011) 1518–1526.

[105]   B. Van Leer, Towards the ultimate conservative difference scheme III. Upstream-centered finite-difference schemes for ideal compressible flow, *J. Comput. Phys.* 23 (1977) 263–275.

[106]   The MathWorks Inc., MATLAB R2015a, (2015).

[107]   A. Shitzer, M. Levy, Transient Behavior of a Rock-Bed Thermal Storage System Subjected to Variable Inlet Air Temperatures: Analysis and Experimentation, *J. Sol. Energy Eng.* 105 (1983) 200–206.

[108]   G.D. Dragutinovic, B.S. Baclic, *Operation of Counterflow Regenerators*, Computational Mechanics Inc., Billerica, MA, 1998.

[109]   R.K. Shah, A.L. London, *Laminar Flow Forced Convection in Ducts*, Academic Press, New York, 1978.

[110]   E. Brück, *Encyclopedia of Materials: Science and Technology*, Elsevier, 2003.

[111]   J.D. Moore, K.P. Skokov, J. Liu, O. Gutfleisch, Procedure for numerical integration of the magnetocaloric effect, *J. Appl. Phys.* 112 (2012) 63920.

[112]   T.F. Petersen, *Numerical modelling and analysis of a room temperature magnetic refrigeration system*, Risø National Laboratory, Technical University of Denmark, 2007.

[113]   R. Bavière, M. Favre-Marinet, S. Le Person, Bias effects on heat transfer measurements in microchannel flows, *Int. J. Heat Mass Transf.* 49 (2006) 3325–3337.

[114]   S. Garimella, William J. Dowling, Mark, S. Garimella, W.J. Dowling, M. Van Der Veen, J.D. Killion, The Effect of Simultaneously Developing Flow on Heat Transfer in Rectangular Tubes, *Heat Transf. Eng.* 22 (2001) 12–25.

[115]   Y.S. Muzychka, M.M. Yovanovich, Laminar Forced Convection Heat Transfer in the Combined Entry Region of Non-Circular Ducts, *J. Heat Transfer.* 126 (2004) 54–61.

[116] K.K. Nielsen, C.R.H. Bahl, K. Engelbrecht, The effect of flow maldistribution in heterogeneous parallel-plate active magnetic regenerators, *J. Phys. D. Appl. Phys.* 46 (2013) 105002.

[117] K.K. Nielsen, K. Engelbrecht, D. V Christensen, J.B. Jensen, A. Smith, C.R.H. Bahl, Degradation of the performance of microchannel heat exchangers due to flow maldistribution, *Appl. Therm. Eng.* 40 (2012) 236–247.

[118] P.J. Heggs, D. Burns, Single-blow experimental prediction of heat transfer coefficients: A comparison of four commonly used techniques, *Exp. Therm. Fluid Sci.* 1 (1988) 243–251.

[119] F. Durst, S. Noppenberger, M. Still, H. Venzke, Influence of humidity on hot-wire measurements, *Meas. Sci. Technol.* 7 (1999) 1517–1528.

[120] K.K. Nielsen, G.F. Nellis, S.A. Klein, Numerical modeling of the impact of regenerator housing on the determination of Nusselt numbers, *Int. J. Heat Mass Transf.* 65 (2013) 552–560.

[121] K. Engelbrecht, C.R.H. Bahl, D. Eriksen, R. Bjørk, K.K. Nielsen, N. Pryds, D. Velazquez, J.A. Lozano, A high frequency rotary active magnetic regenerator device, in: *Delft Days Magnetocalorics*, Delft, The Netherlands, 2011.

[122] R. Bjørk, C.R.H. Bahl, A. Smith, N. Pryds, Review and comparison of magnet designs for magnetic refrigeration, *Int. J. Refrig.* 33 (2010) 437–448.

[123] R. Bjørk, C.R.H. Bahl, A. Smith, N. Pryds, Optimization and improvement of Halbach cylinder design, *J. Appl. Phys.* 104 (2008) 013910.

[124] K.K. Nielsen, C.R.H. Bahl, A. Smith, N. Pryds, J. Hattel, A comprehensive parameter study of an active magnetic regenerator using a 2D numerical model, *Int. J. Refrig.* 33 (2010) 753–764.

[125] A. Smith, K.K. Nielsen, D. V. Christensen, C.R.H. Bahl, R. Bjo/rk, J. Hattel, The demagnetizing field of a nonuniform rectangular prism, *J. Appl. Phys.* 107 (2010) 103910.

[126] A. Afram, F. Janabi-Sharifi, Review of modeling methods for HVAC systems, *Appl. Therm. Eng.* 67 (2014) 507–519.

[127] A. Alahmer, A. Mayyas, A.A. Mayyas, M.A. Omar, D. Shan, Vehicular thermal comfort models; a comprehensive review, *Appl. Therm. Eng.* 31 (2011) 995–1002.

[128] G.G. Maidment, J.F. Missenden, Evaluation of an underground railway carriage operating with a sustainable groundwater cooling system, *Int. J. Refrig.* 25 (2002) 569–574.

[129] A. Gado, *Development of a dynamic test facility for environmental control systems*, University of Maryland, 2006.

[130] S. Sanaye, M. Dehghandokht, A. Fartaj, Temperature control of a cabin in an automobile using thermal modeling and fuzzy controller, *Energy Solut. a*

Sustain. World - Proc. Third Int. Conf. Appl. Energy, May 16-18, 2011 - Perugia, Italy. 97 (2012) 860–868.

[131] W. Li, J. Sun, Numerical simulation and analysis of transport air conditioning system integrated with passenger compartment, *Appl. Therm. Eng.* 50 (2013) 37–45.

[132] H. Khayyam, A.Z. Kouzani, E.J. Hu, S. Nahavandi, Coordinated energy management of vehicle air conditioning system, *MNF 2009 Spec. Issue.* 31 (2011) 750–764.

[133] E.Z.E. Conceição, M.C.G. Silva, J.C.S. André, D.X. Viegas, A Computational Model to Simulate the Thermal Behaviour of the Passengers Compartment of Vehicles, *SAE Tech. Pap.* 1999-01-07 (1999).

[134] A. Mezrhab, M. Bouzidi, Computation of thermal comfort inside a passenger car compartment, *Appl. Therm. Eng.* 26 (2006) 1697–1704.

[135] R. Levinson, H. Pan, G. Ban-Weiss, P. Rosado, R. Paolini, H. Akbari, Potential benefits of solar reflective car shells: Cooler cabins, fuel savings and emission reductions, *Appl. Energy.* 88 (2011) 4343–4357.

[136] W. Liu, Q. Deng, W. Huang, R. Liu, Variation in cooling load of a moving air-conditioned train compartment under the effects of ambient conditions and body thermal storage, *Appl. Therm. Eng.* 31 (2011) 1150–1162.

[137] D.C. Huang, *A dynamic computer simulation model for automobile passenger compartment climate control and evaluation*, Michigan Technological University, 1998.

[138] Ö. Arici, S. Yang, D. Huang, E. Öker, Computer Model for Automobile Climate Control System Simulation and Application, *Int. J. Appl. Thermodyn.* 2 (1999) 59–68.

[139] F. Bjurling, *Transient thermal model of a minibus' cabin and optimization of the air-conditioning control strategies*, Royal Institute of Technology, Stockholm, Sweden, 2013.

[140] ASHRAE, *2009 ASHRAE Handbook. Fundamentals.*, ASHRAE, Atlanta, USA, 2009.

[141] S.E. Laboratory, Type 16: Solar Radiation Processor, in: *TRNSYS 16 Math. Ref.*, University of Wisconsin-Madison, 2007: pp. 286–295.

[142] M. Modest, Radiative Properties of Real Surfaces, in: *Radiat. Heat Transf.*, Academic Press, USA, 2013: pp. 61–128.

[143] P. Berdahl, S.E. Bretz, Preliminary survey of the solar reflectance of cool roofing materials, *Energy Build.* 25 (1997) 149–158.

[144] J. Meyer, HMC sonata: thermal energy efficient vehicle, in: *SAE Automot. Altern. Refrig. Syst. Symp.*, Scottsdale, Arizona, 2002.

[145] U.S.D. of Energy, EnergyPlus, (2013).

[146] Software-Factory Norbert Schmitz, SF Pressure Drop 6.2, (2010).

[147] KSPG Automotive, http://www.kspg.com, n.d.

[148] Y.-G. Park, A.M. Jacobi, Air-Side Heat Transfer and Friction Correlations for Flat-Tube Louver-Fin Heat Exchangers, *J. Heat Transfer.* 131 (2009) 21801.

[149] Y.-G. Park, A.M. Jacobi, The Air-Side Thermal-Hydraulic Performance of Flat-Tube Heat Exchangers With Louvered, Wavy, and Plain Fins Under Dry and Wet Conditions, *J. Heat Transfer.* 131 (2009) 61801.

[150] A. Vaisi, M. Esmaeilpour, H. Taherian, Experimental investigation of geometry effects on the performance of a compact louvered heat exchanger, *Appl. Therm. Eng.* 31 (2011) 3337–3346.

[151] B. Xu, C. Zhang, Y. Wang, J. Chen, K. Xu, F. Li, N. Wang, Experimental investigation of the performance of microchannel heat exchangers with a new type of fin under wet and frosting conditions, *Appl. Therm. Eng.* 89 (2015) 444–458.

[152] Y.Y. Liang, C.C. Liu, C.Z. Li, J.P. Chen, Experimental and simulation study on the air side thermal hydraulic performance of automotive heat exchangers, *Appl. Therm. Eng.* 87 (2015) 305–315.

[153] A. Jokar, S.J. Eckels, M.H. Hosni, Single-Phase Flow in Meso-Channel Compact Heat Exchangers for Air Conditioning Applications, *Heat Transf. Eng.* 31 (2010) 3–16.

[154] J.E. Braun, S.A. Klein, J.W. Mitchell, Effectiveness Models for Cooling Towers and Cooling Coils, *ASHRAE Trans.* 95 (1989) 164–174.

[155] G.-Y. Jin, W.-J. Cai, Y.-W. Wang, Y. Yao, A simple dynamic model of cooling coil unit, *Energy Convers. Manag.* 47 (2006) 2659–2672.

[156] C. Oliet, C.D. Pérez-Segarra, S. Danov, A. Oliva, Numerical simulation of dehumidifying fin-and-tube heat exchangers: Semi-analytical modelling and experimental comparison, *Int. J. Refrig.* 30 (2007) 1266–1277.

[157] B. Torregrosa-Jaime, J.M. Corberán, J. Payá, J.L. Delamarche, Thermal characterisation of compact heat exchangers for air conditioning in electric vehicles, in: *14th UK Heat Transf. Conf.*, Edinburgh, 2015.

[158] G.F. Hewitt, ed., *Heat Exchanger Design Handbook*, Begell House Inc., New York, 1998.

[159] E. 86018, Effectiveness-NTU Relationships for the Design and Performance Evaluation of Two-Stream Heat Exchangers (1991), in: *Eng. Sci. Data Unit 86018 with Amend. A, July 1991*, ESDU International plc, London, 1991: pp. 92–107.

[160] C.-C. Wang, On the Airside Performance of Fin-and-Tube Heat Exchangers, in: S. Kakaç, A.E. Bergles, F. Mayinger, H. Yüncü (Eds.), *Heat Transf. Enhanc. Heat Exch.*, Springer Netherlands, 1999: pp. 141–162.

[161] VDI Gesellschaft Verfahrenstechnik und Chemieingenieurwesen, ed., *VDI Heat Atlas*, 2nd ed., Springer, Düsseldorf, 2010.

[162] R.L. Webb, N.H. Kim, *Principles of Enhanced Heat Transfer*, Taylor & Francis, New York, 2005.

[163] R. Bjørk, A. Smith, C.R.H. Bahl, N. Pryds, Determining the minimum mass and cost of a magnetic refrigerator, *Int. J. Refrig.* 34 (2011) 1805–1816.

[164] B. Torregrosa-Jaime, J. Payá, J. Corberan, Design of Efficient Air-Conditioning Systems for Electric Vehicles, *SAE Int. J. Altern. Powertrains.* 2 (2013) 291–303.

[165] B. Monfared, B. Palm, Optimization of layered regenerator of a magnetic refrigeration device, *Int. J. Refrig.* 57 (2015) 103–111.

[166] Z. Chen, Y. Utaka, Y. Tasaki, Measurement and numerical simulation on the heat transfer characteristics of reciprocating flow in microchannels for the application in magnetic refrigeration, *Appl. Therm. Eng.* 65 (2014) 150–157.

Publications

Publications in peer-reviewed journals

1. <u>B. Torregrosa-Jaime</u>, J. Payá, J.M. Corberán, Application of magnetic cooling in electric vehicles, *Sci. Technol. Built Environ.* (2016) In press.

2. <u>B. Torregrosa-Jaime</u>, J.M. Corberán, J. Payá, K. Engelbrecht, An efficient numerical scheme for the simulation of parallel-plate active magnetic regenerators, *Int. J. Refrig.* 58 (2015) 121–130.

3. <u>B. Torregrosa-Jaime</u>, F. Bjurling, J.M. Corberán, F. Di Sciullo, J. Payá, Transient thermal model of a vehicle's cabin validated under variable ambient conditions, *Appl. Therm. Eng.* 75 (2015) 45–53.

4. <u>B. Torregrosa-Jaime</u>, J.M. Corberán, C. Vasile, C. Muller, M. Risser, J. Payá, Sizing of a reversible magnetic heat pump for the automotive industry, *Int. J. Refrig.* 37 (2014) 156–164.

5. <u>B. Torregrosa-Jaime</u>, J. Payá, J. Corberan, Design of efficient air-conditioning systems for electric vehicles, *SAE Int. J. Altern. Powertrains.* 2 (2013) 291–303.

6. <u>B. Torregrosa-Jaime</u>, C. Vasile, M. Risser, C. Muller, J. Corberan, J. Payá, Application of Magnetocaloric Heat Pumps in Mobile Air-Conditioning, *SAE Int. J. Passeng. Cars - Mech. Syst.* 6 (2013) 520–528.

Publications in congresses

1. <u>B. Torregrosa-Jaime</u>, J. Payá, J.M. Corberán, Integral optimisation of a magnetocaloric air-conditioning system for an electric vehicle, in: *7th IIR/IIF Int. Conf. on Magnetic Refrigeration at Room Temperature THERMAG VII*, Torino, September 2016.

2. <u>B. Torregrosa-Jaime</u>, J.M. Corberán, J. Payá, J.L. Delamarche, Thermal characterisation of compact heat exchangers for air conditioning in electric vehicles, in: *14th UK Heat Transf. Conf.*, Edinburgh, September 2015.

3. <u>B. Torregrosa-Jaime</u>, K. Engelbrecht, J. Payá, J.M. Corberán, A new numerical scheme for the simulation of active magnetic regenerators, in: *Proc. of the 6th IIR/IIF Int. Conf. on Magnetic Refrigeration at Room Temperature THERMAG VI*, Victoria, September 2014.

4. F. Bjurling, J.M. Corberán, J. Payá, <u>B. Torregrosa-Jaime</u>, Control strategies for the air-conditioning in electric vehicles, in: A. Coronas, J.C. Bruno (Eds.), *Avanaces En Ciencias Y Técnicas Del Frío VII. Libro de Actas*, Tarragona, June 2014, pp. 769–777. *Awarded best communication of the conference.*

5. <u>B. Torregrosa-Jaime</u>, J. Payá, J.M. Corberán, C. Malvicino, F. Di Sciullo, ICE Project: mobile air-conditioning system based on magnetic refrigeration. *SAE Technical Paper* 2013-01-0238. SAE World Congress, Detroit, April 2013.

6. <u>B. Torregrosa-Jaime</u>, J.M. Corberán, C. Vasile, C. Muller, M. Risser, J. Payá, Design of a magnetocaloric air-conditioning system for an electric minibus, in: *Proc. of the 5th IIR/IIF Int. Conf. on Magnetic Refrigeration at Room Temperature THERMAG V*, Grenoble, September 2012.

7. <u>B. Torregrosa-Jaime</u>, J. Payá, J.M. Corberán, ICE Project. Modelling of mobile air-conditioning systems for electric vehicles, in: *4th European Workshop MAC and Vehicle Thermal Systems*, Torino, December 2011.

8. J. Payá, <u>B. Torregrosa-Jaime,</u> J.M. Corberán, C. Vasile, Innovative air-conditioning systems for conventional and electric vehicles, in: *13th EAEC European Automotive Congress*, Valencia, June 2011.

Appendix A

Discretization of the AMR fluid equation

The fluid equations for the AMR presented in section 2.2 are repeated for convenience. Eq. (A.1) corresponds to the energy balance in the fluid (Eq. 2.4).

$$\epsilon A_c \rho_f c_f \frac{\partial T_f}{\partial t} = -\dot{m} c_f \frac{\partial T_f}{\partial x} + \epsilon A_c k_f \frac{\partial^2 T_f}{\partial x^2} + h a_s A_c \big(T_r - T_f\big) + \frac{\partial p}{\partial x} \frac{\dot{m}}{\rho_f} \tag{A.1}$$

Conduction in the fluid was demonstrated negligible in typical AMR applications so the corresponding term is obviated. Eq. (A.2) (Eq. 2.10) is subsequently obtained by formulating Eq. (A.1) as a flow-based energy balance for each control volume and integrating the result over the time step. Eq. (A.2) refers to the case in which the fluid flows from the hot to the cold reservoir ($v>0$, Fig. 2.2), while Eq. (A.4) considers the fluid flow from the cold to the hot reservoir ($v<0$).

$$\bar{T}_{f,i}^{n+1} - \bar{T}_{f,i}^{n} = \int_{t^n}^{t^{n+1}} d\bar{T}_{f,i} = \frac{v}{\Delta x} \int_{t^n}^{t^{n+1}} \left[T_f\left(x_{i-\frac{1}{2}}, t\right) - T_f\left(x_{i+\frac{1}{2}}, t\right) \right] dt$$
$$+ \frac{h a_s}{\epsilon \rho_f c_f} \int_{t^n}^{t^{n+1}} (\bar{T}_{r,i} - \bar{T}_{f,i}) dt + \frac{f_f |v^3|}{2 D_h c_f} \Delta t \tag{A.2}$$

$$\bar{T}_{f,i}^{n+1} - \bar{T}_{f,i}^{n} = \int_{t^n}^{t^{n+1}} d\bar{T}_{f,i} = \frac{v}{\Delta x} \int_{t^n}^{t^{n+1}} \left[T_f\left(x_{i+\frac{1}{2}}, t\right) - T_f\left(x_{i-\frac{1}{2}}, t\right) \right] dt$$
$$+ \frac{h a_s}{\epsilon \rho_f c_f} \int_{t^n}^{t^{n+1}} (\bar{T}_{r,i} - \bar{T}_{f,i}) dt + \frac{f_f |v^3|}{2 D_h c_f} \Delta t \tag{A.3}$$

The different approaches proposed for solving the terms in the right-hand side of Eqs. (A.2) and (A.4) are detailed in the following. Finally, the discretized fluid equation is presented.

A.1   Temperature in the boundaries of the control volume

The temperatures at the boundaries of the control volume, $T_f(x_{i-1/2}, t)$ and $T_f(x_{i+1/2}, t)$, are calculated with Eq. (A.1) neglecting the axial conduction and the viscous dissipation terms (Eq. A.4). Fig. A.1 (Fig. 2.3) illustrates this approach.

$$\frac{\partial T_f}{\partial t} + v\frac{\partial T_f}{\partial x} = \frac{ha_s A_c}{\epsilon A_c \rho_f c_f}(T_r - T_f) = \dot{Q}_h \tag{A.4}$$
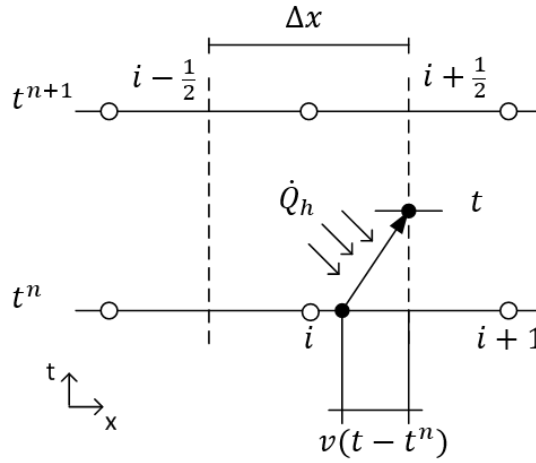
Fig. A.1. Path followed by a fluid particle with v>0 during a time step.

Since $v = dx/dt$, the left-hand side of Eq. (A.4) can be expressed as the total derivative of the fluid temperature with respect to the time (Eq. A.5).

$$\frac{DT_f}{Dt} = \frac{ha_s A_c}{\epsilon A_c \rho_f c_f}(T_r - T_f) \tag{A.5}$$

In the following, four different hypothesis regarding the source term are proposed with the purpose of solving Eq. (A.5).

Hypothesis HEIS 1. Constant heat flux (I).

Hypothesis HEIS 1 assumes that the temperature difference between the solid and the fluid remains constant during the time step, that is, the temperature of the solid varies along with the temperature of the fluid. This temperature difference is calculated with the mean temperatures of the fluid and the solid during the time step. Eq. (A.5) is thus reformulated as Eq. (A.6), where K and K' refer to constant values.

$$\frac{DT_f}{Dt} = \frac{ha_s A_c}{\epsilon A_c \rho_f c_f}\left(T_r - T_f\right) = K\left(\bar{T}_{r,i}^n - \bar{T}_{f,i}^n\right) = K' \tag{A.6}$$

Eq. (A.6) is integrated in order to obtain an expression for $T_f\left(x_{i+1/2}, t\right)$ (Eq. A.7), following the explicit approach in Fig. A.1. The expression for $T_f\left(x_{i-1/2}, t\right)$ is analogue.

$$T_f\left(x_{i+1/2}, t\right) = T_f\left(x_{i+1/2} - v(t - t^n), t^n\right) + K'(t - t^n) \tag{A.7}$$

Therefore, the integral over the time step of $T_f\left(x_{i+1/2}, t\right)$ in Eq. (A.2) can be obtained by integrating the two terms at the right-hand side of Eq. (A.7). In order to solve for the first term in the right-hand side, the spatial distribution of the fluid temperature at time t^n must be known. As explained in section 2.2.1, a linear distribution is assumed based on the mean temperature inside each cell (Eqs. 2.12, A.8). The corresponding slope ($\sigma_{f,i}^n$) is chosen to minimize numerical diffusion (Eq. 2.13).

$$T_f(x, t^n) = \bar{T}_{f,i}^n + (x - x_i)\,\sigma_{f,i}^n \tag{A.8}$$

Applying the expression in Eq. (A.8), the integral of the first right-hand-side term of Eq. (A.7) can be solved as in Eq. (A.9). Eq. (A.10) is the expression for the integral of the second right-hand-side term of Eq. (A.7).

$$\int_{t^n}^{t^{n+1}} T_f\left(x_{i+1/2} - v(t - t^n), t^n\right)dt = \int_{t^n}^{t^{n+1}}\left[\bar{T}_{f,i}^n + \left(x_{i+1/2} - v(t - t^n) - x_i\right)\sigma_{f,i}^n\right]dt$$
$$= \left(\bar{T}_{f,i}^n + \frac{\Delta x}{2}\sigma_{f,i}^n\right)\Delta t - v\sigma_{f,i}^n\frac{\Delta t^2}{2} \tag{A.9}$$

$$\int_{t^n}^{t^{n+1}} K'(t - t^n)dt = \int_{t^n}^{t^{n+1}} K\left(\bar{T}_{r,i}^n - \bar{T}_{f,i}^n\right)(t - t^n)dt = K\left(\bar{T}_{r,i}^n - \bar{T}_{f,i}^n\right)\frac{\Delta t^2}{2} \tag{A.10}$$

In summary, assuming constant heat flux between the solid and the fluid, the integrals in the advection term of Eq. (A.2) ($v>0$) can be expressed as in Eqs. (A.11) and (A.12). **This methodology defines an explicit numerical scheme of second order.**

$$\int_{t^n}^{t^{n+1}} T_f\left(x_{i+1/2}, t\right)dt = \left(\bar{T}_{f,i}^n + \frac{\Delta x}{2}\sigma_{f,i}^n\right)\Delta t - v\sigma_{f,i}^n\frac{\Delta t^2}{2} + \frac{ha_s}{\epsilon\rho_f c_f}\left(\bar{T}_{r,i}^n - \bar{T}_{f,i}^n\right)\frac{\Delta t^2}{2} \tag{A.11}$$

$$\int_{t^n}^{t^{n+1}} T_f\left(x_{i-1/2}, t\right)dt = \left(\bar{T}_{f,i-1}^n + \frac{\Delta x}{2}\sigma_{f,i-1}^n\right)\Delta t - v\sigma_{f,i-1}^n\frac{\Delta t^2}{2}$$
$$+ \frac{ha_s}{\epsilon\rho_f c_f}\left(\bar{T}_{r,i-1}^n - \bar{T}_{f,i-1}^n\right)\frac{\Delta t^2}{2} \tag{A.12}$$

Analogously, the values of these integrals in Eq. (A.3) ($v{<}0$) are given by Eqs. (A.13) and (A.14).

$$
\int_{t^n}^{t^{n+1}} T_f\big(x_{i+1/2}, t\big) dt = \left(\bar{T}_{f,i+1}^n - \frac{\Delta x}{2}\sigma_{f,i+1}^n\right)\Delta t + |v|\sigma_{f,i+1}^n \frac{\Delta t^2}{2}
$$
$$
+ \frac{ha_s}{\epsilon \rho_f c_f}\big(\bar{T}_{r,i+1}^n - \bar{T}_{f,i+1}^n\big)\frac{\Delta t^2}{2}
\tag{A.13}
$$

$$
\int_{t^n}^{t^{n+1}} T_f\big(x_{i-1/2}, t\big) dt = \left(\bar{T}_{f,i}^n - \frac{\Delta x}{2}\sigma_{f,i}^n\right)\Delta t + |v|\sigma_{f,i}^n \frac{\Delta t^2}{2} + \frac{ha_s}{\epsilon \rho_f c_f}\big(\bar{T}_{r,i}^n - \bar{T}_{f,i}^n\big)\frac{\Delta t^2}{2}
\tag{A.14}
$$

Hypothesis HEIS 2. Constant heat flux (II).

As HEIS 1, hypothesis HEIS 2 assumes that the temperature difference between the solid and the fluid remains constant during the time step. However in this case this temperature difference is calculated with the temperatures of the fluid and the solid at the beginning of the time step (Eq. A.15).

$$
\frac{DT_f}{Dt} = \frac{ha_s A_c}{\epsilon A_c \rho_f c_f}\big(T_r - T_f\big) = K\big(\bar{T}_{r,i,0}^n - \bar{T}_{f,i,0}^n\big) = K'
\tag{A.15}
$$

The temperatures at the beginning of the nth time step ($\bar{T}_{i,0}^n$) can be determined for each case by following the scheme in Fig. A.1. For instance, when calculating $T_f\big(x_{i+1/2}, t\big)$ if $v{>}0$, $\bar{T}_{i,0}^n$ equals $T\big(x_{i+1/2} - v(t - t^n), t^n\big)$. This approach is applied to both the fluid and the solid temperatures. Hence a spatial distribution of the solid temperature at each time step has to be defined. Similarly to the fluid, a linear temperature distribution is considered (Eq. A.16), where the slope ($\sigma_{r,i}^n$) is given by Eq. (A.17).

$$
T_r(x, t^n) = \bar{T}_{r,i}^n + (x - x_i)\,\sigma_{r,i}^n
\tag{A.16}
$$

$$
\sigma_{r,i}^n = \frac{\bar{T}_{r,i+1}^n - \bar{T}_{r,i-1}^n}{2\Delta x}
\tag{A.17}
$$

Similarly to case HEIS1, Eq. (A.15) is integrated in order to obtain an expression for $T_f\big(x_{i+1/2}, t\big)$ and the analogue terms. Eqs. (A.7) to (A.9) apply for hypothesis HEIS 2, while the integral of the second right-hand-side term of Eq. (A.7) is given by Eq. (A.18).

$$
\int_{t^n}^{t^{n+1}} K'(t - t^n)dt = \int_{t^n}^{t^{n+1}} K\big(\bar{T}_{r,i,0}^n - \bar{T}_{f,i,0}^n\big)(t - t^n)dt
\tag{A.18}
$$

$$= \int_{t^n}^{t^{n+1}} K\left(T_r\big(x_{i+1/2} - v(t - t^n), t^n\big) - T_f\big(x_{i+1/2} - v(t - t^n), t^n\big)\right)(t - t^n)dt$$

$$= \int_{t^n}^{t^{n+1}} K\big(\bar{T}_{r,i}^n + [x_{i+1/2} - v(t - t^n) - x_i]\,\sigma_{r,i}^n - \bar{T}_{f,i}^n$$
$$- [x_{i+1/2} - v(t - t^n) - x_i]\,\sigma_{f,i}^n\big)(t - t^n)dt$$

$$= K\left[\left(\bar{T}_{r,i}^n - \bar{T}_{f,i}^n + \frac{\Delta x}{2}[\sigma_{r,i}^n + \sigma_{f,i}^n]\right)\frac{\Delta t^2}{2} - v(\sigma_{r,i}^n + \sigma_{f,i}^n)\frac{\Delta t^3}{3}\right]$$

In summary, if hypothesis HEIS 2 is assumed, the integrals in the advection term of Eq. (A.2) ($v>0$) can be expressed as in Eqs. (A.19) and (A.20).

$$\int_{t^n}^{t^{n+1}} T_f\big(x_{i+1/2}, t\big)dt = \left(\bar{T}_{f,i}^n + \frac{\Delta x}{2}\sigma_{f,i}^n\right)\Delta t - v\sigma_{f,i}^n\frac{\Delta t^2}{2}$$
$$+ \frac{ha_s}{\epsilon\rho_f c_f}\left[\left(\bar{T}_{r,i}^n - \bar{T}_{f,i}^n + \frac{\Delta x}{2}[\sigma_{r,i}^n + \sigma_{f,i}^n]\right)\frac{\Delta t^2}{2} - v(\sigma_{r,i}^n + \sigma_{f,i}^n)\frac{\Delta t^3}{3}\right]$$
(A.19)

$$\int_{t^n}^{t^{n+1}} T_f\big(x_{i-1/2}, t\big)dt = \left(\bar{T}_{f,i-1}^n + \frac{\Delta x}{2}\sigma_{f,i-1}^n\right)\Delta t - v\sigma_{f,i-1}^n\frac{\Delta t^2}{2}$$
$$+ \frac{ha_s}{\epsilon\rho_f c_f}\left[\left(\bar{T}_{r,i-1}^n - \bar{T}_{f,i-1}^n + \frac{\Delta x}{2}[\sigma_{r,i-1}^n + \sigma_{f,i-1}^n]\right)\frac{\Delta t^2}{2} - v(\sigma_{r,i-1}^n + \sigma_{f,i-1}^n)\frac{\Delta t^3}{3}\right]$$
(A.20)

Analogously, the values of these integrals in Eq. (A.3) ($v<0$) are given by Eqs. (A.21) and (A.22).

$$\int_{t^n}^{t^{n+1}} T_f\big(x_{i+1/2}, t\big)dt = \left(\bar{T}_{f,i+1}^n - \frac{\Delta x}{2}\sigma_{f,i+1}^n\right)\Delta t + |v|\sigma_{f,i+1}^n\frac{\Delta t^2}{2}$$
$$+ \frac{ha_s}{\epsilon\rho_f c_f}\left[\left(\bar{T}_{r,i+1}^n - \bar{T}_{f,i+1}^n - \frac{\Delta x}{2}[\sigma_{r,i+1}^n - \sigma_{f,i+1}^n]\right)\frac{\Delta t^2}{2} + |v|(\sigma_{r,i-1}^n - \sigma_{f,i-1}^n)\frac{\Delta t^3}{3}\right]$$
(A.21)

$$\int_{t^n}^{t^{n+1}} T_f\big(x_{i-1/2}, t\big)dt = \left(\bar{T}_{f,i}^n - \frac{\Delta x}{2}\sigma_{f,i}^n\right)\Delta t + |v|\sigma_{f,i}^n\frac{\Delta t^2}{2}$$
$$+ \frac{ha_s}{\epsilon\rho_f c_f}\left[\left(\bar{T}_{r,i}^n - \bar{T}_{f,i}^n - \frac{\Delta x}{2}[\sigma_{r,i}^n - \sigma_{f,i}^n]\right)\frac{\Delta t^2}{2} + |v|(\sigma_{r,i}^n - \sigma_{f,i}^n)\frac{\Delta t^3}{3}\right]$$
(A.22)

Hypothesis HEIS 3. Constant wall temperature.

Hypothesis HEIS 3 assumes that the temperature of the solid remains constant in each cell during a time step, that is, the temperature of the solid varies slowly with respect to the fluid. Eq. (A.5) is thus discretized as Eq. (A.23), which refers to the ith spatial node and the nth time step and where K and $T_r = \bar{T}_{r,i}^n$ are constant values.

$$\frac{DT_f}{Dt} = \frac{ha_s A_c}{\epsilon A_c \rho_f c_f}(T_r - T_f) = K(\bar{T}_{r,i}^n - T_f(x,t)) \tag{A.23}$$

As in the previous cases, Eq. (A.23) is integrated as in Eq. (A.24) in order to obtain an expression for $T_f(x_{i+1/2}, t)$ and the analogue terms, following the scheme in Fig. A.1. The solution of Eq. (A.24) is given by Eq. (A.25).

$$\int_{T_f(x_{i+1/2}-v(t-t^n),t^n)}^{T_f(x_{i+1/2},t)} \frac{DT_f}{\bar{T}_{r,i}^n - T_f} = \int_{t^n}^{t} K Dt \tag{A.24}$$

$$T_f(x_{i+1/2}, t) = \bar{T}_{r,i}^n - \left[\bar{T}_{r,i}^n - T_f(x_{i+1/2} - v(t-t^n), t^n)\right]e^{-K(t-t^n)} \tag{A.25}$$

The integral over the time step of $T_f(x_{i+1/2}, t)$ in Eq. (A.2) is therefore obtained by integrating Eq. (A.25). The fluid temperature distribution is assumed linear (Eq. A.8), as explained in case HEIS1.

In summary, if hypothesis HEIS 3 is assumed, the integrals in the advection term of Eq. (A.2) ($v > 0$) can be expressed as in Eqs. (A.26) and (A.27). The expressions for the case $v < 0$ are analogue.

$$\int_{t^n}^{t^{n+1}} T_f(x_{i+1/2}, t)dt = \bar{T}_{r,i}^n \Delta t - \frac{\epsilon \rho_f c_f}{ha_s}\left(\bar{T}_{r,i}^n - \bar{T}_{f,i}^n - \frac{\Delta x}{2}\sigma_{f,i}^n\right)\left(1 - e^{-\frac{ha_s}{\epsilon \rho_f c_f}\Delta t}\right)$$
$$+ \frac{\epsilon \rho_f c_f}{ha_s}v\sigma_{f,i}^n\left[e^{-\frac{ha_s}{\epsilon \rho_f c_f}\Delta t}\Delta t - \frac{\epsilon \rho_f c_f}{ha_s}\left(1 - e^{-\frac{ha_s}{\epsilon \rho_f c_f}\Delta t}\right)\right] \tag{A.26}$$

$$\int_{t^n}^{t^{n+1}} T_f(x_{i-1/2}, t)dt = \bar{T}_{r,i-1}^n \Delta t - \frac{\epsilon \rho_f c_f}{ha_s}\left(\bar{T}_{r,i-1}^n - \bar{T}_{f,i-1}^n - \frac{\Delta x}{2}\sigma_{f,i-1}^n\right)$$
$$\cdot\left(1 - e^{-\frac{ha_s}{\epsilon \rho_f c_f}\Delta t}\right) + \frac{\epsilon \rho_f c_f}{ha_s}v\sigma_{f,i-1}^n\left[e^{-\frac{ha_s}{\epsilon \rho_f c_f}\Delta t}\Delta t - \frac{\epsilon \rho_f c_f}{ha_s}\left(1 - e^{-\frac{ha_s}{\epsilon \rho_f c_f}\Delta t}\right)\right] \tag{A.27}$$

Hypothesis HEIS 4. The wall temperature is a function.

Hypothesis HEIS 4 assumes that the temperature of the solid is a function of space and time, $T_r = T_r(x, t)$. However, if a sufficiently small time step is employed, it is assumed that $T_r(x)$ remains constant during the time step. A linear spatial distribution of the temperature is considered (Eqs. A.16 and A.17), as explained in case HEIS 2. In this case, Eq. (A.5) is expressed as Eq. (A.28).

$$\frac{DT_f}{Dt} = \frac{ha_s A_c}{\epsilon A_c \rho_f c_f}(T_r - T_f) = K(T_r(x, t^n) - T_f(x, t)) \tag{A.28}$$

Eq. (A.28) is integrated numerically as in Eq. (A.29). Due to its implicit character, this integral does not have an analytic solution.

$$\frac{DT}{Dt} = \frac{T_f\big(x_{i+1/2}, t\big) - T_f\big(x_{i+1/2} - v(t - t^n), t^n\big)}{t - t^n} = \frac{K}{2}\Big[T_r^n\Big(x_{i+1/2} - v(t - t^n)\Big)$$
$$-T_f\big(x_{i+1/2} - v(t - t^n), t^n\big) + T_r^n\big(x_{i+1/2}\big) - T_f\big(x_{i+1/2}, t\big)\Big] \tag{A.29}$$

Eq. (A.29) is arranged as Eq. (A.30) in order to obtain an expression for $T_f\big(x_{i+1/2}, t\big)$ and the analogue terms. A linear temperature distribution has been assumed in the control volume, for both the fluid and the solid.

$$T_f\big(x_{i+1/2}, t\big) = \frac{1}{1 + \frac{K(t - t^n)}{2}}\Bigg[\Big(1 - \frac{K(t - t^n)}{2}\Big)T_f\big(x_{i+1/2} - v(t - t^n), t^n\big)$$
$$+ \frac{K(t - t^n)}{2}\Big(T_r^n\Big(x_{i+1/2} - v(t - t^n)\Big) + T_r^n\big(x_{i+1/2}\big)\Big)\Bigg]$$
$$= \frac{1}{1 + \frac{K(t - t^n)}{2}}\Bigg[\Big(1 - \frac{K(t - t^n)}{2}\Big)\big(\bar{T}_{f,i}^n + \big(x_{i+1/2} - v(t - t^n) - x_i\big)\sigma_{f,i}^n\big) \tag{A.30}$$
$$+ \frac{K(t - t^n)}{2}\big(\bar{T}_{r,i}^n + [x_{i+1/2} - v(t - t^n) - x_i]\sigma_{r,i}^n + \bar{T}_{r,i}^n + [x_{i+1/2} - x_i]\sigma_{r,i}^n\big)\Bigg]$$

In summary, if hypothesis HEIS 4 is assumed, the integrals in the advection term of Eq. (A.2) ($v>0$) can be expressed as in Eqs. (A.31) and (A.32). The expressions for the case $v<0$ are analogue.

$$\int_{t^n}^{t^{n+1}} T_f\big(x_{i+1/2}, t\big)dt = \frac{1 - \frac{ha_s}{\epsilon\rho_f c_f}\frac{\Delta t}{2}}{1 + \frac{ha_s}{\epsilon\rho_f c_f}\frac{\Delta t}{2}}\Bigg[\Big(\bar{T}_{f,i}^n + \frac{\Delta x}{2}\sigma_{f,i}^n\Big)\Delta t - v\sigma_{f,i}^n\frac{\Delta t^2}{2}\Bigg]$$
$$+ \frac{\frac{ha_s}{\epsilon\rho_f c_f}\frac{\Delta t}{2}}{1 + \frac{ha_s}{\epsilon\rho_f c_f}\frac{\Delta t}{2}}\Bigg[(2\bar{T}_{r,i}^n + \Delta x\sigma_{r,i}^n)\Delta t - v\sigma_{r,i}^n\frac{\Delta t^2}{2}\Bigg] \tag{A.31}$$

$$\int_{t^n}^{t^{n+1}} T_f\big(x_{i-1/2}, t\big)dt = \frac{1 - \frac{ha_s}{\epsilon\rho_f c_f}\frac{\Delta t}{2}}{1 + \frac{ha_s}{\epsilon\rho_f c_f}\frac{\Delta t}{2}}\Bigg[\Big(\bar{T}_{f,i-1}^n + \frac{\Delta x}{2}\sigma_{f,i-1}^n\Big)\Delta t - v\sigma_{f,i-1}^n\frac{\Delta t^2}{2}\Bigg]$$
$$+ \frac{\frac{ha_s}{\epsilon\rho_f c_f}\frac{\Delta t}{2}}{1 + \frac{ha_s}{\epsilon\rho_f c_f}\frac{\Delta t}{2}}\Bigg[(2\bar{T}_{r,i-1}^n + \Delta x\sigma_{r,i-1}^n)\Delta t - v\sigma_{r,i-1}^n\frac{\Delta t^2}{2}\Bigg] \tag{A.32}$$

A.2   Mean temperature in the cell

As explained in section 2.2.1, the integral of $\bar{T}_i^n$ (Eq. A.33, corresponds to Eq. 2.15) can be approached numerically by different techniques: the implicit method ($\xi{=}1$), the Crank-Nicholson method ($\xi{=}0.5$) and the explicit method ($\xi{=}0$).

$$\int_{t^n}^{t^{n+1}} \bar{T}_i \, dt = \left[(1-\xi)\bar{T}_i^n + \xi\bar{T}_i^{n+1}\right]\Delta t \tag{A.33}$$

A.3   Discretization of the fluid equation

The fluid equations are discretized by substituting the previous expressions. For instance, if hypothesis HEIS 1 is considered, Eq. (A.2) ($v{>}0$) is expressed as Eq. (A.34) for $i{>}1$.

$$
\begin{aligned}
\bar{T}_{f,i}^{n+1} - \bar{T}_{f,i}^n &= \frac{v}{\Delta x}\left(\left[\bar{T}_{f,i-1}^n - \bar{T}_{f,i}^n + \frac{\Delta x}{2}\left(\sigma_{f,i-1}^n - \sigma_{f,i}^n\right)\right]\Delta t - v\left(\sigma_{f,i-1}^n - \sigma_{f,i}^n\right)\frac{\Delta t^2}{2}\right. \\
&\quad \left. + \frac{ha_s}{\epsilon\rho_f c_f}\left[\bar{T}_{r,i-1}^n - \bar{T}_{r,i}^n - \left(\bar{T}_{f,i-1}^n - \bar{T}_{f,i}^n\right)\right]\frac{\Delta t^2}{2}\right) \\
&\quad + \frac{ha_s}{\epsilon\rho_f c_f}\left[(1-\xi)\left(\bar{T}_{r,i}^n - \bar{T}_{f,i}^n\right) + \xi\left(\bar{T}_{r,i}^{n+1} - \bar{T}_{f,i}^{n+1}\right)\right]\Delta t + \frac{f_f|v^3|}{2D_h c_f}\Delta t
\end{aligned}
\tag{A.34}
$$

Cell $i{=}1$ is the inlet of the regenerator when $v{>}0$. In this case, $T_f\left(x_{i-1/2}, t\right)$ equals the inlet temperature from the hot reservoir (T_H, Eq. 2.16 and Fig. 2.2) and the discretized fluid equation is hence Eq. (A.35).

$$
\begin{aligned}
\bar{T}_{f,i}^{n+1} - \bar{T}_{f,i}^n &= \frac{v}{\Delta x}\Delta t\left(T_H - \left[\left(\bar{T}_{f,i}^n + \frac{\Delta x}{2}\sigma_{f,i}^n\right) - v\sigma_{f,i}^n\frac{\Delta t}{2} + \frac{ha_s}{\epsilon\rho_f c_f}\left(\bar{T}_{r,i}^n - \bar{T}_{f,i}^n\right)\frac{\Delta t}{2}\right]\right) \\
&\quad + \frac{ha_s}{\epsilon\rho_f c_f}\left[(1-\xi)\left(\bar{T}_{r,i}^n - \bar{T}_{f,i}^n\right) + \xi\left(\bar{T}_{r,i}^{n+1} - \bar{T}_{f,i}^{n+1}\right)\right]\Delta t + \frac{f_f|v^3|}{2D_h c_f}\Delta t
\end{aligned}
\tag{A.35}
$$

Analogously, Eq. (A.3) ($v{<}0$) is expressed as Eq. (A.36) for $i{<}n_x$.

$$
\begin{aligned}
\bar{T}_{f,i}^{n+1} - \bar{T}_{f,i}^n &= \frac{v}{\Delta x}\left(\left[\bar{T}_{f,i+1}^n - \bar{T}_{f,i}^n - \frac{\Delta x}{2}\left(\sigma_{f,i+1}^n - \sigma_{f,i}^n\right)\right]\Delta t + |v|\left(\sigma_{f,i+1}^n - \sigma_{f,i}^n\right)\frac{\Delta t^2}{2}\right. \\
&\quad \left. + \frac{ha_s}{\epsilon\rho_f c_f}\left[\bar{T}_{r,i+1}^n - \bar{T}_{r,i}^n - \left(\bar{T}_{f,i+1}^n - \bar{T}_{f,i}^n\right)\right]\frac{\Delta t^2}{2}\right) \\
&\quad + \frac{ha_s}{\epsilon\rho_f c_f}\left[(1-\xi)\left(\bar{T}_{r,i}^n - \bar{T}_{f,i}^n\right) + \xi\left(\bar{T}_{r,i}^{n+1} - \bar{T}_{f,i}^{n+1}\right)\right]\Delta t + \frac{f_f|v^3|}{2D_h c_f}\Delta t
\end{aligned}
\tag{A.36}
$$

Cell $i= n_x$ is the inlet of the regenerator when $v<0$. In this case, $T_f\big(x_{i+1/2},t\big)$ equals the inlet temperature from the cold reservoir (T_C, Eq. 2.16 and Fig. 2.2) and the discretized fluid equation is hence Eq. (A.37).

$$
\begin{aligned}
\bar{T}_{f,i}^{n+1} - \bar{T}_{f,i}^{n} = {} & \frac{v}{\Delta x}\Delta t\left(T_C - \left[\left(\bar{T}_{f,i}^{n} - \frac{\Delta x}{2}\sigma_{f,i}^{n}\right) + |v|\sigma_{f,i}^{n}\frac{\Delta t}{2} + \frac{ha_s}{\epsilon\rho_f c_f}\big(\bar{T}_{r,i}^{n} - \bar{T}_{f,i}^{n}\big)\frac{\Delta t}{2}\right]\right) \\
& + \frac{ha_s}{\epsilon\rho_f c_f}\big[(1-\xi)\big(\bar{T}_{r,i}^{n} - \bar{T}_{f,i}^{n}\big) + \xi\big(\bar{T}_{r,i}^{n+1} - \bar{T}_{f,i}^{n+1}\big)\big]\Delta t + \frac{f_f|v^3|}{2D_h c_f}\Delta t
\end{aligned}
\tag{A.37}
$$

For all the hypotheses listed, this methodology defines a numerical scheme to solve the conjugate heat transfer equations which is explicit for the fluid part and implicit for the solid part. From the former expressions, the term $\bar{T}_{f,i}^{n+1}$ can be substituted in the discretized solid equation (Eq. 2.18), which will hence depend explicitly on the temperature of the fluid. This strategy allows for solving Eq. (2.18) efficiently with the tri-diagonal matrix algorithm in order to obtain the temperature distribution in the solid. The temperature distribution in the fluid is subsequently found by substitution in the presented expressions.

Appendix B

MATLAB code of the AMRR model

B.1   AMRR model

```
%%%%%%%%%%%%%%%%%%%%%%%%%%%%%%%%%%%%%%%%%%%%%%%%%%%%%%%%%%%%%%%%%%%%%%%%%%%
%%           Active Magnetic Regenerative Refrigerator Model          %%
%%         developed at the Polytechnical University of Valencia       %%
%%        in collaboration with the Technical University of Denmark    %%
%%        based on the work by K. Engelbrecht (2008) at UW-Madison     %%
%%%%%%%%%%%%%%%%%%%%%%%%%%%%%%%%%%%%%%%%%%%%%%%%%%%%%%%%%%%%%%%%%%%%%%%%%%%

% This input module takes regenerator and machine inputs, converts
them to AMR model inputs and calls the AMR model. Fluid flow rate and
magnetic field are determined for a generic AMRR reciprocating
machine.
% In order to consider the maldistribution effect in a Gd plates
regenerator, 'n' representative channels are modelled. The channels
are independent and its outlets are mixed in the reservoirs.
% The outputs of the regenerator model include the temperature profile
of the fluid and regnerator once cyclical steady state has been
achieved as well as pumping power and heating and cooling loads.

clear %clears the existing variable space before running the model

% Regenerator description
nbed=1; %number of beds in the regenerator
nchan=10; %number of channels per bed
w=.025; %m, width of flow channel in regenerator
L=.050; %m, length of each regenerator bed
e_plate=.001; %m, plate thickness
e_chan=[.0005];%m, channel height(s)

cnk=1; %axial conduction scaling factor
cff=1; %friction factor scaling factor
cNu=1; %Nusselt number scaling factor

n=length(e_chan); %number of representative channels (same height)
```

```matlab
h=(e_plate+e_chan)*(nchan/n); %m, thickness of each homogeneous
section of the stack
Ac=h*w; %m2, cross sectional area of each section

%% AMR inputs
TH=273.15+30; % Hot reservoir temperature, K
TC=273.15+15; %Cold end temperature, K
Qh=[0]; %Thermal load in cold reservoir, W (0 if TC is fixed)

Tamb=TH-1; %Ambient temperature, K

%% Linear machine inputs
for ii=1:n
    pacRAW{ii}=[e_plate,e_plate+e_chan(ii),w,nchan];
end
dblow=0.5; %Relative distance covered by fluid with respect to L
tblow=0.5; %Blow time, s

%% Model parameters
Nxmin=100; %Minimum number of spatial steps
Nt1=5;  %Number of time steps during lag time (piston and regenerator
stopped)
Nt2=30; %Number of time steps during magnetization (regenerator moving
and piston stopped)

tol=0.00001; %convergence tolerance

%% Define the user-defined functions called to determine properties
numlayer=1; %Number of MCM layers in the regenerator
mcm_inp=[293, 1]; %[Curie temp of layer 1, fraction of regerator
occupied by layer 1; ...]
mcmfun={@Gd}; %{MCM property function for layer 1; ...}
fluidfun=@ethgly50; %Fluid properties function
bedcorrfun=@AlignRectChan; %Regenerator correlation function
Navgfun=@Navg_ctt_prof; %Demagnetization factor profile function

%% Convert machine inputs to AMR inputs and call AMR model
muoHapp=cell(1,length(e_chan));
Navg=cell(1,length(e_chan));

for mm=1:length(e_chan)
[mdot, muoHapp, Nx, t, tau, dwell, Vres, Ramb_res,
UA_HHEX]=LinearMach(tblow, dblow, muoH_amp, pacRAW, L, Nxmin, Nt1,
Nt2, fluidfun, bedcorrfun);
xr=L*((1:Nx(mm))'-1/2)/Nx(mm); %Channel spatial grid
Navg{mm} = Navgfun(muoHapp{mm}, xr, TH); %Demagnetization factor
end

%Call AMR model
[ref_cap,heat_rej,Qmag,Qpump,COP,Pdrop,Tr,Tf,U,NTU,t_conv,count,TrC_ave,TrH_ave]=AMRregen_nchan(L,Ac,t,tau,dwell,Nx,mdot,TC,TH,n_beds,tol,cnk,cNu,cff,pacRAW,fluidfun,bedcorrfun,muoHapp,numlayer,mcm_inp,mcmfun,Navg,Qh,Vres,Ramb_res,Tamb,UA_HHEX);
fprintf('\n Finished\n\n')
```

```matlab
function[ref_cap,heat_rej,Qmag,Qpump,COP,Pdrop,Tr,Tf,U,NTU,t_conv,coun
t,TrC_ave,TrH_ave]=AMRregen_nchan(L,Ac,t,tau,dwell,Nx,mdot,TC,TH,n_bed
s,tol,cnk,cNu,cff,pacRAW,fluidfun,bedcorrfun,muoHapp,numlayer,mcm_inp,
mcmfun,Navg,Qh,Vres,Ramb_res,Tamb,UA_HHEX)
%% AMRregen_nchan  Main AMR model that calculates the regenerator
                   temperature profiles and performance at the
                   cyclical steady state, given the physical
                   characteristics of the regenerator and the fluid
                   flow and magnetic field profiles during the AMR
                   cycle. The model can take into account the fluid
                   flow maldistribution as the sum of independent
                   channels. The model can compute the average
                   temperature in the reservoirs.
                   Adapted from Engelbrecht 2008 [11].

%% Configure manually model options
startT=0;%0=start from constant T = TH  1=start from linear T profile
ambloss=0;%0=no losses to the ambient 1= include losses to the ambient
NM=0.5; %Numerical Method: 0=explicit 1=implicit 0.5=Crank Nicholson
TCctt=1;  %1=TC constant 0=TC from equation of cold reservoir
THctt=1;  %1=TH constant 0=TH from equation of hot reservoir

%%INITIALIZATION
%Time
Nt=length(t)-1;

tblow=0;
for j=1:Nt
if ((mdot(j)+mdot(j+1))/2)<0
    tblow=tblow+(t(j+1)-t(j));
end
end

%Spatial grid
xf=cell(1,nchan);
dx=0*(1:nchan);
for mm=1:nchan
ii=1:Nx(mm);
xf{mm}=L*(ii'-1/2)/Nx(mm); %fluid spatial grid
dx(mm)=xf{mm}(2)-xf{mm}(1);
end
xr=xf; %regenerator spatial grid

% Prealocate matrixes for speed
Tf=cell(1,nchan);  %Fluid temperature
Tr=cell(1,nchan);  %Regenerator temperature
TCedg=zeros(Nt,nchan); %Mean T at the cold border of the regenerator
THedg=zeros(Nt,nchan); %Mean T at the hot border of the regenerator
ECedg=0*(1:nchan);

muoH=cell(1,nchan); %Internal magnetic field
Mo=cell(1,nchan); %Magnetization at the time step j
cmuoH=cell(1,nchan);
dsdmuoH=cell(1,nchan);
kr=cell(1,nchan);
sr=cell(1,nchan);
hr=cell(1,nchan);
rhor=cell(1,nchan);
Nuf=cell(1,nchan);
kf=cell(1,nchan);
```

```matlab
v=zeros(Nt,nchan);
deltaP=zeros(Nt,nchan);

%%Bed parameters
nchan=length(Ac);
dh=zeros(size(Ac));
eps=zeros(size(Ac));
as=zeros(size(Ac));

for ii=1:nchan
[dh(ii),eps(ii),as(ii)]=pack_geom(pacRAW{ii},bedcorrfun);
pacCOOKED{ii}=[pacRAW{ii},as(ii),eps(ii),dh(ii),cNu,cff,cnk,L];
end

if startT==0    %%start model with a constant temperature profile (TH)
    for ii=1:nchan
    Tr{ii}(:,1)=TH; %initial regenerator temp
    Tf{ii}(:,1)=TH;  %initial fluid temp
    end
else            %%start model with a ramp temperature profile
    for ii=1:nchan
    Tr{ii}(:,1)=TH-xr{ii}*(TH-TC)/L; %initial regenerator temp
    Tf{ii}(:,1)=TH-xf{ii}*(TH-TC)/L;  %initial fluid temp
    end
end

% Initialize variables before beginning the main loop.
done=0;
count=0; %Number of cycles

E_acum_cycle(1:nchan)=0;
E_init(1:nchan)=0;
ref_load=0;
heat_load=0;
Wpump=0;
Wmag=0;
TC_ave=0;
TrC_ave=0;
TrH_ave=0;

Ef=0*(1:Nt+1);
Er=0*(1:Nt+1);
E_acum=0;
E_fin_total=0;

Wmag_Mo=0;
Wmag_H=0;
Vdot_ave=0;
TCedg_ave=0;
THedg_ave=0;
Nu_ave=0;
kf_ave=0;

TC_evo=TC; %Record evolution of TC until steady state

%Cold reservoir
TrC(1:Nt)=TC;
VrC(1:Nt)=Vres;   %Initial volume of cold reservoir
UA_amb=1/Ramb_res*ambloss;

%Hot reservoir
```

```matlab
TrH(1:Nt)=TH;
VrH(1:Nt)=Vres;   %Initial volume of hot reservoir
UA_hex=UA_HHEX;

%Create interpolant function with material properties and
magnetization data
[interpS, interph0, interpMag]=create_interp(mcmfun);
pac_interpprops={interpS,interph0,interpMag}; %pack interpolants

%Calculate initial internal magnetic field and properties
magpropfun=@mcmprops;
for ii=1:nchan
[muoH{ii}(:,1), Mo{ii}(:,1)] = DeMagIntLayer(Navg{ii}(:,1),mcm_inp,
mcmfun,muoHapp{ii}(:,1),Tr{ii}(:,1),muoHapp{ii}(:,1),numlayer,L,xr{ii}
,interpMag);
[cmuoH{ii}(:,1),dsdmuoH{ii}(:,1),rhor{ii},kr{ii}(:,1),sr{ii}(:,1),hr{i
i}(:,1)]=magpropfun(xr{ii},L,Tr{ii}(:,1),muoH{ii}(:,1),numlayer,mcm_in
p,mcmfun,interpS,interph0);
[muf1,kf1,cf1{ii},rhof,hf1,sf1]=fluidfun(Tf{ii}(:,1));
end
rhor_ave=mean(rhor{1}(:));

%% MAIN LOOP
tic
while(done==0)

for j=1:Nt
time=t(j);
dt=t(j+1)-t(j);

Vdot=(mdot(j)+mdot(j+1))/2/rhof; %Mean flow rate during the time step
v(j,:)=speed_distrib(Vdot,pacRAW,bedcorrfun); %Speed in each channel

if Vdot>0   %%%HOT-TO-COLD%%%%%%%%%%%%%%%%%%%%%%%%%%%%%%%%%%%%%%%%%%%%%

    %Calculate temperature in hot reservoir (hex)
    [mufH,kfH,cfH,rhofH,hfH,sfH]=fluidfun(TrH(j));
    VrH(j+1)=-Vdot*dt+VrH(j);

TrH(j+1)=(1/(rhofH*cfH*VrH(j+1)+NM*(UA_hex*dt+abs(Vdot)*rhofH*cfH*dt))
)*(rhofH*cfH*VrH(j)*TrH(j)-(1-
NM)*abs(Vdot)*rhofH*cfH*dt*TrH(j)+UA_hex*(Tamb-(1-NM)*TrH(j))*dt);
    TH=TH*THctt+(1-THctt)*(TrH(j+1)+TrH(j))/2;

    for ii=1:nchan
    [Tr{ii}(:,j+1), Tf{ii}(:,j+1), THedg(j,ii), TCedg(j,ii),
muoH{ii}(:,j+1), cmuoH{ii}(:,j+1), dsdmuoH{ii}(:,j+1), kr{ii}(:,j+1),
deltaP(j,ii), E_fin(ii), E_acum_timestep, Nuf{ii}(:,j), kf{ii}(:,j)]=
AMRchan(dt,Tf{ii}(:,j),Tr{ii}(:,j),v(j,ii),xr{ii},Nx(ii),TH,TC,Ac(ii),
fluidfun,bedcorrfun,pacCOOKED{ii},magpropfun,muoH{ii}(:,j),cmuoH{ii}(:
,j),dsdmuoH{ii}(:,j),kr{ii}(:,j),rhor{ii},numlayer,mcm_inp,mcmfun,Navg
{ii}(:,j+1),muoHapp{ii}(:,j+1),NM,E_init(ii),pac_interpprops);
    E_init(ii)=E_fin(ii); %For next timestep
    E_acum_cycle(ii)=E_acum_cycle(ii)+E_acum_timestep;

    %Energy leaving the regenerator (-->entering the cold reservoir)
    [mufedg,kfedg,cfedg,rhofedg,hfedg,sfedg]=fluidfun(TCedg(j,ii));
    ECedg(ii)=abs(v(j,ii))*rhofedg*cfedg*dt*eps(ii)*Ac(ii)*TCedg(j,ii);

    %Energy entering the regenerator (<--leaving the hot reservoir)
    [mufedg,kfedg,cfedg,rhofedg,hfedg,sfedg]=fluidfun(TH);
```

```matlab
        EHedg(ii)=abs(v(j,ii))*rhofedg*cfedg*dt*eps(ii)*Ac(ii)*TH;

    end

    %Temperature of the cold reservoir (perfect mixing)
    [mufC,kfC,cfC,rhofC,hfC,sfC]=fluidfun(TrC(j));
    VrC(j+1)=Vdot*dt+VrC(j);

TrC(j+1)=(1/(rhofC*cfC*VrC(j+1)+UA_amb*NM*dt))*(rhofC*cfC*VrC(j)*TrC(j
)+sum(ECedg)+UA_amb*(Tamb-(1-NM)*TrC(j))*dt+Qh*dt);

    %Calculate refrigeration and heating loads
    ref_load=ref_load-sum(ECedg);
    heat_load=heat_load-sum(EHedg);

    %Compute average values of some variables for postprocessing
     Vdot_ave=Vdot_ave+Vdot*dt;
     TCedg_ave=TCedg_ave+TCedg(j,:)*dt;
     TrC_ave=TrC_ave+(TrC(j+1)+TrC(j))/2*dt;
     TrH_ave=TrH_ave+(TrH(j+1)+TrH(j))/2*dt;
     Nu_ave=Nu_ave+mean(Nuf{1}(:,j))*dt;
     kf_ave=kf_ave+mean(kf{1}(:,j))*dt;

elseif Vdot<0   %%%COLD-TO-HOT%%%%%%%%%%%%%%%%%%%%%%%%%%%%%%%%%%%%%%%%%

%Calculate temperature in cold reservoir (thermal losses+thermal load)
    [mufC,kfC,cfC,rhofC,hfC,sfC]=fluidfun(TrC(j));
    VrC(j+1)=Vdot*dt+VrC(j);

TrC(j+1)=(1/(rhofC*cfC*VrC(j+1)+NM*(UA_amb*dt+abs(Vdot)*rhofC*cfC*dt))
)*(rhofC*cfC*VrC(j)*TrC(j)-(1-NM)*abs(Vdot)*rhofC*cfC*dt*TrC(j)
+UA_amb*(Tamb-(1-NM)*TrC(j))*dt+Qh*dt);
    TC=TC*TCctt+(1-TCctt)*(TrC(j+1)+TrC(j))/2;

    for ii=1:nchan
    [Tr{ii}(:,j+1) Tf{ii}(:,j+1) THedg(j,ii) TCedg(j,ii)
muoH{ii}(:,j+1) cmuoH{ii}(:,j+1) dsdmuoH{ii}(:,j+1) kr{ii}(:,j+1)
deltaP(j,ii) E_fin(ii) E_acum_timestep]=
AMRchan(dt,Tf{ii}(:,j),Tr{ii}(:,j),v(j,ii),xr{ii},Nx(ii),TH,TC,Ac(ii),
fluidfun,bedcorrfun,pacCOOKED{ii},magpropfun,muoH{ii}(:,j),cmuoH{ii}(:
,j),dsdmuoH{ii}(:,j),kr{ii}(:,j),rhor{ii},numlayer,mcm_inp,mcmfun,Navg
{ii}(:,j+1),muoHapp{ii}(:,j+1),NM,E_init(ii),pac_interpprops);
    E_init(ii)=E_fin(ii); %For next timestep
    E_acum_cycle(ii)=E_acum_cycle(ii)+E_acum_timestep;

    %Energy leaving the regenerator (-->entering the hot reservoir)
    [mufedg,kfedg,cfedg,rhofedg,hfedg,sfedg]=fluidfun(THedg(j,ii));
    EHedg(ii)=abs(v(j,ii))*rhofedg*cfedg*dt*eps(ii)*Ac(ii)*THedg(j,ii);

    %Energy entering the regenerator (<--leaving the cold reservoir)
    [mufedg,kfedg,cfedg,rhofedg,hfedg,sfedg]=fluidfun(TC);
    ECedg(ii)=abs(v(j,ii))*rhofedg*cfedg*dt*eps(ii)*Ac(ii)*TC;

    end

    %Temperature of the hot reservoir (perfect mixing)
    [mufH,kfH,cfH,rhofH,hfH,sfH]=fluidfun(TrH(j));
    VrH(j+1)=-Vdot*dt+VrH(j);

TrH(j+1)=(1/(rhofH*cfH*VrH(j+1)+UA_hex*NM*dt))*(rhofH*cfH*VrH(j)*TrH(j
)+sum(EHedg)+UA_hex*(Tamb-(1-NM)*TrH(j))*dt);
```

```matlab
        %Calculate refrigeration and heating loads
        heat_load=heat_load+sum(EHedg);
        ref_load=ref_load+sum(ECedg);

        %Compute average values of some variables for postprocessing
        THedg_ave=THedg_ave+THedg(j,:)*dt;
        TrC_ave=TrC_ave+(TrC(j+1)+TrC(j))/2*dt;
        TrH_ave=TrH_ave+(TrH(j+1)+TrH(j))/2*dt;

    else  %%Vdot==0   FLUID STOPPED%%%%%%%%%%%%%%%%%%%%%%%%%%%%%%%%%%%%%%

        for ii=1:nchan
        [Tr{ii}(:,j+1) Tf{ii}(:,j+1) THedg(j,ii) TCedg(j,ii)
muoH{ii}(:,j+1) cmuoH{ii}(:,j+1) dsdmuoH{ii}(:,j+1) kr{ii}(:,j+1)
deltaP(j,ii) E_fin(ii) E_acum_timestep]=
AMRchan(dt,Tf{ii}(:,j),Tr{ii}(:,j),v(j,ii),xr{ii},Nx(ii),TH,TC,Ac(ii),
fluidfun,bedcorrfun,pacCOOKED{ii},magpropfun,muoH{ii}(:,j),cmuoH{ii}(:
,j),dsdmuoH{ii}(:,j),kr{ii}(:,j),rhor{ii},numlayer,mcm_inp,mcmfun,Navg
{ii}(:,j+1),muoHapp{ii}(:,j+1),NM,E_init(ii),pac_interpprops);
        E_init(ii)=E_fin(ii); %For next timestep
        E_acum_cycle(ii)=E_acum_cycle(ii)+E_acum_timestep;
        end

        %Heat losses in the cold reservoir
        [mufC,kfC,cfC,rhofC,hfC,sfC]=fluidfun(TrC(j));
        VrC(j+1)=Vdot*dt+VrC(j);

TrC(j+1)=(1/(rhofC*cfC*VrC(j+1)+NM*UA_amb*dt))*(rhofC*cfC*VrC(j)*TrC(j
)+UA_amb*(Tamb-(1-NM)*TrC(j))*dt+Qh*dt);

        %Heat losses in the hot reservoir
        [mufH,kfH,cfH,rhofH,hfH,sfH]=fluidfun(TrH(j));
        VrH(j+1)=Vdot*dt+VrH(j);

TrH(j+1)=(1/(rhofH*cfH*VrH(j+1)+NM*UA_hex*dt))*(rhofH*cfH*VrH(j)*TrH(j
)+UA_hex*(Tamb-(1-NM)*TrH(j))*dt);

        %Compute average values of some variables for postprocessing
        TrC_ave=TrC_ave+(TrC(j+1)+TrC(j))/2*dt;
        TrH_ave=TrH_ave+(TrH(j+1)+TrH(j))/2*dt;

end

%Calculate pump work
Wpump=Wpump+abs(Vdot)*deltaP(j,1)*dt; %J %same deltaP in all channels

%Compute average values of some variables for postprocessing
TC_ave=TC_ave+TC*dt;
TH_ave=TH_ave+TH*dt;

end

%toc %one cycle simulated
count=count+1;

%Save cold end temperature
TC_ave=TC_ave/tau;
TrC_ave=TrC_ave/tau;
TC_evo(count+1)=TrC_ave;
TrH_ave=TrH_ave/tau;
```

```
%Calculate change in energy over the cycle
for ii=1:nchan
Ef=Ef+sum(Ac(ii)*eps(ii)*rhof*cf1{ii}(1)*Tf{ii}(:,:)*dx(ii),1);
%fluid energy entrained in one bed of the regenerator
Er=Er+sum(Ac(ii)*(1-eps(ii))*rhor{ii}(1)*cmuoH{ii}(:,:).*Tr{ii}(:,:)
*dx(ii),1); %regenerator energy for one bed
end
dE_cycle=abs(Er(:,Nt+1)-Er(:,1))+abs(Ef(:,Nt+1)-Ef(:,1)); %absolute
value of the change in energy over one cycle
Emax=max(Ef+Er); %maximum energy in the solid and fluid during
previous cycle
Emin=min(Ef+Er); %minimum energy in the solid and fluid during
previous cycle
err=abs(dE_cycle/(Emax-Emin)); %figure of merit for cyclical steady
state convergence

%%Energy conservation test over cycle
c=sum(E_acum_cycle)-(sum(E_fin)-0);    %E_init(1)=0
c_rel=c/(sum(E_fin)-0);
c_error(count)=c;

%Check energy conservation with calculated loads (consistency of
estimated outlet temps)
cons_load=ref_load-Wmag+Wpump-(heat_load+(sum(E_fin)-0));

% Accumulate energy for final balance
E_fin_total=E_fin_total+sum(E_fin);
E_acum=E_acum+sum(E_acum_cycle);

if err<tol  %system has reached steady state, exit while loop.
      done=1;
else %steady state has not been achieved, continue to next cycle.

            %Reset variables that are used in the cycle
            Er=0*Er;
            Ef=0*Ef;
            E_acum_cycle=0*E_acum_cycle;
            E_init=0*E_init;
            Wpump=0;
            ref_load=0;
            heat_load=0;
            TC_ave=0;
            TrC_ave=0;
            TrH_ave=0;

            Vdot_ave=0;
            TCedg_ave=0;
            THedg_ave=0;
            Nu_ave=0;
            kf_ave=0;

            VrC(1)=VrC(Nt+1);
            TrC(1)=TrC(Nt+1);
            VrH(1)=VrH(Nt+1);
            TrH(1)=TrH(Nt+1);

            for ii=1:nchan
            Tr{ii}(:,1)=Tr{ii}(:,Nt+1);%initial regen T for next cycle
            Tf{ii}(:,1)=Tf{ii}(:,Nt+1);%initial fluid T for next cycle
            muoH{ii}(:,1)=muoH{ii}(:,Nt+1);
            cmuoH{ii}(:,1)=cmuoH{ii}(:,Nt+1);
```

```
                dsdmuoH{ii}(:,1)=dsdmuoH{ii}(:,Nt+1);
                kr{ii}(:,1)=kr{ii}(:,Nt+1);
                end
            end
end


%% POST-PROCESSING
t_conv=toc      %time to convergence
count           %number of cycles until steady state
c=sum(c_error) %absolute error on energy conservation
c_rel=(E_acum-E_fin_total)/(E_fin_total) %relative error on E cons

%%Performance
ref_cap=ref_load/tau*n_beds; % W, refrigeration rate in W supplied to
the cold reservoir by the entire regenerator
heat_rej=heat_load*n_beds/tau; %W, heat transfer rate from the hot
reservoir in W to the surroundings by the entire regenerator
Qpump=Wpump*n_beds/tau; % W, rate of work for fluid pumping
Qmag=heat_rej-ref_cap-Qpump; %W, rate of magnetic work
COP=ref_cap/(heat_rej-ref_cap); %Thermal COP (not taking into account
mechanical efficiencies)
COP_Carnot=(TC)/(TH-TC); %Carnot efficiency for a cycle operating
between the specified hot and cold reservoir temperatures

if TCctt==0
    TC_span=TrC_ave;
else
    TC_span=TC;
end

if THctt==0
    TH_span=TrH_ave;
else
    TH_span=TH;
end
DT_span=TH_span-TC_span; %Temperature span

Pdrop=max(deltaP(:,1))/10^5; %bar

%%Regenerator performance
mdot_ave=Vdot_ave/tblow*rhof;
Nu_ave=Nu_ave/tblow;
kf_ave=kf_ave/tblow;
V=Ac*L;

cr_ave=0;
cf_ave=0;
for ii=1:nchan
cr_ave=cr_ave+mean(mean(cmuoH{ii}));
cf_ave=cf_ave+mean(cf1{ii});
end
cr_ave=cr_ave/nchan;
cf_ave=cf_ave/nchan;

Cr=sum(mean(rhor{1})*V.*(1-eps)*cr_ave);
Cf=sum(rhof*V.*eps*cf_ave);
R=Cf/Cr;
lambda=tau/2*(1-dwell);

U=mdot_ave*cf_ave*tblow/Cr;    %Utilization
NTU=Nu_ave*kf_ave*Ac(1)*L*as(1)/(dh(1)*mdot_ave*cf_ave); %1 channel
```

```matlab
function [Tr_next Tf_next THedg TCedg muoH_next cmuoH_next
dsdmuoH_next kr_next deltaP E_fin E_acum_timestep Nuf kf
h]=AMRchan(dt,Tf,Tr,v,xr,Nx,TH,TC,Ac,fluidfun,bedcorrfun,pacCOOKED,mag
propfun,muoH,cmuoH,dsdmuoH,kr,rhor,numlayer,mcm_inp,mcmfun,Navg_next,m
uoHapp_next,NM,E_init,pac_interpprops)
%% AMRchan   Core function of the AMR model that solves the spatial
            regenerator temperature profiles and MCM properties along
            one pair channel+plate for the next time step, based on the
            HEIS numerical scheme. The model takes into account the
            demagnetizing effect and the variation of the MCM
            properties along the time step.

%Unpack inputs
eps=pacCOOKED(6);
as=pacCOOKED(5);
dh=pacCOOKED(7);
L=pacCOOKED(11);
dx=xr(2)-xr(1);
xf=xr;

interpS=pac_interpprops{1};
interph0=pac_interpprops{2};
interpMag=pac_interpprops{3};

%Preallocate variables
Tr_next=zeros(size(Tr));
Tf_next=zeros(size(Tf));

slo_f=0*(1:Nx); %Slope of the temperature distribution (FLUID)
slo_r=0*(1:Nx); %Slope of the temperature distribution (SOLID)
left=0*(1:Nx); %Integral T(x=i-1/2, t=j)
right=0*(1:Nx); %Integral T(x=i+1/2, t=j)
a=0*(1:Nx);  % Coefficients of the solid equation
b=0*(1:Nx);
c=0*(1:Nx);
d=0*(1:Nx);

%Calculate properties at current time step
[muf,kf,cf,rhof,hf,sf]=fluidfun(Tf);
Prf=cf.*muf./kf; %Prandtl number
Ref=abs(v)*dh*rhof./muf; %Reynolds number based on hydraulic diameter

[Nuf,ff,kstat,kdisp]=bedcorrfun(pacCOOKED,Ref,Prf,kf,kr,v,muf,rhof,cf,
xf);
dP=ff.*v.^2/(2*dh)*rhof*L/Nx; %Pa, Pressure drop
deltaP=sum(dP);

iter=0;
count_iter=0;
alpha=1;
Tr_prima=Tr;

while (iter==0) %Iteration in time step until T(:,j+1)'=T(:,j+1)

[muoH_next,Mo_next]=DeMagIntLayer(Navg_next,mcm_inp,mcmfun,muoHapp_nex
t,Tr_prima,muoH,numlayer,L,xr,interpMag);

[cmuoH_next,dsdmuoH_next,rhor,kr_next,sr_next,hr_next]=magpropfun(xr,L
,Tr_prima,muoH_next,numlayer,mcm_inp,mcmfun,interpS,interph0);
```

```matlab
    %%Calculate coefficients in the equations
    h=Nuf.*kf/dh;
    Kk=((kr+kr_next)/2)./((cmuoH+cmuoH_next)/2)./rhor;
    Khr=h*as./(rhor*(1-eps))./((cmuoH+cmuoH_next)/2);
    Khf=h./cf*as/(rhof*eps);
    KdP=ff*(abs(v))^3/2/dh./cf;

if(v>0) %%%%%%%%%%%% HOT - TO - COLD (From 1 to Nx) %%%%%%%%%

    %%%%Calculate temperature distribution slopes

        %Solid
        slo_r(1)=(Tr(2)-Tr(1))/dx;
        slo_r(2:Nx-1)=(Tr(3:Nx)-Tr(1:Nx-2))/(2*dx);
        slo_r(Nx)=(Tr(Nx)-Tr(Nx-1))/dx;

        %Fluid  %MC limiter %%%%%%%%%%%%%%%%%%
            up=0*(1:Nx);
            up(1)=2*(Tf(1)-TH)/dx;
            up(2:Nx-1)=2*(Tf(2:Nx-1)-Tf(1:Nx-2))/dx;

            down=0*(1:Nx);
            down(1)=2*(Tf(2)-Tf(1))/dx;
            down(2:Nx-1)=2*(Tf(3:Nx)-Tf(2:Nx-1))/dx;

            cent=0*(1:Nx);
            cent(1)=(Tf(2)-TH)/2/dx;
            cent(2:Nx-1)=(Tf(3:Nx)-Tf(1:Nx-2))/2/dx;

            for i=1:Nx-1
            if down(i)*up(i)<=0
                aux=0;
            elseif abs(down(i))<abs(up(i))
                aux=down(i);
            else
                aux=up(i);
            end

            if cent(i)*aux<=0
                slo_f(i)=0;
            elseif abs(cent(i))<abs(aux)
                slo_f(i)=cent(i);
            else
                slo_f(i)=aux;
            end
            end

            slo_f(Nx)=2*(Tf(Nx)-Tf(Nx-1))/dx;

    %%%% Calculation of integrals T(x=i+1/2, t=j) and T(x=i-1/2, t=j)
    % HEIS 1: mean DT is constant during the timestep
    left(1)=dt*TH; %Integral T(x=i-1/2,t=j)
    left(2:Nx)=dt*(Tf(1:Nx-1)+slo_f(1:Nx-1)'*dx/2+(Khf(1:Nx-
1).*(Tr(1:Nx-1)-Tf(1:Nx-1))-abs(v)*slo_f(1:Nx-1)')*dt/2); %Integral
T(x=i-1/2,t=j)

right(1:Nx)=dt*(Tf(1:Nx)+slo_f(1:Nx)'*dx/2+(Khf(1:Nx).*(Tr(1:Nx)-
Tf(1:Nx))-abs(v)*slo_f(1:Nx)')*dt/2); %Integral T(x=i+1/2,t=j)
```

```
    %%%% Calculation of solid equation coefficients -- a(i)Tr(i-
1,j+1)+b(i)Tr(i,j+1)+c(i)Tr(i+1,j+1)=d(i)

    a(2:Nx)=-NM*Kk(2:Nx)*dt/dx^2;
    b(1)=1+NM*Kk(1)*dt/dx^2+NM*Khr(1)*dt*(1-
Khf(1)*dt*NM/(1+Khf(1)*dt*NM))+NM/((cmuoH(1)+cmuoH_next(1))/2)*(dsdmuo
H(1)+dsdmuoH_next(1))/2*(muoH_next(1)-muoH(1));
    b(2:Nx-1)=1+2*NM*Kk(2:Nx-1)*dt/dx^2+NM*dt*Khr(2:Nx-1).*(1-
Khf(2:Nx-1)*dt*NM./(1+Khf(2:Nx-1)*dt*NM))+NM./((cmuoH(2:Nx-
1)+cmuoH_next(2:Nx-1))/2).*(dsdmuoH(2:Nx-1)+dsdmuoH_next(2:Nx-
1))/2.*(muoH_next(2:Nx-1)-muoH(2:Nx-1));
    b(Nx)=1+NM*Kk(Nx)*dt/dx^2+NM*Khr(Nx)*dt*(1-
Khf(Nx)*dt*NM/(1+Khf(Nx)*dt*NM))+NM/((cmuoH(Nx)+cmuoH_next(Nx))/2)*(ds
dmuoH(Nx)+dsdmuoH_next(Nx))/2*(muoH_next(Nx)-muoH(Nx));
    c(1:Nx-1)=-NM*Kk(1:Nx-1)*dt/dx^2;
    d(1)=Tr(1)+(1-NM)*dt*(Kk(1)/dx^2*(Tr(2)-Tr(1))-Khr(1)*(Tr(1)-
Tf(1)))+NM*dt*Khr(1)/(1+Khf(1)*dt*NM)*(Tf(1)+abs(v)/dx*(left(1)'-
right(1)'))+(1-NM)*dt*Khf(1)*(Tr(1)-Tf(1))+KdP(1)*dt)-(1-
NM)/((cmuoH(1)+cmuoH_next(1))/2)*Tr(1)*(dsdmuoH(1)+dsdmuoH_next(1))/2*
(muoH_next(1)-muoH(1));
    d(2:Nx-1)=Tr(2:Nx-1)+(1-NM)*dt*(Kk(2:Nx-1)/dx^2.*(Tr(3:Nx)-
2*Tr(2:Nx-1)+Tr(1:Nx-2))-Khr(2:Nx-1).*(Tr(2:Nx-1)-Tf(2:Nx-
1)))+NM*dt*Khr(2:Nx-1)./(1+Khf(2:Nx-1)*dt*NM).*(Tf(2:Nx-
1)+abs(v)/dx*(left(2:Nx-1)'-right(2:Nx-1)')+(1-NM)*dt*Khf(2:Nx-
1).*(Tr(2:Nx-1)-Tf(2:Nx-1))+KdP(2:Nx-1)*dt)-(1-NM)./((cmuoH(2:Nx-
1)+cmuoH_next(2:Nx-1))/2).*Tr(2:Nx-1).*(dsdmuoH(2:Nx-
1)+dsdmuoH_next(2:Nx-1))/2.*(muoH_next(2:Nx-1)-muoH(2:Nx-1));
    d(Nx)=Tr(Nx)+(1-NM)*dt*(Kk(Nx)/dx^2*(Tr(Nx-1)-Tr(Nx))-
Khr(Nx)*(Tr(Nx)-
Tf(Nx)))+NM*dt*Khr(Nx)/(1+Khf(Nx)*dt*NM)*(Tf(Nx)+abs(v)/dx*(left(Nx)'-
right(Nx)'))+(1-NM)*Khf(Nx)*dt*(Tr(Nx)-Tf(Nx))+KdP(Nx)*dt)-(1-
NM)/((cmuoH(Nx)+cmuoH_next(Nx))/2)*Tr(Nx)*(dsdmuoH(Nx)+dsdmuoH_next(Nx
))/2*(muoH_next(Nx)-muoH(Nx));

    %%%%% TDMA algorithm

    c(1)=c(1)/b(1); % Division by zero risk.
    d(1)=d(1)/b(1);

    for i = 2:Nx
        temp=b(i)-a(i)*c(i-1);
        c(i)=c(i)/temp;
        d(i)=(d(i)-a(i)*d(i-1))/temp;
    end

    Tr_next(Nx)=d(Nx);
    Tf_next(Nx)=1/(1+Khf(Nx)*dt*NM)*(Tf(Nx)+abs(v)/dx*(left(Nx)-
right(Nx))+Khf(Nx)*dt*((1-NM)*Tr(Nx)+NM*Tr_next(Nx))-Khf(Nx)*dt*(1-
NM)*Tf(Nx)+KdP(Nx)*dt);

    for i=(Nx-1):-1:1
        Tr_next(i)=d(i)-c(i)*Tr_next(i+1);
        Tf_next(i)=1/(1+Khf(i)*dt*NM)*(Tf(i)+abs(v)/dx*(left(i)-
right(i))+Khf(i)*dt*((1-NM)*Tr(i)+NM*Tr_next(i))-Khf(i)*dt*(1-
NM)*Tf(i)+KdP(i)*dt);
    end

    E_acum_timestep=abs(v)*dt*eps*Ac*rhof*cf(Nx)*(TH-
(Tf(Nx)+slo_f(Nx)*(dx-abs(v)*dt)/2))-
1/2*dt*Khf(Nx)*rhof*eps*cf(Nx)*Ac*abs(v)*dt*(Tr(Nx)-
```

```
Tf(Nx))+sum(dP)*abs(v)*Ac*eps*dt-sum(Ac*(1-
eps)*dx*rhor.*(dsdmuoH+dsdmuoH_next)/2.*(Tr+Tr_next)/2.*(muoH_next-
muoH)));

    %%%% Edge temperatures
    THedg=TH;
    TCedg=Tf(Nx)+slo_f(Nx)*(dx-abs(v)*dt)/2+Khf(Nx)*dt/2*(Tr(Nx)-
Tf(Nx))+KdP(Nx)*dt/2;

elseif(v<0) %%%%%%%%%%%% COLD - TO - HOT (From Nx to 1) %%%%%%%

    %%%%Calculate temperature distribution slopes
    %Solid
        slo_r(1)=(Tr(1)-Tr(2))/dx;
        slo_r(2:Nx-1)=(Tr(1:Nx-2)-Tr(3:Nx))/(2*dx);
        slo_r(Nx)=(Tr(Nx-1)-Tr(Nx))/dx;

    %Fluid   %MC limiter %%%%%%%%%%%%%%%%
            up=0*(1:Nx);
            up(2:Nx-1)=2*(Tf(2:Nx-1)-Tf(3:Nx))/dx;
            up(Nx)=2*(Tf(Nx)-TC)/dx;

            down=0*(1:Nx);
            down(2:Nx-1)=2*(Tf(1:Nx-2)-Tf(2:Nx-1))/dx;
            down(Nx)=2*(Tf(Nx-1)-Tf(Nx))/dx;

            cent=0*(1:Nx);
            cent(2:Nx-1)=(Tf(1:Nx-2)-Tf(3:Nx))/2/dx;
            cent(Nx)=(Tf(Nx-1)-TC)/2/dx;

            for i=1:Nx-1
            if down(i)*up(i)<=0
                aux=0;
            elseif abs(down(i))<abs(up(i))
                aux=down(i);
            else
                aux=up(i);
            end

            if cent(i)*aux<=0
                slo_f(i)=0;
            elseif abs(cent(i))<abs(aux)
                slo_f(i)=cent(i);
            else
                slo_f(i)=aux;
            end
            end

            slo_f(1)=2*(Tf(1)-Tf(2))/dx;

    %%%% Calculation of integrals T(x=i+1/2, t=j) and T(x=i-1/2,t=j)
        % HEIS 1: mean DT is constant during the timestep
            right(Nx)=dt*TC; %Integral T(x=i+1/2,t=j)
            right(1:Nx-1)=dt*(Tf(2:Nx)-
dx/2*slo_f(2:Nx)'+(Khf(2:Nx).*(Tr(2:Nx)-
Tf(2:Nx))+abs(v)*slo_f(2:Nx)')*dt/2); %Integral T(x=i+1/2,t=j)
            left(1:Nx)=dt*(Tf(1:Nx)-
dx/2*slo_f(1:Nx)'+(Khf(1:Nx).*(Tr(1:Nx)-
Tf(1:Nx))+abs(v)*slo_f(1:Nx)')*dt/2); %Integral T(x=i-1/2,t=j)
```

```matlab
    %%%% Calculation of solid equation coefficients -- a(i)Tr(i-
1,j+1)+b(i)Tr(i,j+1)+c(i)Tr(i+1,j+1)=d(i)

    a(2:Nx)=-NM*Kk(2:Nx)*dt/dx^2;   %This expressions will change with
time when we consider non-constant properties
    b(1)=1+NM*Kk(1)*dt/dx^2+NM*Khr(1)*dt*(1-
Khf(1)*dt*NM/(1+Khf(1)*dt*NM))+NM/((cmuoH(1)+cmuoH_next(1))/2)*(dsdmuo
H(1)+dsdmuoH_next(1))/2*(muoH_next(1)-muoH(1));
    b(2:Nx-1)=1+2*NM*Kk(2:Nx-1)*dt/dx^2+NM*dt*Khr(2:Nx-1).*(1-
Khf(2:Nx-1)*dt*NM./(1+Khf(2:Nx-1)*dt*NM))+NM./((cmuoH(2:Nx-
1)+cmuoH_next(2:Nx-1))/2).*(dsdmuoH(2:Nx-1)+dsdmuoH_next(2:Nx-
1))/2.*(muoH_next(2:Nx-1)-muoH(2:Nx-1));
    b(Nx)=1+NM*Kk(Nx)*dt/dx^2+NM*Khr(Nx)*dt*(1-
Khf(Nx)*dt*NM/(1+Khf(Nx)*dt*NM))+NM/((cmuoH(Nx)+cmuoH_next(Nx))/2)*(ds
dmuoH(Nx)+dsdmuoH_next(Nx))/2*(muoH_next(Nx)-muoH(Nx));
    c(1:Nx-1)=-NM*Kk(1:Nx-1)*dt/dx^2;
    d(1)=Tr(1)+(1-NM)*dt*(Kk(1)/dx^2*(Tr(2)-Tr(1))-Khr(1)*(Tr(1)-
Tf(1)))+NM*dt*Khr(1)/(1+Khf(1)*dt*NM)*(Tf(1)+abs(v)/dx*(right(1)-
left(1))+(1-NM)*Khf(1)*dt*(Tr(1)-Tf(1))+KdP(1)*dt)-(1-
NM)/((cmuoH(1)+cmuoH_next(1))/2)*Tr(1)*(dsdmuoH(1)+dsdmuoH_next(1))/2*
(muoH_next(1)-muoH(1));
    d(2:Nx-1)=Tr(2:Nx-1)+(1-NM)*dt*(Kk(2:Nx-1)/dx^2.*(Tr(3:Nx)-
2*Tr(2:Nx-1)+Tr(1:Nx-2))-Khr(2:Nx-1).*(Tr(2:Nx-1)-Tf(2:Nx-
1)))+NM*dt*Khr(2:Nx-1)./(1+Khf(2:Nx-1)*dt*NM).*(Tf(2:Nx-
1)+abs(v)/dx*(right(2:Nx-1)'-left(2:Nx-1)')+(1-NM)*dt*Khf(2:Nx-
1).*(Tr(2:Nx-1)-Tf(2:Nx-1))+KdP(2:Nx-1)*dt)-(1-NM)./((cmuoH(2:Nx-
1)+cmuoH_next(2:Nx-1))/2).*Tr(2:Nx-1).*(dsdmuoH(2:Nx-
1)+dsdmuoH_next(2:Nx-1))/2.*(muoH_next(2:Nx-1)-muoH(2:Nx-1));
    d(Nx)=Tr(Nx)+(1-NM)*dt*(Kk(Nx)/dx^2*(Tr(Nx-1)-Tr(Nx))-
Khr(Nx)*(Tr(Nx)-
Tf(Nx)))+NM*dt*Khr(Nx)/(1+Khf(Nx)*dt*NM)*(Tf(Nx)+abs(v)/dx*(right(Nx)-
left(Nx))+(1-NM)*Khf(Nx)*dt*(Tr(Nx)-Tf(Nx))+KdP(Nx)*dt)-(1-
NM)/((cmuoH(Nx)+cmuoH_next(Nx))/2)*Tr(Nx)*(dsdmuoH(Nx)+dsdmuoH_next(Nx
))/2*(muoH_next(Nx)-muoH(Nx));

    %%%%% TDMA algorithm

    c(1)=c(1)/b(1); % Division by zero risk.
    d(1)=d(1)/b(1);

    for i = 2:Nx
        temp=b(i)-a(i)*c(i-1);
        c(i)=c(i)/temp;
        d(i)=(d(i)-a(i)*d(i-1))/temp;
    end

    Tr_next(Nx)=d(Nx);
    Tf_next(Nx)=1/(1+Khf(Nx)*dt*NM)*(Tf(Nx)+abs(v)/dx*(right(Nx)-
left(Nx))+Khf(Nx)*dt*((1-NM)*Tr(Nx)+NM*Tr_next(Nx))-Khf(Nx)*dt*(1-
NM)*Tf(Nx)+KdP(Nx)*dt);

    for i=(Nx-1):-1:1
        Tr_next(i)=d(i)-c(i)*Tr_next(i+1);
        Tf_next(i)=1/(1+Khf(i)*dt*NM)*(Tf(i)+abs(v)/dx*(right(i)-
left(i))+Khf(i)*dt*((1-NM)*Tr(i)+NM*Tr_next(i))-Khf(i)*dt*(1-
NM)*Tf(i)+KdP(i)*dt);
    end

    E_acum_timestep=abs(v)*dt*eps*Ac*rhof*cf(1)*(TC-(Tf(1)-
slo_f(1)*(dx-abs(v)*dt)/2))-
```

```
1/2*dt*Khf(1)*rhof*eps*cf(1)*Ac*abs(v)*dt*(Tr(1)-
Tf(1))+sum(dP)*abs(v)*Ac*eps*dt-sum(Ac*(1-
eps)*dx*rhor.*(dsdmuoH+dsdmuoH_next)/2.*(Tr+Tr_next)/2.*(muoH_next-
muoH));

    %%%% Mean edge temperatures during a timestep
    THedg=Tf(1)-slo_f(1)*(dx-abs(v)*dt)/2+Khf(1)*dt/2*(Tr(1)-
Tf(1))+KdP(1)*dt/2;
    TCedg=TC;


else    %%%%% NO FLOW v=0 %%%%%%%%%%%%%%%%%%%%%%%%%%%%%%%%%%%%%%%

   %%%%Calculate temperature distribution slopes

    %Solid
        slo_r(1)=(Tr(2)-Tr(1))/dx;
        slo_r(2:Nx-1)=(Tr(3:Nx)-Tr(1:Nx-2))/(2*dx);
        slo_r(Nx)=(Tr(Nx)-Tr(Nx-1))/dx;

    %Fluid %MC limiter %%%%%%%%%%%%%%%%%%
            up=0*(1:Nx);
            up(1)=2*(Tf(1)-TH)/dx;
            up(2:Nx-1)=2*(Tf(2:Nx-1)-Tf(1:Nx-2))/dx;

            down=0*(1:Nx);
            down(1)=2*(Tf(2)-Tf(1))/dx;
            down(2:Nx-1)=2*(Tf(3:Nx)-Tf(2:Nx-1))/dx;

            cent=0*(1:Nx);
            cent(1)=(Tf(2)-TH)/2/dx;
            cent(2:Nx-1)=(Tf(3:Nx)-Tf(1:Nx-2))/2/dx;

            for i=1:Nx-1
            if down(i)*up(i)<=0
                aux=0;
            elseif abs(down(i))<abs(up(i))
                aux=down(i);
            else
                aux=up(i);
            end

            if cent(i)*aux<=0
                slo_f(i)=0;
            elseif abs(cent(i))<abs(aux)
                slo_f(i)=cent(i);
            else
                slo_f(i)=aux;
            end
            end

            slo_f(Nx)=2*(Tf(Nx)-Tf(Nx-1))/dx;

    %%%% Calculation of integrals T(x=i+1/2, t=j) and T(x=i-1/2, t=j)
            left(1)=dt*TH; %Integral T(x=i-1/2,t=j)
            left(2:Nx)=dt*(Tf(1:Nx-1)+slo_f(1:Nx-
1)'*dx/2+(Khf(1:Nx-
1).*(Tr(1:Nx-1)-Tf(1:Nx-1))-abs(v)*slo_f(1:Nx-1)')*dt/2); %Integral
T(x=i-1/2,t=j)
```

```matlab
right(1:Nx)=dt*(Tf(1:Nx)+slo_f(1:Nx)'*dx/2+(Khf(1:Nx).*(Tr(1:Nx)-
Tf(1:Nx))-abs(v)*slo_f(1:Nx)')*dt/2); %Integral T(x=i+1/2,t=j)

    %%%%% Calculation of solid equation coefficients -- a(i)Tr(i-
1,j+1)+b(i)Tr(i,j+1)+c(i)Tr(i+1,j+1)=d(i)

    a(2:Nx)=-NM*Kk(2:Nx)*dt/dx^2;   %This expressions will change with
time when we consider non-constant properties
    b(1)=1+NM*Kk(1)*dt/dx^2+NM*Khr(1)*dt*(1-
Khf(1)*dt*NM/(1+Khf(1)*dt*NM))+NM/((cmuoH(1)+cmuoH_next(1))/2)*(dsdmuo
H(1)+dsdmuoH_next(1))/2*(muoH_next(1)-muoH(1));
    b(2:Nx-1)=1+2*NM*Kk(2:Nx-1)*dt/dx^2+NM*dt*Khr(2:Nx-1).*(1-
Khf(2:Nx-1)*dt*NM./(1+Khf(2:Nx-1)*dt*NM))+NM./((cmuoH(2:Nx-
1)+cmuoH_next(2:Nx-1))/2).*(dsdmuoH(2:Nx-1)+dsdmuoH_next(2:Nx-
1))/2.*(muoH_next(2:Nx-1)-muoH(2:Nx-1));
    b(Nx)=1+NM*Kk(Nx)*dt/dx^2+NM*Khr(Nx)*dt*(1-
Khf(Nx)*dt*NM/(1+Khf(Nx)*dt*NM))+NM/((cmuoH(Nx)+cmuoH_next(Nx))/2)*(ds
dmuoH(Nx)+dsdmuoH_next(Nx))/2*(muoH_next(Nx)-muoH(Nx));
    c(1:Nx-1)=-NM*Kk(1:Nx-1)*dt/dx^2;
    d(1)=Tr(1)+(1-NM)*dt*(Kk(1)/dx^2*(Tr(2)-Tr(1))-Khr(1)*(Tr(1)-
Tf(1)))+NM*dt*Khr(1)/(1+Khf(1)*dt*NM)*(Tf(1)+abs(v)/dx*(right(1)-
left(1))+(1-NM)*Khf(1)*dt*(Tr(1)-Tf(1))+KdP(1)*dt)-(1-
NM)/((cmuoH(1)+cmuoH_next(1))/2)*Tr(1)*(dsdmuoH(1)+dsdmuoH_next(1))/2*
(muoH_next(1)-muoH(1));
    d(2:Nx-1)=Tr(2:Nx-1)+(1-NM)*dt*(Kk(2:Nx-1)/dx^2.*(Tr(3:Nx)-
2*Tr(2:Nx-1)+Tr(1:Nx-2))-Khr(2:Nx-1).*(Tr(2:Nx-1)-Tf(2:Nx-
1)))+NM*dt*Khr(2:Nx-1)./(1+Khf(2:Nx-1)*dt*NM).*(Tf(2:Nx-
1)+abs(v)/dx*(right(2:Nx-1)'-left(2:Nx-1)')+(1-NM)*dt*Khf(2:Nx-
1).*(Tr(2:Nx-1)-Tf(2:Nx-1))+KdP(2:Nx-1)*dt)-(1-NM)./((cmuoH(2:Nx-
1)+cmuoH_next(2:Nx-1))/2).*Tr(2:Nx-1).*(dsdmuoH(2:Nx-
1)+dsdmuoH_next(2:Nx-1))/2.*(muoH_next(2:Nx-1)-muoH(2:Nx-1));
    d(Nx)=Tr(Nx)+(1-NM)*dt*(Kk(Nx)/dx^2*(Tr(Nx-1)-Tr(Nx))-
Khr(Nx)*(Tr(Nx)-
Tf(Nx)))+NM*dt*Khr(Nx)/(1+Khf(Nx)*dt*NM)*(Tf(Nx)+abs(v)/dx*(right(Nx)-
left(Nx))+(1-NM)*Khf(Nx)*dt*(Tr(Nx)-Tf(Nx))+KdP(Nx)*dt)-(1-
NM)/((cmuoH(Nx)+cmuoH_next(Nx))/2)*Tr(Nx)*(dsdmuoH(Nx)+dsdmuoH_next(Nx
))/2*(muoH_next(Nx)-muoH(Nx));

    %%%%% TDMA algorithm

    c(1)=c(1)/b(1); % Division by zero risk.
    d(1)=d(1)/b(1);

    for i = 2:Nx
        temp=b(i)-a(i)*c(i-1);
        c(i)=c(i)/temp;
        d(i)=(d(i)-a(i)*d(i-1))/temp;
    end

    Tr_next(Nx)=d(Nx);
    Tf_next(Nx)=1/(1+Khf(Nx)*dt*NM)*(Tf(Nx)+abs(v)/dx*(left(Nx)-
right(Nx))+Khf(Nx)*dt*((1-NM)*Tr(Nx)+NM*Tr_next(Nx))-Khf(Nx)*dt*(1-
NM)*Tf(Nx)+KdP(Nx)*dt);

    for i=(Nx-1):-1:1
        Tr_next(i)=d(i)-c(i)*Tr_next(i+1);
        Tf_next(i)=1/(1+Khf(i)*dt*NM)*(Tf(i)+abs(v)/dx*(left(i)-
right(i))+Khf(i)*dt*((1-NM)*Tr(i)+NM*Tr_next(i))-Khf(i)*dt*(1-
NM)*Tf(i)+KdP(i)*dt);
    end
```

```
    E_acum_timestep=-sum(Ac*(1-
eps)*dx*rhor.*(dsdmuoH+dsdmuoH_next)/2.*(Tr+Tr_next)/2.*(muoH_next-
muoH));

    %%% Edge temperatures
    TCedg=Tf(Nx)+slo_f(Nx)*(dx-abs(v)*dt)/2+Khf(Nx)*dt/2*(Tr(Nx)-
Tf(Nx))+KdP(Nx)*dt/2;
    THedg=Tf(1)-slo_f(1)*(dx-abs(v)*dt)/2+Khf(1)*dt/2*(Tr(1)-
Tf(1))+KdP(1)*dt/2;

    end

    error_iter=max(abs(Tr_next-Tr_prima));

    if error_iter<0.001
        iter=1;
    else
        Tr_prima=alpha*Tr_next+(1-alpha)*Tr_prima;
        count_iter=count_iter+1;
        E_acum_timestep=0;
    end

    end

    %Check energy conservation in the time step
    E_fin=E_init+(sum(eps*Ac*rhof*cf.*Tf_next*L/Nx)+sum((1-
eps)*Ac*L/Nx*rhor.*(cmuoH+cmuoH_next)/2.*Tr_next)-
(sum(eps*Ac*rhof*cf.*Tf*L/Nx)+sum((1-
eps)*Ac*L/Nx*rhor.*(cmuoH+cmuoH_next)/2.*Tr)));
    cons=(E_fin-E_init)-E_acum_timestep;
```

B.2 Magnetocaloric material properties

```
function[cmuoH,dsdmuoH,rhor,kr,sr,hr]=mcmprops(x,L,Tr,muoH,numlayer,in
puts,mcmfunc,interpS,interph0);
%% mcmprops This function calculates the properties of the
          magnetocaloric material across the entire bed.  The bed may
          be composed of multiple layers and each layer may occupy a
          different fraction of the length of the bed. The range of
          nodes occupied by each layer is calculated and the
          properties for each layer are then calculated by calling
          the appropriate material property function (@mcmfunc).
          Adapted from Engelbrecht 2008 [11].
% INPUTS:
% numlayer: number of layers in the bed.
% inputs: array with dimension numlayer x 2. The array contains the
following variables: TCurie and Lfrac. TCurie is the first column of
inputs and Lfrac is the second column. The order of the layers in
inputs goes from x=0 to x=L. For example, the first layer listed
should occupy x=0 to x=Lfrac(1) in the regenerator. The layers must be
put in order in the inputs array and mcmfunc cell array. TCurie is a
row vector that contains the Curie temperature of mcm material in each
layer, TCurie must have numlayer elements in the array.  The units are
K. Lfrac is a row vector that contains the portion of the length of
the regenerator bed occupied by each layer. Lfrac must have numlayer
elements in the array and they must add to zero. Each element must be
in the range 0-1.
```

```matlab
% mcmfunc: cell array that contains the function handle for the
material property function used to evaluate the properties of mcm in
each layer.

%% Parse the inputs array
TCurie=inputs(:,1);
Lfrac=inputs(:,2);
[Nx a]=size(x);

%% Check inputs for errors
sumfrac=sum(Lfrac);
sumfrac=round(100*sumfrac)/100;
if sumfrac ~= 1
    fprintf('Fraction of Layers does not sum to 1')
end

if numlayer>Nx
    fprintf('Number of layers cannot be greater than number of spatial
nodes')
end

[NT a]=size(TCurie);
[NL a]=size(Lfrac);
[Nmcm a]=size(mcmfunc);

if (NT ~= numlayer) || (NL ~= numlayer)
    fprintf('Number of elements in inputs does not equal number of
layers\n')
end

%% If only one mcmfunction is given, the function assumes that every
layer is made of the same material
if Nmcm==1
    mcm=mcmfunc;
    for i=1:numlayer
        mcmfunc{i,1}=mcm{1};
    end
end

[Nmcm a]=size(mcmfunc);
if (numlayer ~= Nmcm)
    fprintf('Number of mcm functions does not equal number of
layers\n')
end

%% Calculate material properties for each layer, 1 - numlayer
xfrac=x/L; %dimensionless regenerator position
xlayer(1)=0; %x position of first layer boundary
j=0;
for i=1:numlayer
    j=j+1;
    numstart(i)=j; %node number of starting position of layer i
    xlayer(i+1)=xlayer(i)+Lfrac(i)*L;%x position of i+1 layer boundary
    while (x(j)<=xlayer(i+1)) & (j<Nx)
        j=j+1;
    end
    numfin(i)=j; %node number of ending position of layer i
    mcmfunction=mcmfunc{i}; %get mcm material function for node i
    Tri=Tr(numstart(i):numfin(i),:); %regenerator T of current layer
    muoHi=muoH(numstart(i):numfin(i),:); %mag field of current layer
```

```
    TCuriei=TCurie(i)*ones((numfin(i)-numstart(i))+1,1); %Curie T of
current layer

[cmuoH(numstart(i):numfin(i),:),dsdmuoH(numstart(i):numfin(i),:),rhola
yer,klayer,sr(numstart(i):numfin(i),:),hr(numstart(i):numfin(i),:)]=mc
mfunction(Tri,TCuriei,muoHi,interpS{i},interph0{i});
    rhor(numstart(i):numfin(i))=rholayer;
    kr(numstart(i):numfin(i))=klayer;
end
kr=kr';
rhor=rhor';




function[cmuoH,dsdmuoH,rhor,kr,sr,hr]=Gd(Tr,TCurie,muoH,interpS,interp
h0);
%% Gd  Sample function of type @mcmfun that computes the
        magnetocaloric material properties by numerically
        differentiating the MCM entropy data. Density and thermal
        conductivity of the MCM are defined here.
        Adapted from Engelbrecht 2008 [11].
%INPUTS:
% Tr: regenerator temperature, K
% TCurie: Curie temperature of the regenerator, K
% muoH: magnetic field for each spatial and temporal step, T.
% interpS: interpolant class with entropy data as function of
regenerator temperature and magnetic field.
% interph0: interpolant class with enthalpy data at 0 magnetic field
as function of regenerator temperature.

%Shift Curie temperature if desired, with respect to actual Curie
temperature of material sample (Tcur_ref).
Tcur_ref=293;
Tr_shift=Tr+(Tcur_ref-TCurie);

delta=0.01;%Tesla
DELTA=0.01;%K

%Interpolate experimental entropy data with interpolant function
So=interpS(Tr_shift,muoH);
Sc1=interpS((Tr_shift-DELTA),muoH);
Sc2=interpS((Tr_shift+DELTA),muoH);
Sd=interpS(Tr_shift,(muoH+delta));

%Numerically differentiate entropy data
cmuoH=Tr.*(Sc2-Sc1)/(2*DELTA); %J/kg-K
dsdmuoH=(Sd-So)/delta; %J/kg-K-Tesla
sr=So;%J/kg-K

rhor=7901; %density in kg/m^3
kr=11; %thermal conductivity in W/m-K

%calculate enthalpy at beginning and end of cycle (muoH=0)
hr=interph0(Tr_shift);
```

```matlab
function [interpS, interph0, interpMag]=create_interp(mcmfun)
%% create_interp  This function creates the interpolant classes
                  corresponding to the entropy of the MCM (interpS),
                  its enthalpy at 0 field (interph0) and its
                  magnetization (interpMag), from .mat files containing
                  the former data as function of the temperature and/or
                  magnetic field. These interpolant classes will be
                  used inside the MCM property functions (@mcmfun)
                  with the same name as the data files.

[Nmcm a]=size(mcmfun);
interpS=cell(1,Nmcm);
interph0=cell(1,Nmcm);
interpMag=cell(1,Nmcm);

for i=1:Nmcm
mcmfunction=mcmfun{i}; %get mcm material function for node i

load (func2str(mcmfunction),'-mat'); %load .mat file with material
properties
interpS{i}=griddedInterpolant({T,B},S,'spline');
interph0{i}=griddedInterpolant(T,h_0,'linear');

load (sprintf('%s%s',func2str(mcmfunction),'mag'),'-mat'); %load .mat
file with magnetization data
interpMag{i}=griddedInterpolant({Tarr,Barr},Magarr,'spline');
end
```

B.3 Fluid properties

```matlab
function[muf,kf,cf,rhof,hf,sf]=ethgly50(Tf);
%% create_interp  This is a sample function of type @fluidfun that
                  sets the fluid properties employed by the AMR model.
                  Specifically, this function contains constant
                  property values of ethylene glycol solution at 50%.
                  Adapted from Engelbrecht 2008 [11].

muf=0.0032*ones(size(Tf)); %Viscosity, N-s/m^2
kf=0.394*ones(size(Tf)); % Thermal conductivity, W/m-K
cf=3551*ones(size(Tf)); %Specific heat capacity, J/kg-K
rhof=1030.7; %Density, kg/m^3

%Calculate enthalpy entropy
T_ref = 273.15-36.8; %K, reference point for this fluid
hf=cf.*(Tf-T_ref); %J/kg
sf=cf.*log(Tf/T_ref); %J/kg-K
```

B.4 Demagnetizing effect

```matlab
function [muoH_int, Mo] = DeMagIntLayer(Navg,mcm_inp,mcmfunc,muoH_app,
Tr,muoH_init,numlayer,L,x,interpMag)
%% DeMagIntLayer  This function calculates the internal magnetic field
%                 (muoH_int) in the regenerator based on the applied
%                 field (muoH_app), the demagnetizing factor profile
%                 (Navg) and the magnetization characteristics of each
%                 material in the bed as a function of the temperature
%                 and the internal magnetic field (interpMag). All
%                 along the fluid flow direction. muoH_init is a
%                 initial guess for the internal magnetic field to
%                 speed up convergence. See function mcmprops.m to
%                 learn about how the range of nodes occupied by each
%                 layer is calculated.

%% Parse the inputs array
TCurie=mcm_inp(:,1);
Lfrac=mcm_inp(:,2);
[Nx a]=size(x);

%% If only one mcmfunction is given, the function assumes that every
% layer is made of the same material
[Nmcm a]=size(mcmfunc);
if Nmcm==1
    mcm=mcmfunc;
    for i=1:numlayer
        mcmfunc{i,1}=mcm{1};
    end
end

[Nmcm a]=size(mcmfunc);

% Adapt Navg if it is a constant
[nrow a]=size(Navg);
if nrow==1
    Navg=Navg*ones(Nx,1);
end

xlayer(1)=0; %x position of first layer boundary
j=0;
for i=1:numlayer
    j=j+1;
    numstart(i)=j; %node number of starting position of layer i
    xlayer(i+1)=xlayer(i)+Lfrac(i)*L;%x position of i+1 layer boundary
    while (x(j)<=xlayer(i+1)) & (j<Nx)
        j=j+1;
    end
    numfin(i)=j; %node number of ending position of layer i
    mcmfunction=mcmfunc{i}; %get mcm material function for node i
    magfunc=str2func(sprintf('%s%s',func2str(mcmfunction),'mag'));
    Tri=Tr(numstart(i):numfin(i),:);
    muoH_appi=muoH_app(numstart(i):numfin(i),:);
    muoH_initi=muoH_init(numstart(i):numfin(i),:);
    Navgi=Navg(numstart(i):numfin(i),:);
    TCuriei=TCurie(i)*ones((numfin(i)-numstart(i))+1,1);

    iter=1;
    count_iter=0;
```

```matlab
    muoH_inti=muoH_initi;

    % Calculate demagnetizing field iteratively from magnetization
    while iter
    Moi=magfunc(Tri,TCuriei,muoH_inti,interpMag{i});
    muoH_int_new=muoH_appi+Navgi.*Moi;

    if max(abs(muoH_int_new-muoH_inti))<0.001
    iter=0;
    end

    muoH_inti=muoH_int_new;
    count_iter=count_iter+1;
    end

    muoH_int(numstart(i):numfin(i),:)=muoH_inti;
    Mo(numstart(i):numfin(i),:)=Moi;

end


function Navg=Navg_ctt_prof(muoH,e_chan,e_plate)
%% Navg_ctt_prof  This is a sample function of type @Navgfun that sets
                  the average demagnetizing factor (Navg) profile,
                  which must be defined for all the spatial and time
                  grid. Specifically, this function sets a constant
                  Navg value.

[Nx, Nt]=size(muoH);
Navg=-0.25*ones(Nx, Nt);
```

B.5 Parallel-plate regenerator correlations

```matlab
function[dh,eps,as]=pack_geom(inputs,bedcorrfun);
%% pack_geom  This function calculates model parameters (hydraulic
             diameter, porosity and specific surface area) for
             several packing geometries. The HEIS numerical scheme
             has been developed for the parallel-plate geometry so
             this is the only one included here.
             Adapted from Engelbrecht 2008 [11].
%INPUTS:
% inputs: an array that contains different information about the
regenerator geometry for each type of regenerator. For the case of the
parallel-plates geometry, inputs must be set as follows:
% 1. Dx, plate thickness [m]
% 2. Px, plate spacing (from plate center to plate center) [m]
% 3. w, channel width (case of a rectangular channel) [m]
% 4. dummy variable

geometry=func2str(bedcorrfun);

if (strcmp(geometry,'SphPart2')==1) %spherical particle geometry

    % See Engelbrecht 2008 [11]

elseif(strcmp(geometry,'AlignRect')==1)%parallel-plates regenerator
```

```matlab
    %%parse the input variable
    Dx=inputs(1); %plate thickness
    Px=inputs(2); %plate-to-plate spacing
    %processing...
    as=2/Px;
    eps=1-Dx/Px;
    dh=4*eps/as;

elseif(strcmp(geometry,'AlignRectChan')==1 |
strcmp(geometry,'AlignRectGeom')==1)%aligned rectangular plates
regenerator with rectangular channels

%%parse the input variable
Dx=inputs(1); %plate thickness
Px=inputs(2); %plate-to-plate spacing
w=inputs(3);  %channel width
%processing...
as=2/Px;
eps=1-Dx/Px;
h=Px-Dx;
dh=2*h*w/(h+w);

elseif(strcmp(geometry,'Cyl')==1)%cylindrical microchannels

 % See Engelbrecht 2008 [11]

else
error('geometry not yet coded or mismatch error with geometry and
inputs');
end


function  [v]=speed_distrib(V_amp,pacRAW,bedcorrfun)
%% speed_distrib  This function calculates the fluid velocity in each
                  of the 'nchan' channels of a plates stack given the
                  total volumetric flow rate through the stack 'V_amp',
                  considering that the pressure drop across the
                  channels is the same. The heights of the channels can
                  be different.

n=length(pacRAW);
nchan=pacRAW{1}(4); %Number of channels in the stack
w=pacRAW{1}(3); %Channel width
h=zeros(size(pacRAW));
v=zeros(size(pacRAW));
aux=0;

geometry=func2str(bedcorrfun);

if(strcmp(geometry,'AlignRect')==1)%parallel-plates regenerator

for ii=1:n
 h(ii)=pacRAW{ii}(2)-pacRAW{ii}(1); %Channel height
end

for ii=1:n
    v(ii)=V_amp/w*h(ii)^2/(sum(h.^3)*nchan/n); %nchan/n is the number
of channels with the same heigth
end
```

```matlab
elseif(strcmp(geometry,'AlignRectChan')==1 |
strcmp(geometry,'AlignRectGeom')==1)%aligned rectangular plates
regenerator with rectangular channels

for ii=1:n
    h(ii)=pacRAW{ii}(2)-pacRAW{ii}(1); %Channel height
    aux=aux+(h(ii)*w)^3/(h(ii)+w)^2*nchan/n; %nchan/n is the number of
channels with the same heigth
end

for ii=1:n
    v(ii)=V_amp*(h(ii)*w)^2/((h(ii)*w)^3+(h(ii)+w)^2*(aux-
(h(ii)*w)^3/(h(ii)+w)^2));
end

else
    error('geometry not yet coded or mismatch error with geometry and
inputs');
end




function[Nu_corr,f,dummy,dummy]=AlignRectChan(inputs,Re,Pr,kf,kr,v,muf
,rhof,cf,xf);
%% AlignRectChan  Function of type @bedcorrfun. Calculates the Nusselt
                number and friction factor of the fluid flow through
                a rectangular channel, taking into account the
                entrance effect.

Dx=inputs(1); %Plate thickness
Px=inputs(2); %Plate+channel thickness [m]
w=inputs(3);  %Channel width, [m]
eps=inputs(6); %Volumetric porosity, 0 < eps < 1
dh=inputs(7); %Hydraulic diameter, [m]
cNu=inputs(8); %Scaling factor for Nusselt number
cff=inputs(9); %Scaling factor for friction factor
[n m]=size(Re);
dummy=0; %Dummy output kept for compatibility

%% Calculate friction factor
if Re>0
f=cff*96./Re;
else
    f=0*ones(size(Re));
end

%% Calculate Nusselt number
if Re>0

r=(Px-Dx)/w; %Channel height to width ratio

%Sha and London - uniform heat flux fully-developed Nu
Nu_fd=8.235*(1-2.0421*r+3.0853*r^2-2.4765*r^3+1.0578*r^4-0.1861*r^5);

%Muzychka and Yovanovich - Entrance effect
    sqA=((Px-Dx)*w)^(1/2);
    Re_sqA=Re*sqA/dh;
    Nu_fd_sqA=Nu_fd*sqA/dh;
    x_sqA=xf./(sqA*Re_sqA.*Pr);
```

```matlab
    fPr=0.886./(1+(1.909.*Pr.^(1/6)).^4.598).^(1/4.598);
    fRe=12/(r^(1/2)*(1+r)*(1-192*r/pi^5));
    m_blend=2.27+1.65*Pr.^(1/3);

Nu1_sqA=((fPr./(x_sqA.^(1/2))).^m_blend+((0.517*(fRe./x_sqA).^(1/3)).^
5+Nu_fd_sqA^5).^(m_blend/5)).^(1./m_blend);
    Nu1=Nu1_sqA*dh/sqA;

    if v<0 %Flip Nu because the fluid entrance is at x=L
        Nu1=Nu1(size(Nu1):-1:1);
    end

%Calculate DF to account for 2D conduction in plates, DF = 1/(1+Bi/3)
h_conv=Nu1.*kf/dh;
Bi=h_conv*Dx/2./kr;
DF=1./(1+Bi/3);
Nu_Bi=DF.*Nu1;


Nu_corr=cNu*Nu_Bi;


else %v=0 -> Conduction between fluid and solid
    Rcond=(Dx/4)./kr+((Px-Dx)/2)./kf;
    Nu_corr=dh./(kf.*Rcond);
end
```

B.6   AMR machine architecture

```matlab
function [mdot, muoHapp,  Nx, tnode, tau, dwell, Vres, Ramb_res,
UA_HHEX]=LinearMach(tblow, dblow, muoH_amp, pacRAW, L, Nxmin, Nt1,
Nt2, fluidfun, bedcorrfun)
%% LinearMach  This function calculates the inputs for the AMR model
%              (magnetic field and fluid flow as function of AMR cycle
%              time and characteristics of the reservoirs) of a
%              generic AMRR with reciprocating architecture. The model
%              sets the fluid flow profile considering the flow
%              maldistruibution.
%INPUTS:
%tblow: blow time [s]
%dblow: relative length swept by incoming fluid, with respect to L
%muoH_amp: amplitude of applied magnetic field [T]
%pacRAW{ii} = [e_plate,e_plate+e_chan(ii),w,nchan] Regenerator packing
%L: regenerator length [m]
%Nxmin: Minimum number of spatial steps in the channels
%Nt1: Number of time steps for lag time (1)
%Nt2: Number of time steps for magnetization time (2)
%fluidfun: function for fluid properties
%bedcorrfun: function for geometry-related parameters

%% 1. Set cycle times

%%% 1.1. Lag time
 tlag1=Nt1*0.1; %s, lag in control software before moving magnet
 tlag2=Nt1*0.1; %s, lag in control software before moving regenerator
 Nt1_2=Nt1;

%%% 1.2. Magnetization time
aplate=1000; %m/s2, magnet acceleration
```

```matlab
vplate=0.35; %m/s, magnet velocity
dplate=0.030+L; %m, distance from no-field region to high-field region

tacc_plate=vplate/aplate;
dacc_plate=0.5*aplate*tacc_plate^2;
if dacc_plate>(dplate/2)
    tacc_plate=(dplate/aplate)^(0.5);
    vacc_plate=aplate*tacc_plate;
    tmag=2*tacc_plate;
else
    tacc_plate=vplate/aplate;
    tconstv_plate=(dplate-2*dacc_plate)/vplate;
    tmag=2*tacc_plate+tconstv_plate;
end

%%% 1.3. Blow time (acceleration + established flow + deceleration)
dpist=L*dblow;       %Length swept by fluid, [m]
apist=100; %[m/s2]
if (tblow^2)<(4*dpist/apist)
error('Fluid acceleration setting is too low to sweep dblow meters in
tblow seconds');
end

vpist=(tblow-sqrt(tblow^2-4*dpist/apist))/(2/apist);
tconstv_pist=(dpist-vpist^2/apist)/vpist;
if tconstv_pist<0
    vpist=(tblow+sqrt(tblow^2-4*dpist/apist))/(2/apist);
    tconstv_pist=(dpist-vpist^2/apist)/vpist;
end
tacc_pist=(tblow-tconstv_pist)/2;

%% 2. Calculate number of time steps for max CFL in each channel
during blow period

%%% 2.1. Calculate fluid speed in each representative channel
(rectangular ducts)
[nfil,nchan_mald]=size(pacRAW); %Number of channels with different
heighths
nchan=pacRAW{1}(4); %Number of channels per bed

Ac_chan=0;
for ii=1:nchan_mald
   Ac_chan=Ac_chan+(pacRAW{ii}(2)-pacRAW{ii}(1))*pacRAW{ii}(3);
end
Ac_chan=Ac_chan*nchan/nchan_mald; %Total cross-sectional area of
channels

Vdot_amp=vpist*Ac_chan;  %Total fluid volume flow rate
vchan=speed_distrib(Vdot_amp,pacRAW,bedcorrfun);

%%% 2.2. Calculate number of time steps for CFL=1 in most restrictive
channel
dx=L/Nxmin;
v_chan_amp=max(vchan);

dt4=dx/v_chan_amp; %CFL=1=vdt/dx;
Nt4=ceil(tconstv_pist/dt4);
CFL4=v_chan_amp*(tconstv_pist/Nt4)/dx %Verify CFL=<1
```

```
Nt3=1;
vmax_chan_ramp=v_chan_amp-(v_chan_amp/Nt3)/2;
dt3=dx/vmax_chan_ramp;
Nt3_new=ceil(tacc_pist/dt3);

done=0;

while (done==0)
    if Nt3==Nt3_new
        done=1;
    else
        Nt3=Nt3_new;
        vmax_chan_ramp=v_chan_amp-(v_chan_amp/Nt3)/2;
        dt3=dx/vmax_chan_ramp;
        Nt3_new=ceil(tacc_pist/dt3);
    end
end

%%% 2.3. Calculate number of spatial nodes for dt4 value fixed
Nx=0*vchan;

for ii=1:length(vchan)
if vchan(ii)~= max(vchan)
    dx=vchan(ii)*dt4; %CFL=1=vdt/dx;
    Nx(ii)=floor(L/dx);
else
    Nx(ii)=Nxmin;
end
end

%% 3. Set cycle timing

%%% 3.1. Number of time steps to each event
Ntstart1=Nt1; %regenerator/magnet starts accelerating
Ntstop1=Nt2+Ntstart1; %regenerator/magnet stops in magnetic field
Ntpiststart1=Ntstop1+Nt1_2;%fluid starts flowing
Ntpistacc1=Ntpiststart1+Nt3; %fluid flow reaches constant velocity
Ntpistdec1=Ntpistacc1+Nt4; %fluid flow begins to decelerate
Ntpiststop1=Ntpistdec1+Nt3; %fluid stops flowing
Ntstart2=Ntpiststop1+Nt1; %regenerator/magnet starts accelerating
Ntstop2=Ntstart2+Nt2; %regenerator/magnet stops outside magnetic field
Ntpiststart2=Ntstop2+Nt1_2;%fluid starts flowing
Ntpistacc2=Ntpiststart2+Nt3; %fluid flow reaches constant velocity
Ntpistdec2=Ntpistacc2+Nt4; %fluid flow begins to decelerate
Ntpiststop2=Ntpistdec2+Nt3;%fluid stops flowing
Ntend=Ntpiststop2;

%%% 3.2. Build cycle arrays: time, flow, regenerator/magnet position
%Initialize arrays
tnode(1:Ntend+1)=0;
pplate(1:Ntend+1)=-dplate; %Position of the center of the regenerator
velpist(1:Ntend+1)=0;

for ii=2:Ntstart1+1 %Lag time 1 - Fluid stopped, regen stopped out of
mag field
    tnode(ii)=tnode(ii-1)+tlag1/Nt1; %dt1;
end
for ii=Ntstart1+2:Ntstop1+1 %Magnetization - Fluid stopped, regen
moving inside mag field
    tnode(ii)=tnode(ii-1)+tmag/Nt2;
```

```matlab
        if dacc_plate>(dplate/2) %constantly accelerating
        if tnode(ii)<(tlag1+tacc_plate)
            pplate(ii)=pplate(1)+0.5*aplate*(tnode(ii)-tlag1)^2;
        else
            pplate(ii)=-dplate/2+vacc_plate*(tnode(ii)-
(tlag1+tacc_plate))-0.5*aplate*(tnode(ii)-(tlag1+tacc_plate))^2;
        end
        else %reaches max velocity
        if tnode(ii)<(tlag1+tacc_plate)
            pplate(ii)=pplate(1)+0.5*aplate*(tnode(ii)-tlag1)^2;
        elseif tnode(ii)<(tlag1+tacc_plate+tconstv_plate)
            pplate(ii)=pplate(1)+dacc_plate+vplate*(tnode(ii)-
(tlag1+tacc_plate));
        else
            pplate(ii)=-dacc_plate+vplate*(tnode(ii)-
(tlag1+tacc_plate+tconstv_plate))-0.5*aplate*(tnode(ii)-
(tlag1+tacc_plate+tconstv_plate))^2;
        end
        end

end
for ii=Ntstop1+2:Ntpiststart1+1 %Lag time 2 - Fluid stopped, regen
stopped inside mag field
    tnode(ii)=tnode(ii-1)+tlag2/Nt1_2;%dt2;
    pplate(ii)=0;
end
for ii=Ntpiststart1+2:Ntpistacc1+1 %Cold to hot blow - Piston
accelerating, regen stopped inside mag field
    tnode(ii)=tnode(ii-1)+tacc_pist/Nt3;%dt3;
    pplate(ii)=0;
    velpist(ii)=-apist*(tnode(ii)-(tlag1+tmag+tlag2));
end
for ii=Ntpistacc1+2:Ntpistdec1+1 %Cold to hot blow - Piston moving,
regen stopped inside mag field
    tnode(ii)=tnode(ii-1)+tconstv_pist/Nt4;%dt4;
    pplate(ii)=0;
    velpist(ii)=-vpist;
end
for ii=Ntpistdec1+2:Ntpiststop1+1 %Cold to hot blow - Piston
decelerating, regen stopped inside mag field
    tnode(ii)=tnode(ii-1)+tacc_pist/Nt3;%dt3;
    pplate(ii)=0;
    velpist(ii)=-vpist+apist*(tnode(ii)-
(tlag1+tmag+tlag2+tacc_pist+tconstv_pist));
end
for ii=Ntpiststop1+2:Ntstart2+1 %Lag time 1 - Fluid stopped, regen
stopped inside mag field
    tnode(ii)=tnode(ii-1)+tlag1/Nt1;%dt1;
    pplate(ii)=0;
end
tstart2=2*tlag1+tmag+tlag2+tblow;
for ii=Ntstart2+2:Ntstop2+1 %Demagnetization - Fluid stopped, regen
moving out of mag field
    tnode(ii)=tnode(ii-1)+tmag/Nt2;%dt2;
    if dacc_plate>(dplate/2) %constantly accelerating
        if tnode(ii)<(tstart2+tacc_plate)
            pplate(ii)=-0.5*aplate*(tnode(ii)-tstart2)^2;
        else
            pplate(ii)=-dplate/2-vacc_plate*(tnode(ii)-
(tstart2+tacc_plate))+0.5*aplate*(tnode(ii)-(tstart2+tacc_plate))^2;
```

```matlab
        end
    else %reaches max velocity
            if tnode(ii)<(tstart2+tacc_plate)
                pplate(ii)=-0.5*aplate*(tnode(ii)-tstart2)^2;
            elseif tnode(ii)<(tstart2+tacc_plate+tconstv_plate)
                pplate(ii)=-dacc_plate-vplate*(tnode(ii)-
(tstart2+tacc_plate));
            else
                pplate(ii)=pplate(1)+dacc_plate-vplate*(tnode(ii)-
(tstart2+tacc_plate+tconstv_plate))+0.5*aplate*(tnode(ii)-
(tstart2+tacc_plate+tconstv_plate))^2;
            end
    end
end
for ii=Ntstop2+2:Ntpiststart2+1 %Lag time 2 - Fluid stopped, regen
stopped out of mag field
    tnode(ii)=tnode(ii-1)+tlag2/Nt1_2;%dt2;
end
tpiststart2=2*tlag1+2*tmag+2*tlag2+tblow;
for ii=Ntpiststart2+2:Ntpistacc2+1 %Hot to cold blow - piston
accelerating, regen stopped out of mag field
   tnode(ii)=tnode(ii-1)+tacc_pist/Nt3;%dt3;
   velpist(ii)=apist*(tnode(ii)-tpiststart2);
end
for ii=Ntpistacc2+2:Ntpistdec2+1 %Hot to cold blow - piston moving,
regen stopped out of mag field
   tnode(ii)=tnode(ii-1)+tconstv_pist/Nt4;%dt4;
   velpist(ii)=vpist;
end
for ii=Ntpistdec2+2:Ntpiststop2+1 %Hot to cold blow - piston
decelerating, regen stopped out of mag field
   tnode(ii)=tnode(ii-1)+tacc_pist/Nt3;%dt3;
   velpist(ii)=vpist-apist*(tnode(ii)-
(tpiststart2+tacc_pist+tconstv_pist));
end


[muf,kf,cf,rhof,hf,sf]=fluidfun(293);
mdot=rhof*Ac_chan*velpist'; %Total mass flow rate entering the bed vs
time
tau=tlag1*2+2*tmag+tlag2*2+2*tblow;
dwell=1-2*tblow/tau;


%% 4. Set applied magnetic field in regenerator in time and space
% The magnet is a generic magnet based in an efficient arrangement in
% Tagliafico 2013 ATE 52, in which the high field region provides
% constant applied magnetic field muoHapp.
% High field region measures L m and is centered at x=0 m
% Low field region measures 30 mm and is at both sides of HF region.
% Field in LW region decreases linearly from muoHapp to 0.02 T.

%%% 4.1. Build generic magnetic field profile
dx_B=0.001; %Spatial step for definition of mag field profile, [m]
Nx_NF=L/dx_B;
Nx_LF=(dplate-L)/dx_B;
Nx_HF=L/dx_B;


x=(-dplate-L/2:dx_B:L/2); %Position corresponding to mag field profile

B(1:(Nx_NF+Nx_LF+Nx_HF)+1)=0; %Magnetic field profile array
m=muoH_amp/(dplate-L); %In LF region, B=mx+b(linear increase of field)
```

```
b=(dplate-L/2)*m;
for ii=Nx_NF+2:(Nx_NF+Nx_LF)
B(ii)=m*x(ii)+b;
end
for ii=(Nx_NF+Nx_LF+1):(Nx_NF+Nx_LF+Nx_HF+1)
B(ii)=muoH_amp;
end


%%% 4.2. Build magnetic field array for each different channel (x,t)
muoHapp=cell(1,nchan_mald);


for mm=1:nchan_mald
    for ii=1:Nx(mm)
        muoH(ii,:)=interp1(x,B,(pplate-L/2+(ii-1/2)*L/Nx(mm)));
    end
    muoHapp{mm}=muoH;
end


%% 5. Volume of reservoir and losses to ambient
ins=1; %1= insulation on the cold reservoir   0=remove insulation

Vres=Ac_chan*(dpist+0.001); %Initial volume of reservoir (m)
e_ais=0.02*ins; %Insulation thickness (m)
k_ais=0.035;    %Thermal conductivity of insulation (W/m/K)
k_pist=0.5;     %Thermal conductivity of piston or displacer (W/m/K)
hconv_ri=100;   %Convection coeff. with the regenerator fluid (W/m2/K)
hconv_re=10;    %Convection coefficient with the air (W/m2/K)
UA_HHEX=0.1;    %UA of HEX in hot reservoir (W/K)


Lr_ave=0.001+dpist/2;  %Average length of reservoir during cycle


diapist=2*sqrt(Ac_chan/pi); %Cylindrical reservoir
Rconv_ri=1/((pi()*(diapist/1000)^2/4+pi()*(diapist/1000)*Lr_ave)*hconv
_ri);
Rconv_re=1/((pi()*(diapist/1000)^2/4+pi()*((diapist/1000)+2*e_ais)*Lr_
ave)*hconv_re);
Rcond_r=log(((diapist/1000)+2*e_ais)/(diapist/1000))/(2*pi()*Lr_ave*k_
ais);
Rcond_z=0.01/(pi()*(diapist/1000)^2/4*(k_pist));
Rcond=1/(1/Rcond_r+1/Rcond_z);


Ramb_res=Rconv_ri+Rcond+Rconv_re;
```